DEVELOPMENT AND ADVANCED CHARACTERIZATION OF NOVEL CHEMICALLY AMPLIFIED RESISTS FOR NEXT GENERATION LITHOGRAPHY

A Dissertation
Presented to
The Academic Faculty

by

Cheng-Tsung Lee

In Partial Fulfillment
of the Requirements for the Degree
Doctor of Philosophy in the
School of Chemical and Biomolecular Engineering

Georgia Institute of Technology
December 2008

DEVELOPMENT AND ADVANCED CHARACTERIZATION OF NOVEL CHEMICALLY AMPLIFIED RESISTS FOR NEXT GENERATION LITHOGRAPHY

Approved by:

Dr. Clifford L. Henderson, Advisor
School of Chemical and Biomolecular Engineering
Georgia Institute of Technology

Dr. Laren M. Tolbert
School of Chemistry
Georgia Institute of Technology

Dr. Dennis W. Hess
School of Chemical and Biomolecular Engineering
Georgia Institute of Technology

Dr. Joseph W. Perry
School of Chemistry
Georgia Institute of Technology

Dr. William J. Koros
School of Chemical and Biomolecular Engineering
Georgia Institute of Technology

Date Approved: September 3, 2008

DEDICATION

To my parents, family, and wonderful wife, Yi-Ying, for all their encouragement, support, and love.

ACKNOWLEDGEMENTS

I would like to thank many people for their help and support to the completion of this thesis work. First of all, I would like to express my greatest gratitude to my thesis advisor, Professor Clifford L. Henderson, for taking me as his graduate student and having me to work on a variety of projects mainly related to advanced lithography materials and processing during my stay in his research group. His mentoring and guidance supported and motivated me to overcome problems and achieve goals in my research works. These research works also exposed me to the most pioneering field of research and development essential for the future success of advanced lithography technologies and semiconductor industry. I would like to express my thanks to Professor Dennis W. Hess, Professor William J. Koros, Professor Joseph W. Perry, and Professor Laren M. Tolbert for serving on my thesis committee and providing valuable suggestions and advise of my research work. I would also like to acknowledge Intel Corporation for sponsoring most of my research works.

I would like to thank people who impacted the works presented in this thesis. I am grateful to have the pleasure to work with Dr. Mingxing Wang and Dr. Kennth E. Gonsalves in Department of Chemistry of University of North Carolina at Charlotte for the development and study of novel polymer-bound-PAG resist materials. I am grateful to have Richard A. Lawson in Henderson research group collaborating and studying novel resist materials. Dr. Wang Yueh, Dr. Jeanette M. Roberts, Dr. Todd R. Younkin, and Dr. Ernisse S. Putna in Intel Corporation are also gratefully acknowledged for their suggestion and discussion of my research works and projects. I wish them the best in their future works and careers.

I would like to thank Devin K. Brown and Dr. Raghunath Murali in Microelectronics Research Center of Georgia Institute of Technology for their assistance and useful discussion on the training and operation of the electron-beam lithography system. I would also like to thank many of the past and present members in Henderson and Hess research group. In particular, many thanks to Dr. Yueming Hua for his help on thin metal films deposition and thin-film metrology using atomic force microscopy, to Dr. Ashiwini K. Sinha for many useful discussions and enormous supports on the training of instruments, to Dr. Galit Levitin and Dr. Ingu Song for their support of x-ray photoelectron spectroscopy, and to Hua-Wei Chu and Aparna Boddapati for their support and assistance.

Finally, I would like to thank my parents for all their support and the encouragement they have made over these years to make my pursuing of advanced degrees possible. I would also like to thank my dear wife Yi-Ying for her love, understanding, and patience during these four years of my graduate study.

TABLE OF CONTENTS

LIST OF TABLES

LIST OF FIGURES

LIST OF ABBREVIATIONS

CAR	Chemically amplified resist
CD	Critical dimension
CMOS	Complementary metal–oxide–semiconductor
DRAM	Dynamic random access memory
EB, EBL	Electron-beam, electron-beam lithography
EUV, EUVL	Extreme ultraviolet, extreme ultraviolet lithography
EUV-MET	EUV micro-exposure tool
EUV-IL	EUV interference lithography
FET	Field-effect transistor
FTIR	Fourier transform infrared spectroscopy
^{1}H NMR	Proton-1 nuclear magnetic resonance
IC	Integrated circuit
ICP	Inductively coupled plasma
IDE	Interdigitated electrode
ILS	Image log slope
LELE	Litho-etch-litho-etch
LER	Line edge roughness
LPCVD	Low pressure chemical vapor deposition
LWR	Line width roughness
NA	Numerical aperture
NGL	Next generation lithography
NILS	Normalized image log slope
OPC	Optical proximity correction
PAG	Photoacid generator
PEB	Post-exposure bake
RIE	Reactive ion etch
SEM	Scanning electron microscope
UV/VIS	Ultraviolet/visible
XPS	X-ray photoelectron spectroscopy

SUMMARY

The microelectronics industry has made remarkable progress with the development of integrated circuit (IC) technology which depends on the advance of micro-fabrication and integration techniques. On one hand, next-generation lithography (NGL) technologies which utilize extreme ultraviolet (EUV) and the state-of-art 193 nm immmersion and double patterning lithography have emerged as the promising candidates to meet the resolution requirements of the microelectronic industry roadmap. On the other hand, the development and advanced characterization of novel resist materials with the required critical imaging properties, such as high resolution, high sensitivity, and low line edge roughness (LER), is also indispensable. In conventional multi-component chemically amplified resist (CAR) system, the inherent incompatibility between small molecule photoacid generator (PAG) and the bulky polymer resin can lead to PAG phase separation, PAG aggregation, non-uniform PAG and acid distribution, as well as uncontrolled acid migration during the post-exposure baking (PEB) processes in the resist film. These problems ultimately create the tri-lateral tradeoff between achieving the desired lithography characteristics. Novel resist materials which can relief this constraint are essential and have become one of the most challenging issues for the implementation NGL technologies.

This thesis work focuses on the development and characterization of novel resist materials for NGL technologies. In the first part of the thesis work, advanced characterization techniques for studying resist fundamental properties and lithographic performance are developed and demonstrated. These techniques provide efficient and

precise evaluations of PAG acid generation, acid diffusivity, and intrinsic resolution and LER of resist materials. The applicability of these techniques to the study of resist structure-function relationships are also evaluated and discussed. In the second part of the thesis work, the advanced characterization and development of a novel resist system, the polymer-bound-PAG resists, are reported. The advantages of direct incorporation of PAG functionality into the resist polymer main chain are investigated and illustrated through both experimental and modeling studies. The structure-function relationships between the fundamental properties of polymer-bound-PAG resists and their lithographic performance are also investigated. Recommendations on substantial future works for characterizing and improving resist lithographic performance are discussed at the end of this thesis work.

CHAPTER 1

MICROELECTRONICS AND MICROLITHOGRAPHY

1.1 Microelectronics

Integrated circuit (IC) technology has undergone rapid and dramatic improvements over the past 50 years. The rapid developments have led to the incredibly complex and powerful IC devices which are pervasive today in everything from computers to toaster ovens. In the early 1940s, electronic devices were originally composed of giant and cumbersome vacuum tubes which consumed large quantity of power, generated huge quantities of heat, and occupied huge amount of space to operate. The next revolution in electronic devices was the result of the invention of the world's first transistor device, developed and demonstrated by Walter Bardeen, John Brattain, and William Shockley at Bell Labs in 1947.[1-3] This originally macroscopic and crude device quickly led to the single field-effect transistor (FET) device that was composed of four terminals known as the gate, drain, source and body/substrate. The basic structure of a packaged device and a schematic of the internal device are shown in figure 1.1. The P-type and N-type silicon regions are areas of the silicon substrate doped with electron acceptors (e.g. Boron) and donors (e.g. Phosphorus), respectively. By applying sufficient positive voltage bias on the gate electrode above a threshold value, the electrons in the P-type silicon accumulate at the interface of the P-type silicon and the gate oxide insulator and create a conductive N-channel. This conductive channel extends and connects the source and the drain, and the electronic current is conducted through it when a voltage bias is applied to source and drain electrodes. By switching the gate voltage above and behold the threshold value, the transistor can be modulated between its ON (i.e. electrons flowing drain to source) and OFF (i.e. no current flow between source and drain). This

simple electronic analog to a valve constitutes the basic functional device that helped usher in the era of modern microelectronics.

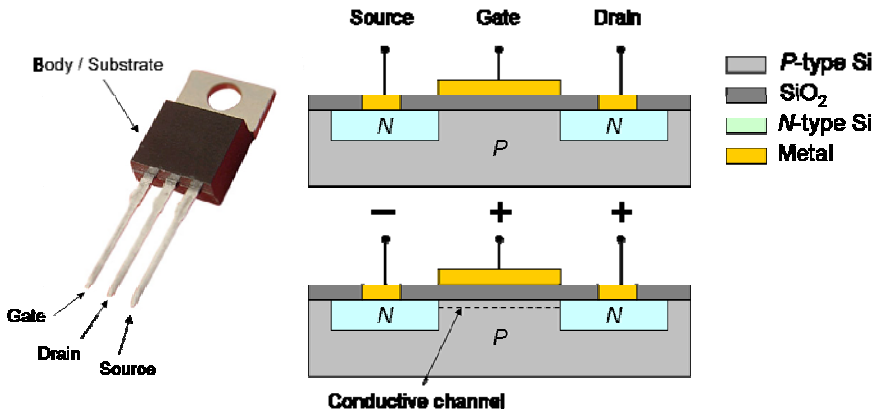

Figure 1. 1 The structure of a single N-channel FET and the working function diagram.

Despite the invention of the transistor prototype, the design and materials used for connections between transistors were still complex and unreliable, meaning that high-volume and high-density fabrication could not be realized by using the original design concept. The next big advance came when Jack Kilby and Robert Noyce invented the first monolithic IC fabrication technology which integrated all the necessary passive and active components into a single piece of semiconductor material (silicon or germanium). Monolithic IC technology solved many of the problems associated with the increase of circuit feature density, connections between devices, and mechanical fatigue of the solder joints.[4] Monolithic technology opened the era of micro-fabrication for making solid-state devices, such as capacitors, inductors, transistors, and interconnects on the same piece of silicon. In this way, the space between devices can be greatly reduced and the density of active devices making up an electronic circuit can be increased many thousands times over that achievable with discrete or single-transistor device. A cross-section view of a scanning electron microscopy (SEM) image of a modern microprocessor is shown in figure 1.2. The front-end processing includes the fabrication of high resolution poly gate

and contact structures at the individual transistor level of the IC structure (i.e. at the bottom of the layers near the silicon substrate) The back-end processing includes the construction of larger-sized contacts and interconnects above the transistor level that connects the individual transistors in various ways to make complex logic and memory devices possible.

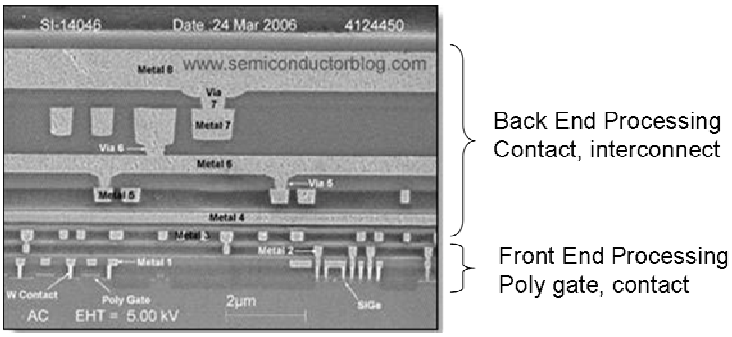

Figure 1. 2 SEM cross-section image of a die of an Intel mobile chip "Yonah".[5]

The consistent trends of increasing transistor density and number in electronic devices was first observed and predicted by Intel Corporation® co-founder Gordon E. Moore in 1965, and his statements about this trend have now become the well known Moore's Law.[6] Moore's Law essentially states that the number of transistors that can be inexpensively placed into an IC chip is increasing exponentially and doubles approximately every two years. Although originally based on a very limited set of device data over only a few generations of IC devices, this trend has continued for more than half a century and is not expected to stop at least for another decade and perhaps much longer.[7] Today, commercially available IC devices integrate more than one hundred million transistors in a single chip, quite an improvement over the single isolated transistor first developed in 1947. Intel Corporation® announced the first quad-core processor which integrates more than 800 million transistors fabricated using so-called 45 nm high-k metal gate silicon technology in the fourth quarter of the year 2006.[8] This 45

nm technology provides nearly doubled transistor capacity in the same silicon space as compared to the previous 65 nm technology generation announced in early 2005, as well as higher device performance and reduced leakage power. The continuous shrinking down of transistor size not only delivers greater performance leaps in succeeding generations of modern electronic devices, but also provides the dramatic breakthroughs observed in energy consumption efficiency over time.

1.2 Microlithography

The fabrication of high density IC devices today requires manufacturing methods that possess nanometer scale resolutions. The ability to manufacture ever smaller transistor circuit elements that are critical to IC technology progression has been enabled by advancements in the *microlithography* techniques and materials used to pattern hierarchical layers which make up the functionality of IC devices. Microlithography refers to the process involved in transferring the desired micro- or nano-scale patterns from a designed circuit pattern to each layer of a semiconductor device. Microlithography involves a variety of steps ranging from mask making to the final development of relief images in a soft-masking layer coated on a substrate that will be used in subsequent etching or implementation steps to template the operation. The process steps in microlithography are conceptually very simple, as shown in figure 1.3. The substrate is first spin-coated with a polymer thin film material called a *photoresist*. Photoresist is typically an organic material designed such that exposure to radiation can change the physiochemical properties of the photoresist and enable the solubility switch of the photoresist film in appropriate solvents or aqueous-base solutions. The desired circuit pattern, which has been previously made on a *photomask* or *reticle*, is transferred to this photoresist film via exposure through the photomask using a lithography tool (e.g.

projection stepper or projection scanner) equipped with a radiation source (e.g. ultraviolet (UV) radiation generated by a Hg/Xe lamp). A *development* process which selectively removes the photoresist film via the solubility difference of the exposed and unexposed regions is then performed by soaking or spraying the photoresist film in a developing solution. The patterned photoresist film is used as a masking layer (i.e. a soft-mask) to protect and isolate the covered regions of the substrate from processes such as plasma dry etching and ion implementation. The photoresist layer is finally stripped away from the substrate to complete patterning of a layer.

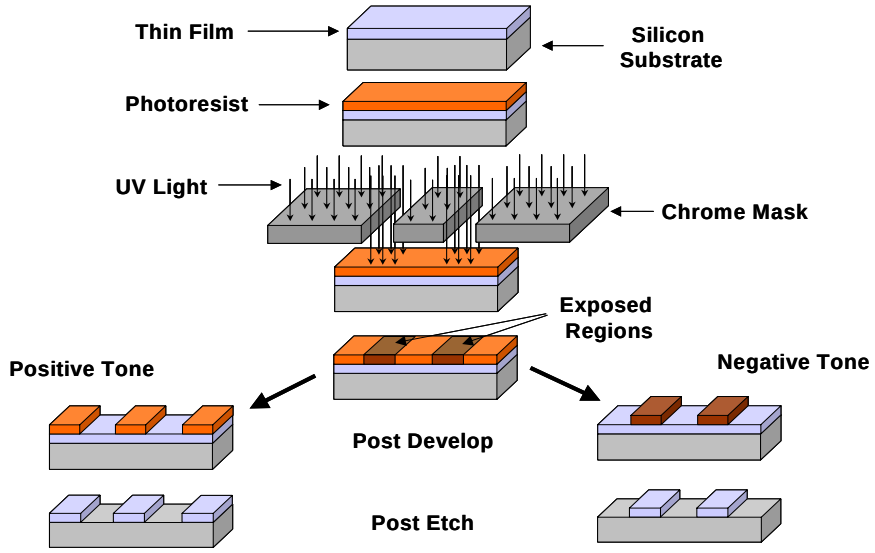

Figure 1. 3 General concept of the lithography and pattern formation processes

One of the major drives of microlithography technology over the past 50 years has been to develop higher resolution exposure optics and tools which are capable of producing aerial images of smaller feature sizes. The theoretical resolution *R* and depth of focus *DOF* of an optical projection exposure system used today for lithography purpose can be simply described using a diffraction-limited model similar to the Rayleigh criterion as shown in equation (1.1).

$$R = k_1 \frac{\lambda}{NA}$$
$$DOF = \pm k_2 \frac{\lambda}{NA^2} \tag{1.1}$$

Here k_1 and k_2 are primarily parameters that accounts for the capability, such as chemical and development contrasts, of a photoresist material to resolve a particular aerial image pattern (typically in the range of 0.3 to 0.8), λ the wavelength of the exposure radiation, and NA the numerical aperture of the optical projection lens. NA of an optical system is a dimensionless number that characterizes the range of angles over which the optical lens can accept or emit light and is defined as equation (1.2).

$$NA = n \times \sin\theta \tag{1.2}$$

Here n is the index of refraction of the medium in which the lens is working (1.0 for air, 1.33 for pure water, and up to 1.56 for oils), and θ the half-angle of the maximum cone of light that can enter or exit the lens. As can be seen in equation (1.1), methods for increasing resolution and depth of focus of optical projection exposure tools are to decrease the wavelength of the radiation used, or to improve the resist material properties to increase k_1 and k_2. These methods have indeed been put into practice by transitioning the radiation wavelength from the 436 nm (G-line) and 365 nm (I-line) wavelengths used early on to the currently most advanced optical systems operating at 193 nm. The achievable aerial image resolution under the Rayleigh criterion at different wavelength and NA is listed in table 1.1.[9]

Obviously the resolution capability of optical lithography is fundamentally limited by diffraction phenomenon and thus the radiation wavelength. Research is ongoing to develop alternative lithography technologies which can eliminate the diffraction limitation and support the continuation of Moore's Law. Technologies having

Table 1. 1 Parameters and resolutions of stepper optics.

Wavelength (nm)	Numerical aperture (NA)	Rayleigh resolution (μm)	Year of first use	Light source
436	0.30	0.89	1982	Hg arc lamp (G-line)
365	0.45	0.49	1990	Hg arc lamp (I-line)
365	0.60	0.37	1994	Hg arc lamp (I-line)
248	0.50	0.30	1994	Hg arc lamp or KrF excimer laser
248	0.60	0.25	1997	KrF excimer laser
248	0.70	0.22	1999	KrF excimer laser
193	0.75	0.16	2001	ArF excimer laser
193	0.85	0.14	2003	ArF excimer laser

the potential for printing sub-50 nm technology nodes are termed as *Next Generation Lithography* (NGL) technologies. Among the thought of NGL candidates, the first trial is pushing the existing resolution of 193 nm lithography technologies further. *Immersion lithography* is one class of techniques that replaces the usual air gap between the objective lens and the photoresist surface with a liquid medium having higher refractive index than air. A typical immersion lithography setup is illustrated in figure 1.4. An additional step which is different from dry lithography is that the immersion liquid is continuously injected into the gap between the objective lens and the photoresist film surface and removed while exposure in progress. According to fundamental Fourier optics (equation 1.1 and 1.2) the resolution is enhanced by a factor equal to the refractive index of the liquid. For the case if using pure water as the immersion liquid at 193 nm wavelength, the refractive index is 1.44 and a resolution enhancement is approximately 40% of the highest achievable resolution of 193 nm dry lithography. Immersion lithography has been successfully implemented in the fabrication of 65 nm and 45 nm node critical layers.[10] It is currently expected that 193 nm immersion lithography can further extend its resolution capability down to 32 nm technical node through the development and use of fluids with higher refractive indexes.[11]

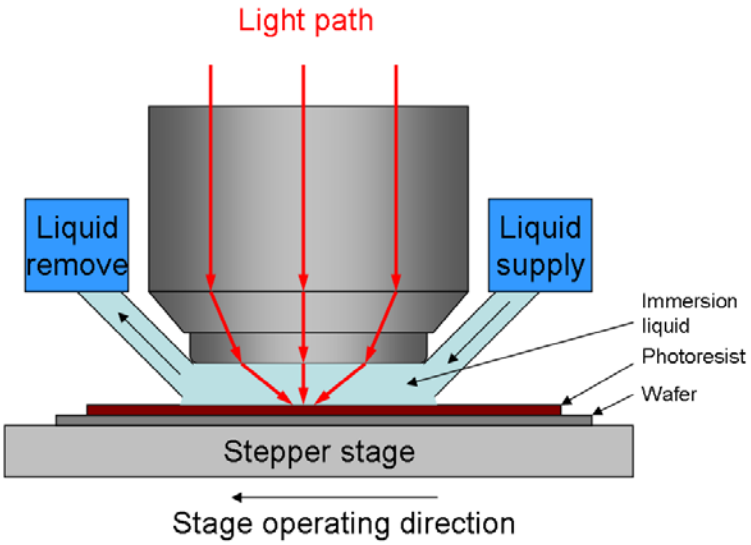

Figure 1. 4 Diagram of a typical immersion lithography optics.

Another class of enhanced 193 nm technologies is the *double patterning* technique which is introduced for the fabrication of 32 nm node and beyond. As implied by the name, double patterning technique achieved advanced resolution by generating the final pattern via the overlapping of two separate patterning processes (i.e. by repeating some combination of lithography and/or etch steps to build each patterned layer). This technique has several different versions as shown in figure 1.5, depending on the design and sequence of processing steps. Double exposure method decomposes the final dense mask pattern into two separate semi-dense masks which are patterned on the same resist layer to produce the desired pattern.[12] Heterogeneous mask is a method which applies a litho-etch-litho-etch (LELE) process to generate dense pattern.[13] The first lithography step transfers the pattern onto a hard mask through the first etch, while the second lithography transfers the pattern between patterns on the hard mask and the final pattern on the substrate is generated through the second etch step.

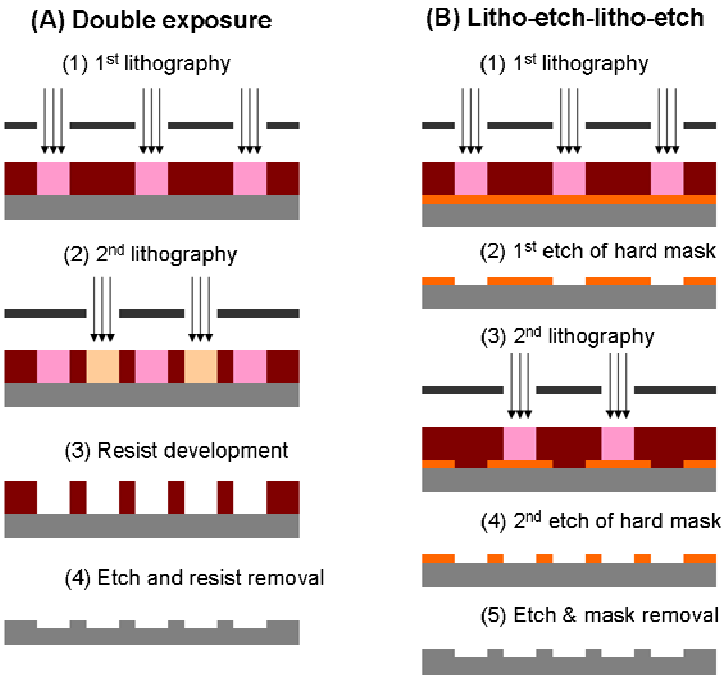

Figure 1. 5 Double patterning techniques for fabricating dense pattern via (A) double exposure and (B) LELE approaches.

Extreme ultra-violet lithography (EUVL) has been selected as one of the most promising NGL technologies for sub-32 nm resolution patterning.[14-16] Using the wavelengths of radiation in the range of 11~14 nm, reflecting optics can be made by constructing multilayer films with moderate efficiency. For example a defect-free multilayer reflector composed by alternating layers of high-Z and low-Z materials, such as Molybdenum(Mo)/Silicon(Si), can give a small but effective difference between refractive indexes at each interface. A typical EUV mirror made with coatings of such alternating films can reflect about 65% of the incident photons. Such reflection efficiency enables the implementation of projection optics and reduction imaging in an EUVL system. Typical design of EUV optics composes of a laser or discharge generated plasma generating EUV radiation source, a multilayer reflecting photomask, and several multilayer projection mirrors, as shown in figure 1.6. The use of a very small exposure wavelength can take advantage of using small numerical aperture optics that enhances the

resolution without losing depth of focus. Many of the imaging problems associated with mask design and fabrication can also be eliminated by the use of reduction optics. Because the photons in EUVL system are reflected by several mirrors before they hit the wafer, only 1 to 2% of the original photons can finally hit the target. Before EUVL can be installed for mass fabrication, research and development on advanced EUV power sources are necessary for shortening the exposure time and improving the wafer throughput.

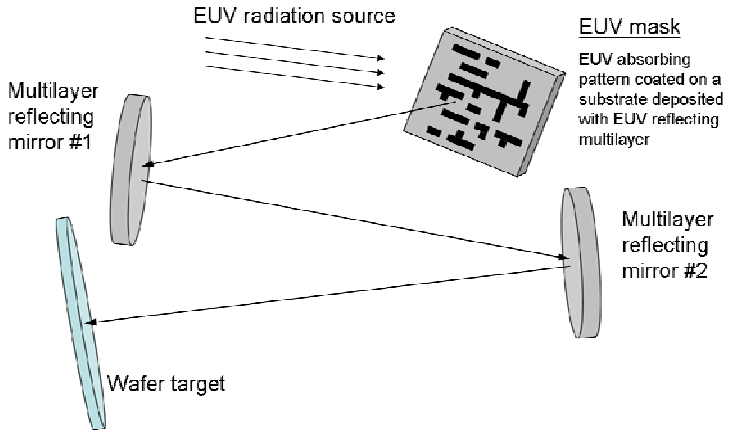

Figure 1. 6 A schematic illustration of EUV lithography optics.

Another promising NGL for sub-32 nm resolution patterning is the use of high resolution direct-writing *electron-beam lithography* (EBL), also known as the *maskless lithography* technology.[17] High resolution EBL system uses thermally-enhanced field emission electron source, such as heated tungsten/zirconium dioxide (W/ZrO_2), to generate electron beam with small source/beam size (~20 nm), low energy spread (~0.9 eV), enhanced brightness (~10^8 A/cm^2/sr), and high system stability. As shown in figure 1.7, pattern data is inputted into a console and decomposed into small fields for patterning. The patterning is controlled by both the movement of the workstage and the deflection of the electron beam controlled by electromagnetic optics (deflectors).[18]

Electrons with 50~100 keV energy have extremely short wavelength and are typically used for the direct writing of patterns for small scale fabrication of photomask or wafer. The extreme short wavelength property of high energy electron beam leads to the required dimension for diffraction phenomenon being atomic level and shows the potential of patterning feature size below 10 nm resolution. EBL also has extremely large depth of focus, usually several microns, providing the relief from major diffraction limitations associated with traditional optical lithography. EBL however has electron scattering effect when electrons passing through matter that may cause the degradation of resolution and the generation of proximity effects. On the other hand, a single beam EBL system which can not transfer patterns to the wafer in parallel has relatively low wafer production efficiency. There is only few wafers productivity per day in contrast to several hundreds produced by optical projection steppers. The throughput limitation of EBL is still the major expense of achieving high resolution and is currently the bottleneck for mass production.

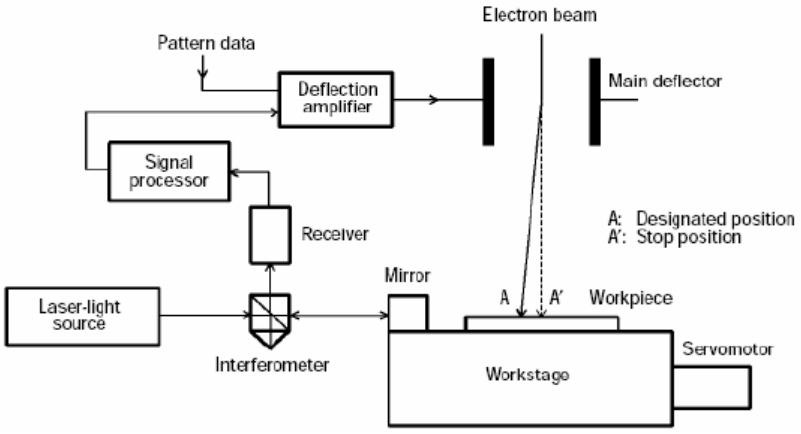

Figure 1. 7 Schematic illustration of the EB direct writing lithography system.[18]

1.3 Photoresist materials

In conjunction with the development of lower wavelength exposure tools and alternative techniques for patterning higher resolution features as mentioned in section 1.2, the corresponding improvements in photoresist material are necessary for the successful implementation of advanced lithography tools and techniques (i.e. effectively reducing k_1 and k_2 factors for each wavelength generation over its lifetime). As listed in table 1.1, the first two radiation wavelengths (i.e. G-line and I-line) were originally generated using mercury (Hg) arc lamps, but when the transition was made to the implementation of 248 nm (DUV) lithography, the photon output of a mercury lamp at 248 nm was significantly weaker as compared to G-line and I-line wavelengths. Such a dramatic reduction in the output of photons at the exposure wavelength required the development of new photoresist materials that possessed much higher photosensitivity as compared to the common resists used for the G-line and I-line exposure tools. This higher sensitivity was required to maintain and ultimately improve wafer throughput of the lithographic process. Originally the resist materials used in G-line and I-line lithography technologies were dissolution inhibition-based resists, known as diazonaphthoquinone-novolac or novolac/DNQ photoresists.[19] The structure and the imaging mechanisms of a typical novolac/DNQ photoresist are illustrated in figure 1.8.

Novolac/DNQ resists utilize a hydrogen bonding-based interaction which controls dissolution inhibition/acceleration of the novolac resin via the photoreaction of the DNQ molecule. The dissolution inhibition mechanism was successfully applied as the primary imaging mechanism for nearly 30 years in G-line and I-line lithography before the problems were encountered in resist sensitivity in switching to 248 nm (i.e. so-called deep-ultraviolet or DUV technology).

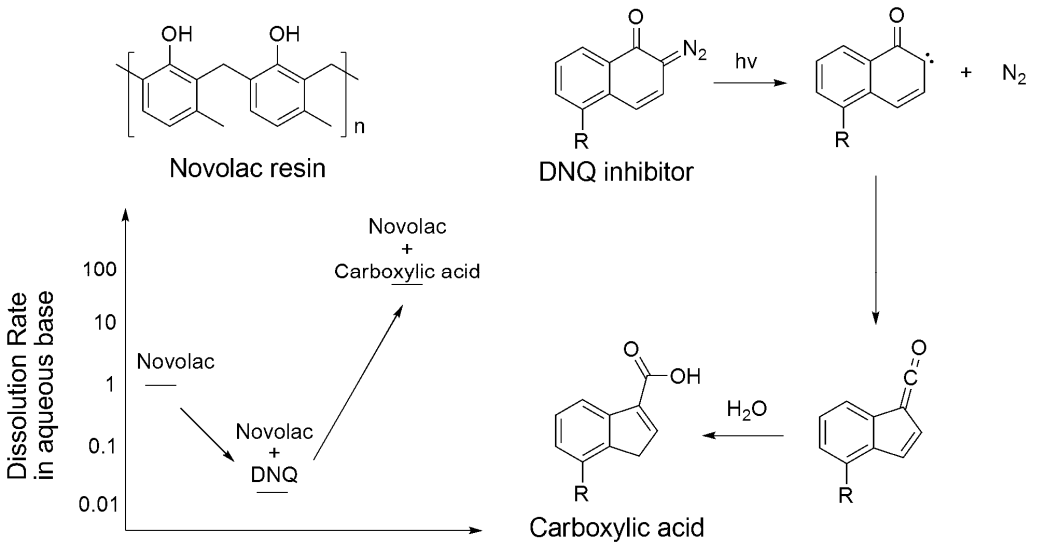

Figure 1. 8 Photoreaction of DNQ molecule and the imaging mechanism of a novolac/DNQ photoresist.

The dramatic decrease of photon generation efficiency at DUV wavelength region leads to this imaging mechanism no longer useful both due to the opacity and the slow photospeed of these materials (i.e. they would have required extremely long exposure times). Photosensitivity issue led to the birth and the follow-up development of so-called *chemically amplified resists* (CARs).[20] CARs have been the dominant high resolution photoresist platform technology beginning with the DUV exposure tool generation. The related development and characterization of CARs are discussed in chapter 2. CARs have been the workhorse resist material of the semiconductor industry for approximately 15 years, but such materials are now approaching what appear to be performance roadblocks that threaten the continued success of their implementation in NGL technologies. The understanding of the physiochemical properties and limitations of modern CARs and the use of this knowledge for developing novel resist materials with improved lithography performance which can enable successful implementations of NGL technologies is an overarching goal of the thesis work.

1.4 References

[1] Bardeen, J.; Brattain, W., The transistor, a semi-conductor triode, *Phys. Rev.* **1948**, *74*, 230-231.

[2] Brattain, W.; Bardeen, J., Nature of the forward current in germanium point contacts, *Phys. Rev.* **1948**, *74*, 231-232.

[3] Shockley, W., The path to the conception of the junction transistor, *IEEE Trans. Elec. devices* **1976**, *ED-23*, 597-620.

[4] Reid, T., The chip: *How two Americans invented the microchip and launched a revolution*, Simon and Schuster **1984**, New York, USA.

[5] The cross-section SEM image is reprinted from semiconductorblog.com website. (http://www.semiconductorblog.com/index.php?tag=packaging)

[6] Moore, G. E., Cramming more components onto integrated circuits, *Electronics* **1965**, 38.

[7] Kanellos, M., Moore's law to roll on for another decade, *CNET News.com* **2003**. (http://news.cnet.com/2100-1001-984051.html)

[8] Krzanich, B.; Natarajan, S., Intel silicon & manufacturing update, **2007**. (http://download.intel.com/pressroom/kits/events/idffall_2007/BriefingSilicon &TechManufacturing.pdf).

[9] Levinson, H. J., Optical pattern formation, in *Principle of lithography, 2nd Edition*, SPIE Optical Engineering Press, **2004**, Bellingham, Washington, USA.

[10] Grose, D., 2007 Technology Analyst Day, Sunnyvale, California, USA. (http://www.amd.com/us-en/assets/content_type/DownloadableAssets/ July2007AMDAnalystDayDougGrose)

[11] Borodovsky, Y., Marching to the beat of Moore's Law, *Proc. SPIE* **2006**, *6153*, 615301.

[12] Double exposure is the basis of the dual dipole lithography (DDL) developed by Brion Technology Inc. (http://www.brion.com/dpt_ddl_summary.asp).

[13] Bailey, G. E.; Tritchkov, A.; Park, J.-W.; Hong, L.; Wiaux, V.; Hendrickx, E.; Verhaegen, S.; Xie, P.; Versluijs, J., Double pattern EDA solutions for 32 nm HP and beyond, *Proc. SPIE* **2007**, *6521*, 65211K.

[14] Gwyn, C. W.; Stulen, R.; Sweeney, D.; Attwood, D., Extreme ultraviolet lithography, *J. Vac. Sci. Technol.* B **1998**, *16*, 3142-3149.

[15] Fontaine, B. L.; Deng, Y.; Kim, R.; Levinson, H. J.; Okoroanyanwu, U.; Sandberg, R.; Wallow, T.; Wood, O., Extreme ultraviolet lithography: from research to manufacturing, *J. Vac. Sci. Technol.* B **2007**, *25*, 2089-2093.

[16] Wu, B.; Kumar, A., Extreme ultraviolet lithography: a review, *J. Vac. Sci. Technol.* B **2007**, *25*, 1743-1761.

[17] McCord, M. A.; Rooks, M. J., Electron beam lithography, in *Handbook of Microlithography, Micromachining, and Microfabrication Vol.1 Microlithography*, SPIE Optical Engineering Press, **1997**, Bellingham, Washington, USA.

[18] Brown, D. K.; Murali, R.; Current nanolithography research summary, in Microelectronic Research Center (MiRC) Nanolithography website (http://www.nanolithography.gatech.edu/EBL_current_research.htm)

[19] Dammel, R. R., Diazonaphthoquinone-*based resists*, SPIE Optical Engineering Press, **1993**, Bellingham, Washington, USA.

[20] Ito, H.; Willson, C. G., Chemical amplification in the design of dry developing resist materials. *Polymer Eng. and Sci.* **1983**, *23*, 1012-1018.

CHAPTER 2

DEVELOPMENT AND CHARACTERIZATION OF CHEMICALLY AMPLIFIED RESISTS

2.1 Concept of Chemical Amplification

Before the introduction of DUV lithography, novolac/DNQ resist platform have supported the G-line and I-line lithography technologies for many years as mentioned in chapter 1. While switching from 365 nm to 248 nm radiation wavelengths for enhancing the resolution down to 0.25 μm and 0.13 μm, the significant decrease of photon density which can be generated by the exposure tool, as well as the strong absorbance of the novolac resin at 250 nm regions, brought out the insufficient photosensitivity issue of the resist material. Resist photosensitivity is one of the major parameters to be considered in semiconductor industry because it directly impacts wafer throughput and therefore device manufacturing cost. Efforts had been made for improving novolac/DNQ resist photosensitivity by modifying its chemical structures and compositions, however the enhancement came out being merely marginal since the *quantum efficiency*, which is expressed as the number of DNQ molecules transformed per photon absorbed, is still within the range of 0.2~0.3 and can not exceed 1.0 by definition. The utilization of DUV lithography technology indeed required a novel resist platform and a new imaging concept which can provide over several orders photosensitivity improvement than novolac/DNQ resists.

The concept of chemical amplification was proposed and introduced by Hiroshi Ito, Grant Willson, and Jean Frechet in 1982 in order to deal with the resist

photosensitivity issue associated with DUV lithography.[1] The design concept of a chemical amplification system, and thus a CAR, is that the initial photochemistry produces a catalyst which can interact with the surrounding polymer matrix to pursue a cascade of chain reactions which can chemically enhance the resist imaging process. CAR was first introduced into microelectronics fabrication by IBM in the late-1980s for producing millions of 1-Mbit and 16-Mbit dynamic random access memory (DRAM) devices by DUV lithography.[2,3] The CAR used in DRAM fabrication that time was a blended system composed of a polymer resin and a photoactive compound, as shown in figure 2.1. The polymer resin is a poly(4-hydroxystyrene) (pHOST) protected by an acid-labile *tert*-butoxycarbonyl (t-BOC) functional group. The photoactive compound was a triphenylsulfonium hexafluoroantimonate ($TPS.SbF_6$) which generates acid upon photo-decomposition and is normally termed as the *photoacid generator* (PAG). The CAR was composed of 4.75 wt% $TPS.SbF_6$ to the total solid.

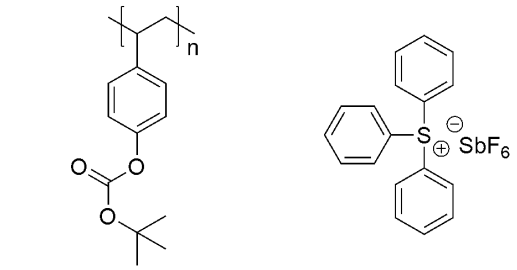

t-BOC protected pHOST $TPS.SbF_6$

Figure 2. 1 The structure and composition of the first CAR introduced by IBM.

The imaging mechanism of a CAR is shown in figure 2.2. The first step is called PAG acid generation, in which the $TPS.SbF_6$ molecule absorbs the photon energy upon exposure to radiation and produces a strong hexafluoroantimonic acid ($H^+SbF_6^-$). The second step is called acid-catalyzed *deprotection*, in which the generated acid catalytically cleaves the lipophilic carbonates of polymer subunits and renders them into

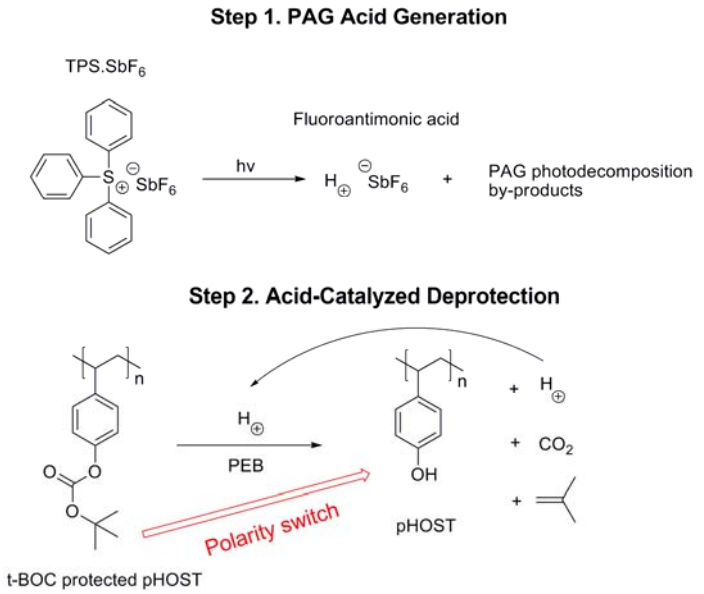

Figure 2. 2 Imaging mechanisms of CARs

hydrophilic sites, such as the hydroxyl group in this case. In general, the deprotection reaction requires elevated temperatures and can be promoted by performing a post-exposure bake (PEB) of the resist film. The catalytic chain length of each acid has been determined being several hundreds under moderate PEB conditions.[4] A positive-tone pattern is then developed by rinsing the resist film into an aqueous base developer, such as a 0.26 N tetramethylammonium hydroxide (TMAH) solution, to dissolve the deprotected polymer (i.e. pHOST). A negative-tone image can also be obtained by using a non-polar organic solvent such as anisole to dissolve protected polymer (i.e. t-BOC protected pHOST). As opposed to hydrogen bond based interaction which regulates dissolution inhibition/acceleration in novolac/DNQ resists, the protection/deprotection scheme in CARs provides resin polarity switch which can create extraordinary solubility differences (more than 5-order dissolution rate difference in aqueous base solutions) between protected and deprotected polymers. This high solubility contrast leads to a resist material which has the capability to relieve very small features with very sharply-defined pattern edges. The polarity switch scheme can also prevent the image distortion

effect caused by solvent swelling which is commonly experienced in negative-tone resists using cross-linking dissolution inhibition as the patterning mechanism.

Various PAGs have been synthesized and used in CARs for different exposure techniques. The structures of PAGs commonly used in CAR are shown in figure 2.3. PAGs can be categorized into two major groups: *ionic* and *non-ionic* PAGs. Iodonium and sulfonium salts, which are often called onium salts, are major ionic PAGs. Triarylsulfonium salts are the most thermally-stable PAGs which possess thermal-decomposition temperatures at around 350^{o}C. Sulfonate esters and sulfonyl compounds, which generate strong sulfonic acids when exposure to radiation, have also been developed as non-ionic PAGs for the use in CARs.[5,6] The photodecomposition mechanisms of triarylsulfonium slats are illustrated in figure 2.4.[7,8] The direct PAG photolysis is proposed to occur from the singlet excited state to give a predominant heterolytic cleavage along with some homolytic cleavage. In a viscous medium such as a solid-state resist film, the cage effect dominates the distribution of PAG photodecomposition products. Acids generated through PAG photodecomposition can be organic or metallic depending on the anions used in the PAG molecule.

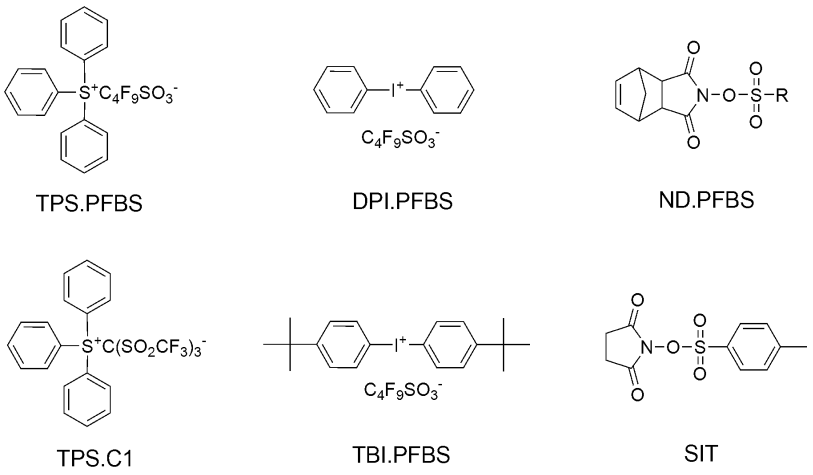

Figure 2. 3 Structures of PAGs commonly used in CARs

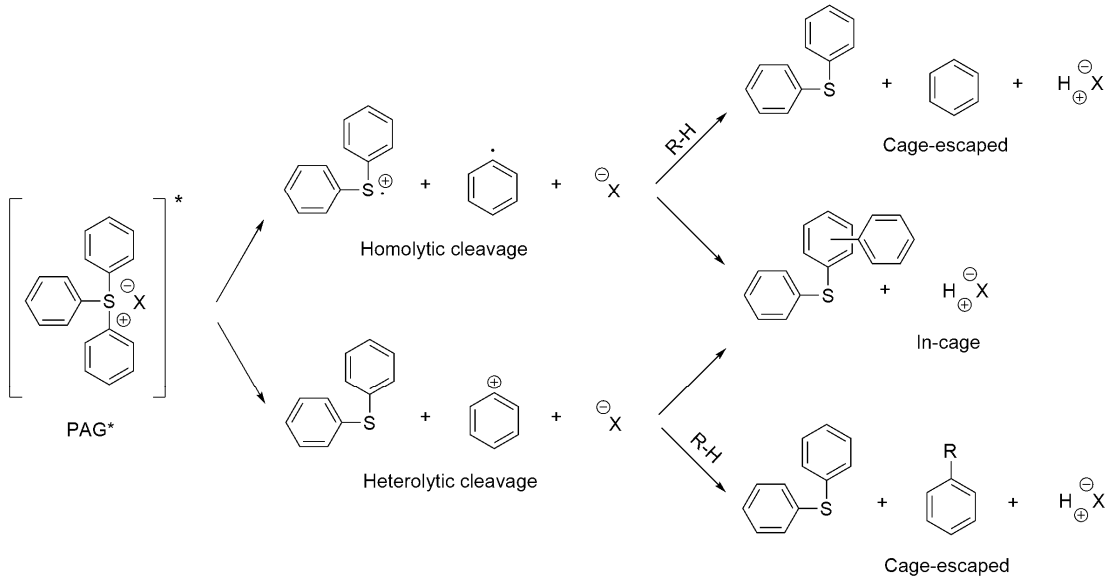

Figure 2. 4 Radiation-induced decomposition and acid generation mechanisms of triphenylsulfonium salts.

Acid-catalyzed deprotection of resist polymer to generate base-soluble acidic functional groups, such as carbolic and carboxylic acids, is the major imaging mechanism of positive-tone CARs. Functional groups chosen to create lipophilic polymers can be classified into two major categories: *high-activation energy* and *low-activation energy* protecting groups. Carbonates, esters, and ethers are the most common examples of high-activation energy protecting groups used in CARs. PEB at moderate temperatures ($70^{o}C$~$110^{o}C$) is normally required for an efficient deprotection of these high-activation energy protecting groups. Examples of the acid-catalyzed deprotection mechanisms of these protecting groups are illustrated in figure 2.5. The acidolysis of carbonate, ester, and ether normally do not require a stoichiometric amount of water as the proton source and thus the acid generated through PAG photodecomposition is not consumed by one single deprotection reaction, but can be regenerated to carry out hundreds of deprotection reactions before being deactivated.

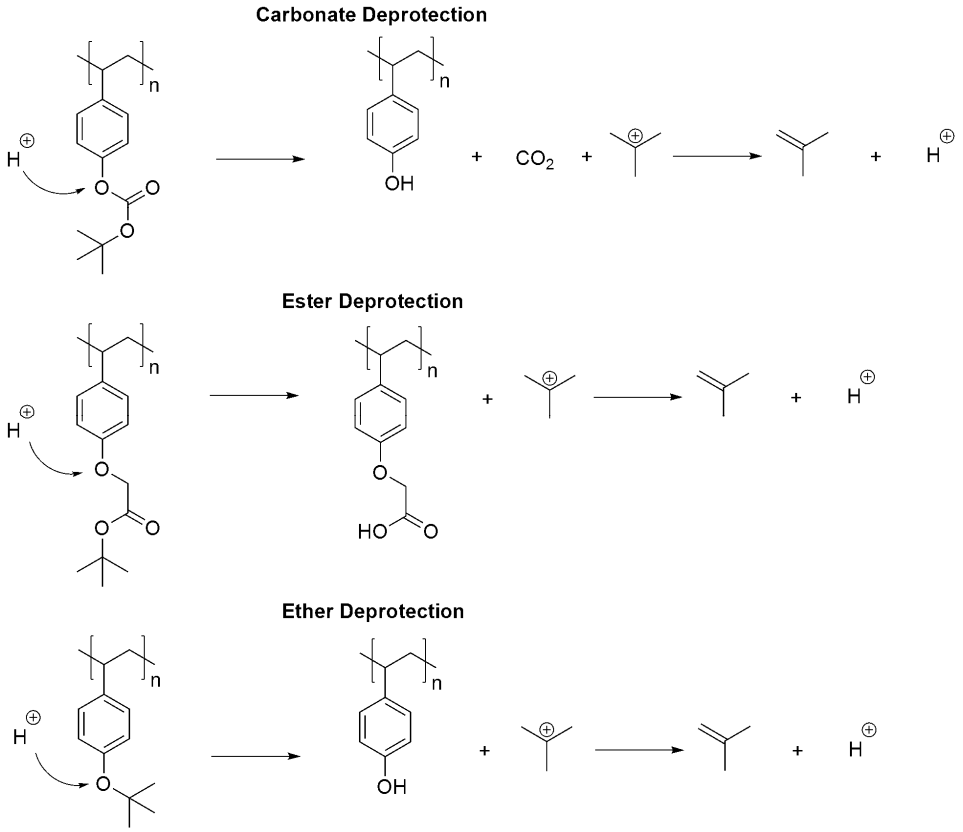

Figure 2. 5 Acid-catalyzed cleavages of carbonate, ester, and ether protecting groups.

Acetal and ketal groups are common examples of the low-activation energy protecting groups used in CARs. Low-activation energy CARs were introduced in early 1990's by Nobuaki Hayashi via blending triflate PAGs with tetrahydropyranyl (THP) protected pHOST resin for DUV lithography.[9] Researchers from IBM also proposed low-activation energy CARs with ketal-based protecting groups for sub-50 nm half-pitch patterning.[10] In many cases the deprotection of low-activation energy systems is an acid-catalyzed hydrolysis which requires the involvement of water to complete the catalytic cycle, as shown in figure 2.6. Under room temperature ketal and acetal protecting groups can be cleaved readily upon the presence of strong acid. No PEB is required for carrying out the deprotection reactions.

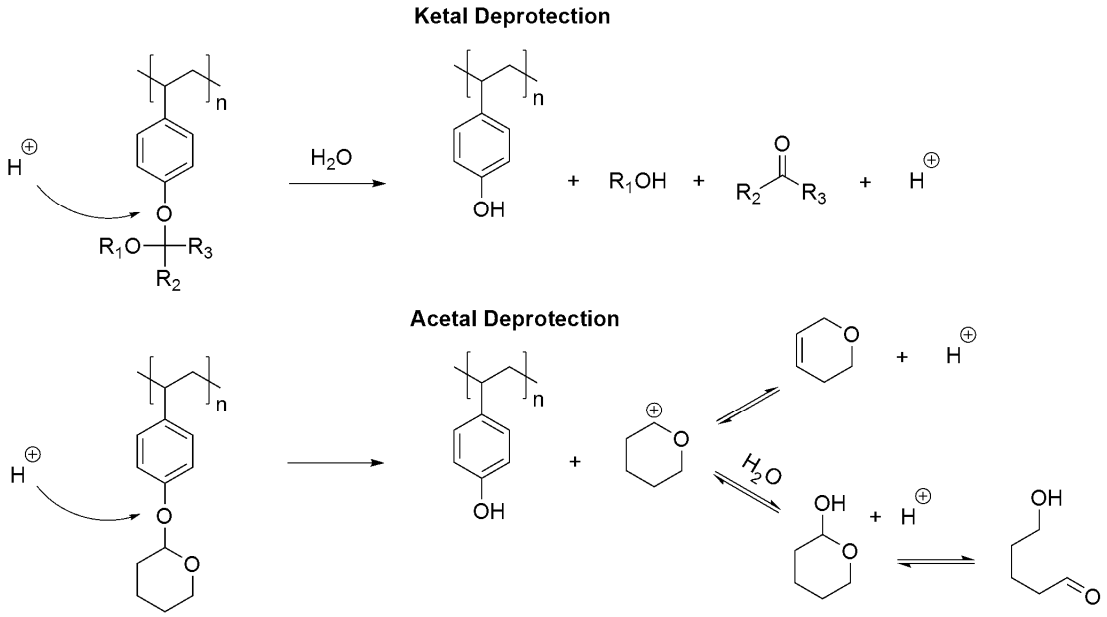

Figure 2. 6 Acid-catalyzed cleavages of ketal and acetal protecting groups.

2.2 Challenges of Modern Chemically Amplified Resists

Research and development of resist material play a critical but challenging role for the realization of every generation of lithography technologies. CARs have served for more than two decades as the high sensitivity and high resolution patterning media in semiconductor industry. To date, positive-tone CARs are still based on a blending formulation consisting of more than 95 wt% polymer resin and less than 5 wt% PAG. Such blended-PAG CARs are known to have a number of potential problems. First, the poor compatibility between bulky polymeric resins and small PAG molecules may limit PAG loading capability in a resist formulation. Poor compatibility may also lead to microscopic PAG distribution heterogeneity or even serious PAG aggregation in the resist film. The direct impacts of low PAG loading and non-uniform PAG distribution are the reduction of resist sensitivity and pattern uniformity. Second, blended-PAG CARs may have serious resist image blur due to excessive acid diffusion during resist PEB, as

shown in figure 2.7. Image blur is defined as the broadening of the critical dimension (CD) of the final resist pattern compared to the original aerial image CD.[11-13] Initially PAG photodecomposition and acid generation in the resist film only happen in regions exposed to radiation. PEB process not only induces the acid-catalyzed deprotection of the polymer resin, but also leads to the diffusion of acid molecules towards unexposed regions and pushes resist deprotection front outward. Finally the resist CD after development is larger than the original designed on the photomask. Acid diffusion, to certain level, is required for improving resist sensitivity since a higher acid diffusivity leads to a longer acid-catalytic chain length of each acid molecule and thus a more sensitive resist material. For acid-catalytic chain length of several hundreds, the resulting image blur of a line pattern is about several to tens nanometers. Acid-catalytic chain length of this magnitude works fine when patterning feature sizes larger than 100 nm, where the acceptable CD error is more than 10 nm. However image blur of blended-PAG CARs has shown serious challenge on achieving desired resolution, as well as the resist process window (i.e. the exposure and focal latitudes within which the resist CD error is acceptable), while intending to print features with sub-100 nm resolution.[14,15]

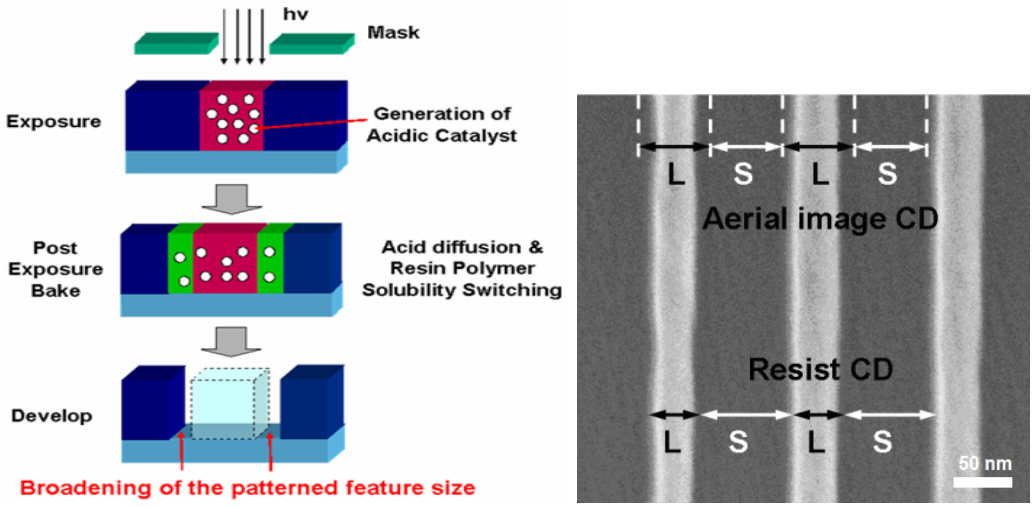

Figure 2. 7 Illustration of acid diffusion-induced resist image blur and the difference of line (L) and space (S) CDs between aerial and resist image of a positive-tone CAR.

The third problem associated with blended-PAG CARs for sub-100 nm resolution is resist pattern non-uniformity. Resist pattern non-uniformity happened at the edge of the developed resist line is normally called *line edge roughness* (LER). Another term which defines the fluctuation of resist CD is called *line width roughness* (LWR). LER and LWR determine the variations of edge position and line width of a resist feature occur quickly over the length of the feature respectively. LER and LWR are caused by a number of statistically fluctuating effects at nanometer-scale dimensions during the lithography process. Exposure optics may introduce edge roughness via the shot noise (i.e. photon flux variation) of the aerial image.[16,17] On the other hand, the physiochemical nature of the resist material may also affect resist pattern uniformity. For example, the statistical distributions of chemical species in the resist, such as PAG molecules and photo-generated acids[18,19], the random walk nature and the extent of acid diffusion during chemical amplification process[20,21], and the non-zero size of resist polymers being dissolved during resist development process (i.e. the single-pixel resolution of the development process)[22,23], may introduce significant fluctuations that affect LER and LWR. Figure 2.8 illustrates the pattern edge roughness introduced by the combining effect of acid distribution and diffusion. Every acid molecule generated in the resist film creates a deprotection volume in the resist matrix during PEB. These small amount but highly diffusive acid molecules generated by the photodecomposition of PAGs in the

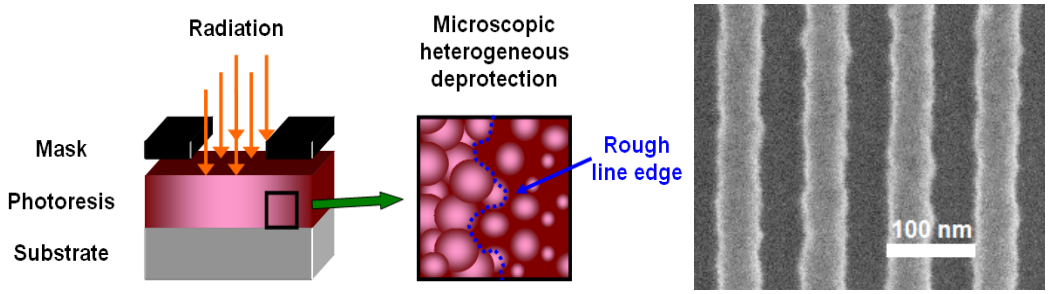

Figure 2. 8 Microscopic illustration of acid distribution and diffusion induced resist pattern edge roughness and a SEM image showing the LER and LWR of resist lines.

resist film result in large and non-uniformly distributed deprotection volumes after PEB. The overlapping of these deprotection volumes leads to serious image blur and rough resist deprotection front which is then transferred to the resist development profile and eventually to the thin film underneath.

Resist image blur and line edge roughness are not newly observed phenomena. They have already existed in lithography since the introduction of CARs two decades ago. However the continued reduction of resist feature size starts to significantly amplify their effects on IC device performance and challenge the precise control of resist CD and pattern uniformity. Researches have proved that the roughness of a gate pattern structure in complementary metal–oxide–semiconductor (CMOS) transistor devices is specifically damaging because the high fields generated at the sharp features along a rough gate layer lead to device performance degradation.[24-26] In particular, the leakage current and thus also power consumption and heat generation of CMOS devices have been directly linked to the roughness of the gate.[27]

Beside each single problem associated with blended-PAG CARs, the material nature of traditional CARs has placed the major limitation and challenge of their applicability to NGL technologies. As mentioned above, CARs have problems including low PAG solubility and thus low PAG loading capability, PAG aggregation and segregation that lead to microscopic composition heterogeneity of a resist film, and acid diffusion that leads to image blue and loss of CD control. These problems are originated from the blend nature of the resist material and ultimately create a tri-lateral tradeoff between achieving desired characteristics of high resolution, high sensitivity, and low LER/LWR through formulation changes of blended-PAG CARs (the RSL tradeoff). For example, the low PAG loading capability of the resist leads to the requirement of high acid diffusivity (i.e. long acid-catalytic chain length) in order to achieve fast photospeed. However high acid diffusivity causes image blur and degrades the achievable resolution of the resist material. High acid diffusivity may also induce LER/LWR to final resist

pattern profile. Base additives may be applied to confine photoacid diffusion at the latent image line edge via quenching acid molecules diffusing from exposed regions[28], however base molecules in exposure regions may neutralize acids that reduces photospeed and may result in unwanted LER due to possible heterogeneous distribution and diffusion of base quenchers in the resist film. The RSL tradeoff has also been theoretically analyzed and proved having the relationship as shown in equation (2.2).[29]

$$(LER)^2 \times (Dose) \times (Size_{\min}) = Const. \qquad (2.2)$$

In order to eliminate the tradeoff effect brought out by the blend nature of traditional CARs, novel resist material design concept that can achieve all three characteristics (i.e. high resolution, high photospeed, and low LER/LWR) will be critical for the continuation of CARs for high resolution patterning using NGL technologies.

2.3 Characterization of Chemically Amplified Resists

2.3.1 PAG Acid Generation Kinetics

Since the first step of the imaging mechanisms of CARs is the photodecomposition of PAGs to generate acid catalysts, acid generation rate and concentration upon exposure to radiation in the resist film are important factors in resist design, processing, and modeling. A great deal of effort has been devoted to studying PAG photoreaction process and quantifying PAG acid generation. Solution-based spectrofluorometric/spectrophotometric techniques are the most popular methods for

characterizing PAG acid generation.[30-32] The basic concept of these methods is applying flood exposures with incremental doses to resist films spin-coated on wafers, and then dissolving the resist films into solutions containing acid-sensitive dyes. Acid concentration is quantified by measuring the absorbance or fluorescence associated with the protonation of dye molecules. On-wafer spectrofluorometric techniques are similar in nature to solution-based techniques, only the spectrometric measurements are performed on solid-state resist films.[33,34] Acid-sensitive fluorescent dyes are introduced into the resist formulation prior to its spin-casting onto a silicon wafer. The fluorescence of acid-sensitive dyes in the exposed film is directly measured from the resist film via a fluorescent microscope and the acid concentration produced by certain exposure energy can then be determined efficiently.

Beside spectrometric techniques mentioned above, methods utilizing other physiochemical properties to monitor PAG acid generation in resist film upon exposure were also proposed and applied to PAG photochemistry studies. A standard addition technique for determining PAG acid generation in a typical CAR film was developed recently.[35,36] A small quantity, relative to PAG, of base quencher is added into resist solution prior to resist film casting and exposure. Assuming the acid concentration required to deprotect the polymer resin and achieve dose-to-clear (i.e. the smallest dose at which the exposed resist film can be totally removed after development) is the same under the same resist formulation and processing conditions, the addition of base can neutralized the acid and the dose-to-clear should increase proportional to the base concentration added into the resist formulation. The PAG acid generation can then be determined by correlating the resist dose-to-clear with base quencher concentration.

Another newly developed technique for determining PAG acid generation is called interdigitated electrode (IDE) sensor method.[37,38] IDE sensor with high density, interdigitated, and nano-sized electrodes is utilizes to measure the capacitance change of a resist film when exposed to small incremental doses. Because the net dielectric

properties, and thus the capacitance of the resist film changes due to the presence of of acid molecules, the PAG acid generation can be determined by properly analyzing the capacitance versus exposure dose data.

2.3.2 Acid Diffusivity

The quantification of acid-catalytic chain length, or acid diffusivity in the resist film, is another major research field since it directly correlates to the imaging property of a resist material. In addition, as image blur caused by acid diffusion towards the unexposed region of the resist film has become a significant effect on achievable resolution and pattern uniformity of a resist material, a great deal of effort has also been poured into the development of techniques for determining acid diffusivity in a resist film. Ion conductivity is one category of techniques for measuring acid diffusivity in solid-state film.[39,40] After determining acid concentration C_{acid} generated in the resist film via solution-based spectrometric methods mentioned in section 2.3.1, the effective acid diffusion coefficient D_{eff} and the corresponding acid diffusion length L of certain diffusion time t can be determined via the Nernst-Einstein equation, as shown in equation (2.2).

$$D_{eff} = \frac{\sigma kT}{q^2 C_{Acid}}$$
$$L = \sqrt{2 D_{eff} t} \qquad (2.2)$$

Here σ is the ion conductivity of the resist film, k the Boltzman constant, T the measurement temperature, and q the ionic charge of the diffusing species.

Another technique commonly used in determining acid diffusivity in a resist film is the modeling of experimentally-measured resist profile change after development to extract acid diffusion length and acid diffusion coefficient.[41,42] High contrast aerial image is applied to expose the resist film and to generated high contrast initial acid distribution profile in the resist film. Image blur extent caused by acid diffusion towards the unexposed region is then monitored by the resist profile after development, and the resist profile is then fitted using acid reaction-diffusion models to extract the acid diffusion coefficient.

Spectrometric techniques were also introduced into the study of acid diffusion in the resist film. Molecular probe such as acid-sensitive dyes have been applied to detect acid migration in the resist film, and acid diffusion coefficients, as well as acid diffusion length, were extracted via modeling the resist latent image with diffusion models.[43,44] A surface exposure method which utilizes FTIR spectroscopy to monitor the deprotection extent of a t-BOC protected pHOST resist film exposed near the film surface using a 193 nm radiation wavelength has also been reported.[45] The reaction-diffusion model applied to the extraction of acid diffusion coefficients includes detailed description of resist physics and chemistry during PEB that can provide more precise determination of acid diffusivity in a resist film.

2.3.3 Resist Intrinsic Patterning Capabilities

In addition to fundamental parameters such as PAG acid generation rate and acid diffusivity in a resist film, resist intrinsic patterning performance is normally the most direct indication of a resist's capabilities in achieving the required lithographic performance of NGL technologies. Among the patterning capabilities most critical to the resist design and lithography societies, the ultimate resolution, the minimum CD bias, and the LER/LWR performance are the most important factors for evaluating a resist

material. Normally these patterning capabilities of a resist material are determined using modern lithography techniques and equipments which possess the capability of generating aerial image with satisfactory resolution and quality. For the development of resist materials for sub-50 nm resolution patterning, EUVL and direct-writing EBL are currently-available techniques which can provide the required resolution for test. Nowadays the EUV Micro-Exposure Tool (EUV-MET) in Lawrence Berkeley National Laboratory, USA and the EUV Interference Lithography (EUV-IL) tool in Paul Scherrer Institute, Switzerland can deliver dense feature resolution down to 25 and 12.5 nm respectively.[46,47] Modern high accelerating voltage, thermally-assisted field emission direct-writing EBL systems have also demonstrated the capability in patterning dense and isolated features on silicon substrate with sizes below 30 nm and 10 nm respectively.[10,48] Generally these high-resolution lithography tools are applied to analyze the lithography performance of resist materials despite the aerial image quality provided by these tools may be insufficient to probe resist intrinsic patterning capabilities.

2.4 Motivation of Thesis Work

Chemical amplification concept is still in demand for providing highly-sensitive resist materials for NGL technologies which utilize high energy and short wavelength radiation sources. However, a novel CAR platform with rational design to relief or overcome the RSL tradeoff between achieving desired lithography performance is necessary for a successful implementation of NGL technologies. The development and characterization of novel CAR platforms that can solve the aforementioned basic problems associated with traditional blended-PAG CARs are essential and are the major subjects of the thesis work.

As the problems mentioned in section 2.2, acid diffusion is required for improving resist sensitivity, however it also brings side effects such as image blur and LER/LWR.

One concept of maintaining resist sensitivity without relying high acid diffusivity (i.e. long acid-catalytic chain length) is to increasing initial acid concentration in the resist film. However the PAG loading of traditional blended-PAG CARs is limited by poor PAG solubility, PAG distribution heterogeneity, and PAG aggregation in the resist film. A novel resist design which can improve PAG loading and fix PAG distribution problem is essential to the success of high PAG loading resist concept. The concept of direct incorporation of PAG into the polymer main chain has been developed recently and has been reported being one potential route to high performance CAR design.[49,50] This class of resist materials is generally termed as the *polymer-bound-PAG resists*. The design principles behind binding PAG molecules to the polymer chain are: (1) attachment of the PAG to the polymer chain should allow for substantially higher maximum PAG loadings capability that can help to produce higher photospeed resists and (2) designs where the acid generated from the PAG remains bound to the polymer should substantially reduce acid diffusion and thus improve resolution and lower LER/LWR. Thus, the design concepts of polymer-bound-PAG resists have the potential of relieving the RSL tradeoff suffered by traditional blended-PAG CARs. Although several early generations of polymer-bound-PAG resists have been reported showing the potential of achieving sub-100 nm resolution capability, advanced characterization of their lithographic performance, as well as the advanced design of mature polymer-bound-PAG resists for sub-50 nm resolution patterning has not been performed thus far. Meanwhile, the correlations between resist structures and the major lithographic performance, such as sensitivity, resolution, LER/LWR, as well as other processing-related performance, have not been address yet.

The advance of characterization techniques is also essential for successful developments of resist materials. For the characterization of PAG acid generation in resist film, solution-based spectrometric methods are labor and material intensive that is generally not as convenient and precise as the on-wafer solid-state techniques. Although

many on-wafer techniques have been reported and have shown general success in providing a reliable protocol for quantifying PAG acid generation, each of them has drawbacks that have limited their application. The standard addition technique requires formulating resists with varying loadings of base quencher. The technique is obviously labor and material intensive, and is not applicable to polymer films which can not develop images. The IDE sensor method requires the fabrication of a centimeter-sized capacitance sensor with intricate and nanometer-sized interdigitated electrodes. This fabrication requires reliable nano-fabrication facilities and skills, and is usually not feasible to many laboratories and academic units. The on-wafer fluorometric spectroscopy techniques use extremely low dye loadings attempting to avoid accidental sensitization of PAG acid generation through energy transfer pathway. This sensitization effect was not quantified, and the use of the low dye loadings limits the measurement of PAG acid generation with very low PAG conversions. Most importantly, the impact of the efficiency of proton-dye contact in a solid-state film, and the effect of matrix composition and dye loading on the quantification of PAG acid generation were not analyzed yet.

Although several techniques for characterizing acid diffusivity in a resist film have been reported and some acid diffusion coefficients in several resist matrices have been reported, each of them has assumptions that may over simplify resist composition and processing effects and lead to error estimation of the real acid diffusivity. The resolution and sensitivity of ion conductivity is limited by the number and density of electrodes used to measure the capacitance of the resist film. However the fabrication of small but high density electrodes is labor intensive. Besides, in a resist film acid-catalyzed deprotection may produce acidic functional groups such as carbolic or carboxylic acids. Such acidic products may affect the dielectric properties of the resist film and introduce error to extracted diffusion coefficient. Diffusion length methods mainly rely on the experimental-modeling of resist development profile to extract acid

diffusion coefficient. A reliable model for describing resist development step is essential for the validation of these methods. Although several empirical resist development models have been proposed[51], the mechanism and kinetics of resist development process is still under investigation, and extra efforts are required to determine resist dissolution parameters. The incorporation of resist development step into the model for extracting acid diffusion may affect the confidence of using these methods. Latent image methods utilize absorbent or fluorescent probes to detect acid migration and extract acid diffusivity through model fitting. In principle this technique is superior to others since it utilizes only the relationship between PEB time/temperature and the variation of probe absorbance or fluoroscence. However previous methods still rely on generating high contrast exposure to create high initial acid concentration contrast in the resist film for modeling purpose. The determination of the initial acid concentration profile may not be precise due to the complex photochemistry occurred in the resist film. On the other hand, these methods may suffer from the lack of sensitivity and resolution for determine reliable diffusion coefficient of acids with low diffusivity.

For the characterization of resist intrinsic patterning capabilities, modern lithography equipments may provide satisfactory resolution for probing the resolution limit of resist materials. However the aerial image quality delivered by these tools may have insufficient contrast that may introduce effects on resist patterning performance. A lithography technique which can provide both high resolution and high contrast aerial image is essential for studying resist intrinsic patterning capabilities and the structure-property relationships.

Works presented in this thesis describe efforts to the characterization and development of novel CARs for NGL technologies. Advanced characterization techniques for determining PAG acid generation rate, acid diffusion coefficient, and resist patterning capabilities such as resolution and LER/LWR are developed and demonstrated in the first four chapters (chapter 3~6). The development and

characterization of novel polymer-bound-PAG resists are experimentally demonstrated and the correlation between polymer-bound-PAG resist properties and the lithographic performance are theoretically analyzed in the next three chapters (chapter 7~9). Additional studies which correlate resist material functions, such as PAG acid generation rate and etch resistance to material structures and properties are reported in Chapter 10. The summary of the whole thesis work and recommendations for future works of novel resist material development are discussed in Chapter 11.

2.5 References

[1] Ito, H.; Willson, C. G., Chemical amplification in the design of dry developing resist materials, *Polym. Eng. Sci.* **1983**, *23*, 1012-18.

[2] Maltabes, J. G.; Holmes, S. J.; Morrow, J. R.; Barr, R. L.; Hakey, M. C.; Reynolds, G.; Brunsvold, W. R.; Willson, C. G.; Clecak, N. J.; MacDonald, S. A.; Ito, H., 1X deep-UV lithography with chemicalification for 1-micron DRAM production, *Proc. SPIE* **1990**, *1262*, 2-7.

[3] Holmes, S. J.; Levy, R.; Bergendahl, A. S.; Holland, K. L.; Maltabes, J. G.; Knight, S. E.; Norris, K. C.; Poley, D., Deep-ultraviolet lithography for 500-nm devices, *Proc. SPIE* **1990**, *1264*, 61-70.

[4] McKean, D. R.; Schaedeli, U.; MacDonald, S. A., Acid photogeneration from sulfonium salts in solid polymer matrices, *J. Polym. Sci., Part A: Polym. Chem.* **1989**, *27*, 3927-3935.

[5] Asakura, T.; Yamato, H.; Ohwa, M., Novel photoacid generators, *J. Photopolym. Sci. Technol.* **2000**, *13*, 223-230.

[6] Yamato, H.; Asakura, T.; Hintermann, T.; Ohwa, M., Novel nonionic photoacid generator releasing strong acid for chemically amplified resists, *Proc. SPIE* **2004**, *5376*, 103-114.

[7] Dektar, J. L.; Hacker, N. P., Photochemistry of triarylsulfonium salts, *J. Am. Chem. Soc.* **1990**, *112*, 6004-6015.

[8] Tagawa, S.; Nagahara, S.; Iwamoto, T.; Wakita, M.; Kozawa, T.; Yamamoto, Y.; Werst, D.; Trifunac, A. D., Radiation and photochemistry of onium salt

acid generators in chemically amplified resists, *Proc. SPIE* **2000**, *3999*, 204-213.

[9] Hesp, S. A. M.; Hayashi, N.; Ueno, T., Tetrahydropyranyl- and furanyl-protected polyhydroxystyrene in chemically amplified systems, *J. Appl. Polymer Sci.* **1991**, *42*, 877-883.

[10] Wallraff, G. M.; Medeiros, D. R.; Sanchez, M.; Petrillo, K.; Huang, W. –S.; Rettner, C.; Davis, B.; Larson, C. E.; Sundberg, L.; Brock, P. J.; Hinsberg, W. D.; Houle, F. A.; Hoffnagle, J. A.; Goldfarb, D.; Temple, K.; Wind, S.; Bucchignano, J., Sub-50 nm half-pitch imaging with a low activation energy chemically amplified photoresist, *J. Vac. Sci. Technol. B* **2004**, *22*, 3479-3484.

[11] Itani, T.; Yoshino, H.; Hashimoto, S.; Yamana, M.; Samoto, N.; Kasama, K., Photoacid diffusion in chemically amplified deep-UV (DUV) resists, *ACS Symposium Series* **1998**, *706*, 110-125.

[12] Zhang, P. L.; Eckert, A. R.; Willson, C. G.; Webber, S. E.; Byers, J., Acid diffusion through polymer films, *Proc. SPIE* **1997**, *3049*, 898-909.

[13] Fedynyshyn, T. H.; Thackeray, J. W.; Georger, J. H.; Denison, M. D., Effect of acid diffusion on performance in positive deep-ultraviolet resists, *J. Vac. Sci. Technol. B* **1994**, *12*, 3888-94.

[14] Van Steenwinckel, D.; Lammers, J. H.; Leunissen, L. H. A.; Kwinten, J. A. J. M., Lithographic importance of acid diffusion in chemically amplified resists, *Proc. SPIE* **2005**, *5753*, 269-280.

[15] Schmid, G. M.; Stewart, M. D.; Wang, C. –Y.; Vogt, B. D.; Prabhu, V. M.; Lin, E. K.; Willson, C. G., Resolution limitations in chemically amplified photoresist systems, *Proc. SPIE* **2004**, *5376*, 333-342.

[16] Gallatin, G. M., Continuum model of shot noise and line edge roughness, *Proc. SPIE* **2001**, *4404*, 123-132.

[17] Yuan, L.; Neureuther, A., Investigation of shot noise induced line-edge roughness by continuous model based simulation, *Proc. SPIE* **2004**, *5376*, 312-321.

[18] Jablonski, E. L.; Prabhu, V. M.; Sambasivan, S.; Lin, E. K.; Fischer, D. A.; Goldfarb, D. L.; Angelopoulos, M.; Ito, H., Near edge x-ray absorption fine structure measurements of surface segregation in 157 nm photoresist blends, *J. Vac. Sci. Technol. B*, **2003**, *21*, 3162-3165.

[19] Hirayama, T.; Shiono, D.; Matsumaru, S.; Ogata, T.; Hada, H.; Onodera, J.; Arai, T.; Sakamizu, T.; Yamaguchi, A.; Shirashi, H.; Fukuda, H.; Ueda, M., Depth profile and line-edge roughness of low-molecular-weight amorphous electron beam resists, *Jpn. J. Appl. Phys.* **2005**, *44*, 5484-5488.

[20] Yoshizawa, M.; Moriya, S., Study of the acid-diffusion effect on line edge roughness using the edge roughness evaluation method, *J. Vac. Sci. Technol. B* **2002**, *20*, 1342-1347.

[21] Yamamoto, H.; Kozawa, T.; Saeki, A.; Okamoto, K.; Tagawa, S.; Ohmori, K.; Sato, M.; Komano, H., Effect of acid diffusion and polymer structure on line edge roughness, *Jpn. J. Appl. Phys*. **2007**, *46*, 6187-6190.

[22] Yamaguchi, T.; Yamazaki, K.; Namatsu, H., Influence of molecular weight of resist polymers on surface roughness and line-edge roughness, *J. Vac. Sci. Technol. B* **2004**, *22*, 2604-2610.

[23] Patsis, G. P.; Gogolides, E., Effects of model polymer chain architectures and molecular weight of conventional and chemically amplified photoresist on line-edge roughness. Stochastic simulations, *Microelectronic Eng.* **2006**, *83*, 1078-1081.

[24] Oldiges, P.; Lin, Q.; Petrillo, K.; Sanchez, M.; Ieong, M.; Hargrove, M., Modeling line edge roughness effects in sub-100 nm gate length devices, *International Conference on Simulation of Semiconductor Processes and Devices* **2000**, 131-134.

[25] Diaz, C. H.; Tao, H. –J.; Ku, Y. –C.; Yen, A.; Young, K., An experimentally validated analytical model for gate line-edge roughness (LER) effects on technology scaling, *IEEE Electron Device Letters* **2001***, 22*, 287-289.

[26] Wu, J.; Chen, J.; Liu, K., Transistor width dependence of LER degradation to CMOS device characteristics, *International Conference on Simulation of Semiconductor Processes and Devices* **2002**, 95-98.

[27] Lee, J. –Y.; Shin, J.; Kim, H. –W.; Woo, S. –G.; Cho, H. –K.; Han, W. –S.; Moon, J. –T., Effect of line-edge roughness (LER) and line-width roughness (LWR) on sub-100-nm device performance, *Proc. SPIE* **2004**, *5376*, 426-433.

[28] Pawloski, A. R.; Christian; Nealey, P.F., The multifunctional role of base quenchers in chemically amplified photoresists, *Chem. Mater.* **2002**, *14*, 4192-4201.

[29] Gallatin G. M., Resist blur and line edge roughness, *Proc. SPIE* **2005**, *5754*, 38-52.

[30] Pohlers, G.; Scaiano, J., A novel photometric method for the determination of photoacid generation efficiency using benzothiazole and xanthene dyes as acid sensors, *Chem. Mater.* **1997**, *9*, 3222-3230.

[31] Okoranyanwu, U.; Byers, J.; Cao, T.; Webber, S.; Willson, C. G., Monitoring photoacid generation in chemically amplified resist systems, *Proc. SPIE* **1998**, *3333*, 747-757.

[32] Cameron, J.; Fradkin, L.; Moore, K.; Pohlers, G., Comparison of methods for acid quantification: Impact of resist components on acid generation efficiency, *Proc. SPIE* **2000**, *3999*, 190-203.

[33] Feke, G. D.; Grober, R. D.; Pohlers, G.; Moore, K.; Cameron, J. F., On-wafer spectrofluorometric method for determination of relative quantum yields of photoacid generation in chemically amplified resists, *Anal. Chem.* **2001**, *73*, 3472-3480.

[34] Ray, K.; Mason, M. D.; Grober, R. D., Quantum yields of photoacid generation in 193-nm chemically amplified resists by fluorescence imaging spectroscopy, *Chem. Mater.* **2004**, *16*, 5726-5730.

[35] Pawloski, A.; Nealey, P., A standard addition technique to quantify photoacid generation in chemically amplified photoresist, *Chem. Mater.* **2001**, *13*, 4154-4162.

[36] Pawloski, A; Szmanda, C.; Nealey, P., Evaluation of the standard addition method to determine rate constants for acid generation in chemically amplified photoresist at 157 nm, *Proc. SPIE* **2001**, *4345*, 1056-1065.

[37] Berger, C. M.; Byers, J. F.; Henderson, C. L., Using interdigitated electrodes for measuring photoacid generator kinetics in chemically amplified resists, *J. Electrochem. Soc.* **2004**, *151*, G119-G130.

[38] Berger C. M.; Henderson, C. L., Improved method for measuring photoacid generator kinetics in polymer films using normalized interdigitated electrode capacitance data, *J. Vac. Sci. Technol. B* **2004**, *22*, 1163-1173.

[39] Itani, T.; Yoshino, H.; Hashimoto, S.; Yamana, M.; Samoto, N.; Kasama, K., A study of acid diffusion in chemically amplified deep ultraviolet resist, *J. Vac. Sci. Technol. B* **1996**, *14*, 4226-4228.

[40] Fedynyshyn, T. H.; Thackeray, J. W.; Georger, J. H.; Denison, M. D., Effect of acid diffusion on performance in positive deep ultraviolet resists, *J. Vac. Sci. Technol. B* **1994**, *12*, 3888-3894.

[41] Schlegel, L.; Ueno, T.; Hayashi, N.; Iwayanagi, T., Determination of acid diffusion in chemically amplified positive deep ultraviolet resists, *J. Vac. Sci. Technol. B* **1991**, *9*, 278-289.

[42] Fedynyshyn, T. H.; Cronin, M. F.; Szmanda, C. R., The relationship between critical dimension shift and diffusion in negative chemically amplified resist systems, *J. Vac. Sci. Technol. B* **1991**, *9*, 3380-3386.

[43] Jessop, J.; Goldi, S.; Scranton, A.; Blanchard, G.; Rangarajan, B.; Capodieci, L.; Subramanian, R.; Templeton, M., Characterizing acid mobility in chemically amplified resists via spectroscopic methods, *Proc. SPIE* **1999**, *3678*, 914-922.

[44] Richter, E.; Hien, S.; Sebald, M., Acid diffusion analysis in the chemically amplified CARL resist, *Microelectronic Eng*. **2000**, *53*, 479-483.

[45] Houle, F. A.; Hinsberg, W. D.; Morrison, M.; Sanchez, M. I.; Wallraff, G.; Larson, C.; Hoffnagle, J., Determination of coupled acid catalysis-diffusion process in a positive-tone chemically amplified photoresist, *J. Vac. Sci. Technol. B* **2000**, *18*, 1874-1885.

[46] Naulleau, P., "Characterization of advanced EUV resists using the Berkeley MET tool" (December 10, 2006). Lawrence Berkeley National Laboratory, USA, Paper LBNL-62124. (http://repositories.cdlib.org/lbnl/LBNL-62124).

[47] Solak, H. H.; Ekinci, Y.; Kaser, P.; Park, S., Photon-beam lithography reaches 12.5 nm half-pitch resolution, *J. Vac. Sci. Technol. B* **2007**, *25*, 91-95.

[48] Brown, D. K.; Murali, R., Current nanolithography research summary, Microelectronic Research Center (MiRC), Georgia Institute of Technology, USA. (http://nanolithography.gatech.edu/index.html).

[49] Wu, H.; Gonsalves, K. E., Preparation of a photoacid generating monomer and its application in lithography, *Adv. Funct. Mater.* **2001**, *11*, 271-276.

[50] Wu, H.; Gonsalves, K. E., A novel single-component negative resist for DUV and electron beam lithography, *Adv. Mater.* **2001**, *13*, 195-197.

[51] Burns, S. D., Understanding fundamental mechanisms of photoresist dissolution; PhD thesis **2003**, The University of Texas at Austin, USA.

CHAPTER 3

ON-WAFER QUANTIFICATION OF RESIST DEPROTECTION RATE FOR CHARACTERIZING PAG ACID GENERATION[†]

One of the most important characters of CARs is the dramatically enhanced photospeed (i.e. the photosensitivity) under DUV and 193 nm radiation than traditional novolac/DNQ resist system. As described in chapter 2, the fast photospeed of a positive-tone CAR is enabled by the introduction of an acid-catalyzed deprotection reaction scheme that modulates the solubility of the resist polymer through a two-step reaction sequence. In this way, the deprotection extent of the polymer and the resulting impact on the resist solubility is greatly amplified as compared to the initial number of photochemical reaction elements (i.e. the acids). Understanding and quantifying acid generation from PAG photodecomposition is therefore an important factor for resist material design. A precise quantification of PAG acid generation upon radiation is also helpful to the development of lithography modeling tools used in a variety of areas such as exposure tool optimization and optical proximity correction (OPC). It should also be noted though that the method and environment in which the PAG photoreaction is studied are important. For example, PAG acid generation in a solid-state polymer film has been previously reported to be enhanced by energy transfer from the polymer to the PAG.[1,2] Such polymer sensitization pathways must be considered and should be useful for

---

[†] Material presented in this chapter has appeared in part in previously published articles:

Lee, C. –T.; Jarnagin, N. D.; Wang, M.; Gonsalves, K. E.; Roberts, J. M.; Yueh, W.; Henderson, C. L., Fundamental studies of the properties of photoresists based on resins containing polymer-bound acid generators, *Proc. SPIE* **2006**, *6153*, 61532E.

Lee, C. –T.; Yueh, W.; Roberts, J. M.; Henderson, C. L., A simple method for measurement of acid generator photoreaction kinetics in formulated, chemically amplified resist films, *Electrochem. Solid-State Lett.* **2007**, *10*, H273-H277.

enhancing PAG sensitivity and increasing photospeed of a resist matrerial. Methods which can measure PAG acid generation rate and under photolysis and radiolysis, as well as determine PAG acid generation efficiency through direct PAG excitation and indirect polymer sensitization pathways, is beneficial for understanding resist radiation chemistry in future NGL technologies and for high-sensitivity resist material design.

3.1 Theory

3.1.1 Resist Thin Film Optics

There are two major subjects essential to a precise description of PAG acid generation behavior in a resist film during the exposure process. The first subject is so called the *thin film optics* since it describes the absorption, propagation, and interference of radiation in a thin resist film spin-coated on a flat substrate. The absorption of radiation energy within a medium can be empirically expressed by Lambert law developed by Johann Heinrich Lambert in 1760, as shown in equation (3.1).

$$\frac{dI}{dz} = -\alpha I \tag{3.1}$$

Here I is the intensity of light traveling in the z-direction through the medium depth and α is the absorption coefficient of the medium. Lambert law simply describes the probability of photons being absorbed by the molecules over a certain small distance traveled in the medium. Assuming a homogeneous medium, (i.e. α is not a function of z), integration of equation (3.1) yields an expression that describes the intensity profile of light in the medium, as shown in equation (3.2).

$$I(z) = I_0 e^{-\alpha z} \tag{3.2}$$

Here I_0 is the intensity of light at z=0 (i.e. the film surface) and is termed as the nominal light intensity. The molecular absorption of photon energy can be described by the interaction of dielectric property of the molecule and the electric field of the light, and can be implicitly described by using a complex index of refraction $\tilde{n}$, as shown in equation (3.3).

$$\tilde{n} = n + i\kappa \tag{3.3}$$

Here n is the refractive index indicating the phase velocity of the light and κ is the extinction coefficient indicating the amount of absorption loss when the light propagates through the material. The extinction coefficient is related to the absorption coefficient of the material, as shown in equation (3.4).

$$\alpha = \frac{4\pi\kappa}{\lambda} \tag{3.4}$$

Here λ is the wavelength of the light. The concentration dependence of the absorbing species in the medium is described by August Beer in 1852, as shown in equation (3.5).

$$\alpha = \sum a_i c_i \tag{3.5}$$

Here a_i is the molar absorption coefficient and c_i is the molar concentration of the absorbing species i. For the case of exposing a thin resist film spin-coated on a thick and

flat silicon wafer, the propagation and interference of the normally incident light and the light reflected from the silicon substrate result in a phenomenon called *standing wave* effect in the resist film. The standing wave in the resist film causes heterogeneous distribution of the radiation intensity across the resist film depth. A radiation intensity distribution has the direct impact on PAG acid generation and distribution and should be precisely characterized in order to evaluate PAG acid generation in the resist film when exposure to radiation. Consider a monochromatic plane wave which is used for exposing a thin resist film. The phase change and absorption of the electric field when traveling through a medium can be represented by equation (3.6).

$$E(z) = e^{ikz} = e^{i2\pi\tilde{n}z/\lambda} \tag{3.6}$$

Here k is defined as the propagation constant (equal to $2\pi\tilde{n}/\lambda$) of the plane wave. When the electric field normally strikes the interface of two adjacent layers i and j, part of the light will be transmitted into layer j and part of the light will be reflected back to layer i. By assuming the electric field of light is continuous across the interface between layer i and j, a transmission coefficient τ_{ij} for a normally incident plane wave traveling from layer i to layer j is defined as equation (3.7).[3]

$$\tau_{ij} = \frac{2\tilde{n}_i}{\tilde{n}_i + \tilde{n}_j} \tag{3.7}$$

On the other hand, the light reflected off interface back into layer i is defined by a reflection coefficient ρ_{ij}, as shown in equation (3.8).

$$\rho_{ij} = \frac{\tilde{n}_i - \tilde{n}_j}{\tilde{n}_i + \tilde{n}_j} \tag{3.8}$$

By using equations (3.6)~(3.8), one can now describe the electric field distribution in a resist film with thickness D spin-coated on a thick silicon substrate, as shown in figure 3.1

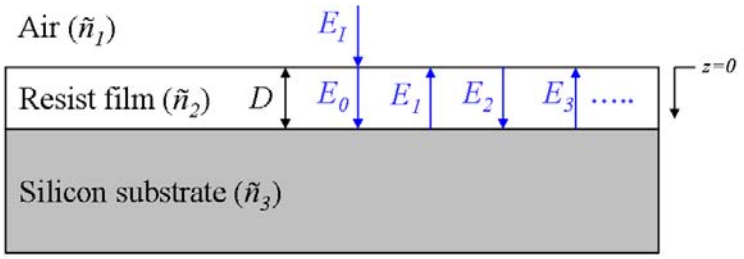

Figure 3. 1 Illustration of an electric field traveling through a resist film spin-coated on a flat silicon substrate.

If an electric field E_I is illuminated on the resist film surface, the transmitted electric field is $\tau_{12}E_I$. The transmitted plane wave travels through the resist film and the electric filed in the resist film can be represented as equation (3.9).

$$E_0(z) = \tau_{12} E_I e^{i2\pi\tilde{n}_2 z/\lambda} \tag{3.9}$$

When the transmitted electric field eventually reach the bottom of the resist film, part of the electric field is reflected off the resist-silicon interface and travel back to the resist film. The reflected electric field can be represented as equation (3.10).

$$E_0(z = D) = \tau_{12} E_I \rho_{23} e^{i2\pi\tilde{n}_2 D/\lambda} \tag{3.10}$$

The complex exponential term in equation (3.10) represents the phase change and the absorption of the electric field when transmitting through the resist film and can be defined as the internal transmittance of the resist, τ_D, as shown in equation (3.11).

$$\tau_D = e^{i2\pi\tilde{n}_2 D/\lambda} \tag{3.11}$$

The first reflected electric field travels back up through the resist and the propagation of the field can be represented by equation (3.12).

$$E_1(z) = \tau_{12} E_I \rho_{23} \tau_D e^{i2\pi\tilde{n}_2 (D-z)/\lambda} = \tau_{12} E_I \rho_{23} \tau_D^2 e^{-i2\pi\tilde{n}_2 z/\lambda} \tag{3.12}$$

Once the reflected wave reaches the resist film surface, part of the wave is reflected back to the resist film and give a electric field $E_2(z)$. This new field again travels through the resist film, reaches the resist-silicon interface, and is partially reflected back to the resist film and give another electric field $E_3(z)$. The electric field of these two waves can be represented by equation (3.13).

$$\begin{aligned} E_2(z) &= E_1 \rho_{21} \rho_{23} \tau_{12} \tau_D^2 e^{i2\pi\tilde{n}_2 z/\lambda} \\ E_3(z) &= E_1 \rho_{21} \rho_{23}^2 \tau_{12} \tau_D^4 e^{-i2\pi\tilde{n}_2/\lambda} \end{aligned} \tag{3.13}$$

By calculating the reflection of the electric field repeatedly, the total electric field within the thin resist film, $E_T(z)$, is the sum of each $E_j(z)$ and can be represented as equation (3.14).

$$\begin{aligned} E_T(z) &= E_1 \tau_{12} \left(e^{i2\pi\tilde{n}_2 z/\lambda} + \rho_{23} \tau_D^2 e^{-i2\pi\tilde{n}_2 z/\lambda} \right) S \\ S &= 1 + \rho_{21} \rho_{23} \tau_D^2 \left(1 + \rho_{21} \rho_{23} \tau_D^2 \left(1 + \cdots \right. \right. \end{aligned} \tag{3.14}$$

The geometric series S can be simply converged to equation (3.15).

$$S = \frac{1}{1 + \rho_{12}\rho_{23}\tau_D^2} \tag{3.15}$$

Thus, the total electric field resided in the resist film becomes equation (3.16).

$$E_T(z) = \frac{E_I\left(e^{i2\pi\tilde{m}_2 z/\lambda} + \rho_{23}\tau_D^2 e^{-i2\pi\tilde{m}_2 z/\lambda}\right)}{1 + \rho_{12}\rho_{23}\tau_D^2} \tag{3.16}$$

After knowing the electric field distribution in the resist film, the intensity profile in the resist film can then be calculated using equation (3.17).

$$I(z) = \frac{n_2\left|E_T(z)\right|^2}{n_1\left|E_I\right|^2} \tag{3.17}$$

For the illumination of a 0.5 μm poly(hydroxystyrene) (pHOST) film spin-coated on a thick silicon substrate, the intensity profile in pHOST film created by a monochromatic radiation at 248 nm wavelength can be calculated by the equations described above and is shown in figure 3.2.

In most cases the illumination source, such as a He-Xe lamp commonly used in G-line and I-line lithography tools, provides radiations with multiple wavelengths. The resulting polychromatic intensity profiles in the resist film were determined by summing up the properly weighted relative spectral intensity at each wavelength in each spatial position in the film to calculate the net intensity profile, $I_{poly}(z)$, as a function of the depth in the resist film, as shown in equation (3.18).

$$I_{poly}(z) = \sum \omega_{\lambda_i} I_{\lambda_i}(z) \tag{3.18}$$

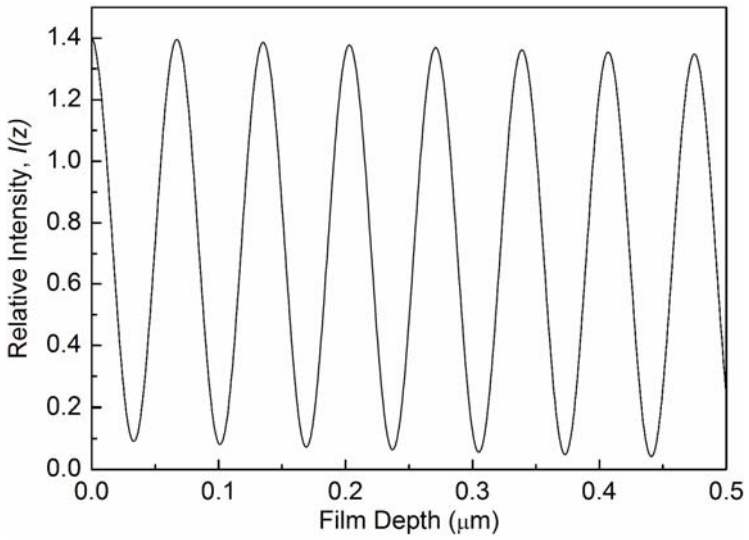

Figure 3. 2 The standing wave intensity profile in a 0.5 μm of PHOST film on a silicon substrate for 248 nm exposure.

Here $\omega_{\lambda i}$ is the ratio of the light intensity at wavelength λ_i to the summation of the total light intensity at each wavelength delivered by an illumination source.

3.1.2 Resist Photochemistry and Exposure Kinetics

Once a precise description of radiation intensity profile in the resist film is determined, the next step is to describe the photochemistry and exposure kinetics occurs in the resist film. As illustrated in chapter 2, a typical CAR is composed of a PAG and a polymer resin. When exposure to radiation, the PAG molecule typically absorbs photon energy molecularly or atomically and being excited or ionized, depending on the radiation energy applied. The excited PAG molecule proceeds to complex reaction pathways to decompose and generates acid and other byproducts. In some cases, especially when high energy radiation sources such as EUV and EB are used, the photon energy significantly exceeds the ionization potential of most of the organic materials, and the absorption of photon energy becomes atomic. In this case polymer resin also absorbs

photon energy and transfer the energy to the PAG molecule through polymer sensitization pathways. The photolysis of PAGs in CARs is typically complicated and different between cases. However for application purpose, the major piece of information that is important and require precise quantification is the amount of acid produced under a given exposure dose. Therefore a far simpler approach is commonly utilized for the description of the PAG photochemistry. The photon absorption, the decomposition of the PAG, and the generation of acid are usually irreversible steps and can be described as a general reaction, as shown in equation (3.19).

$$\mathrm{PAG} \xleftrightarrow{h\nu} \mathrm{PAG}^{*} \rightarrow \mathrm{Acid} \tag{3.19}$$

Here PAG^{*} represents the excited or ionized form of the PAG. Assuming all reactions are first-order to the reactants, the reaction mechanism in equation (3.19) can be represented by simple chemical kinetics, as shown in equation (3.20).

$$\begin{aligned}
\frac{dC_{PAG}}{dt} &= k_2 C_{PAG*} - k_1 C_{PAG} \\
\frac{dC_{PAG*}}{dt} &= k_1 C_{PAG} - (k_2 + k_3) C_{PAG*} \\
\frac{dC_{Acid}}{dt} &= k_3 C_{PAG*}
\end{aligned} \tag{3.20}$$

Here C_{PAG}, C_{PAG*}, and C_{Acid} represent the concentrations of PAG, PAG^{*}, and acid, respectively. Before exposure to radiation, C_{PAG} is equal to $C_{PAG,ini}$ which represents the initial PAG loading in the resist film, and there is no PAG^{*} and acid presented ($C_{PAG*}=C_{Acid}=0$). The first part of the reactions (i.e. the photon absorption of the PAG molecule) is typically on the order of nanoseconds. It is typically useful to assume that the excitation and de-excitation of PAG happen in a very short time scale and C_{PAG*}

reaches its steady-state immediately after the absorption of photon energy. Under such assumption, the overall kinetics representing the photodecomposition of PAG can be written as equation (3.21).

$$\frac{dC_{PAG}}{dt} = -KC_{PAG}$$
$$K = \frac{k_1 k_3}{k_2 + k_3} \tag{3.21}$$

The overall rate constant K is proportional to the intensity (i.e. the photon flux) of the exposure radiation received by the PAG molecule. By relating PAG decomposition and acid generation to the intensity of radiation, equation (3.21) can be re-written as the form in equation (3.22).

$$\frac{dC_{PAG}}{dt} = -CIC_{PAG} \tag{3.22}$$

Here C is commonly known as the Dill C parameter representing the standard exposure rate constant of PAG photodecomposition. Dill C parameter is originated from the early work by Frederick Dill and coworkers at the IBM T. J. Watson Research Center in Yorktown, New York in 1975.[4] Researchers developed a description of the imaging behavior of photoresists with a three parameter model (typically termed as Dill A, B, and C parameters) for novolac/DNQ resist systems. Since PAG decomposition exhibits no bleaching behavior and no significant change in absorption is observed upon exposure in CARs, the intensity profile in the resist film does not change significantly with the PAG decomposition extent. The Dill A and B parameters, which describe the absorption of the resist film, are not essential to a precise description of the exposure kinetics of a CAR film. The Dill C parameter is developed as an “optical sensitivity term” and in principle

represents the absorption cross-section of the PAG, $\sigma_{PAG\text{-}abs}$, to the photon and the quantum yield of the decomposition reaction Φ (i.e. the fraction of absorbed photons that produce the chemical change), as shown in equation (3.23).[5]

$$C = \Phi\sigma_{PAG-abs}\left(\frac{\lambda}{hc}\right) = \frac{\Phi B_E}{v} = \frac{\Phi a_{PAG}\lambda}{N_A hc} \tag{3.23}$$

Here N_A is Avogadro's number (N_A=6.022×10^{23} atoms/mol) and B_E is Einstein's coefficient which is the speed of light in a medium times the absorption cross-section of a molecule and divided by the energy of the photon. B_E of a PAG can be represented in equation (3.24).

$$B_E = v\sigma_{PAG-abs}\left(\frac{\lambda}{hc}\right) = \frac{\sigma_{PAG-abs}}{n}\left(\frac{\lambda}{h}\right) = \frac{a_{PAG}\lambda}{nN_A h} \tag{3.24}$$

The Dill C parameter is a more industry-interested parameter which represents all the effects, such as intrinsic PAG property, resist matrix, and exposure radiation source, on PAG decomposition and acid generation. By applying the calculated radiation intensity profile in the resist film, the corresponding PAG and acid concentrations after certain exposure time, t, can be represented as equation (3.25).

$$\begin{aligned} C_{PAG}(z) &= C_{PAG,ini}(z)e^{-CI(z)t} = C_{PAG,ini}(z)e^{-CE(z)} \\ C_{Acid}(z) &= C_{PAG,ini}(z) - C_{PAG}(z) = C_{PAG,ini}(z)\left(1 - e^{-CE(z)}\right) \end{aligned} \tag{3.25}$$

Here $E(z)$ is the exposure dose delivered by the radiation source under certain intensity and exposure time. According to the theoretical deviation of equations representing the intensity distribution profile, PAG photochemistry, and exposure kinetics, one is possible

to quantify PAG acid generation and determine the Dill C parameter of a PAG in a specific resist matrix environment under a specific exposure radiation source. By setting the resist formulation with a specific initial PAG loading $C_{PAG}(z)$, and determining the intensity profile in the resist film through the thin film optics calculation, the Dill C parameter can be extracted by fitting the measured PAG or acid concentrations under different exposure doses to the kinetic model in equation (3.25). Although the model derived here is based on the assumption of PAG absorption of photon energy to generate acid, the model can also be applied to the case where polymer sensitization is involved in PAG acid generation with high accuracy, as shown in equation (3.26).

$$C \propto a_{PAG}\Phi_{PAG} + a_{Polymer}\Phi_{Polymer} \tag{3.26}$$

Here $a_{Polymer}$ is the molar absorption of the polymer, $\Phi_{Polymer}$ the efficiency of polymer sensitization for PAG acid generation. The extracted Dill C parameter is then represents the combined contribution to acid generation through direct PAG excitation or ionization and indirect PAG sensitization by polymer matrix absorption of photon energy.

3.2 Experimental Procedure

Except the determination of the resist film intensity profile, the determination of PAG acid generation behavior and the Dill C parameter also requires the precise quantification of PAG or acid concentrations in the resist film upon exposure to radiation. As mentioned in chapter 2, the products generated through PAG photodecomposition typically exhibits no significant variation of the absorption behavior and can not be quantified using common spectrometric techniques such as UV/VIS and FTIR spectrometry. Indirect protocols for detecting and quantifying PAG or acid

concentrations in the resist film is usually required for monitoring PAG decomposition and acid generation. On the other hand, the typically low PAG loading (less than 5 wt%, 10^{-2}~10^{-3} mol/L in a solid-state resist film) used in CARs also requires precise and high sensitivity techniques to quantify acid concentration. In this chapter the initial deprotection rate of resist films with incremental exposure doses are measured and used to the quantification of PAG acid generation in the resist film.

3.2.1 Resist Deprotection Kinetics Model

The technique developed to the quantification of PAG acid generation and acid concentration is to monitor acid-catalyzed deprotection of the resist film during PEB. The major advance of this method is that it uses Fourier transform infrared (FTIR) spectroscopy as the tool to quantitatively measure the deprotection reaction rate of an exposed resist film during PEB. This deprotection rate information can subsequently be modeled to extract PAG acid generation rate constant (i.e. the Dill C parameter) in the resist film. To understand this process, a detailed model of the reactions and kinetics occurring in a CAR film during PEB is required. For example the deprotection rate of a partially *tert*-butoxycarbonyl (t-BOC) protected pHOST can generally be described as the combination of a second-order acid-catalyzed reaction, a second-order auto-catalyzed reaction, and a first-order thermolytic reaction, as shown in equation (3.27).

$$\frac{dC_P(z)}{dt} = -k_{Acid}C_P(z)C_{Acid}(z) - k_{Auto}C_P(z)C_M(z) - k_{Thermo}C_P(z) \qquad (3.27)$$

Here $C_P(z)$ is the concentration of t-BOC protected subunit, k_{Acid}, k_{Auto}, and k_{Thermo} the rate constants of acid-catalyzed, auto-catalyzed, and thermolytic reactions, respectively, $C_M(z)$

the concentration of deprotected subunit (i.e. the HOST) produced by the deprotection reaction in the resist film, which possesses a reasonably acidic proton at an elevated PEB temperature. Auto-catalyzed reaction describes the deprotection of polymer via the acidic deprotected polymer subunits in the polymer resin, while thermolytic reaction describes the thermal decomposition of the protecting groups of the polymer.

For resist polymer protected with high-activation energy functional groups, such as t-BOC and butoxycarbonyl groups, the auto-catalyzed and thermolytic deprotections may significantly occur only at high PEB temperature (>120 ^{o}C). The thermal decomposition behavior of a partially-protected t-BOC pHOST (Mw 12,020, 26 mol% protection, DuPont Electronic Materials) is analyzed by a thermogravimetric analysis instrument (TGA, Q500^{TM}, TA Instruments) and the result is shown in figure 3.3. The first 15 wt% weight loss at ~120 ^{o}C is assigned as the auto-catalyzed deprotection and the 3 wt% weight loss at ~190 ^{o}C is assigned as the thermolytic deprotection of the t-BOC group. In this case, these two deprotection reactions only significantly occur when the temperature is higher than 120 ^{o}C.

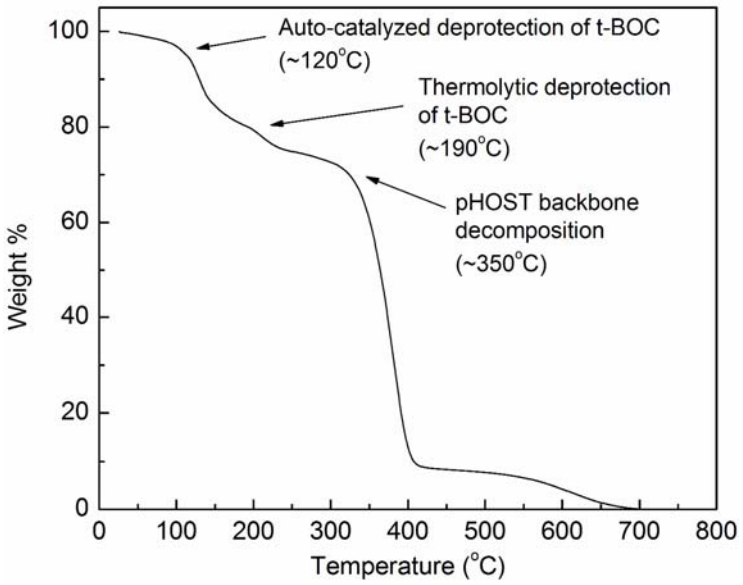

Figure 3. 3 TGA of a partially t-BOC protected pHOST.

Under mild PEB temperatures (70 ^{o}C~110 ^{o}C), the auto-catalyzed and thermolytic deprotection of a resist polymer protected by high-activation energy groups are insignificant and negligible if compared with the acid-catalyzed deprotection. The deprotection rate of the resist polymer is then directly proportional to the amount of acid molecules presented in the resist film after exposure and can be simply described by equation (3.28).

$$\frac{dC_P(z)}{dt} \cong -k_{Acid} C_P(z) C_{Acid}(z) \tag{3.28}$$

Using this fact, in conjunction with equations (3.25) and (3.28), it is possible to relate the properties of two identical resist samples processed at the same PEB temperature in terms of their relative deprotection rate, relative acid concentrations, and the exposure dose used for each sample in the following manner.

$$\frac{dC_{P,i}(z)/dt}{dC_{P,ref}(z)/dt} \cong \frac{C_{Acid,i}(z)}{C_{Acid,ref}(z)} = \frac{\left(1-e^{-CE_i(z)}\right)C_{P,i}(z)}{\left(1-e^{-CE_{ref}(z)}\right)C_{P,ref}(z)} \tag{3.29}$$

Here the subscripts *i* and *ref* distinguish the two different resist samples, one exposed to a dose $E_i(z)$ and the other exposed to an arbitrarily chosen reference dose $E_{ref}(z)$. In practice, a dose array can simply be exposed onto a single silicon wafer coated with resist film and all these exposure doses are processed simultaneously under the same conditions. The use of two samples processed at different exposure doses and their relative properties is advantageous in that it avoids the need for knowledge of the exact PAG or protecting group concentrations in the resist. The basic procedure for determining Dill C parameter

via this method then becomes straightforward. The initial exposure dose profile in the resist film for each dose can be calculated by resist thin film optics introduced in section 3.1.1. The corresponding acid profile in the resist film can then be calculated by equation (3.25) with an initial guess of the Dill C parameter. The deprotection level of the resist polymer is monitored by the quantitative FTIR spectrometry. The initial deprotection rates of resist films with different exposure doses are determined by simply fitting the deprotection data to an appropriate function and calculating the slopes of these fitting curves. By choosing one exposure dose as a reference, the relative initial deprotection rate and the corresponding exposure dose can be fitted to the model shown in equation (3.29) by simply iterating and adjusting the Dill C parameter until the error between the calculated relative initial acid concentration and the experimentally measured relative initial deprotection rate is minimized. The overall experimental and modeling procedure is illustrated schematically in figure 3.4.

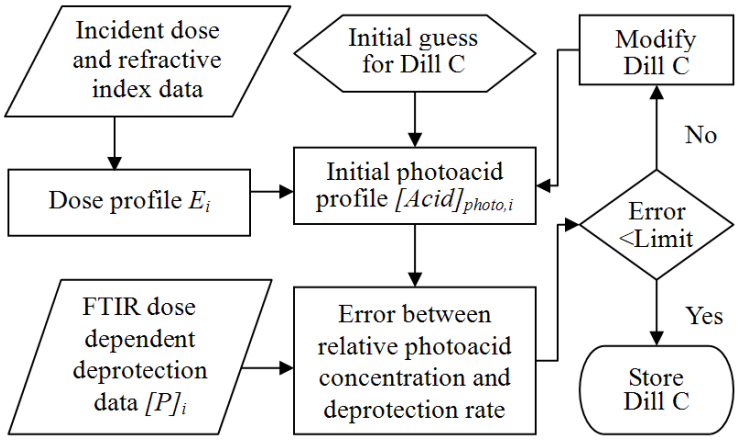

Figure 3. 4 Scheme of the general procedure developed for determining the Dill C parameter of a chemically amplified resist.

3.2.2 Resist Materials and Processing

Resist materials used in this work are made from a resist solution containing 15.1 wt% partially-portected t-BOC pHOST (Mw 12,020, 26 mol% protection, DuPont Electronic Materials) blended with 3.0 wt% triphenylsulfonium trifluoromethylsulfonate (TPS.TFMS, Mw=412.15, Sigma Aldrich Co.) in propylene glycol monomethylether acetate (PGMEA, Sigma Aldrich Co.). Prime grade silicon wafers are sequentially deposited with a 25 nm titanium film as the adhesion layer and a 250 nm gold film as the infrared reflecting layer using an electron-beam evaporation system (CVC SC 5000 e-beam evaporator, CVC Inc.) and used as the substrates for FTIR reflectance measurements. The resist solution is filtered through a 0.2 μm Teflon syringe filter and spin-coated onto gold-deposited silicon wafers to form resist films with thickness of approximately 580 nm. Resist films are soft-baked at 80°C for 90 sec on a contact hot plate to remove residual casting solvent. Film thicknesses are measured using a variable-angle spectroscopic ellipsometer (V-VASE, J. A. Woollam Inc.) by fitting the ellipsometry spectra with a Cauchy model representing the resist film in the non-absorbing wavelength region (500 ~ 1000 nm). The refractive indexes of the resist film in the DUV wavelength region (200 ~ 300 nm) are then determined from the ellipsometry data by fitting the refractive indexes of the Cauchy model with fixed parameters and film thickness. The resist films are exposed using an Oriel Instruments exposure source (model no. 87530-1000, Hg-Xe arc lamp) filtered using a 248 nm bandpass filter (bandwidth 11 nm at full width and half maximum, FWHM). The intensity of the lamp source is measured to be 1.21 mW/cm^2 using a Molectron PM3 power probe and an EPM2000 energy meter. Reflectance FTIR spectra are collected using an FTIR microscope (IRscope II microscope, Bruker AXS Inc.) connected to a Bruker IFs66vS FTIR/ Raman system. Deprotection levels of resist films are determined by monitoring the intensity of the carbonyl stretching peak associated with the t-BOC group (1755 cm^{-1}), while the C-H out-of-plane bending of the para-substituted benzene (827 cm^{-1}) is used as an internal standard for normalizing the collected FTIR data which may be subject to

possible background shifts due to the variations in resist film thickness and substrate reflectance between samples. The PEB time dependent FTIR spectra of the partially-protected t-BOC pHOST resist film after exposure are illustrated in figure 3.5. Every FTIR measurement was collected from an average of 128 scans. The t-BOC carbonyl stretching peak intensity is monitored and assumed to be linearly proportional to t-BOC concentration (i.e. the protection ratio) of the polymer resin. The measured peak intensities of the exposed and baked samples are converted to resist protection level by calibrating the measured intensity to the intensities of 26 mol % and 0 mol % protection samples.

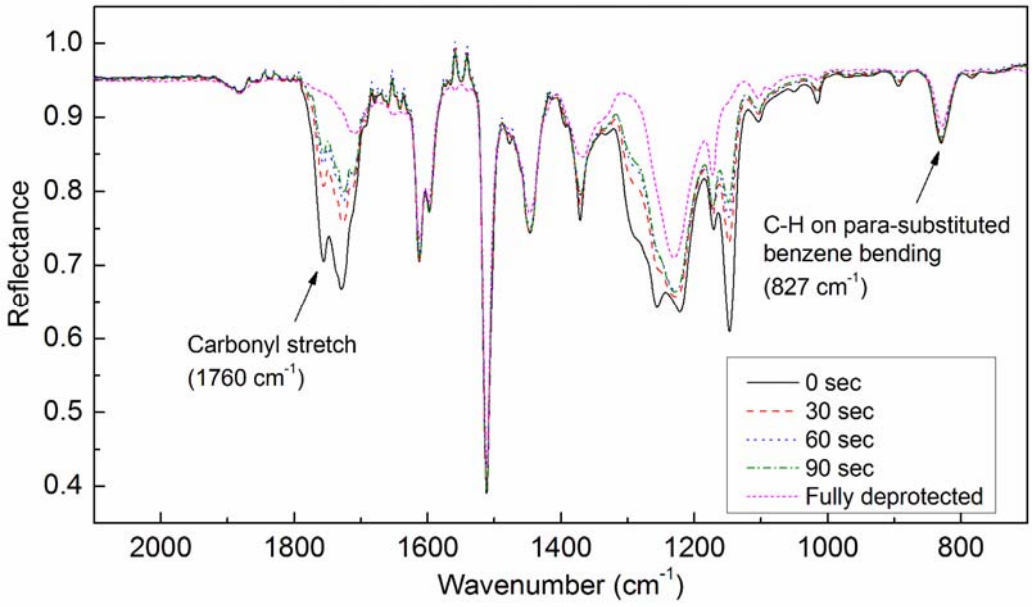

Figure 3. 5 FTIR spectra of partially-protected t-BOC pHOST resist films subject to the same DUV exposure dose but different PEB time.

3.3 Results and Discussion

3.3.1 Polychromatic DUV Intensity Profile

DUV exposure of a thin resist film spin-coated on a reflective substrate, such as the gold-coated substrates used in this work, leads to the formation of standing wave intensity profiles in the resist film as mentioned in section 3.1.1. The DUV irradiance received by the resist film is calculated by multiplying the emission spectrum of the Hg-Xe arc lamp and the transmission spectrum of the 248 nm bandpass filter used in this work and is shown in figure 3.5. The percentage of intensity received by the resist film at each wavelength was calculated by integrating the area under the irradiance curve at each wavelength and divided by the total intensity of the whole spectrum.

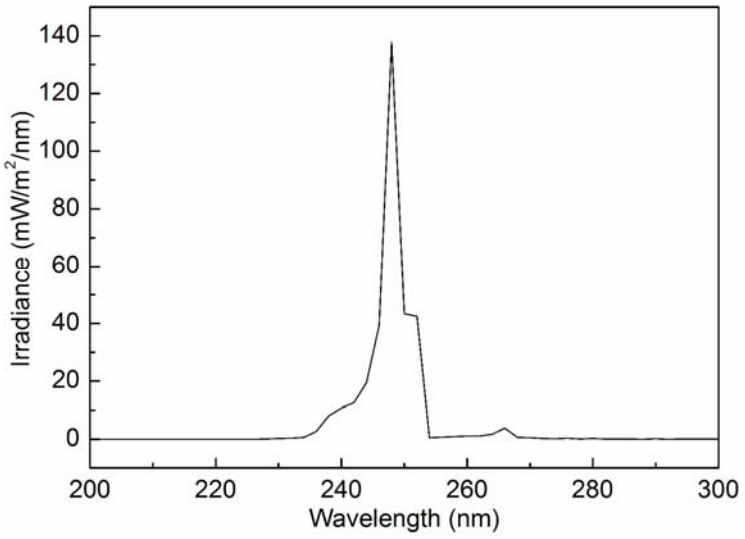

Figure 3. 6 Irradiance spectrum after the overlay of a 248nm bandpass filter and a Xe-Hg lamp spectrum.

The standing wave intensity profile in the resist film created by this DUV illumination spectrum in the resist films is calculated and the standing wave intensity profiles are then used to determine the exposure dose of each resist film sample for Dill C parameter extraction based on the exposure time and nominal lamp intensity for each sample. The decomposition of the PAG molecules during exposure may change the refractive indexes of the resist film that may change the radiation intensity profile in the

resist film and affect the deposited dose profile. Figure 3.7 shows the calculated polychromatic intensity profiles of both PAG-existed and PAG-decomposed films. The intensity profile of the PAG-decomposed film is calculated from a sample exposed to DUV radiation for 500 seconds, a dose high enough to decompose essentially most of the PAG molecules in the resist film. An average 5.36% difference at the peaks of the intensity profile is observed between these two samples. This intensity difference shows the maximum exposure dose variations might happen during exposure if the change in DUV refractive indexes is assumed to be proportional to the PAG decomposition level. The resulting dose variation may affect the determination of Dill C and should be evaluated if one only uses the intensity profile measured from an unexposed sample to calculate the dose and initial acid profile.

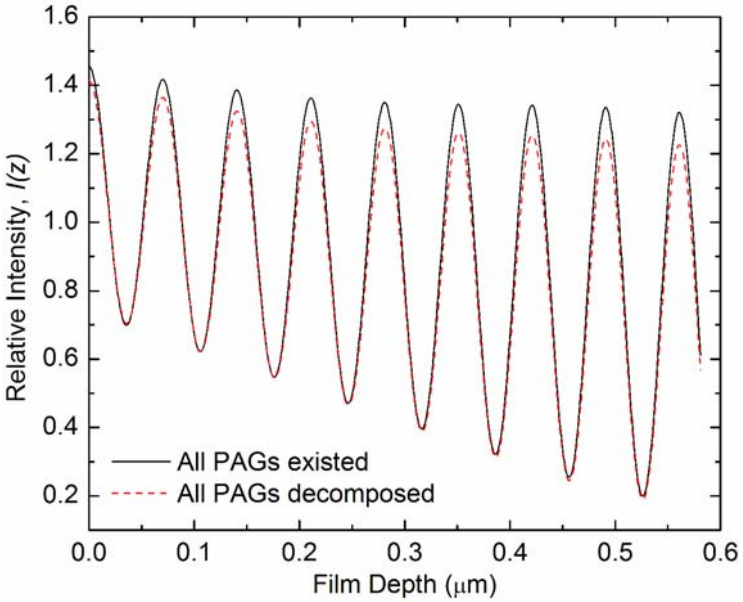

Figure 3. 7 Intensity profiles in PAG-existed and PAG-decomposed resist films.

3.3.2 Evaluation and Sensitivity Test of the Model

A deterministic reaction-diffusion model which includes all major resist chemistry and physics, such as acid-catalysis, auto-catalysis, acid diffusion, acid loss, PAG acid generation efficiency, and different initial polymer protecting ratio, is built to simulate the possible mechanisms leading to changes in acid concentration and polymer deprotection level in a CAR during PEB. This model is then used to generate simulated deprotection data sets as a function of exposure dose and PEB conditions for theoretical resists possessing with different resist physiochemical properties (e.g. different levels of acid diffusion, different acid-catalyzed deprotection rates, different auto-catalyzed deprotection rates, varying levels of acid loss, etc.). The generated simulation data with different model parameter settings is then used to test the performance of the Dill C parameter extraction model described in equation (3.29) in the face of different levels of acid diffusion and various reaction conditions. The resist film for these simulations is represented as a layered set of n slabs with a thickness Δz (n=1001 and Δz=0.58 nm). The calculated standing wave profile through the resist film depth is assigned to each slab at the corresponding z position. The initial acid concentration of each slab at a certain exposure dose is generated using equation (3.25) multiplied by an acid generation efficiency of the PAG, which is defined as the percentage of PAG molecules that actually generate acids when exposed to radiation. The deprotection of the protected polymer subunits is modeled using equation (3.27). Possible loss of acid from the film is modeled using a first-order acid loss reaction mechanism to represent possible airborne base neutralization or acid volatilization. Fick's second law with a constant diffusion coefficient is employed for modeling acid diffusion between slabs in the resist film due to initial acid concentration gradients set up by absorption and standing wave effects during the exposure of the resist film. The joint effect of acid diffusion and acid loss on acid concentration and distribution is represented in equation (3.30). A discrete form of the acid diffusion part, as shown in equation (3.31), is implemented for the calculations.

$$\frac{dC_{Acid,i}}{dt} = D_{eff}\nabla^2 C_{Acid,i} - k_{loss}C_{Acid,i} \tag{3.30}$$

$$C_{Acid,i} \cong \frac{\Delta z}{\sqrt{2\pi\sigma^2}}\sum_{j=1}^{n} C_{Acid,j}\, e^{-(z_i - z_j)^2/2\sigma^2} \tag{3.31}$$

Here $\sigma = (2D_{eff}t)^{0.5}$ represents the one-dimensional acid diffusion length at a given PEB time t and an effective diffusion coefficient D_{eff}, k_{loss} the rate constant of acid loss. The results showed that theoretically broad ranges of the acid diffusivity (D_{eff} = 0.0~100.0 nm^2/sec), acid loss (k_{loss} = 0.0~0.9 sec^{-1}), and acid generation efficiency (10~100%) have no significant effect (< 1% extracted Dill C error; Dill C is set as 0.04 cm^2/mJ) on the applicability of this method. Low initial polymer protection ratio and high auto-catalyzed reaction rate however may introduce significant error to the Dill C extraction method developed in this work. Figure 3.8 shows the criteria where the auto-catalyzed reaction due to the combination of these two factors contributes significant deprotection contents and causes an unacceptable error to this method. In cases where the ratio of the auto-catalyzed to acid-catalyzed rate constants (k_{Auto}/k_{Acid}) is below 5.0×10^{-5}, it appears that this method is quite robust and insensitive to other material property variations (i.e. less than 5% error in extracted Dill C value, as the red line indicated in the figure). The dependence of Dill C extraction error on k_{Auto}/k_{Acid} and the exact Dill C value is also illustrated in figure 3.9. This method can also provide precise extraction of the Dill C parameter through the whole range of exact Dill C values while k_{Auto}/k_{Acid} is below 2.5×10^{-5}. The partially protected t-BOC pHOST polymer resin used in this work has 26 mol% protection and has been calculated to have k_{Auto}/k_{Acid} equal to 3.02×10^{-7}, according to the reaction rate constants reported.[6] This value is within the parameter space of theoretically less than 1% error in determining the Dill C parameter, as indicated by the blue dot in both figure 3.8 and 3.9. In general, auto-catalyzed deprotection effect can be

prevented in high-activation energy systems by using moderate bake conditions and does not significantly affect the physical accuracy of this method.

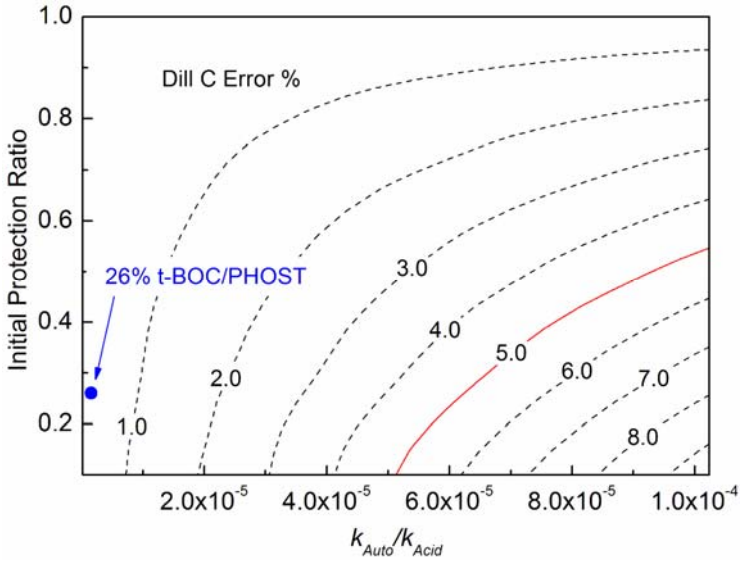

Figure 3. 8 Dependence of Dill C parameter extraction error on k_{Auto}/k_{Acid} and the initial polymer protecting level.

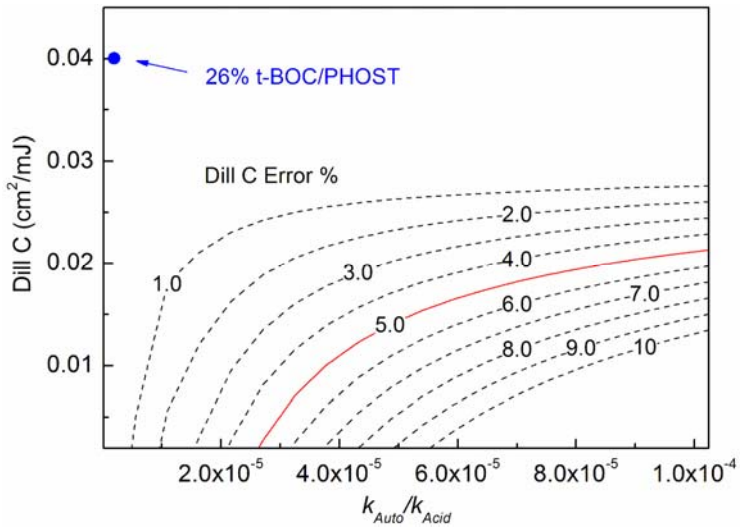

Figure 3. 9 Dependence of Dill C parameter extraction error on k_{Auto}/k_{Acid} and the exact Dill C value.

The change of refractive indexes in the resist film due to the photolysis of the PAG may result in variations of the radiation intensity profile in the resist film. Simulation data used to test the new Dill C parameter extraction method is generated using an intensity profile calculated using the refractive indexes of an PAG-existed resist film, but as a worst case scenario it is analyzed using the intensity profile calculated from the refractive indexes of the PAG-decomposed resist film. This exercise shows the extreme case where the maximum intensity profile variation may exist between the conditions used to generate the experimental data and the conditions simulated during data analysis due to PAG photolysis. In this case, however, only a small deviation (~5.0% error of the extracted Dill C parameter) is observed. This result suggests that typical variations in the refractive indexes of a CAR film during exposure do not likely result in any significant error in the Dill C parameters extracted from the experimental data which are analyzed without consideration of such refractive index changes.

3.3.3 Dill C Parameter Extraction

Resist films composed of partially-protected t-BOC pHOST and TPS.TFMS PAG are prepared according to the materials and methods described in section 3.2.2. Resist films are exposed to incremental exposure doses ranging from 3.62 to 42.21 mJ/cm^2 and baked for times between 0 and 90 seconds at 55°C. FTIR reflectance data of each sample are collected and translated into a t-BOC protection level as shown in figure 3.10. The deprotection extent is observed to be proportional to the dose deposited in the resist film and the amount of acid generated. A slight decrease in protection level (> 5 mol%) of the samples is observed for all the samples before PEB and is assumed to be due to the room-temperature deprotection of the polymer in the presence of a strong acid while the samples are being exposed. The initial deprotection rates of different exposure doses are

obtained by calculating the first derivative of the fitting curves at time zero. The model fitting results using equation (3.29) to the calculated initial deprotection rates are shown in figure 3.11. Each fitting curve, as well as the corresponding Dill C parameter, was calculated by taking one of the exposure doses as a reference dose and its initial deprotection rate as the reference deprotection rate. The average Dill C value extracted from two repeated experimental FTIR deprotection data sets is 0.0409 cm^2/mJ (±0.0023 cm^2/mJ, 95% confidence level), which is well within the range of literature for reported Dill C values (0.037~0.055 cm^2/mJ) for this PAG in similar matrices as determined by other methods.[7-9] Therefore, both the sensitivity analysis and the demonstrated capability of using this method to extract a reasonable and self-consistent Dill C parameter for an experimental resist formulation show that this technique is both experimentally simple and accurate for studying PAG acid generation in high-activation energy resist systems. The method described here, however, is valid only for resist films which show negligible auto-catalyzed deprotection under the experimental conditions.

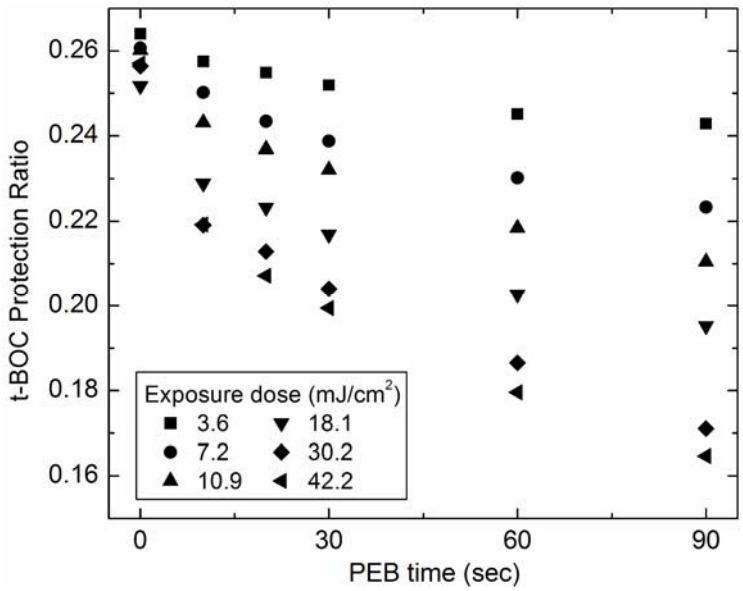

Figure 3. 10 Deprotection ratio of t-BOC protected pHOST subject to different DUV exposure dose and PEB time.

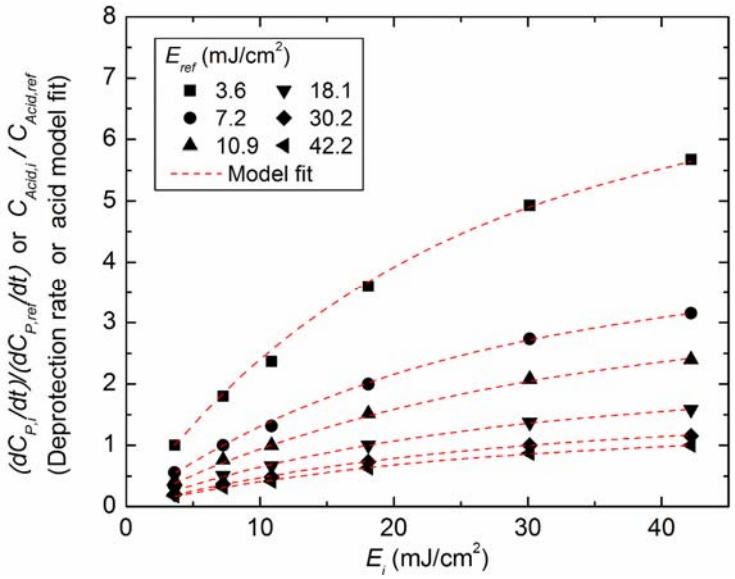

Figure 3. 11 Relative initial deprotection rates and the model fitting results of resist films under different DUV exposure dose.

3.4 Conclusions

The development of a new method for extracting Dill C parameters for PAGs in protected resist polymers using quantitative FTIR measurement of polymer deprotection rates is reported in this chapter. In this method, the PEB time dependent deprotection extent of the resist polymer is measured by FTIR spectroscopy and translated to the protection level of the resist film. The deprotection rate as a function of exposure dose and PEB time is calculated from the slope of a first-order exponential decay curve fit to the protection ratio data. The Dill C parameter is extracted by fitting the relative initial acid concentrations to the calculated relative deprotection rates for two resist samples exposed to different doses. The sensitivity of this method to confounding variables is evaluated by performing Dill C parameter extractions on simulated deprotection rate data sets. The results show small ($\leqq$ 5% error) effects caused by acid diffusion during PEB, acid loss during PEB, acid generation efficiency, and small variations in the refractive indexes of the resist film during exposure. However, it is found that resists which display

significant auto-catalytic deprotection can not be reliably analyzed using this simple method. This method is demonstrated to successfully yield a Dill C parameter of 0.0409 cm^2/mJ for a high-activation energy resist consisting of a TPS.TFMS and a partially-protected t-BOC pHOST. This result is consistent with other reported values for similar resist systems determined using other methods. More detailed resist model is necessary for using quantitative FTIR spectrometry of resist deprotection rates to extract Dill C parameters for resist systems which possess low-activation energy protection groups and systems which in general exhibit significant auto-catalytic deprotection during PEB.

3.5 References

[1] Hacker, N. P.; Welsh, K. M., Mechanistic studies on the poly(4-tert-butoxy carbonyloxystyrene)/triphenylsulfonium salt photoinitiation process, *Proc. SPIE* **1991**, *1466*, 384-393.

[2] Hacker, N. P.; Hofer, D. C.; Welsh, K. M., Photochemical and photophysical studies on chemically amplified resists, *J. Photopolym. Sci. Technol.* **1992**, *5*, 35-46.

[3] Mack, C. A., Analytical expression for the standing wave intensity in photoresist, *Appl. Opt.* **1986**, *25*, 1958-1961.

[4] Dill, F. H.; Hornberger, W. P.; Hauge, P. S.; Shaw, J. M., Characterization of positive photoresist, *IEEE Trans. Electron Devices* **1975**, *ED22*, 445-452.

[5] Mack, C. A., Absorption and exposure in positive photoresist, *Appl. Opt.* **1988**, *27*, 4913-4919.

[6] Wallraff, G.; Hutchinson, J.; Hinsberg, W.; Houle, F.; Seidel, P.; Johnson, R.; Oldham, W., Thermal and acid-catalyzed deprotection kinetics in candidate deep ultraviolet resist materials, *J. Vac. Sci. Technol. B* **1994**, *12*, 3857-3862.

[7] Cameron, J. F.; Chan, N.; Moore, K.; Pohlers, G., Comparison of acid-generating efficiencies in 248 and 193-nm photoresists, *Proc. SPIE* **2001**, *4345*, 106-117.

[8] Szmanda, C. R.; Brainard, R. L.; Mackevich, J. F.; Awaji, A.; Tanaka, T.; Yamada, Y.; Bohland, J.; Tedesco, S.; Dal'Zotto, B.; Bruenger, W., Measuring acid generation efficiency in chemically amplified resists with all three beams, *J. Vac. Sci. Technol. B* **1999**, *17*, 3356-3361.

[9] Pawloski, A. R.; Szmanda, C. R.; Nealey, P. F., Evaluation of the standard addition method to determine rate constants for acid generation in chemically amplified photoresist at 157 nm, *Proc. SPIE* **2001**, *4345*, 1056-1065.

CHAPTER 4

ON-WAFER ELLIPSOMETRY OF ACID-SENSITIVE DYES FOR CHARACTERIZING PAG ACID GENERATION IN RESIST FILMS[†]

The characterization method described in chapter 3 provides a fast and convenient protocol for quantifying PAG acid generation in a real CAR formulation by monitoring the deprotection rate of the resist polymer using FTIR spectrometry. However its application is still limited by several requirements related to material property and technical operation. First, real resist polymer resins (i.e. polymers with protecting groups) are required since the change of protection level is used as the probe of PAG acid generation. Significant error may occur when using this method to resist polymers with low-activation energy protecting groups which can undergo significant auto-catalyzed deprotection induced by the acidic subunits in polymer composition at elevated PEB temperature. On the other hand, a several hundred nanometer film thickness is generally required for obtaining a significant signal-to-noise ratio measurement from a general single-bounce FTIR spectrometry. Such restriction limits its application to the study of PAG acid generation in ultra-thin resist film (< 100 nm film thickness) which is essential to NGL technologies. In this chapter, another method which can determine PAG acid generation in ultra-thin polymer films, as well as low-activation energy resist films, is developed and demonstrated. In addition to the advance of the applicability to more

---

[†] Material presented in this chapter has appeared in part in previously published articles:

Lee, C. –T.; Yueh, W.; Roberts, J. M.; Younkin, T. R.; Henderson, C. L., A new technique for studying photoacid generator chemistry and physics in polymer films using on-wafer ellipsometry and acid-sensitive dyes, *Proc SPIE* **2008**, 6923, 692316.

Lee, C. –T.; Yueh, W.; Henderson, C. L., Quantifying Acid Generation from Photoacid Generators in Polymer Films Using On-Wafer Ellipsometry and Acid-Sensitive Dyes, *J. Vac. Sci. Technol. B*, submitted.

general material properties, the capabilities of using this method to study PAG acid generation rate under low-energy photolysis and high-energy radiolysis, as well as determine the efficiency of acid generation through direct PAG excitation and indirect polymer sensitization pathways are also developed and demonstrated.

4.1 Theory

4.1.1 Electronic Absorption Spectroscopy of Molecules

Upon the irradiation by an electromagnetic wave, a molecule may absorb the incident photon to increase the energy of its atoms and electrons depending on the photon energy and the molecular structure. The overall energy (E_{Tot}) of a molecule is the sum of contributions from electronic (E_{Elec}), vibrational (E_{Vib}), and rotational (E_{Rot}) energies, as shown in equation (4.1).

$$E_{Total} = E_{Elec} + E_{Vib} + E_{Rot} \tag{4.1}$$

The energy levels representing these three electronic transitions, as well as the photon energy of different radiation sources, are illustrated in figure 4.1. The energy changes involved in electronic transition of the molecule orbital are considerably greater than those involved in vibration and rotation of the molecular structures, and are sensitive to the electron cloud distribution in the molecule. Such energy changes are correspond to radiation energy in UV (200~400 nm) and visible (VIS, 400~800 nm) spectra regions. Typically the absorption of photon energy within this wavelength region induces the excitation of an electron from one molecular orbital with lower energy to another with

higher energy. Generally the absorption of UV/VIS photon energy can promote one electron from the highest occupied molecular orbital (HOMO) to a lowest unoccupied molecular orbital (LUMO), and the photon energy required to carry out this electronic promotion is specific to the structure of the molecule. This electron jumping causes the re-distribution of the electron cloud of the molecule and thus the spatial configuration of the molecule. The UV/VIS absorption specta of molecules can be applied to determine the structure and the electronic transition of a molecule, and is often called *electronic spectroscopy* technology. In some cases the energy difference between molecular orbital is within the magnitude of the bond enthalpies of typical molecules, and the electronic transition may lead to chemical reactions involving chemical bond breakage, such as the photolysis of PAGs in CARs.

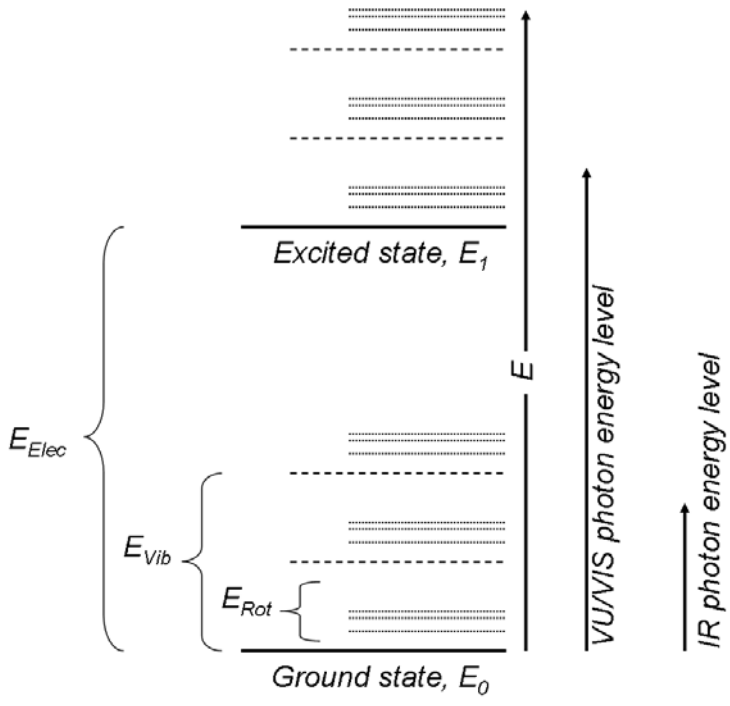

Figure 4. 1 Schematic energy level diagram of molecular orbitals and photons within different wavelength regions.

Molecular orbital theory states that the excitation (i.e. the electronic transition) of a molecule through the absorption of radiation in UV/VIS regions involves the promotion of its electrons from a bonding (σ or π) or non-bonding orbital (n), usually refer to the *ground state*, to an anti-bonding orbital (σ^* or π^*), usually refer to the *excited state*. The energy levels of bonding orbitals, as well as possible electronic transitions of a molecule upon the absorption of radiation, are illustrated in figure 4.2. In principle every chemical structure in a molecule is correspond to a electronic transition upon radiation, however the transition of a electron from a s orbital to an anti-bonding orbital requires higher energy and shorter wavelength radiation (usually < 400 nm). There are only certain types of molecular structures and electronic transitions of those structures involved in UV/VIS radiation. The molecular structures containing covalently unsaturated groups such as double or triple bonds, or in some cases the long-pair electrons, are essentially responsible for the absorption in UV/VIS regions and are often called *chromophores* of a molecule. The general order of energy required for various electronic transitions is shown in equation (4.2).

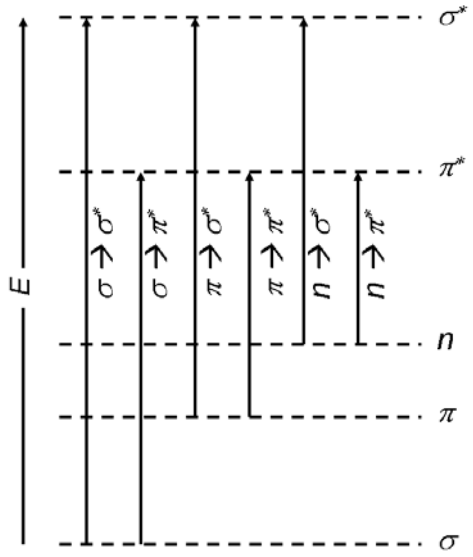

Figure 4. 2 Relative energy diagram of molecular orbitals and electronic transitions.

$$n \rightarrow \sigma^* \geq \pi \rightarrow \pi^* > n \rightarrow \pi^* \qquad (4.2)$$

The energy required for an electronic transition is in principle quantized and theoretically a discrete line is expected for each electronic transition. However in practice every molecule may possess different vibrational and rotational states with relatively small energy difference if compared to the energy of electronic transition. The direct consequence of statistical distribution of these states is the formation of a broad absorption band, which is the superimposition of electronic absorptions of molecules accompanying the same electronic transition, but different vibrational and rotational levels, in an electronic spectrum. Since the electronic absorption is specific to certain chromophore structure of a molecule, UV/VIS spectroscopy is extensively used as a powerful tool of structural and quantitative analysis.[1] Beer-Lambert Law is often applied to relate the absorbance of a particular substance to its concentration, as shown in equation (4.3).

$$\log \frac{I_0}{I} = A = \varepsilon c l \qquad (4.3)$$

Here I_0 is the intensity of the incident radiation, I the intensity of radiation after transmitted through the media of interest, A the absorbance or optical density, ε the molar absorptivity, c the concentration of the molecule interested, and l the penetration length of the sample. This technique is highly sensitive to the variation of molecular concentration since the molar absorbance of chromophores is usually high that gives excellent signal-to-noise ratio for quantifying molecule concentration by monitoring the

intensity of the absorption peaks in the spectrum. Some molecules, which are usually called *dyes*, are small molecules which are sensitive to environmental changes, such as the pH value or polarity of the solution. Using UV/VIS spectrometry of dye molecules as a tool to probe the change of media properties has become a popular indirect method to trace the changes of properties in physical and chemical systems.

4.1.2 On-Wafer Ellipsometry of Dye Absorption

For the spectrometric method used in this section to determine PAG acid generation in CARs, an ultra-high sensitivity and resolution on-wafer ellipsometry technique is developed to measure the absorption of acid-sensitive dyes in a solid-state polymer film, rather than the use of traditional UV/VIS spectrometric method. There are problems associated with the use of traditional UV/VIS spectrometry to determine PAG acid generation in polymer films. First, a standard solid-state UV/VIS spectrometry measures the absorption of a medium as described in previous section and equation (4.3). The absorption of radiation depends on the not only the concentration of the absorbing species, but also the film and substrate thickness (the penetration length l). For the study of PAG acid generation upon exposure to radiation, UV/VIS spectrometry measures only the absorption of samples exposed to radiation with different doses. The small absorbance variation due to the variation of sample or substrate thickness may result in significant background shift of the absorption spectrum and introduce error to the quantification of acid concentration. Unlike FITR spectrometry technique of which one single narrow-bend peak associates to one single chemical structures of a molecule, and internal reference absorption peaks associated to unchanged chemical structures of a molecule can be applied to calibrate spectra collected from different samples, UV/VIS spectrometry measures the electronic transition of a molecule and usually has broad-band

absorption, especially in a solid-state sample that the absorbing molecules have more contacts, interactions, and energy transition with the surrounding environment. Usually there is no clear and stable internal reference peaks can be used for calibration purpose. Second, the use of Beer-Lambert law requires the prerequisite that the medium, a solution or a solid-state film, is dilute enough so that the absorption hindrance effect can be prevent. However the concentration of dyes loaded in a solid-state film for detecting acid molecules is several-order higher than that in the solution phase and is far exceed the suggested concentration range for UV/VIS spectrometry. Finally, the standard substrates used in UV/VIS spectrometry, such as quartz (fused silica) and glass, may limit its application to specific exposure tools, such as modern EUVL and EBL systems which allow only the use standard silicon wafer as the substrate for sample preparation and loading. These problems place the major limitations of using standard UV/VIS spectrometry for quantifying PAG acid generation with acceptable resolution, sensitivity, and convenience.

In stead of using standard UV/VIS spectrometry, an on-wafer ellipsometry technique for quantifying PAG acid generation is developed in this work. Typically ellipsometry measures the polarization changes of light upon transmitting through or reflecting from a thin film. The exact nature of the polarization change is determined by the interaction of the electromagnetic field with the physical and electronic property of the material (i.e. thickness, complex refractive index or dielectric function tensor). Although optical techniques are inherently diffraction limited that may degrade their resolution and sensitivity, ellipsometry technique can exploits both the phase information and the polarization state of the light that achieves the resolution and sensitivity to angstrom level. A standard setup of an ellipsometry measurement is shown in figure 4.3. Electromagnetic radiation is emitted from a light source with an incident angle θ_{in}. The incident radiation is linearly polarized by a polarizer. The radiation then passes through an optional compensator, which can further modulate the phase of the incident radiation,

and falls onto the sample with an electric field E_{in}. The radiation with an electric field E_{ref} is reflected from the sample film and then passes through another optional compensator and a second polarizer, which is normally called the analyzer, and finally falls into the detector.

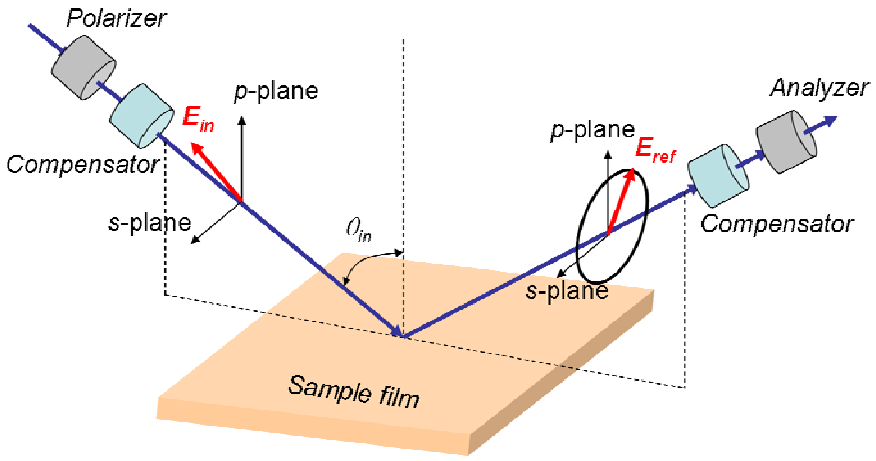

Figure 4. 3 Schematic of an ellipsometry experiment setup.

Ellipsometry measures the change of polarization states of radiation reflected from a thin film.[2] The measured values, denoted as R_s and R_p, are the amplitudes of the *s* and *p* components of the radiation after reflection and are normalized to their value before the reflection. The ratio of these two values is correlated to two Stokes parameters by the fundamental ellipsometry equation (4.4)

$$\tan(\Psi)e^{i\Delta} = \frac{R_p}{R_s} \tag{4.4}$$

Here $\tan(\Psi)$ is the amplitude ratio and Δ is the phase shift of radiation upon reflection, respectively. Since ellipsometry measures the ratio of two amplitudes of radiation

polarization, the measurement is self-consistent and can be highly accurate and reproducible. Possible measurement errors existed in UV/VIS spectroscopy can be intrinsically prevented. The phase measurement allows ellipsometry technique being highly sensitive to ultra-thin film (< 100 nm). The optical constants (i.e. the index of refraction, $\tilde{n}(\lambda)=n(\lambda)+i\kappa(\lambda)$) of a polymer film at each wavelength λ can be determined by the following scheme. The thickness and the dispersion behavior of the polymer film can be determined by using a three-term Cauchy equation model, as shown in equation (4.5), to fit the non-absorbing regions of the collected ellipsometry spectrum (500 ~ 1000 nm). The index of refraction $\tilde{n}(\lambda)$ is then determined by using a point-by-point fitting of $\tilde{n}(\lambda)$ of the Cauchy model with fixed parameters at each wavelength in the absorbing regions (200 ~ 400 nm).

$$n(\lambda) = A + \frac{B}{\lambda^2} + \frac{C}{\lambda^4} \tag{4.5}$$

For a complex index of refraction, the extinction coefficient $\kappa(\lambda)$ determines the decrease speed of the amplitude of the incident wave. The film absorption coefficient of the film at every wavelength is directly correlated to $\kappa(\lambda)$ and can be calculated according to equation (4.6).

$$\alpha(\lambda) = \frac{4\pi\kappa(\lambda)}{\lambda} \tag{4.6}$$

The measured and model-fitted ellipsometry spectra collected at three different incident angles of a poly(hydroxylstyrene) (pHOST) film spin-coated on a flat silicon wafer, as well as the extracted indexes of refraction, are shown in figure 4.4.

4.1.3 Properties of Acid-Sensitive Dyes

PAG loadings in traditional CARs are typically less than 5 wt% of the total solid that leads to the concentration of generated acid upon exposure to radiation being around the level of 10^{-2}~10^{-3} mol/L in a solid-state resist film. For a successful application of spectrometry for quantifying PAG acid generation in CARs, the dye molecule must be sensitive to the presence of Lewis and Bronsted acids and undergo large spectroscopic shifts upon interaction with the acid molecule in order to monitor and quantify PAG acid generation, especially for the study of a solid-state resist film where the broadening of the absorption band is common. In this work, an acid-sensitive dye, Coumarin 6 (C6, Mw=350.44, Sigma Aldrich), is chosen as the UV/VIS tag in this method to quantify PAG acid generation in a polymer film upon exposure to radiation. The physiochemical properties of C6 in solution phase and solid-state films have been carefully investigated and reported.[3] Upon the presence of acid, the proton attaches exclusively to the ring nitrogen of C6 molecule, forms a protonated monocation ($C6^+$), and changes the electron cloud distribution of the original neutral C6 molecule. The protonation of C6 upon photodecomposition of a triphenylsulfonium trifluoromethylsulfonate (TPS.TFMS) and the generation of acid, as well as the resonance structures of $C6^+$, are illustrated in figure 4.5.

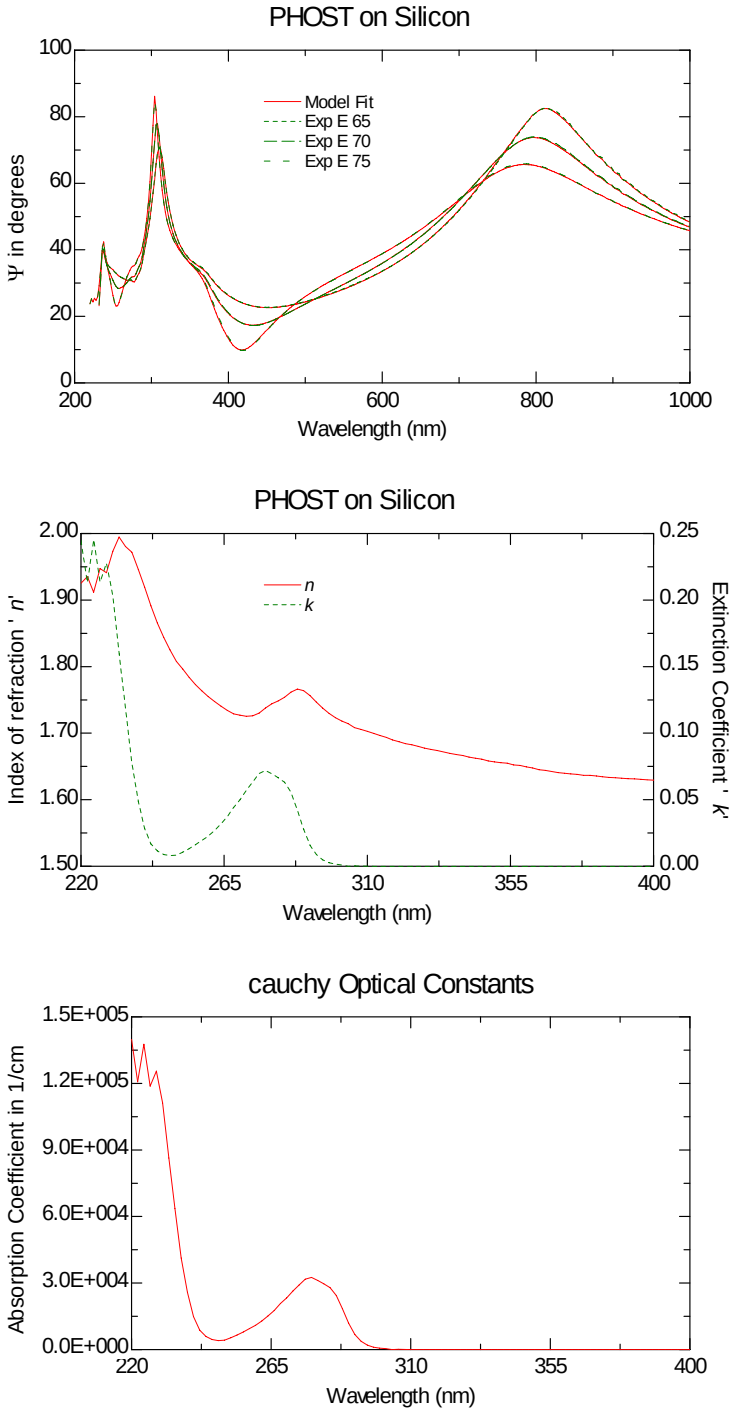

Figure 4. 4 The measured and model-fitted ellipsomtery spectra (top), the extracted DUV optical constants (middle), and the calculated DUV absorption coefficients (bottom) of a pHOST thin film (150 nm) spin-coated on a flat silicon wafer.

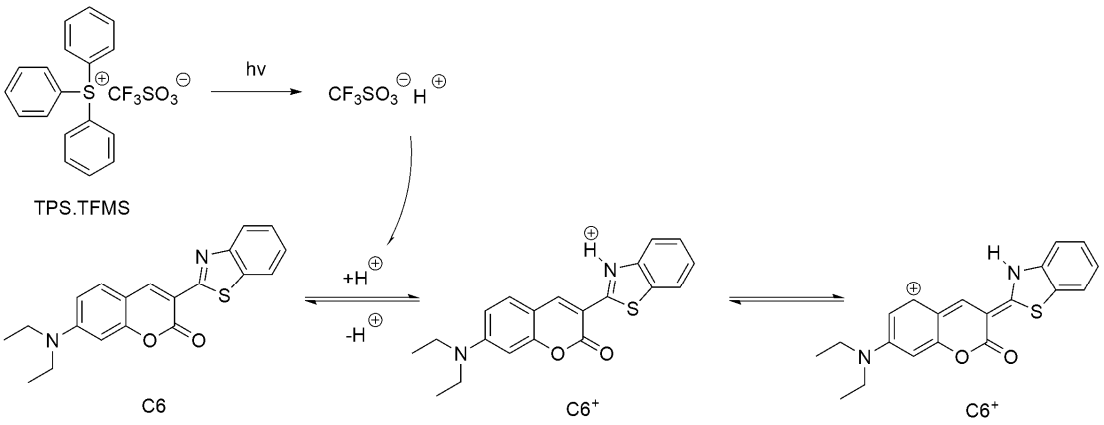

Figure 4. 5 Illustration of the protonation of C6 upon photodecomposition of TPS.TFMS and the generation of an acid, as well as the resonance structures of $C6^+$.

Solution phase absorbance of C6 and $C6^+$ is performed to test the applicability of using C6 to probe the presence of superacids generated from PAGs photodecomposition. As shown in figure 4.6, the absorption peak of C6, $\lambda_{max,C6}$, is measured at 456 nm in acetonitrile solution. A significant red-shift of the absorption peak is found upon the addition of a trifluoromethanesulfonic acid ($H^+CF_3SO_3^-$, Mw=150.08, Fluka), resulting in an absorption peak, $\lambda_{max,C6+}$, at 520 nm for the monocation species. The large red-shift, on the order of ~65 nm, is attributed to the change-transfer interaction which occurs from the electron-rich diethylamino moiety to the ring protonated benzothiazole.[3,4]

By introducing the on-wafer ellipsometry technique mentioned in previous section, C6 can also be applied to detect and quantify acid in thin polymer films. The absorption of pHOST and poly(methyl methacrylate) (pMMA, Mw=15,000, Sigma Aldrich) films containing 5 wt% TPS.TFMS and equal mol% C6, before and after DUV exposure, are shown in figure 4.7. Blue-shifts of the absorption peaks are observed in both C6 and $C6^+$ spectra when switching the polymer matrix from a polar pHOST to a non-polar pMMA. Since the polarity of a molecule usually changes with electronic transition, the position and the intensity of absorption peak of the dye may be shifted depending on the polarity of the polymer matrix.

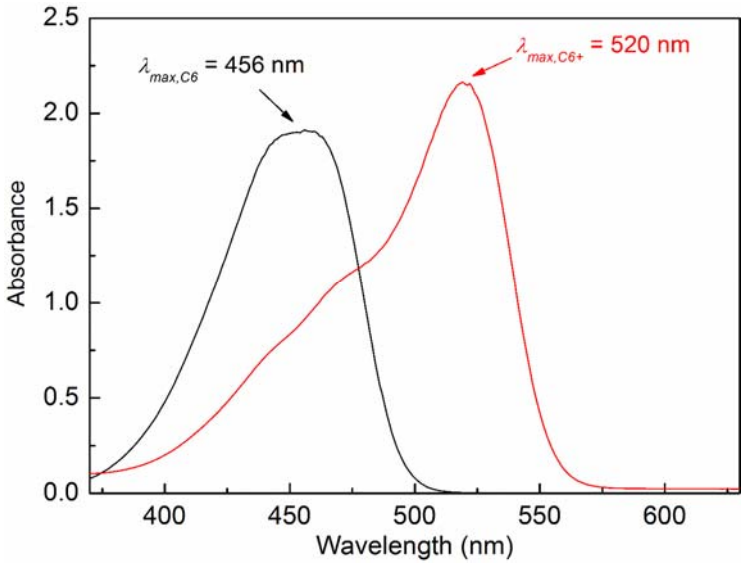

Figure 4. 6 Absorption spectra of 3.0×10^{-5} mol/L C6 in acetonitride solution for the neutral species and the monocation formed upon the addition of $H^+CF_3SO_3^-$.

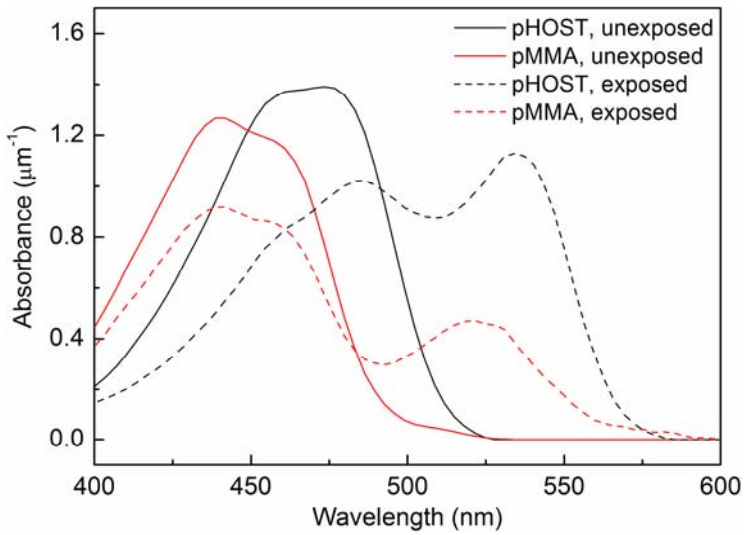

Figure 4. 7 C6 absorption spectra of pHOST and pMMA films containing TPS.TFMS and C6 extracted using the on-wafer ellipsometry method.

The aggregation behavior of C6 molecules in solution and solid state application has been reported and showed an additional absorption band at 550 nm region in addition to the 450 nm absorption.[3] In the spectra shown in figure 4.7, there is no absorption band

observed around 550 nm wavelength region, suggesting that C6 aggregation behavior is not present in the polymer film with the C6 concentration used in this work.

4.2 Experimental Procedure

The procedure of using on-wafer ellipsometry technique and acid-sensitive dye to study PAG acid generation in polymer films is demonstrated in this section. The acid-sensitive dye, C6, is used as a proton indicator to monitor PAG acid generation in a polymer film. TPS.TFMS is used as the PAG studied in this work. pMMA is used as the resin for studying PAG acid generation through direct PAG excitation pathway for since pMMA has insignificant absorption at DUV (248nm) wavelength region if compared to PAG molecules (0.04 μm^{-1} at 248 nm, several tens order lower than PAGs). DUV absorbing polymer such as pHOST is used as the matrix for studying polymer sensitization pathway for PAG acid generation since pHOST has been reported to enable efficient energy transfer to PAG for decomposition and acid generation.[5,6] Polymer solutions are prepared by dissolving PAG, polymer resin, and C6 in cyclohexanone (reagentplus grade, Sigma Aldrich). The structures of the polymers and PAG used in this work are shown in figure 4.8.

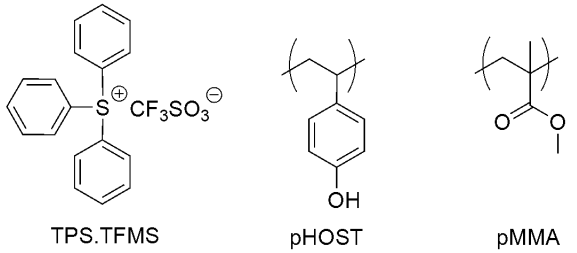

Figure 4. 8 The structures of polymer resins and PAG used in this work.

Polymer films (~150 nm in thickness) are prepared by spin-coating the polymer solution onto primed silicon wafers and baked at 100 ^{o}C for 2 minutes to remove residual solvent. A variable-angle spectroscopic ellipsometer (V-VASE, J. A. Woollam Inc.) is used to collect the ellipsometry spectra of PAG and dye doped polymer films. For the measured ellipsometry spectra of each polymer film, the film thickness is determined by fitting the Cauchy model to the non-absorption region spectrum (600~1000 nm). Exposure intensity profile deposited in the film is calculated by using the optical constants obtained by fitting the refractive indexes of the Cauchy model with fixed parameters to the spectrum in the DUV wavelength region (200~370 nm). The optical constants of $C6^{+}$ was determined by fitting the refractive indexes of the Cauchy model with fixed parameters to the dye absorption region of the spectrum (370~600 nm) The corresponding film and dye absorptions is then calculated by equation (4.6). Polymer films are exposed using an Oriel Instruments exposure source (model 87530-1000, Hg-Xe arc lamp) filtered by a 248 nm bandpass filter (bandwidth ~11 nm, FWHM). The polychromatic DUV intensity profile in the polymer films is calculated using the method reported in chapter 3 and is used to calculate energy deposited in the polymer film. The amount of acid generated though the photodecomposition of PAGs when subject to DUV radiation can be quantified by determining the absorption of $C6^{+}$ and the correlation between $C6^{+}$ absorption and acid concentration. Figure 4.9 shows an example of ellipsometry spectra of a polymer film doped with PAG and C6. The general use of the collected ellipsometry spectra for determining PAG acid generation in the resist film is also illustrated.

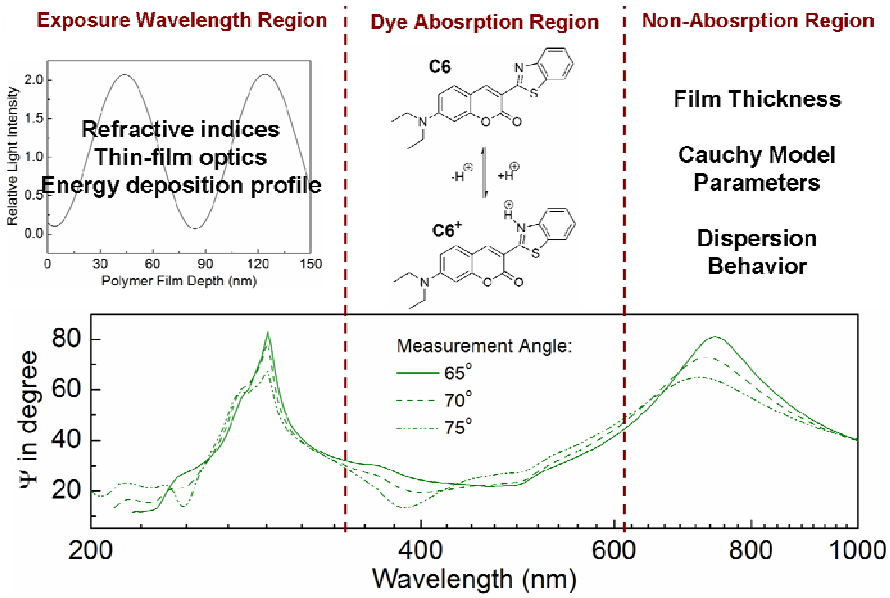

Figure 4. 9 The general use of the ellipsometry spectra of a polymer film doped with PAG and C6 spin-coated on a silicon wafer and exposed to DUV radiation.

4.3 Results and Discussion

Calibration between $C6^+$ absorption and the acid concentration in the polymer film is made by mixing varying amounts of trifluoromethanesulfonic acid into the polymer solutions containing fixed amount of C6 and spin-casting films from these solutions. The correlations between $C6^+$ absorbance and acid concentration in pHOST and pMMA films are obtained with highly-confident linear relationships, as shown in figure 4.10.

PAG acid generation upon exposure to DUV radiation is monitored by this technique. Figure 4.11 shows C6 absorbance spectra of pHOST films (5 wt% TPS.TFMS and equal mole C6 loadings) exposed to incremental doses as determined via this ellipsometry technique. $C6^+$ absorbance in polymer films increases as the applied DUV dose increase, and a self-consistent absorbance shift from C6 to $C6^+$ is observed. The presence of a clear *isosbestic* point in the spectra indicates the excellent self-

normalization function between measurements of different samples, as well as the capability of using ellipsometry spectrometry to quantify the protonation of C6 upon PAG photodecomposition and acid generation.

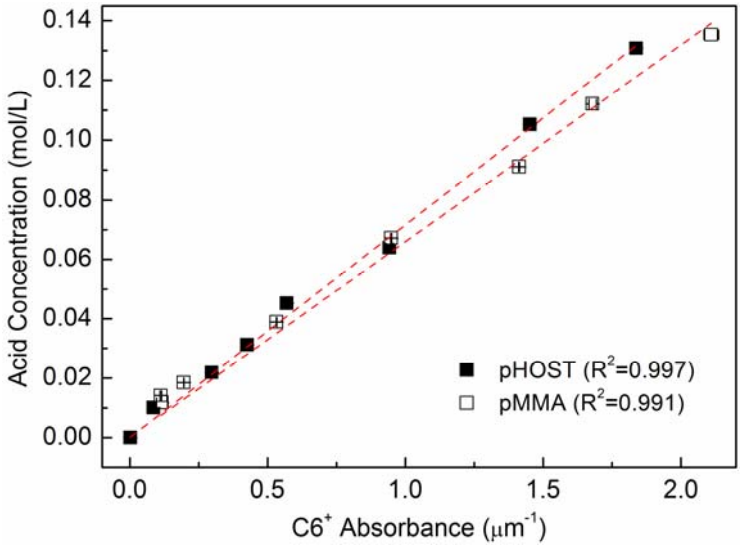

Figure 4. 10 Calibration curves of acid concentration and $C6^+$ absorbance in pHOST and pMMA films.

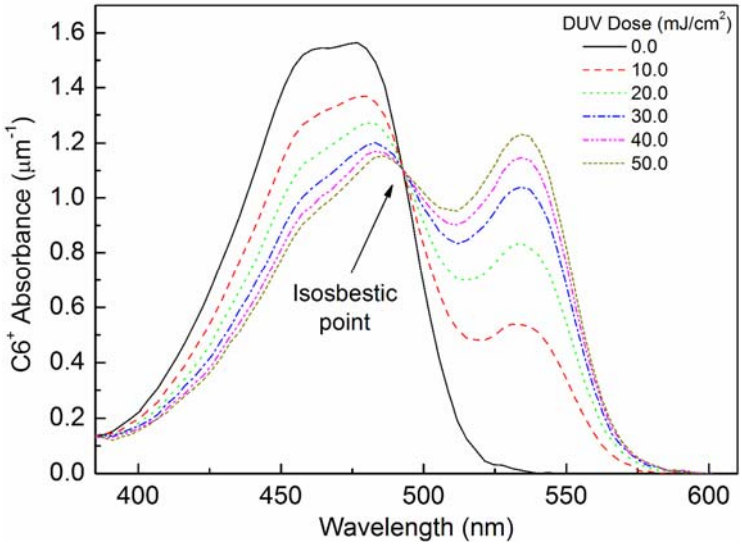

Figure 4. 11 C6 absorbance spectra of pHOST films (5 wt% TPS.TFMS and equal mole C6 loadings) exposed to incremental DUV doses extracted using the on-wafer ellipsometry technique.

Potential confounding effects associated with the use of solid-state acid-sensitive dye method have not been carefully investigated and reported. It is necessary to address these effects before using this technique for further studies. Major effects such as $C6^+$ stability under ambient conditions and the probability of proton-dye contact in a solid-state film are investigated. Polymer films containing equal mole TPS.TFMS and C6 in pHOST and pMMA matrices are prepared and exposed to DUV radiation (30 mJ/cm^2). The dependences of acid concentration on post-exposure delay and PEB are monitored and illustrated in figure 4.12. Changes of acid concentration are observed in both polymer films. Acid concentration in pHOST film shows a fast and apparent decrease as the post-exposure delay time increase. Airborne bases such as ammonia, amines, or n-methyl pyrrolidone (NMP) usually possess higher basicity than C6. These molecules may diffuse into the polymer film and deprotonate $C6^+$ and trap the proton, thus decrease the apparent concentration of photogenerated acid. Immediate measurement right after the exposure or the experimental operation under a base free environment is essential for preventing this problem. PEB of pHOST and pMMA films show increases in apparent acid concentration of 7.5% and 40.5%, respectively, when compared with samples without any PEB. The mass density of a pHOST film consisting of 1.5 mol% TPS.TFMS and 1.5 mol% C6 molecules is determined being 1.16 g/cm^3 using the method describes in chapter 5. In this case the average spacing of each PAG and C6 molecule is approximately 10 nm if a homogeneous distribution of components is assumed. Under room temperature (25^{o}C) the trifluoromethanesulfonic acid generated from TPS.TFMS photodecomposition possesses a diffusion coefficient smaller than 10^{-5} nm^2/sec in a pHOST matrix as calculated from the acid diffusivity data in chapter 5. The low acid diffusivity and the relatively large spacing between generated acid and dye molecules indicate that acid may has low probability being detected by the dye without any thermal treatment. This effect is even more significant under high exposure dose since a large portion of the dye molecules have been consumed by the acids. The acid diffusivity increases to 10^{-2} nm^2/sec at 70 ^{o}C

that can provide significantly higher acid diffusivity than that at room temperature. This result suggests that the probability of proton-dye contact in a polymer film can be relatively low when a PEB is not applied and this can lead to significant error in quantifying acid concentration. A physical model which can describe the dependence of proton-dye contact probability on PEB temperature is essential to the quantification of PAG acid generation in polymer film. This effect appears to be less important in a pHOST matrix, and may be due to the formation of inter- and intramolecular hydrogen bondings among hydroxyl groups in the polymer. The hydrogen bonding network may facilitates proton migration and transfer between subunits and proton-dye contact.[7,8] The slight increase in detected acid concentration in a pMMA film over time at room temperature is probably due to the slow room temperature diffusion of the proton in the non-polar pMMA matrix which slowly increases the number of protons being detected by dye molecules.

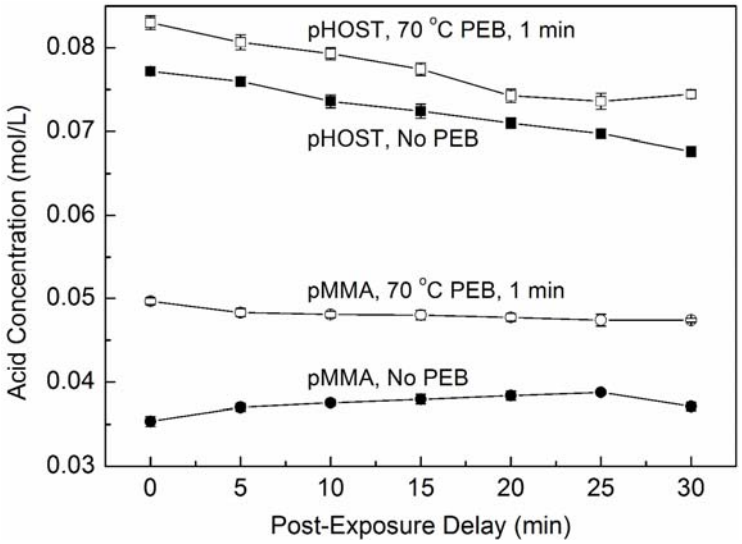

Figure 4. 12 Effects of PEB and post-exposure delay on acid concentration quantified by $C6^+$ absorbance in pHOST and pMMA films.

The effect of C6 loading on PAG sensitization and acid generation is also evaluated. Polymer films (150 nm in thickness) containing identical pMMA and TPS.TFMS loadings, but different C6-to-TPS.TFMS loading ratios, are prepared, exposed, and baked (at 70 ^{o}C for 1 min). Acid concentrations in polymer films are measured and an acid generation rate of each sample is determined by linearly fitting the data as shown in figure 4.13. Changing C6 loading shows no significant effect on PAG acid generation that indicates C6 sensitization pathway for PAG acid generation is negligible. The average acid generation rate for all C6-to-TPS.TFMS loading ratios is 0.00221 ± 0.00015 ((mol/L)/(mJ/cm2), 95% confidence). The small variations in acid generation rate among samples are not statistically significant and do not follow any particular order or trend. These variations are likely the result of small variations in polymer film thickness or lamp intensity that lead to small variation of energy deposition profile in different polymer films.

-

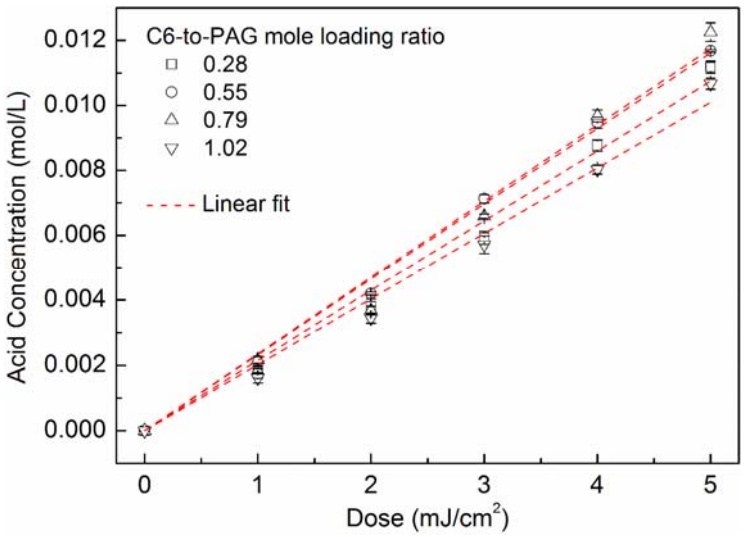

Figure 4. 13 Effect of C6 loading on PAG acid generation under DUV exposure.

Photodecomposition of a PAG molecule into its products is generically assumed to be a first-order kinetics that can be readily described by equation (4.7)

$$C_{Acid} \equiv C_{PAG,ini}\left(1 - e^{-CE}\right) \tag{4.7}$$

Here $C_{PAG,ini}$ and C_{Acid} are the initial PAG concentration and acid concentration after exposure, respectively. E is the exposure dose and C is the Dill C parameter representing acid generation rate constant.[9] When using dye to monitor acid generation in a polymer film, the observed acid concentration ($C_{Acid,obs}$) may be lower than the actual acid concentration if the proton and C6 do not have sufficient time or mobility to encounter and react with each other. A simple modification of the original PAG acid generation model in equation (4.7) can be made by adding one additional parameter to describe the relationship between $C_{Acid,obs}$ and C_{Acid} as shown in equation (4.8).

$$C_{acid,obs} \cong FC_{acid} = FC_{PAG,ini}\left(1 - e^{-CE}\right) \tag{4.8}$$

Here F represents the proton-dye contact efficiency (i.e. the fraction of generated acids that reacts with the dye molecules) and is primarily a function of the proton diffusivity and polymer film composition. Proton diffusivity is affected by many factors including matrix polarity, counter-anion size, and PEB temperature. At this point only one single F parameter is used to describe these effects in order to facilitate the model fitting process. An optimization strategy is employed for determining C and F parameters of the samples studied in this work. By measuring $C_{Acid,obs}$ at different PEB temperatures and exposure doses, a global C and different F parameters for describing proton-dye contact efficiency under different PEB temperatures can be extracted by fitting equation (4.8) to the measured acid concentration versus dose data.

Figure 4.14 and table 1 show the measured acid concentration data and the model fitting results of TPS.TFMS in pHOST and pMMA films (Polymer : TPS.TFMS : C6 =

97 : 1.5 : 1.5, molar ratio) under DUV exposure and different PEB conditions (no PEB and 70 ^{o}C PEB for 1 min). Acid generation rate constants for TPS.TFMS in pHOST and pMMA are determined being 0.0421 cm^2/mJ and 0.0237 cm^2/mJ, respectively. The PAG acid generation rate in pHOST is in good agreement with the values reported by other methods and the technique reported in chapter 3.[10-13] The acid generation rate constant in pMMA is 43.7% lower than that in pHOST, suggesting that the presence of a polymer sensitization pathway in pHOST plays an significant role for TPS.TFMS acid generation in this polymer. The use of this technique to the study of polymer structure and radiation source effects on acid generation of different PAGs is performed and the results are provided in chapter 10.

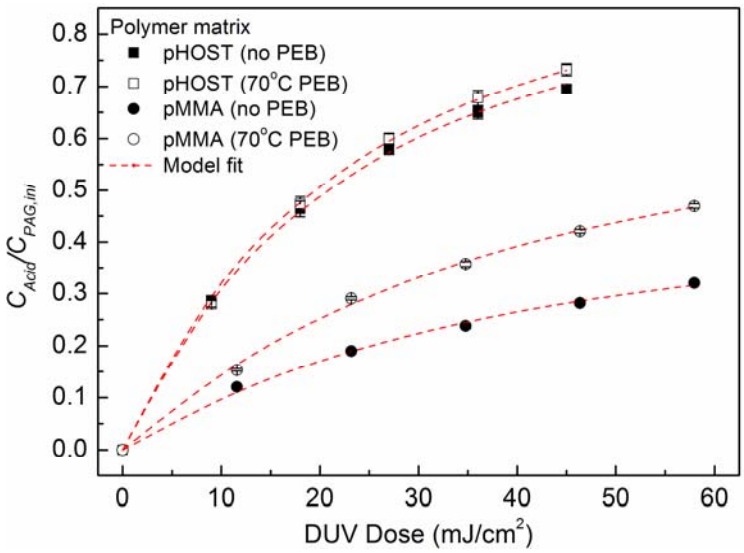

Figure 4. 14 Acid generation rate and model fitting results of TPS.TFMS in pHOST and pMMA films under DUV exposure.

Table 4. 1 Extracted Dill C and F parameters of TPS.TFMS acid generation in pHOST and pMMA films.

Resin	PEB condition	*C*-parameter (95% confidence)	*F*-parameter (95% confidence)
pHOST	No PEB	0.0421 (0.0022)	0.9492 (0.0169)
	70 °C, 1 min		0.9853 (0.0174)
pMMA	No PEB	0.0237 (0.0039)	0.4787 (0.0299)
	70 °C, 1 min		0.7087 (0.0424)

4.4 Conclusions

In this chapter, another fast, convenient, and material-saving technique for studying PAG acid generation in solid-state polymer films has been developed and demonstrated. This method utilizes on-wafer ellipsometry to determine the absorption behavior of an acid-sensitive dye, which is incorporated into the polymer film as a acid indicator. The validity of this new analytical method is verified by comparing the results in selected PAG-polymer combinations with results obtained from studies using different techniques. The presence of airborne base can decrease the concentration of $C6^+$ and lead to an underestimation of the real acid generation rate constant. C6 loading, up to 1:1 C6:PAG, shows no significant C6 sensitization effect on TPS.TFMS acid generation. The importance of using a PEB step to modulate photoacid-dye contact efficiency and thus extract an accurate PAG acid generation rate constant is demonstrated. The use of this technique to compare the importance of direct PAG excitation versus polymer sensitization for acid generation in the case of TPS.TFMS is also demonstrated. This study serves as the starting point for building the structure-property relationships necessary for intelligent PAG and polymer matrix design to optimize exposure energy utilization in CARs. The experimental design here also demonstrates the capability of

using this technique and different polymer matrix to probe PAG acid generation through direct PAG excitation and indirect polymer sensitization pathways that is important to the development and design of sensitive PAGs and resist materials for NGL technologies.

4.5 References

[1] Field, L. D.; Sternhell, S.; Kalman, J. R., In chapter 2 of *Organic structures from spectra, 3rd ed.* **2002**, John Wiley and Sons Ltd, New York, USA.

[2] Tompkins, H. G.; Irene, E. A., *Handbook of ellipsometry*, **2005**, William Andrew Inc., Heidelberg, Germany.

[3] Corrent, S.; Hahn, P.; Pohlers, G.; Connolly, T. J.; Scaiano, J. C.; Forne´s, V.; Garcı´a, H., Intrazeolite photochemistry. 22. Acid-base properties of Coumarin 6. Characterization in solution, the solid state, and incorporated into supramolecular systems, *J. Phys. Chem. B* **1998**, *102*, 5852-5858.

[4] Scaiano, J. C.; Laferriere, M.; Ivan, M. G.; Taylor, G. N., A protocol for the verification of acid generation in 157 nm lithography, *Macromolecules* **2003**, *36*, 6692-6694.

[5] Hacker, N. P.; Welsh, K. M., Mechanistic studies on the poly(4-tert-butoxy carbonyloxystyrene)/triphenylsulfonium salt photoinitiation process, *Proc. SPIE* **1991**, *1466*, 384-393.

[6] Hacker, N. P.; Hofer, D. C.; Welsh, K. M., Photochemical and photophysical studies on chemically amplified resists, *J. Photopolym. Sci. Technol.* **1992**, *5*, 35-46.

[7] Li, D.; Brisson, J., Hydrogen bonds in poly(methyl methacrylate)-poly(4-vinyl phenol) blends: 1. Quantitative analysis using FTIR spectroscopy, *Polymer* **1998**, *39*, 793-800.

[8] Itani, T.; Yoshino, H.; Hashimoto, S.; Yamana, M.; Samoto, N.; Kasama, K., Relationship between remaining solvent and acid diffusion in chemically amplified deep ultraviolet resists, *Jpn. J. Appl. Phys.* **1996**, *35*, 6501-6505.

[9] Dill, F. H.; Hornberger, W. P.; Hauge, P. S.; Shaw, J. M., Characterization of positive photoresist, *IEEE Trans. Electron Devices* **1975**, *ED22*, 445-452.

[10] Berger, C. M.; Byers, J. D.; Henderson, C. L., Using interdigitated electrodes for measuring photoacid generator kinetics in chemically amplified resists, *J. Electrochem. Soc.* **2004**, *151*, G119-G130.

[11] Lee, C. –T.; Yueh, W.; Roberts, J. M.; Henderson, C. L., A simple method for measurement of photoacid generator photoreaction kinetics in formulated, chemically amplified photoresist films, *Electrochem. Solid-State Lett.* **2007**, *10*, H273-H277.

[12] Cameron, J. F.; Chan, N.; Moore, K.; Pohlers, G., Comparison of acid-generating efficiencies in 248 and 193-nm photoresists, *Proc. SPIE* **2001**, *4345*, 106-117.

[13] Pawloski, A. R.; Szmanda, C. R.; Nealey, P. F., Evaluation of the standard addition method to determine rate constants for acid generation in chemically amplified photoresist at 157 nm, *Proc. SPIE* **2001**, *4345*, 1056-1065.

CHAPTER 5

IN SITU CHARACTERIZATION OF ACID DIFFUSIVITY IN CHEMICALLY AMPLIFIED RESIST FILMS[†]

CARs operate by an acid-catalyzed deprotection mechanism of the polymer matrix as introduced in chapter 2. Resist resolution is affected if the original distribution of acid molecules generated during exposure changes due to acid migration during PEB. The higher the acid diffusivity (i.e. longer acid-catalytic chain length), the more serious the resist image blur problem and thus the lower the resist resolution. For the characterization of a CAR, it is important to determine acid diffusivity in the resist film during PEB. It can be more beneficial to the development of novel CAR materials if effects, such as acid size, acid reactivity, and resist matrix properties, on acid diffusivity can be well determined and correlated. This chapter describes the development of an experimental-modeling technique for determining acid diffusivity in a resist film. The application of this technique to studying acid size and matrix property effects is also demonstrated and reported.

5.1 Theory

The diffusion behavior of small molecules in a space can be described by the

---

[†] Material presented in this chapter has appeared in part in previously published articles:

Lee, C. –T.; Yueh, W.; Henderson, C. L., In situ technique for determining acid diffusion behavior in chemically amplified resist films via mesoscale stochastic acid reaction-diffusion modeling of bulk resist deprotection chemistry, *J. Vac. Sci. Technol. B*, submitted.

Lee, C. –T.; Yueh, W.; Henderson, C. L., Effects of acid and matrix properties on acid reaction-diffusion behavior in chemically amplified resists., *Chem. Mater.*, submitted.

equilibrium of a thermodynamic system.[1] Consider a single-component system (i.e. there is only one species of molecules in the system) with constant temperature T and pressure P, the chemical potential μ is defined as the partial molar Gibbs free energy as shown in equation (5.1).

$$\mu = \left(\frac{\partial G}{\partial n} \right)_{T,P} \tag{5.1}$$

Here G is the Gibbs free energy. Chemical potential μ can also be related to the thermodynamic activity a as shown in equation (5.2).

$$\mu = \mu_0 + RT \ln a \tag{5.2}$$

Here μ_0 is the standard/reference chemical potential, R the ideal gas constant. Along the spatial coordinates of the system, the spatial gradient of μ is the partial derivative of equation (5.2) as shown in equation (5.3).

$$\nabla \mu = \frac{RT}{c} \nabla c \tag{5.3}$$

Here c is the species concentration. Since the driving force of diffusion is the chemical potential gradient of the species, the diffusive flux J (i.e. the amount of species flow through per unit area) is assumed to be proportional to the spatial gradient of the chemical potential, and thus the spatial gradient of the species concentration as shown in equation (5.4).

$$J \propto \nabla \mu = \frac{RT}{c} \nabla c \tag{5.4}$$

The relationship between diffusive flux and the concentration gradient can be correlated by defining a diffusion coefficient D as shown in equation (5.5) which is know as *Fick's first law* of diffusion.

$$J = -D \nabla c \tag{5.5}$$

Fick's first law of diffusion is used for the description of a system under steady-state diffusion. Consider a control volume in a space where the species flow in and out of the control volume, the net change of species concentration in the control volume is equal to the net flux of species across the boundary of the control volume. The mass balance relationship is shown in equation (5.6) which is also know as the *equation of continuity* or *Fick's second law* describing the mass flux and distribution of a non-steady or continually changing state of a diffusion system.

$$\frac{\partial c}{\partial t} = \nabla \cdot J = \nabla \cdot \left(D \nabla c \right) \tag{5.6}$$

Fick's first and second laws are commonly applied to the study of species diffusion behavior in various systems. The solutions (theoretical or numerical) of these two equations can be applied to specifically-designed experimental systems to extract the diffusion coefficients of interest. For the application to studying acid diffusion in a CAR film, the use of Fick's second law is more common since the resist film is usually thin (few microns to a hundred nanometers) and the available acid source is usually limited. Researchers intend to design experimental configurations, such as pattern-wise exposure

of a resist film or a bilayer film stack contain an acid feeding layer and an acid detection layer, to generate a high contrast initial acid distribution profile in order to monitor acid migration and use Fick's second law to extract acid diffusion coefficient. However these methods suffer intrinsic problems mentioned in chapter 2, such as poor precision, low sensitivity, and in some cases lacking the applicability of *in situ* study. These fundamental issues limit their applicability to the study of many CAR systems.

In this chapter, a novel concept and the corresponding technique for determining acid diffusivity in a resist film are developed and demonstrated. Consider a condition where a resist film is flood exposed and all the PAGs have been photodecomposed and generate acids. From a macroscopic point of view a constant and uniform acid concentration in the bulk resist film is usually assumed in this case and no acid diffusion is expected since there is no concentration gradient in the resist film. In reality, acid molecules are sparsely distributed in the resist film. Acid distribution heterogeneity does exist and create microscopic acid concentration gradient which serves as the driving force for microscopic acid diffusion. In an extreme case each acid molecule randomly migrates during the baking process from its initial position to other locations in the resist film. Such microscopic acid diffusion behavior in a flood-exposed resist film can also be well described by Fick's second law.

Consider seven adjacent cubic cells with the same edge length l in a three-dimensional (3D) space described by a Cartesian coordinate as shown in figure 5.1. The cell size represents the volume which is small enough that the microscopic heterogeneity of molecular distribution can be captured. The center red cell indicates the cell occupied by molecules of interest and the six adjacent cells are empty initially.

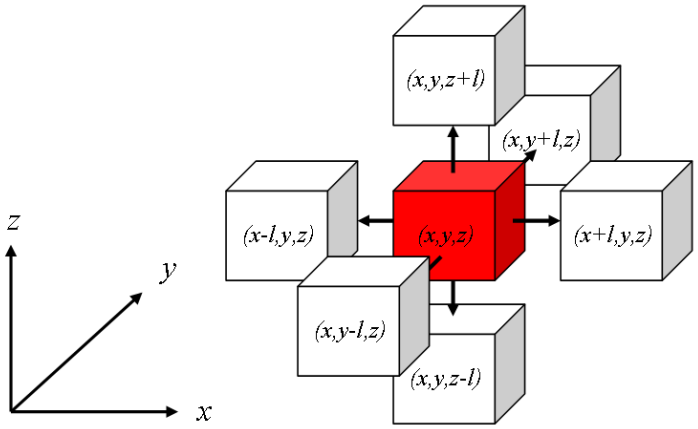

Figure 5. 1 Illustration of single molecule diffusion through random walk.

For any pair of cells containing the center cell and one adjacent cell, there is a molecular concentration gradient existed in this small two-cell volume. The concentration gradient can serve as the driving force pushing molecules diffusing from the center cell to any of the adjacent cells with the same probability. Assuming isotropic molecule diffusivity among cells in this system (i.e. constant diffusion coefficient), the rate equation of moving molecules from the center cell to a positive x direction can be derived from equation (5.6) and is shown as equation (5.7).

$$r_{Diff,+x} = \left(\frac{\partial n}{\partial t}\right)_{+x} = D\frac{\partial^2 n}{\partial x^2} \tag{5.7}$$

Since there are six adjacent cells in a 3D spatial system and the probabilities of diffusing to any of them are the same, the overall diffusion rate can be represented as equation (5.8).

$$r_{Diff,overall} = \left(\frac{\partial n}{\partial t}\right)_{overall} = 2D\left(\frac{\partial^2 n}{\partial x^2} + \frac{\partial^2 n}{\partial y^2} + \frac{\partial^2 n}{\partial z^2}\right) \tag{5.8}$$

Here the factor 2 indicates the doubled probability that the molecule can diffuse to two directions (positive and negative) in each dimension. By using the fact that microscopic acid distribution heterogeneity does exits in a bulk resist film containing small amount of acid molecules, it is possible to extract acid diffusion coefficient in a resist film by fitting resist bulk property changes, such as the deprotection extent of a resist matrix, to an acid reaction-diffusion model describing microscopic acid migration and reaction behavior.

5.2 Experiment and Model Description

5.2.1 FTIR Spectrometry of Resist Matrix Deprotection

In this work, the deprotection extent of a flood exposed resist film is measured and used as the data to determine acid diffusivity using a mesoscale model fitting method described in the next section. For the formulation of resist solutions, a fully *tert*-butoxycarbonyl (t-BOC) protected poly(p-hydroxystyrene) (pHOST) solids (pTBOCST) is synthesized and used as the polymer resin.[2] Triphenylsulfonium triflate (TPS.TFMS, Mw 412.45, Sigma Aldrich), bis(tert-butylphenyl)iodonium perfluorobutanesulfonate (TBI.PFBS, Mw 692.43, Sigma Aldrich), and triphenylsulfonium hexafluoroantimonate ($TPS.SbF_6$, Mw 499.13, Midori Kagaku) are individually used as PAG in the formulation. Resist solutions are prepared by dissolving 10 wt% solids (with respect to the total solution weight) into propylene glycol monomethylether acetate (PGMEA, Sigma Aldrich). The material structures are illustrated in figure 5.2 and the corresponding compositions of resist solutions are listed in table 5.1.

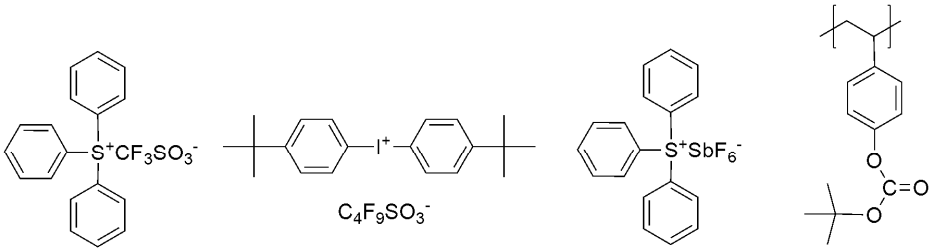

Figure 5. 2 Structures of protected polymer resin and PAGs used in this work.

Table 5. 1 The compositions of resist solutions used in this work.

Resist solution	PAG loading (wt% to solid)	Resin subunit to PAG mole ratio
pTBOCST + TPS.TFMS	0.46	547
pTBOCST + TBI.PFBS	0.77	402
pTBOCST + $TPS.SbF_6$	0.40	405

Prime grade silicon wafers are sequentially coated with a 25 nm titanium as the adhesion layer and a 250 nm gold as the infrared reflection layer via an electron-beam evaporation system (CVC SC 5000 e-beam evaporator, CVC Inc.) and used as the substrate for FTIR reflectance measurements. Resist films are prepared by spin-coating the solutions onto the gold-deposited wafer and post-applied baked at 100^{o}C for 2 minutes on a contact hot plate to remove residual casting solvent. Resist film thickness is measured being around 500 nm using a variable-angle spectroscopic ellipsometer (V-VASE, J. A. Woollam Inc.). The resist films are flood exposed at a dose of 200 mJ/cm^2 using an Oriel Instruments exposure source (model no. 87530-1000, Hg-Xe arc lamp) filtered using a 248 nm bandpass filter (bandwidth 11 nm, FWHM). Such long exposure time ensures full PAG decomposition and acid generation in the resist film. PEB at different temperature (70 ~ 110 ^{o}C) and time (0 ~ 90 sec) was followed after exposure. Exposure and PEB are performed in a base-free environment in order to eliminate possible acid loss kinetics through acid-base neutralization. The reflectance FTIR spectra

are collected using an FTIR microscope (IRscope II microscope, Bruker AXS Inc.) connected to a Bruker IFs66vS FTIR/ Raman system. Deprotection levels in the resist films are determined by monitoring the intensity of the carbonyl stretching peak associated with the t-BOC group (1755 cm^{-1}), while the C-H out-of-plane bending of the para-substituted benzene (827 cm^{-1}) is used as an internal standard for normalization of the collected FTIR data with respect to possible variations in resist film thickness and substrate reflectance of different samples.

5.2.2 Mesoscale Resist Model

A mesoscale resist model is developed to simulate the microscopic acid reaction-diffusion behavior in a flood exposed resist film during PEB process. The FTIR spectrometry of resist deprotection extent mentioned in previous section is fitted by the model to extract acid diffusion coefficients. The resist model is built by a 3D lattice containing 125,000 cubic cells (50×50×50) with the same size to represent the volume of the resist film simulated. The cell volume is set as the size approximated to a subunit of the resist polymer (i.e. a t-BOC protected HOST) or an acid molecule. The structure of the mesoscale resist model is illustrated in figure 5.3.

The volume and edge length of each cell in the 3D lattice are determined by measuring the molar density of the resist film using a quartz crystal microbalance (QCM, PLO-10 Phase Lock Oscillator, Maxtek Inc.). The frequencies of a 5 MHz gold-plated quartz crystal disk (model # SC-501-1) before and after resist coating are measured. The resist film on QCM disk is prepared using the same process as the film spin-coated on a gold-deposited silicon wafer.

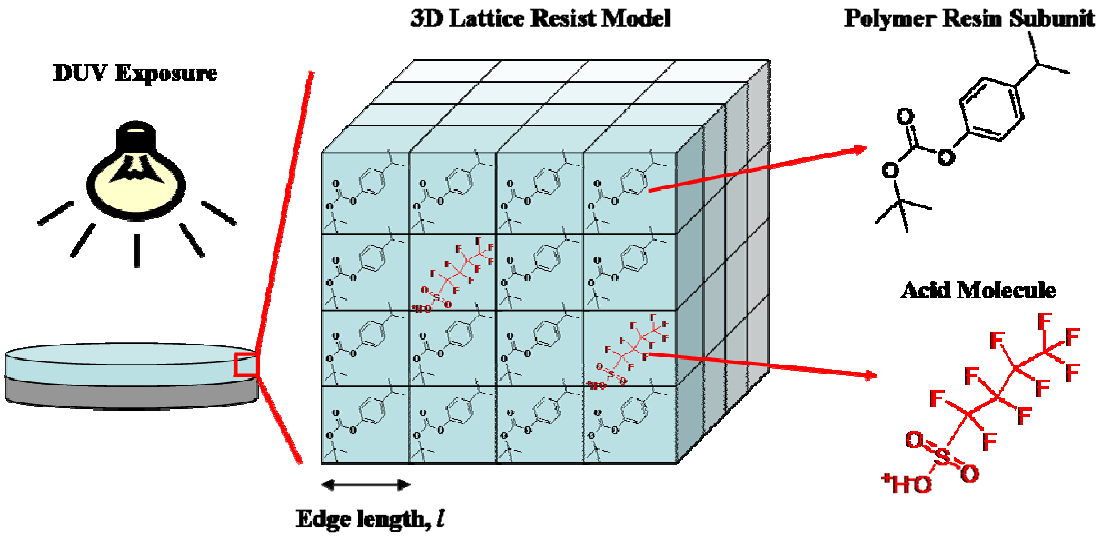

Figure 5. 3 Illustration of the developed mesoscale resist model for acid reaction-diffusion modeling.

The mass of the resist film m_{resist} on the QCM disk can be calculated using equation (5.9) which is simply a variation of the Sauerbrey equation.[3]

$$m_{resist} = \frac{f_{blank} - f_{coated}}{C_f} \tag{5.9}$$

Here f_{blank} and f_{coated} are frequencies of the QCM disk before and after coating the resist film, respectively. C_f is a constant related to crystal intrinsic properties and can be calculated using equation (5.10).

$$C_f = \frac{2f_q^2}{\rho_q \nu_q} \tag{5.10}$$

Here f_q is the resonant frequency of the bare crystal (nominally 5.0 MHz), ρ_q the density of the quartz crystal (2.649 g/cm^3), and ν_q the shear wave velocity of the AT cut quartz

crystals used in this study (332,200 cm/s). Resist film thickness on the QCM disk is measured using a ellipsometer. Resist molar density can be precisely calculated once the mass and the volume of the resist film on the disk are measured. The mass density of a pTBOCST film used in this work is determined as 1.14 g/cm^3. The corresponding molar density and the edge length of the cell used in the mesoscale resist model are 0.004872 mol/cm^3 and 0.698 nm, respectively.

5.2.3 Stochastic Acid Reaction-Diffusion Modeling

In the beginning of the modeling, all cells in the 3D lattice are randomly assigned either a polymer subunit or an acid molecule according to the resist film composition to initialize the resist model. Major physical and chemical phenomena in the resist film during PEB are simulated by a stochastic acid reaction-diffusion model using an exact stochastic simulation algorithm.[4,5] The fundamental hypothesis of the stochastic formulation of chemical kinetics is that the *stochastic reaction probability function* a_μ which characterizes the likelihood of reaction R_μ to happen in a reaction volume V in the next reaction time interval δt can be defined as equation (5.11).

$$a_\mu = c_\mu h_\mu \delta t \equiv \text{average probability that a particular reaction } R_\mu \text{ will occur in } V \text{ in the next time interval } \delta t \tag{5.11}$$

Here c_μ is the stochastic reaction rate constant, h_μ the number of distinct molecular reactant combinations for reaction R_μ found to be present in V within the time interval δt. For a simple bimolecular reaction, c_μ can be approximately correlated to the reaction rate constant k_μ commonly used in a deterministic kinetics by equation (5.12). The corresponding h_μ for this bimolecular reaction is represented as equation (5.13).

$$k_\mu \doteq Vc_\mu \tag{5.12}$$

$$h_\mu = X_1 X_2 \tag{5.13}$$

Here X_1 and X_2 represent the number of molecules of reactant 1 and 2 in V within the time interval δt. The fundamental hypothesis of the stochastic simulation algorithm can be applied and extended to the acid reaction-diffusion system of a resist film.

For the description of chemical reactions in the stochastic modeling, major reactions occur in the resist film during PEB are acid-catalyzed and auto-catalyzed deprotections of the polymer resin, as shown in figure 5.4. Acid-catalyzed deprotection is the second imaging mechanism of a positive-tone CAR as described in chapter 2. Auto-catalyzed deprotection is also a reaction of which some polymer subunits, such as the carbolic acid in this case, may possess acidity high enough to effectively deprotect the polymer resin at elevated PEB temperature.

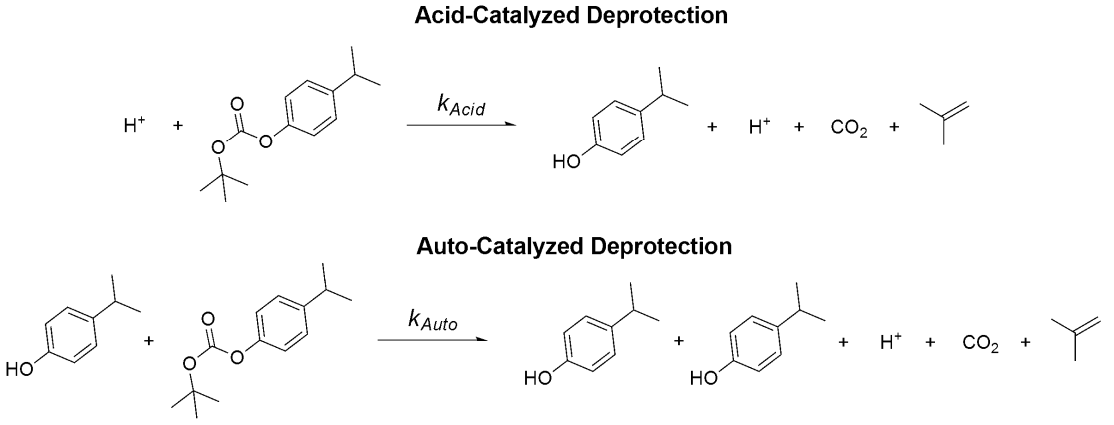

Figure 5. 4 Acid-catalyzed and auto-catalyzed deprotections of pTBOCST.

The probability functions of acid-catalyzed and auto-catalyzed deprotection reactions in a cell can be written as equation (5.14) and (5.15).

$$a_{Acid} = c_{Acid} h_{Acid} \delta t = c_{Acid} X_{Acid} X_{tBOC} \delta t \quad (5.14)$$

$$a_{Auto} = c_{Auto} h_{Auto} \delta t = c_{Auto} X_{HOST} X_{tBOC} \delta t \quad (5.15)$$

In the case of acid-catalyzed deprotection, X_{Acid} and X_{tBOC} can be either 0 or 1 depending on the absence or presence of an acid molecule and a t-BOC protection group in the cell, respectively. In the case of auto-catalyzed deprotection, X_{tBOC} can be either 0 or 1 depending on the absence or presence of a t-BOC protecting group in the cell, and X_{HOST} can be an integer between 0 and 6 depending on the number of HOST functional groups adjacent to the cell of interest. Stochastic reaction rate constants c_{Acid} and c_{Auto} can be obtained by using equation (5.12) while the deterministic reaction rate constants, k_{Acid} and k_{Auto}, of acid-catalyzed and auto-catalyzed deprotections can be determined using simple experimental-modeling methods.

For the description of acid diffusion in a stochastic modeling, acid diffusivity in a resist film is mainly influenced by a number of factors, such as PEB temperature, acid size, and the property of the polymer matrix. The acid diffusion model developed in this work takes all these effect into considerations. PEB temperature and acid size effects on acid diffusivity are inherent in the model since acid size and PEB temperature are independent variables which one can control through experimental design. For the matrix property effect, deprotection reactions in the resist film during PEB change polarity and electron affinity of the polymer resin that creates heterogeneity of local matrix property and may locally affect acid diffusivity. Multiple acid diffusion coefficients representing acid diffusivity in different polymer matrices are included in the model to deal with this important physical phenomenon. In the present case of a pTBOCST polymer, it has been reported that acid molecule possesses different diffusivity in t-BOC protected pHOST and pHOST polymers.[6] Acid molecule shows at least 1-order higher diffusion coefficient in t-BOC protected pHOST than that in pHOST under the same PEB temperature, mainly

due to the plasticizing effect and non-polar nature of the t-BOC functionality. The multi-diffusivity model developed in this work is illustrated in figure 5.5. On the other hand, the deprotection of t-BOC functionality generates carbon dioxide and isobutene which have high volatility and can evaporate from the resist film rapidly. The losing weight in deprotected matrix may result in the shrinkage of the resist volume that may also affect acid migration since the length scale of the resist film has changed. It is necessary to take into account the volume change effect into the model in order to have more precise extraction of acid diffusion coefficient. For a pTBOCST film a 42% film thickness loss is observed in a fully-deprotected film. This resist volume shrinkage is used to re-calculate the edge lengths of cells containing protected and deprotected polymer subunits.

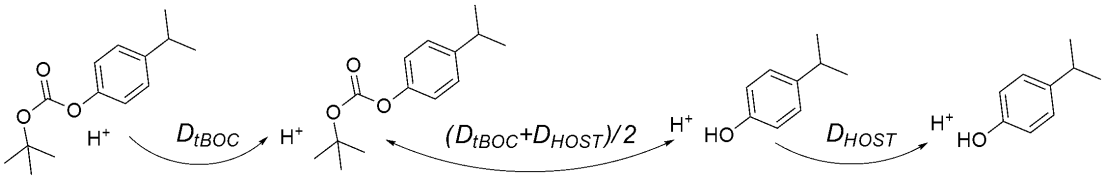

Figure 5. 5 Multiple acid diffusivity model describing acid reaction-diffusion in a pTBOCST film.

The corresponding stochastic probability functions describing one acid molecule hopping from one cell to another adjacent cell can be derived from equation (5.8) are shown in equation (5.16) ~ (5.18).

$$a_{tBOC\to tBOC} = 2D_{tBOC}\left(\frac{3X_{Acid}}{l_{tBOC}^2}\right)\delta t = \frac{6D_{tBOC}X_{Acid}}{l_{tBOC}^2}\delta t \tag{5.16}$$

$$a_{tBOC\leftrightarrow HOST} = 2\left(\frac{D_{tBOC}+D_{HOST}}{2}\right)\left\{\frac{3X_{Acid}}{\left[\left(l_{tBOC}+l_{HOST}\right)/2\right]^2}\right\}\delta t = \frac{12\left(D_{tBOC}+D_{HOST}\right)X_{Acid}}{\left(l_{tBOC}+l_{HOST}\right)^2}\delta t \tag{5.17}$$

$$a_{HOST\to HOST} = 2D_{HOST}\left(\frac{3X_{Acid}}{l_{HOST}^2}\right)\delta t = \frac{6D_{HOST}X_{Acid}}{l_{HOST}^2}\delta t \tag{5.18}$$

Here X_{Acid} can be either 0 or 1 depending on the absence or presence of the acid molecule in the cell. l_{tBOC} and l_{HOST} are the edge lengths of the t-BOC protected HOST and HOST, respectively. In this case 0.698 nm and 0.582 nm are obtained for l_{tBOC} and l_{HOST}, respectively. Since the PEB temperature used in this work is well below the glass transition temperature, acid molecule migration in a resist film is mainly relied on statistical polymer chain fluctuation which creates transient free volume in the matrix that allow the acid molecule to hop from one site to another. The acid hopping description in this model is valid in representing such microscopic acid random-walk behavior in a polymer film.

The stochastic acid reaction-diffusion modeling is performed by a *direct method* which contains the following steps:

Step 0: Initialize resist model by assigning polymer subunits and acid molecules into the cells of model lattice according to resist composition.

Step 1: Determine hopping direction of each acid molecule i by using a random number d_i.

Step 2: Calculate and store the values of stochastic probability functions associated with each reaction and diffusion using equations (5.14) ~ (5.18) for the current model condition.

Step 3: Calculate and store the sum of reaction and diffusion probability functions as shown in equation (5.19). Parameters *M, N, O, P, Q* represents the total number of reactions or diffusions available in current model condition.

$$a_0 = \sum_{i=1}^{M} a_{Acid,i} + \sum_{i=1}^{N} a_{Auto,i} + \sum_{i=1}^{O} a_{tBOC \rightarrow tBOC,i} + \sum_{i=1}^{P} a_{tBOC \leftrightarrow HOST,i} + \sum_{i=1}^{Q} a_{HOST \rightarrow HOST,i} \quad (5.19)$$

Step 4: Generate a pair of unit-interval uniform random numbers r_1 and r_2 and calculate the time τ for the next step (reaction or diffusion) to occur using equation (5.20). By placing all the available reactions and diffusions in a raw, determine the next step ν (a reaction or diffusion) to occur within the time interval τ by using the r_2 and the constraint in equation (5.21).

$$\tau = \left(\frac{1}{a_0}\right) \ln\left(\frac{1}{r_1}\right) \quad (5.20)$$

$$\sum_{i=1}^{\nu-1} a_i < r_2 a_0 < \sum_{i=1}^{\nu} a_i \quad (5.21)$$

Step 5: Increase the current simulation time by τ and update the change of the model condition after the reaction or diffusion occurred. For example, deprotect a cell if a deprotection reaction occurred, or update the new acid position and generate another random number d_i to determine the next acid hopping direction if an acid hopping occurred.

Step 6: Repeat steps 2-5 until the simulation time reaches the termination time of the simulation.

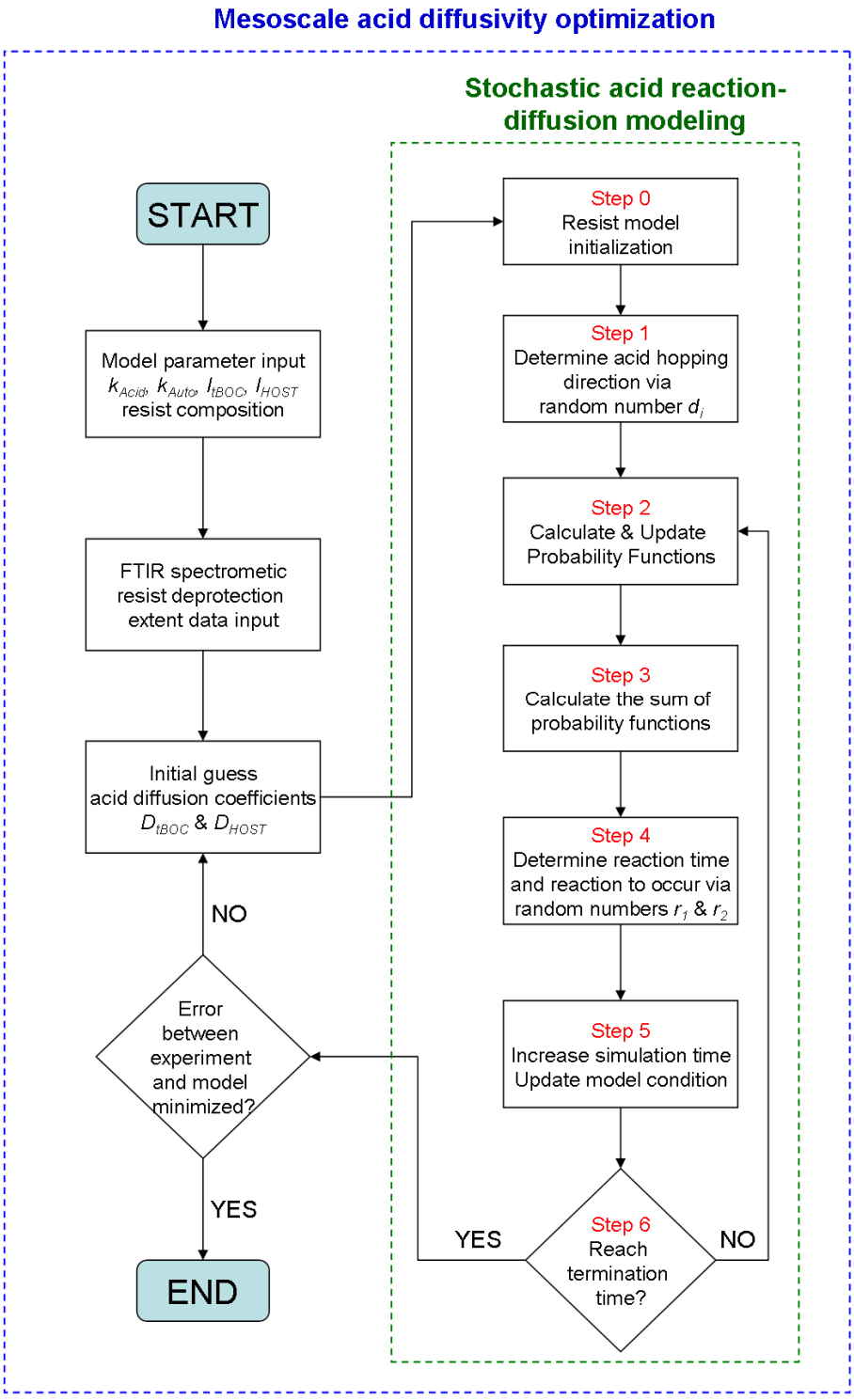

Figure 5. 6 Flow chart showing scheme of mesoscale stochastic acid reaction-diffusion experimental-modeling for determining acid diffusivity in a CAR film.

For each optimization process, the deprotection ratio of the resist film is calculated via dividing the number of the remaining protecting cells by the total number of cells of the system. Acid diffusion coefficients are obtained by averaging the extracted acid diffusion coefficients of 20 optimization results and the corresponding standard deviation is also calculated. The flow chart of a complete acid reaction-diffusion experimental-modeling for determining acid diffusivity in resist film is illustrated in figure 5.6.

5.3 Results and Discussion

5.3.1 Extraction of Acid Diffusion Coefficients

Normally acid-catalyzed deprotection reaction is significantly fast at the presence of super acids, such as those described in section 5.2.1, if compared with acid diffusion in the polymer matrix. The acid-catalyzed deprotection can be assumed to occur immediately when an acid molecule hops to a cell containing a protected subunit. On the other hand, since the acid-catalyzed cleavage of t-BOC protecting group is a high-activation energy process, auto-catalyzed deprotection induced by the weak acidity of phenol is insignificant if compared with acid-catalyzed deprotection under moderate PEB temperature. Simulation of auto-catalyzed deprotection of a partially-protected t-BOC pHOST film using a deterministic kinetic model is performed to determine the contribution of resin deprotection due to auto-catalysis. The auto-catalyzed deprotection kinetics used in this study are listed in equation (5.22) and (5.23).[7]

$$\text{pTBOCST} \xrightarrow{k_1} \text{pHOST} \tag{5.22}$$

$$\text{pTBOCST} + 2\text{pHOST} \xrightarrow{k_2} 3\text{pHOST} \qquad (5.23)$$

Literature reported values of k_1 and k_2 are used in the simulation. The PEB time dependent deprotection ratio of the polymer matrix at different PEB temperature and initial protection level are shown in figure 5.7. It is clear that the deprotection caused by auto-catalysis is less than 0.3 mol% even under the most extreme PEB condition (110 ^{o}C PEB temperature and 10 mol% protection) possibly existed in the experiments described in section 5.2.1. This level of deprotection is insignificant and the auto-catalyzed deprotection reaction can be neglected from the mesoscale stochastic acid reaction-diffusion model. Finally a detailed acid reaction-diffusion model can be simplified to an acid diffusion-limited model for the study of acid diffusivity in a pTBOCST film (i.e. high-activation energy protecting group) to relief the computational burden and complexity.

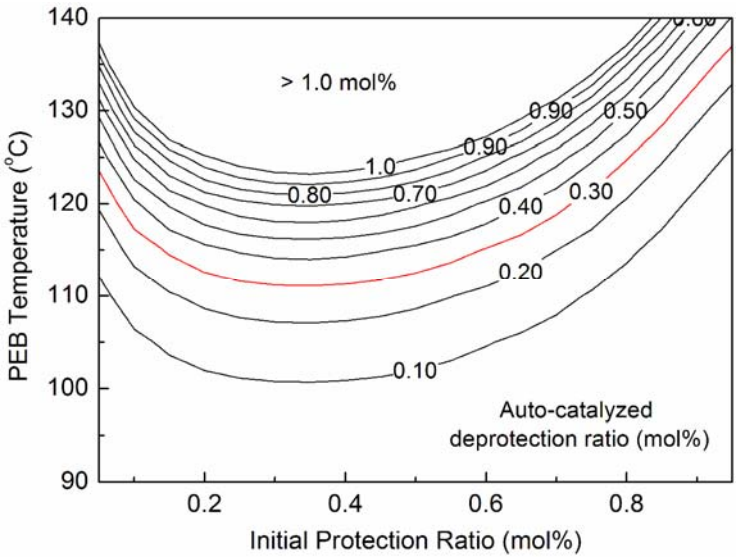

Figure 5. 7 PEB temperature and initial protecting ratio effects on auto-catalyzed deprotection ratio of a t-BOC protected pHOST film.

Experimental data and the best model fit for PFBS acid-catalyzed deprotection of a pTBOCST film are shown in figure 5.8. The close fits to the data indicate that overage the PEB temperature range (80 ~ 100 ^{o}C) the mesoscale stochastic acid reaction-diffusion model can well describes the resist physics and chemistry, even effects such as acid loss or free volume formation in the resist film are not included in the model. The best fit acid diffusion coefficients are listed in table 5.2. Acid diffusion coefficients in the same resist system extracted by a "surface exposure" experimental-modeling method are also listed for comparison.[6] At 85^{o}C and 95^{o}C PEB temperatures, mesoscale stochastic acid reaction-diffusion model extracts PFBS acid diffusion coefficients which are less than a order difference comparing to the values reported by surface exposure method. Previous techniques all require the creation and characterization of high contrast initial acid distribution profile. Since the mesoscale stochastic model needs only the deprotection data measured from flood-exposed resist films, the easy of experimental operation and no need of acid profile characterization greatly facilitates the applicability of using this technique to study acid diffusion in resist films for different lithography technologies.

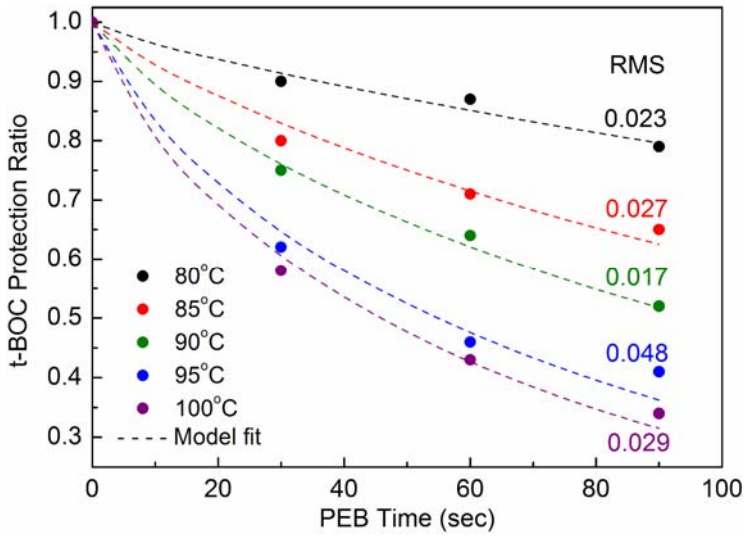

Figure 5. 8 Experimental data and the best fit acid reaction-diffusion model of PFBS acid-catalyzed deprotection in a pTBOCST resist film.

Table 5. 2 Extracted and literature reported PFBS acid diffusion coefficients in pTBOCST and pHOST matrices

Mesoscale Stochastic Model

PEB Temperature (°C)	D_{tBOC} (nm^2/sec)	D_{HOST} (nm^2/sec)
80	0.40657	0.049787
85	1.637443	0.081114
90	2.35082	0.130092
95	7.098759	0.216566
100	13.50947	0.251031

Surface Exposure Model[6]

PEB Temperature (°C)	D_{tBOC} (nm^2/sec)	D_{HOST} (nm^2/sec)
65	0.05	0.004
75	0.22	0.01
85	1.0	0.04
95	3.5	0.08
105	15	0.1

Arrhenius relationships of these extracted acid diffusion coefficients at different PEB temperature are shown in figure 5.9 and compared to those obtained by the surface exposure method in order to check the validity of determining PEB temperature dependence of acid diffusion coefficients using this method, The dependence of acid diffusivity in a polymer film on PEB temperature below glass transition temperature (Tg) can be well described by an Arrhenius relationship as shown in equation (5.24).

$$D(T) = D_0 e^{\left(-E_a/RT\right)} \tag{5.24}$$

Here E_a is the activation energy of acid diffusion in the resist film and D_0 is the pre-exponential factor. Acid diffusion coefficients in both pTBOCST and pHOST matrices show good linear fits in the Arrhenius plot. The obtained activation energies for PFBS acid diffusing in pTBOCST and pHOST matrices are 44.42 kcal/mol and 22.13 kcal/mol, respectively. The pre-exponential factors for PFBS acid diffusion in pTBOCST and

pHOST matrices are 1.52×10^{27} nm^2/sec and 2.60×10^{12} nm^2/sec respectively. The difference in diffusion coefficients and Arrhenius parameters between mesoscale stochastic modeling method and surface exposure method are probably due to the difference in resist film preparation process. In this work the resist film is post-applied-bake at 90 ^oC which is 40 ^oC lower than the baking temperature applied in surface exposure method (130 ^oC). A 90 ^oC baking temperature may leave more residual solvent in the resist film that may serve as channel for enhancing acid diffusion, and result in higher extracted acid diffusion coefficients than films baked at 130 ^oC. On the other hand, a thinner film (0.2 μm) has been reported showing a faster deprotection rate and thus higher acid diffusivities than a thicker film (1.2 μm) in a pTBOCST resist film through the real cause has not been investigated.[6] In this work a 500 nm film thickness is used, and therefore the extracted acid diffusivities with higher values can also be expected.

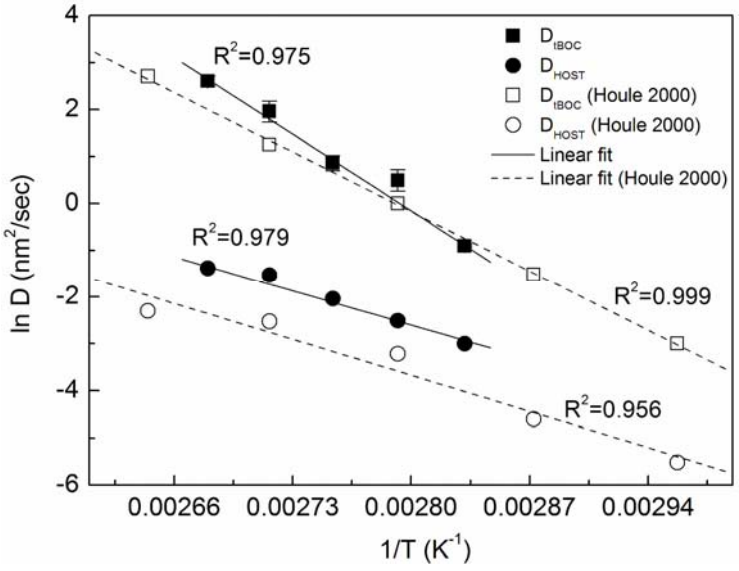

Figure 5. 9 Arrhenius plots of PFBS acid diffusion coefficients in pTBOCST and pHOST matrices extracted from mesoscale stochastic modeling method and the surface exposure method reported by Houle et. al.[6]

Beside the capability of extracting acid diffusion coefficients in different polymer matrices and the modeling of resist deprotection effect on acid diffusivity, the mesoscale stochastic model can also trace microscopic acid migration behavior during PEB. The model traces the position and the number of deprotection of each acid molecule that allows the study of PEB temperature and time effects on average acid catalytic chain length and average acid displacement from its initial position. PFBS acid catalytic chain length in a pTBOCST matrix with different PEB temperature and time is shown in figure 5.10. A saturation of chain length growth is observed at every PEB temperature, indicating that the overlapping of deprotection volume created by each acid molecule while resist deprotection extent increase. The calculated several tens to hundreds catalytic chain lengths also indicate the overestimated acid-catalytic deprotection capability (more than several hundreds catalytic chain length) predicted using other over-simplified models and methods.

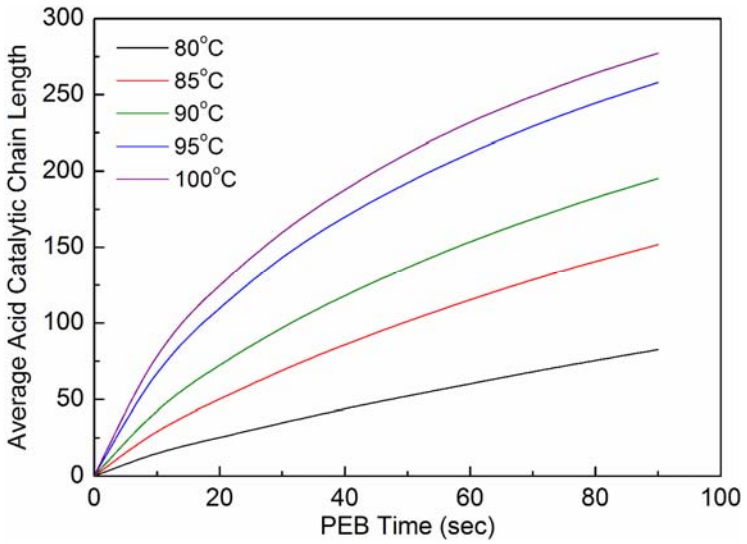

Figure 5. 10 Average PFBS acid catalytic chain length in a pTBOCST film.

Acid reaction-diffusion effect on average acid displacement of PFBS acid in a pTBOCST matrix is also shown in figure 5.11. Significant jump followed by a rapid slow

down of acid displacement increase is observed in every PEB temperature and the saturation of acid displacement while increasing PEB temperature is also detected. This behavior is mainly due to the trapping of acid molecules in pHOST matrix which possesses higher electron affinity and polarity than pTBOCST matrix. Such observations also indicate that the correlation between acid diffusion induced image blur and PEB time is relatively insignificant. Resist CD bias caused by acid diffusion may be determined at the early stage of the PEB process.

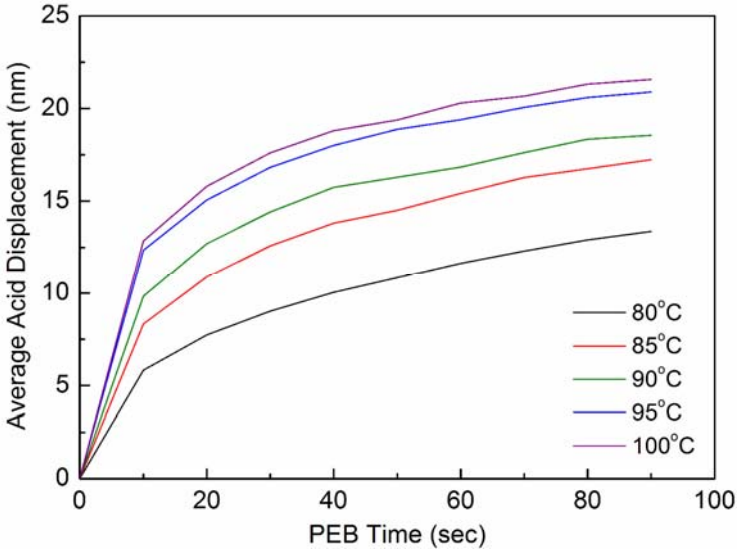

Figure 5. 11 Average PFBS acid displacement from the initial position in a pTBOCST film.

5.3.2 Effects of Acid Properties on Acid Diffusivity

Effects of chemical and physical properties of photo-generated acid on its diffusion behavior in a resist matrix are studied using the mesoscale stochastic modeling method in this section. PAGs which generate TFMS, PFBS, SbF_6 acids are used and compared to investigate effects of their properties on their diffusion behavior in a pTBOCST matrix during PEB process. Possible effects are investigated by looking at the

extracted diffusion coefficients and their dependence on matrix properties and PEB temperature. The experimental deprotection extent and the best fit of pTBOCST/acid matrices under 90°C PEB were shown in figure 5.12. The observed deprotection rate is a function of acid anion size (i.e. the deprotection rate decrease as the acid anion size increase). The extracted acid diffusion coefficients in pTBOCST and pHOST matrices are also listed in table 5.3. When switching from an acid with smaller anion (i.e. TFMS acid) to an acid with larger anion (i.e. PFBS or SbF_6 acids), it is clear that the decrease of deprotection rate is mainly due to the decrease of acid diffusivity in pTBOCST matrix. A decrease of acid diffusivity in pHOST matrix is also observed, however the acid size effect is not as significant as that in pTBOCST matrix.

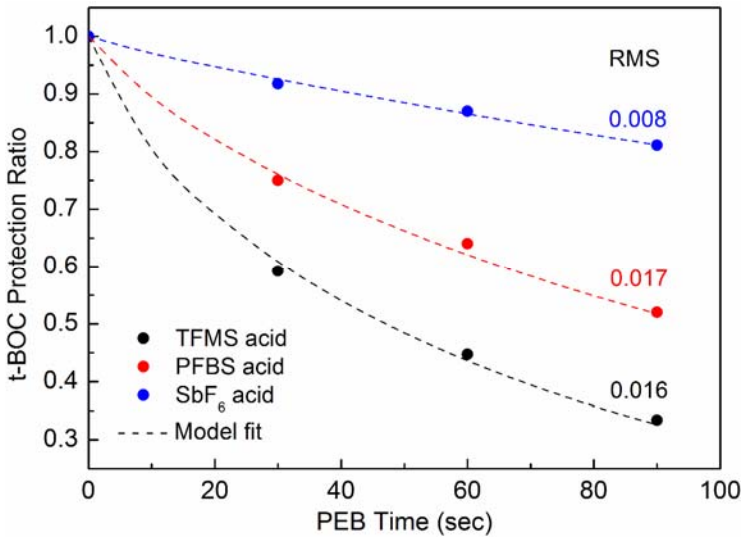

Figure 5. 12 Experimental data and the best model fit for acid-catalyzed deprotection at 90 °C PEB in pTBOCST resist films with different acids.

Table 5. 3 Extracted diffusion coefficients of acids at 90°C PEB

Acid type	D_{tBOC} (nm^2/sec)	D_{HOST} (nm^2/sec)
TFMS acid	56.41	0.35
PFBS acid	2.35	0.13
SbF_6 acid	0.16	0.10

Catalytic chain lengths of different acids are compared and shown in figure 5.13. SbF_6 acid has giant anion due to the giant antimony core if compared with those sulfonate anions of TFMS and PFBS acids. This giant acid anion significantly reduces the diffusivity of SbF_6 acid, and decreases its catalytic chain length down to less than a hundred at 90 ^oC PEB. The average acid displacement is calculated being less than 15 nm, as shown in figure 5.14. Such results explain why using TPS.SbF_6 PAG as the acid generator in pTBOCST resist system can significantly improve the control of image blur than other PAGs in this study.

The dependences of diffusion behavior of different acids on PEB temperature in pTBOCST and pHOST matrices are also investigated by looking at the Arrhenius relationships of diffusion. Arrhenius plots are generated by extracting diffusion coefficients of acids at different PEB temperatures, as shown in figure 5.15. The corresponding activation energies and pre-exponential factors are also determined and listed in table 5.4. For acid diffusion in a pTBOCST matrix, the activation energy increase as the acid anion size increase. This behavior is expected since the larger the acid size, the higher the transition energy required for overcoming the energy barrier of diffusion in a solid-state film. However an opposite trend is observed when acid diffusing in a pHOST matrix. The larger the acid size, the smaller the activation energy of diffusion. Currently there is no literature reporting and addressing this opposite acid diffusion behavior in a pHOST matrix. In principle, there are two major factors, relative to acid property, controlling acid diffusivity in a solid-state film. One is the acid size effect which is already addressed in previous discussion. The other is the interaction of acid molecule with the polymer matrix. For example, acid molecule is a conjugated pair consisting of a positively-charged proton and negatively-charge anion. In most cases the proton of a strong acid can not stay along and is generally attached to the polymer matrix rather than the anion. The proton can not migrate far away from its counter anion in order to maintain the electronic property of the polymer film; hence the interaction between

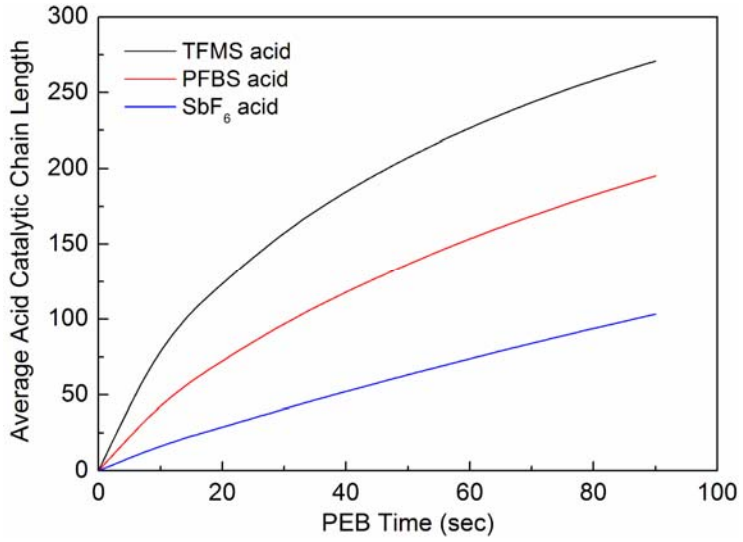

Figure 5. 13 Average catalytic chain lengths of acids in pTBOCST film at 90 ^{o}C PEB.

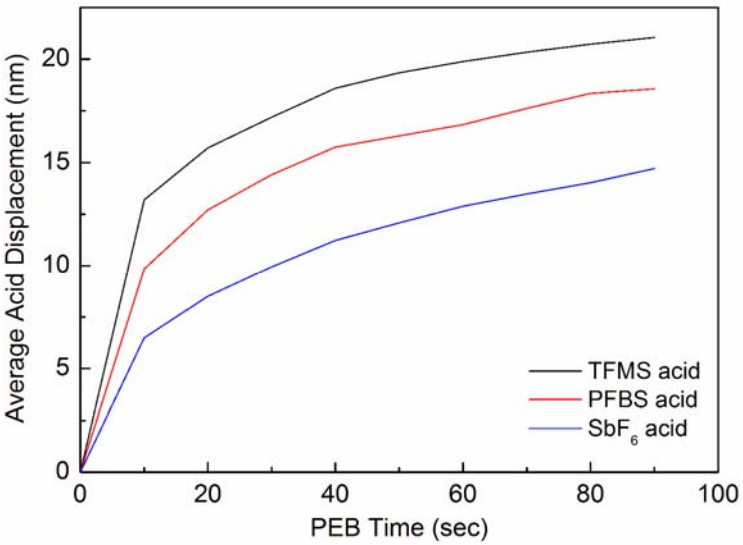

Figure 5. 14 Average displacements of acids from the initial position in pTBOCST film at 90 ^{o}C PEB.

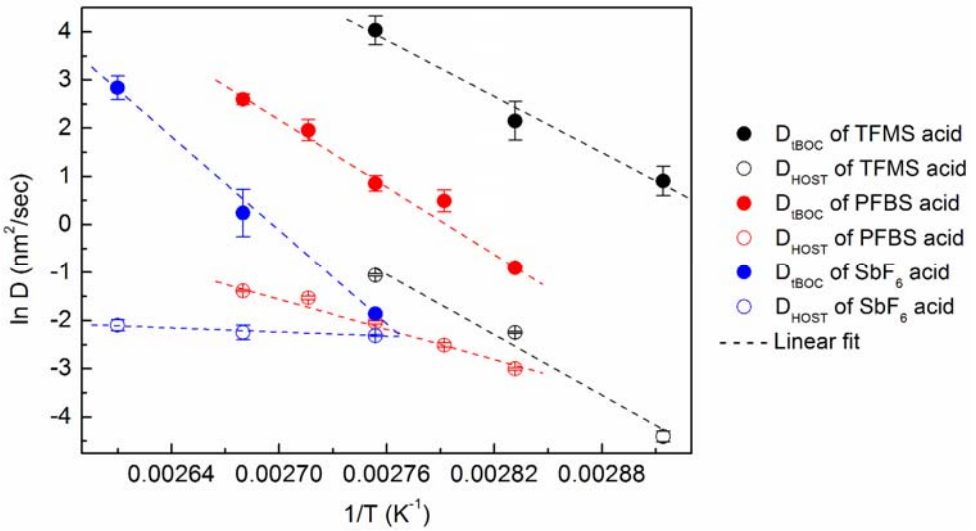

Figure 5. 15 Arrhenius plots of diffusion coefficients of acids in pTBOCST and pHOST matrices.

Table 5. 4 Arrhenius parameters of extracted acid diffusion coefficients

pTBOCST matrix		
Acid type	E_a (kcal/mol)	D_0 (nm^2/sec)
TFMS acid	38.62	8.74E+24
PFBS acid	44.42	1.52E+27
SbF_6 acid	64.92	1.67E+38
pHOST matrix		
Acid type	E_a (kcal/mol)	D_0 (nm^2/sec)
TFMS acid	41.57	4.34E+24
PFBS acid	22.13	2.60E+12
SbF_6 acid	2.97	5.93

matrix and proton or acid anion may dominate and control acid diffusion behavior. In a polar matrix such as pHOST investigated in this work, proton is expected to have higher affinity to the hydroxyl group of pHOST, and the proton transfer between hydroxyl groups (inter-chain or intra-chain) in a pHOST matrix requires a more correct orientation of the polymer chain to facilitate the transfer. The transfer of acid proton in a pHOST matrix is illustrated in figure 5.16. The antimony core of the SbF_6 acid results in a giant

anion that leads to the proton being close to the anion. Such giant anion may act as a significant hindrance of correct chain orientation for proton transfer and may limit the diffusion of SbF_6 acid in a pHOST matrix, as indicated by red arrows in figure 5.16. The acid diffusivity may become insensitive to the change of PEB temperature as shown in figure 5.15 and table 5.4. In the case of TFMS acid such anion hindrance effect is not significant since the anionic core is relatively small. PFBS acid shows the acid diffusion property between TFMS and SbF_6 acids. Acid anion hindrance effect is in principle not significant in a pTBOCST matrix since the t-BOC group is less polar and less electron rich if compared with the hydroxyl group. The proton transfer between t-BOC groups is easier and less limited by the need of a correct polymer chain orientation. Besides, t-BOC group acts as the plasticizer that allows more chain orientation flexibility and higher probability for proton transfer between groups. Acid diffusivity in a pTBOCST matrix is therefore mainly dominated by the size of acid anion as expected.

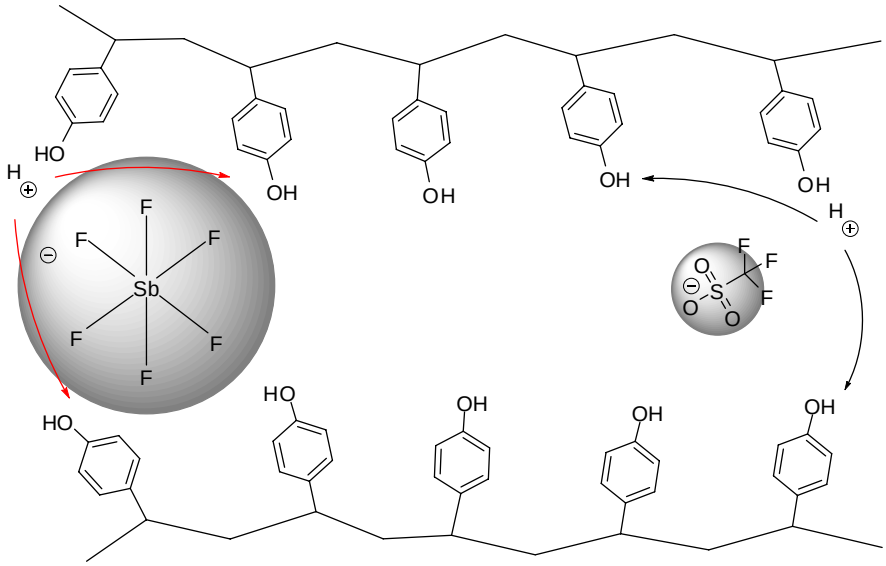

Figure 5. 16 Illustration of SbF_6 acid anion hindrance effect on proton transport between pHOST subunits.

5.4 Conclusions

In this chapter, a mesoscale stochastic experimental-modeling technique for studying acid diffusion behavior in a solid-state resist film has been developed and demonstrated. For the modeling part a mesoscale resist model has been built to represent the composition of a resist film. A stochastic acid reaction-diffusion process has been applied to simulate major resist physics and chemistry during PEB. Since the model can simulate and trace microscopic random walk behavior of acid molecules and polymer subunit deprotection reaction, this technique requires only the deprotection history of a flood-exposed resist film baked at elevated temperature to extract acid diffusion coefficient with high precision. The ease of experimental operation and initial acid distribution characterization significantly extends the applicability of this technique to resist materials designed for various lithography technologies and exposure sources. This technique is validated by comparing the extracted acid diffusion coefficients of a pTBOCST/PFBS acid system to the literature values obtained by a surface exposure method. This technique has also been applied to the study of acid property and polymer matrix effects on acid diffusivity. The results indicate that acid with larger anion has lower diffusivity in a solid-state polymer film in general. In a non-polar pTBOCST matrix, larger acid anion leads to higher activation energy of acid diffusion. However an opposite trend is observed in a pHOST matrix. The diffusivity of a SbF_6 acid is insensitive to the change of PEB temperature. This opposite trend may be due to the hindrance effect of the giant SbF_6 anion that reduces the proton transfer probability between hydroxyl groups and thus limits acid diffusivity.

5.5 References

[1] Doremus, R. H., *Diffusion of reactive molecules in solids and melts*, John Wiley & Sons **2002**, New York, USA.

[2] Benita M. Comeau. Ph.D. Dissertation **2007**, Georgia Institute of Technology.

[3] Lu, C.; Czanderna, A., In chapter 2 of *Applications of Piezoelectric Quartz Crystal Microbalances*, **1984**, Elsevier, New York, USA.

[4] Gillespie, D. T., A general method for numerically simulating the stochastic time evolution of coupled chemical reactions, *J. Comput. Phys.* **1976**, *22*, 403-434.

[5] Gillespie, D. T., Exact stochastic simulation of coupled chemical reactions, *J. Phys. Chem.* **1977**, *81*, 2340-2361.

[6] Houle, F. A.; Hinsberg, W. D.; Morrison, M.; Sanchez, M. I.; Wallraff, G.; Larson, C.; Hoffnagle, J., Determination of coupled acid catalysis-diffusion process in a positive-tone chemically amplified photoresist, *J. Vac. Sci. Technol. B* **2000**, *18*, 1874-1885.

[7] Wallraff, G.; Hutchinson, J.; Hinsberg, W.; Houle, F.; Seidel, P.; Johnson, R.; Oldham, W., Thermal and acid-catalyzed deprotection kinetics in candidate deep ultraviolet resist materials, *J. Vac. Sci. Technol. B* **1994**, *12*, 3957-3862.

CHAPTER 6

HIGH RESOLUTION LITHOGRAPHY TECHNIQUE FOR PROBING RESIST INTRINSIC PATTERNING PERFORMANCE[†]

The development of novel resist material for NGL is targeting applications for sub-50 nm technology nodes. The characterization of resist patterning performance requires lithography techniques which can faithfully represent the intrinsic patterning capability, such as CD control and LER performance, of a resist material without the interference of issues associated with the exposure optics, such as photon shot noise and poor intensity contrast of the aerial image. The major factors which are essential for a satisfactory lithography technique are the capability in generating aerial image with sub-50 nm resolution while still maintaining high aerial image contrast. In this chapter, a lithography technique for determining resist intrinsic patterning performance is developed and demonstrated. The use of a 100 kV direct-write EB of a resist film spin-coated on a free standing silicon nitride membrane is demonstrated having ultra-high resolution, aerial image quality, uniform energy deposition profile throughout the resist depth, and minimized shot noise through a Monte Carlo EB trajectory and energy deposition simulation. We also experimentally demonstrate the capability of this technique in determining resist intrinsic CD bias and LER behavior with sub-50nm

---

[†] Material presented in this chapter has appeared in part in previously published articles:

Wang, M.; Jarnagin, N. D.; Lee, C. –T.; Henderson, C. L.; Yueh, W.; Roberts, J. M.; Gonsalves, K. E., Novel polymeric anionic photoacid generators (PAGs) and corresponding polymers for 193 nm lithography, *J. Mater. Chem.* **2006**, *16*, 3701-3707.

Lee, C. –T.; Wang, M.; Jarnagin, N. D.; Gonsalves, K. E.; Roberts, J. M.; Yueh, W.; Henderson, C. L., Photosensitivity and line edge roughness of novel polymer-bound PAG photoresists, *Proc SPIE* **2007**, *6519*, 65191E.

Lawson, R. A.; Lee, C. –T.; Yueh, W.; Tolbert, L; Henderson, C. L., Expoxide functionalized molecular resists for high resolution electron beam lithography, *Microelectronic Eng.* **2008**, *85*, 959-962.

feature size resolution. Superiorities in probing resist intrinsic patterning performance using this technique is illustrated by comparing the patterning results of resist materials using this technique to those produced by other modern lithography techniques, such as dry 193 nm and EUV lithography techniques.

6.1 Introduction

In order to faithfully represent the intrinsic patterning performance, or the structure-property relationships of a resist material, a lithography technique which can minimize the effects associated with exposure equipment and demonstrate resist patterning behavior directly correlated to the material properties are essential for novel resist material design and development. As the principles of microlithography mentioned in chapter 1, the aerial image pattern deposited into the resist film is defined by the illumination light source which passes through a condenser lens, a photomask, an objective lens, and is then projected onto the resist film surface. Since light is an electromegnatic radiation which possesses the wave nature, the light is first diffracted to different orders when passing through the photomask, and is then re-collected by the objective lens. The quality of the aerial image (i.e. how faithful the aerial image can represent the digital image designed on the photomask) is determined by the number of diffraction orders which can be collected by the objective lens (i.e. the higher the diffraction order can be captured by the lens, the better the aerial image quality). It is this diffraction effect that limits the intrinsic resolution, as well as the aerial image quality, of optical exposure tools. As the feature size on the photomask shrinks, the edge acuity of the light intensity distribution (i.e. the aerial image contrast) decrease.[1] Aerial image feature will finally be below the contrast of the resist material and eventually no longer resolved if even smaller feature is considered.

The quality of an aerial image delivered by an exposure tool is generally evaluated by the maximum contrast of the achievable intensity profile and is defined as the image log slope (ILS) as equation (6.1).

$$\mathrm{ILS} = \frac{1}{I(x)} \frac{dI(x)}{dx} \tag{6.1}$$

Here $I(x)$ is the aerial image intensity at a lateral position x. ILS is a function of the image width and is not a global evaluation of aerial image quality with different resolution. ILS is usually multiplied by the width of the image one desired to print in the resist film and becomes a normalized image log slope (NILS) which is dimensionless and is shown in equation (6.2).

$$\mathrm{NILS} = w \frac{1}{I(x)} \frac{dI(x)}{dx} \tag{6.2}$$

Here w is the width of the image. As the dramatic down-scaling of the IC feature for improving the efficiency and speed of the final electronic devices, it is obvious that the exposure tool needs to deliver aerial image with higher ILS in order to maintain the same NILS. The capability of a lithographic technique which can print sub-50 nm feature sizes with high NILS is essential for evaluating the lithography performance of novel resist materials. Otherwise the poor aerial image contrast can significantly affect the patterning quality of the resist material, and resist material property effects on patterning performance can not be clearly expressed. Obviously the currently available dry 193 nm exposure tools for academic research purpose are not able to pattern dense feature below 50 nm resolution.[2] The modern EUV exposure equipments accessible to public also possess only moderate (< 8.0) to low NILS when patterning sub-50 nm dense features.[3]

The shot noise in these equipments is expect being 5~10% of the nominal dose delivered in the exposed area. Another approach for patterning sub-50 nm feature with high aerial image quality is using high acceleration voltage direct writing EB and scanning to generate the designed pattern.. In principle the minimum achievable feature size of direct-write EBL is close to a single electron beam diameter generated by the EB column. A 100 kV EBL system has been demonstrated having the capability of making sub-10 nm isolated line pattern on a hydrogen silsesquioxane (HSQ, flowable oxide) negative-tone resist.[4] However such direct EB writing system usually use thick and dense materials, such as silicon or quartz wafers, as the underlying substrate which can strongly back-scatter the incident electrons to the resist film and result in a so called *proximity effect* in typical EBL system. Such proximity effect usually significantly degrades the achievable NILS and resolution of a resist material since the amount of back-scattered electrons can be more than 10% of the incident electron, and the back-scattering distance of the incident electrons at the resist plane can be several tens microns away from the original beam position. Moreover, the proximity effect also creates non-uniform energy deposition profile along the resist film depth since the back-scattered electron usually possess lower energy and selectively deposited its energy near the resist/substrate interface. The more energy deposited in the bottom of the resist layer results in an undercut and a tilted sidewall of the developed resist pattern profile. This undercut profile will degrade the resolution of the resist material due to the weaker mechanical strength of the resist pattern at the undercut position. This non-uniform resist pattern profile may also complicate the evaluation of resist patterning performance, such as the resolution, CD bias, and LER through a general top-down SEM image. The development of a lithography technique which can provide sub-50 nm dense feature resolution with minimized exposure tool effect on resist patterning performance is essential to determine the intrinsic patterning performance of a resist material, as well as the investigation of the

fundamental structure-function relationships which are vital to the improvement of desired resist patterning properties.

6.2 Experimental Procedure

6.2.1 Design and Fabrication of Ultra-Thin Silicon Nitride Membrane

In this chapter a patterning technique which utilizes high energy direct-writing EBL and ultra-thin silicon nitride membrane substrate to eliminate electron back-scattering effect is developed and characterized. The first step of this technique is the design and fabrication of an ultra-thin silicon nitride membrane as the substrate for EBL. A prime grade double-side-polished (DSP), [100] oriented silicon wafer (100 mm in diameter; 0.4 mm in thickness) is cleaned by first immersing the wafer into a Piranha solution containing 98% sulfonic acid (H_2SO_4, Mallinckrodt Baker, Inc) and 30% hydrogen peroxide (H_2O_2, Mallinckrodt Baker, Inc) (3:1 volume ratio) at 120 ^oC for 10 min in order to remove possible organic deposites on the wafer surface. The wafer is then rinsed with de-ionized water and immersed into a buffered oxide solution containing H_2O: hydrufluoric acid (HF, Mallinckrodt Baker, Inc) (20:1 volume ratio) at room temperature for 10 seconds to strip the native silicon oxide layer away from the wafer surface. The cleaned wafer is then deposited with a 50 nm amorphous silicon nitride layer on both sides through a low-pressure chemical vapor deposition (LPCVD) process in a furnace reactor (TYTAN Furnace, Tystar Corp.) at 850 ^oC for 10 minutes using dichlorosilane (DCS, 17 sccm) and ammonia (NH_3, 100 sccm) as the precursors. The design of the precursor flow rates is to deposit silicon-rich, low tensile stress silicon nitride layer. The index of refraction, film thickness, and uniformity of the deposited silicon nitride layer are measured and determined using a variable angle spectroscopic ellipsometer (V-VASE, J. A. Woollam Inc.) by fitting the ellipsometry data with a Cauchy model in the non-

absorbing wavelength (500~1000 nm). The index of refraction is measured as 2.22 at a wavelength of 600 nm as shown in figure 6.1, and the film is expected to possess low tensile stress (< 150 MPa). The variations of film thickness and refractive index across a 100 mm wafer are 0.07 nm and 0.0004 respectively (95% confidence), showing the high uniformity of the deposited silicon nitride layer.

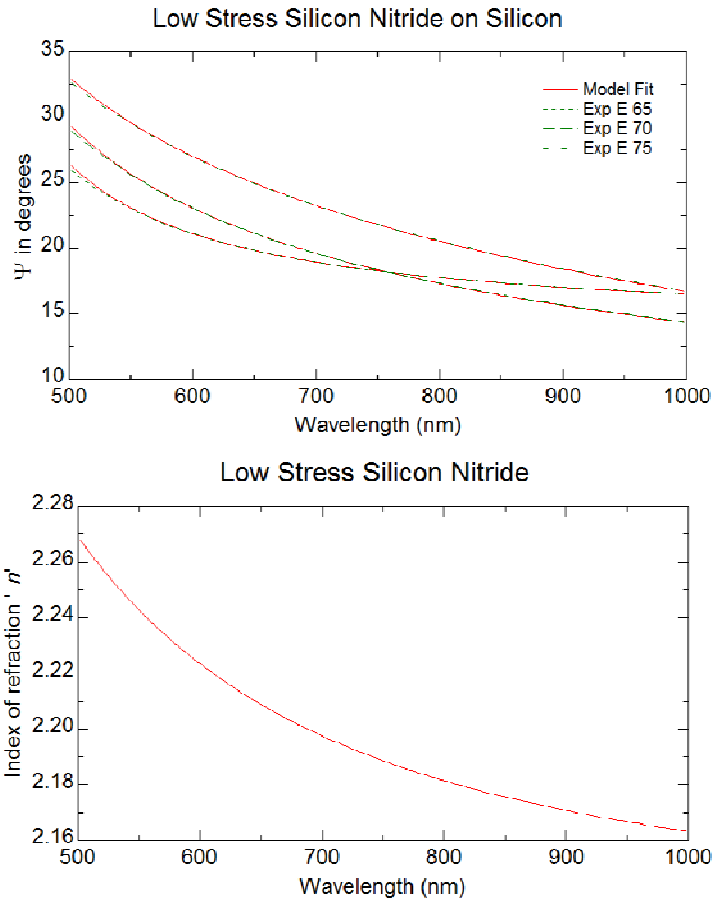

Figure 6. 1 Model fitting of the ellipsometry spectra and the extracted refractive indexes of an ultra-thin low tensile stress silicon nitride layer (50 nm) on a silicon wafer.

The open windows designed for silicon through-etch on one side of the silicon nitride deposited DSP wafer are patterned using a novolac/DNQ based photoresist (Microposit S1813, Shipley Co., Inc.) and an exposure system equipped with an optical

mask aligner (365~405 nm wavelength exposure, Optical Associates, Inc.). The patterned wafer is dry-etched using an inductively coupled plasma etcher (ICP, Plasma-Therm Inc.) and tetrafluoromethane (CF_4) as the etchant. The exposed silicon in the open windows is anisotropically wet-etched through by soaking the wafer into an aqueous solution containing 35 wt% potassium hydroxide (KOH, Fisher Chemical, Inc.) and 14 wt% isopropyl alcohol (IPA, EMD Pharmaceuticals, Inc.) at 95^{o}C for 4 hours. The wafer is then cleaned again by a Piranha solution and the windows containing free-standing silicon nitride membrane (squares with 130 +/- 25 nm edge length, depending on the wafer thickness) are obtained on the other side of the DSP wafer. The overall fabrication process of an ultra-thin silicon nitride membrane wafer is illustrated in steps 1~5 in figure 6.2.

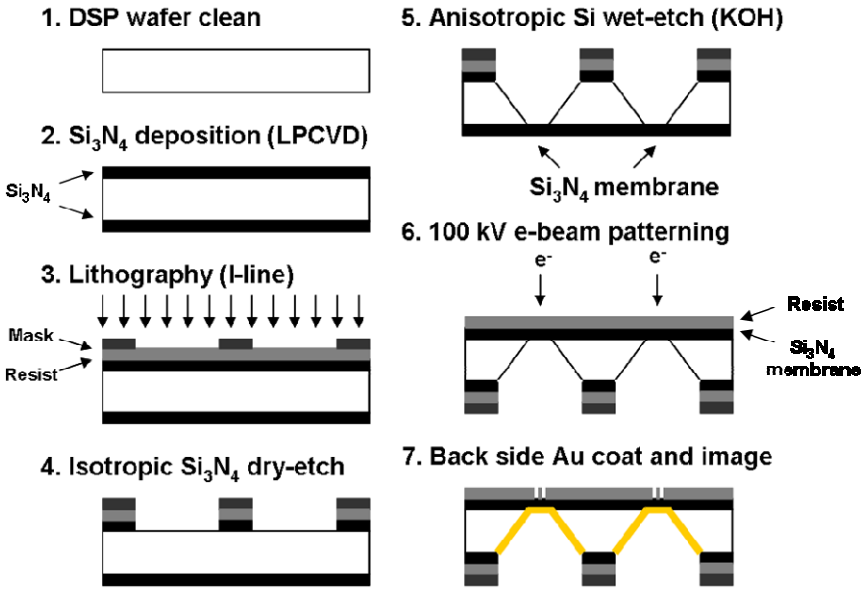

Figure 6. 2 Schemes of silicon nitride membrane fabrication, resist patterning, and preparation for SEM imaging.

6.2.2 Resist Film Patterning and Imaging

The silicon nitride membrane wafer is first primed with a 1,1,3,3,3-hexamethyl-disilazane solution (HMDS, ICN Biomedicals, Inc.). A 100 nm resist film is prepared by spin-coating the resist solution onto the primed wafer and baked at 100 ^{o}C for 2 minutes. Resist film thickness is measured using the ellipsometry method mentioned in section 6.2.1. Resist film in the silicon nitride membrane window is patterned using a 100 kV direct-write EBL system (JBX-9300FS EBL, JEOL Ltd.).[4] The beam current is set at 2 nA and the beam diameter is determined as 8 nm. The patterned resist film is post-exposure baked and developed according to the processing parameters of the resist material used. A 20 nm gold layer is sputtered onto the back side of the silicon nitride membrane using a gold sputtering system (Hummer Sputter System, Anatech) and used as the charge dissipation layer for SEM imaging. The resist pattern is then imaged under a thermally-assisted field emission SEM (JEOL-1530 SEM, JEOL Ltd.) with 2~5 kV operation voltages. The cross-section illustration of the ultra-high aerial image quality patterning setup and the charge accumulation behavior before and after back-side Au coating is shown in figure 6.3. The front-side and back-side views of the silicon nitride membrane window are also shown in figure 6.4.

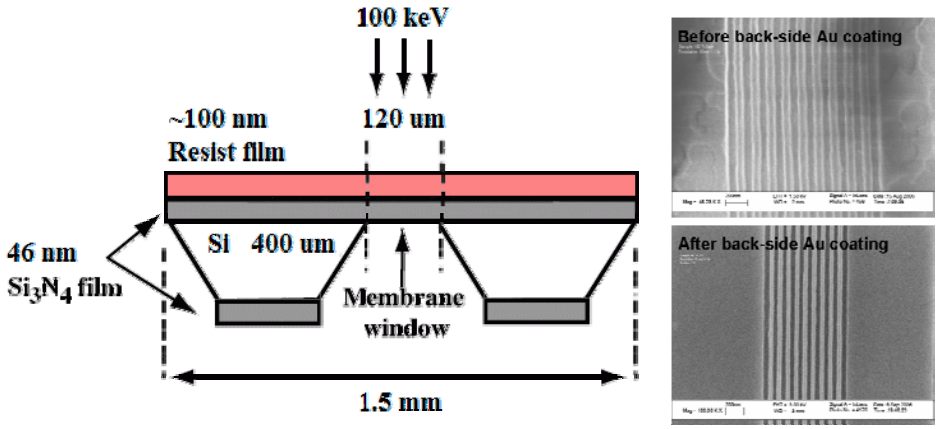

Figure 6. 3 Illustration of the high aerial image quality patterning setup and the charge accumulation behavior before and after backside gold coating.

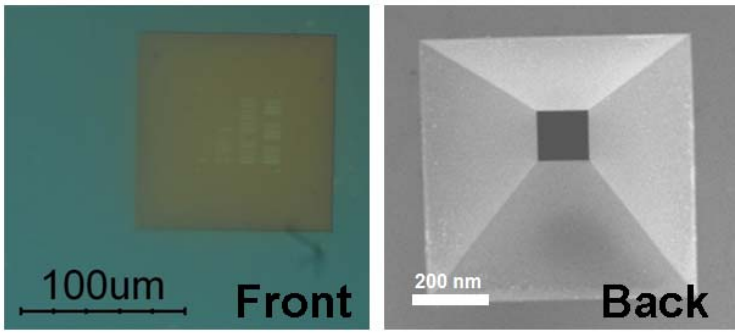

Figure 6. 4 The front-side (with patterned resist film) and the back-side views of the silicon nitride membrane window.

6.2.3 Resist Pattern Analysis

Acquired SEM images of resist line pattern are off-line processed and analyzed by an in-house developed program to determine resist CD and LER. The pixel size information of a SEM image is read into the program and the background intensity is calculated by averaging the pixel intensity of the bulk region (the resist film region for a positive-tone resist and the substrate region for a negative-tone resist) and subtracted from the pixel intensity of the raw SEM image. The background-adjusted data is then normalized to the maximum intensity, usually located at the resist line edge, of the SEM image. A pixel intensity scan normal to the resist line edge is performed and the edge position of the resist line is determined using a threshold intensity value 0.3~0.5. The line edge profile is then applied to an adaptive Gaussian-noise filtering step with a specific filtering width (3~5 pixels) if necessary (i.e. the original SEM image has low image contrast or noisy). A standard procedure for determining resist line edge position via the in-house developed program is shown in figure 6.5. Resist CD, 3σLER, and 3σLWR are calculated and averaged from 5 resist lines using equation (6.3)~(6.5), 10 nm

measurement pitch between collected edge positions, and a 1.0 μm inspection length for each resist line.

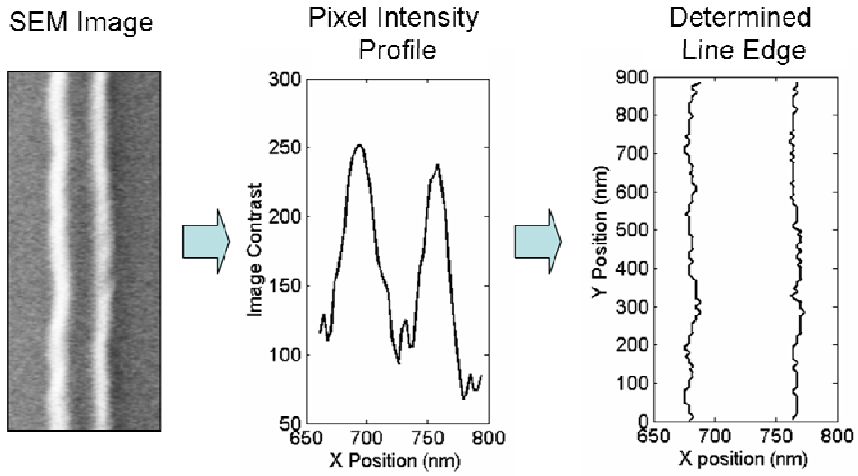

Figure 6. 5 Illustration of scheme for determining resist line edge position using the in-house program developed in this work.

$$CD = \left| x_{1,Avg} - x_{2,Avg} \right| \tag{6.3}$$

$$3\sigma LER = 3\sqrt{\frac{\sum_{i=1}^{N}\left(x_1(y_i) - x_{1,Avg}\right)^2}{N-1}} \tag{6.4}$$

$$3\sigma LWR = 3\sqrt{\frac{\sum_{i=1}^{N}\left(\left|x_1(y_i) - x_2(y_i)\right| - CD\right)^2}{N-2}} \tag{6.5}$$

Here $x_1(y_i)$ and $x_2(y_i)$ are the x positions of the right and left edges of a resist line at a y position y_i. $x_{1,Avg}$ and $x_{2,Avg}$ are the average edge positions of the right and left edges of a resist line. N is the total number of edge positions selected for calculation. In addition to average LER/LWR values calculated from equation (6.3)~(6.5), the developed program can also perform spatial frequency analysis of the edge roughness and determine the origin and contribution of resist LER. Fourier transform of the edge roughness data

$(x_1(y_1)-x_{1,Avg},\ x_1(y_2)-x_{1,Avg},\ x_1(y_3)-x_{1,Avg},\ \ldots\ ,\ x_1(y_N)-x_{1,Avg})$ yields the spatial frequency dependency of the LER, and the square of the Fourier amplitude, as a function of the spatial frequency K, is termed as the *power spectrum* $P(K)$. Power spectrum is generally used to investigate the correlation between the edge position and roughness, and determine the spatial-frequency dependent contribution and origin of the observed LER. A typical interpretation of the power spectrum is shown in figure 6.6. The area under the spectrum is proportional to the square of the LER value, and a higher $P(K)$ value indicates a higher contribution to total LER at the spatial frequency K. In general, low-spatial frequency (large length scale, several tens to hundreds nanometers) roughness of resist pattern is mainly due to acid diffusion and resist processing effects. High-spatial frequency (small length scale, several to tens nanometers) roughness is mainly due to shot noise (in non-chemically amplified resists) and material size effects.

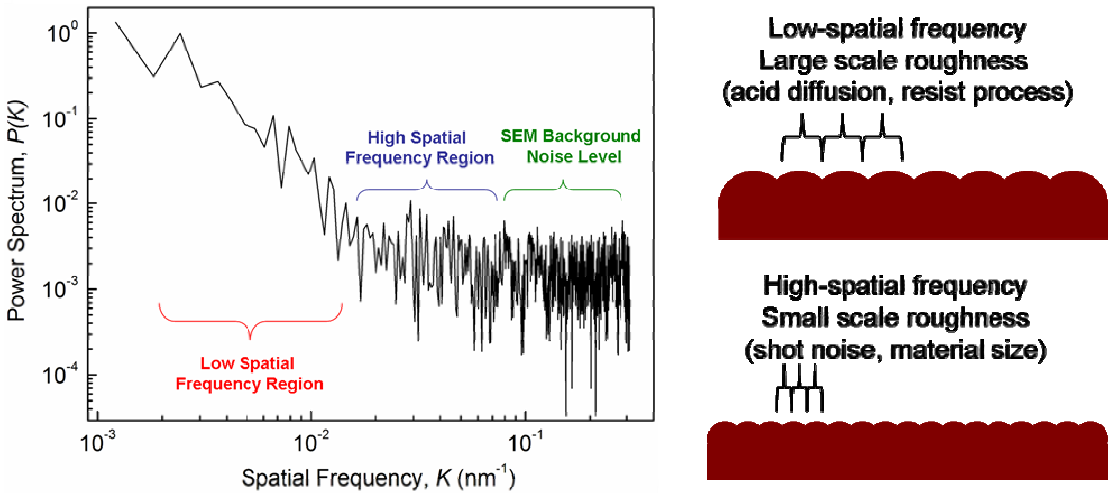

Figure 6. 6 Spatial frequency analysis of resist line edge roughness and a typical interpretation of the power spectrum.

6.3 Results and Discussion

6.3.1 Energy Deposition in the Resist Film

The column (electron optics) of a JEOL-9300FS EBL system is illustrated in figure 6.7.[4] The electron beam is generated by a ZrO/W emitter and focused on the workpiece surface through four electronic lenses. An objective aperture is placed right above the objective lens to control electrons getting into the objective lens. The single-beam size is determined by both the objective aperture and the beam current (i.e. the electron flux) used in the system. A larger aperture size or a higher beam current gives a larger electron flux into the objective lens, and a larger electron flux increases the repulsion effect between incident electrons and results in a larger beam diameter. For the high resolution patterning method used in this and the follow-up chapters, the diameter of the objective aperture is set to 60 μm and the beam current is set to 2 nA. The dependence of aperture size and beam current on the beam diameter is illustrated in figure 6.8. The beam diameter used in this work is 6~8 nm according to the curve in figure 6.8.

Effects of electron acceleration voltage and substrate backscattering on electron trajectories and energy deposition in the resist film are investigated by using a Monte Carlo simulator (Casino v2.42), and the theoretical detail of the simulator can be found in a published user manual.[5] Basically the simulator implements a partial elastic cross-section of atoms to calculate the scattering angle and the trajectory of incident electrons in polymer films and substrates.[6] The energy loss of an incident electron (i.e. energy deposited in the polymer film or the substrate) between collisions with atoms is determined by a continuous energy loss function, and the collision and energy loss repeat until the electron energy is less than 50 eV or the electron escape the polymer film surface or the underlying substrate.[7]

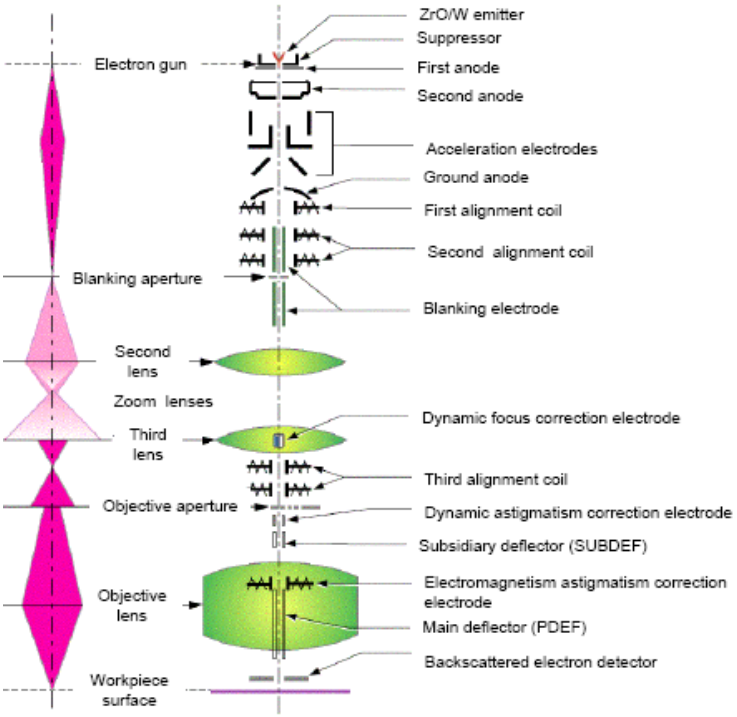

Figure 6. 7 Illustration of the column of a 100 kV JEOL-9300FS EBL system.[4]

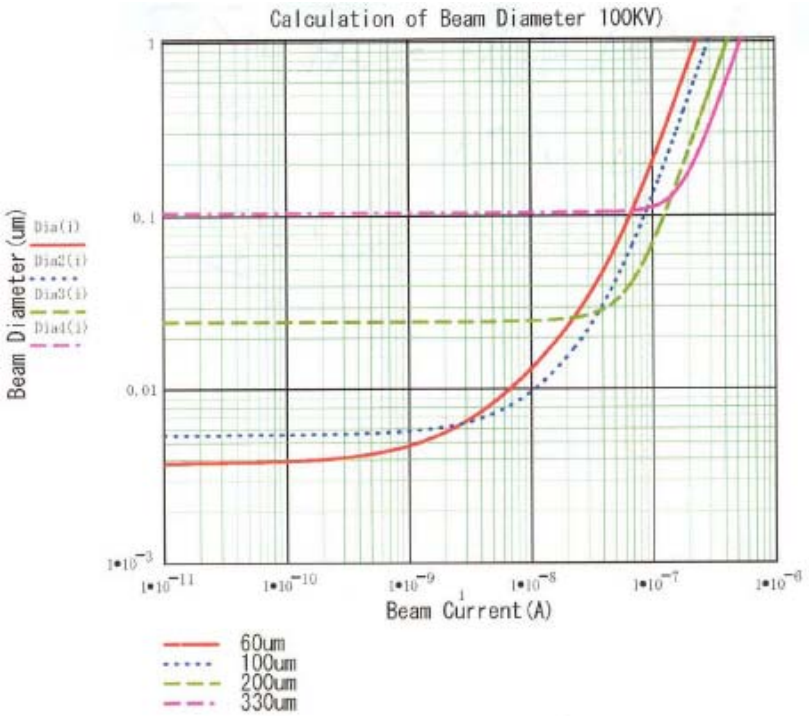

Figure 6. 8 The dependence of electron beam diameter on the objective aperture diameter and electron beam current of a JEOL-9300FS EBL system.[4]

A two-layer model representing a 100 nm poly(4-hydroxystyrene) (pHOST) layer (density=1.0 g/cm^3) above a 50 nm silicon nitride membrane (density=1.73 g/cm^3) is built to represent the high resolution patterning setup developed in this chapter and is used for energy deposition analysis. The trajectories of 2,000 electrons in this two-layer model with a 8.0 beam diameter and different electron acceleration voltages are simulated and represented in figure 6.9. The spreading of the electron trajectories of the primary incident electron beam while penetrating the polymer and the membrane is termed as the *forward scattering*. Electron forward scattering is mainly due to electron-electron and electron-atom interactions that deflect the primary electrons by a typically small angle and statistically broaden the beam diameter in the resist and further in the higher density substrate. Such effect can result in a significant broadening of the original beam profile at the bottom of the polymer layer. The increase in effective beam diameter d_f in nanometers due to forward scattering can be calculated by an empirical model, as shown in equation (6.6).[8]

$$d_f = 0.9\left(\frac{R_t}{V_b}\right)^{1.5} \tag{6.6}$$

Here R_t is the polymer film thickness in nanometers and V_b is the electron acceleration voltage in kilovolts. This effect can be reduced by using thinner polymer film or higher energy electrons (i.e. high acceleration voltage) to reduce the probability of interactions and the deflecting angle. As the resist patterning method developed in this work, the effective beam diameter increase at the bottom of the polymer layer is calculated being less than 1.0 nm which in principle can provide high pattern uniformity across the whole resist film depth.

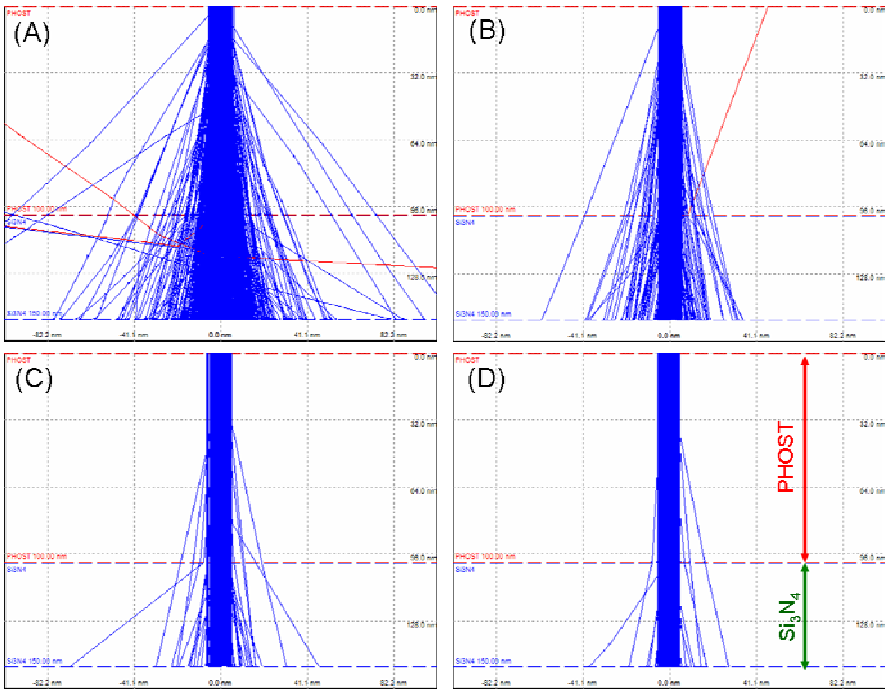

Figure 6. 9 Simulated electron trajectories and the broadening of a 8 nm electron beam in a two-layer model consisting of a 100 nm pHOST film on a 50 nm Si_3N_4 membrane at (A) 20 kV, (B) 40 kV, (C) 70 kV, and (D) 100 kV acceleration voltages.

The major purpose of using free-standing silicon nitride membrane is to eliminate electron *back scattering* from the underlying substrate. Electron backscattering is defined as the escape of an incident electron, which exhibits larger deflection angle while colliding with atoms in the polymer film or the substrate, from the polymer surface. This phenomenon usually happens in the substrate layer since it possesses higher density and is several-order thicker than the polymer film. A backscattering coefficient μ_b is defined as the ratio of the number of incident electrons deflected and escaped from the polymer surface ($n_{e,escape}$) to the total number of incident electrons ($n_{e,incident}$), as shown in equation (6.7).

$$\mu_b = \frac{n_{e,escape}}{n_{e,incident}} \tag{6.7}$$

The backscattering coefficients of a 100 nm pHOST film on a 50 nm silicon nitride membrane or a thick silicon substrate under different electron acceleration voltages are calculated and shown in figure 6.10. More than 10% of the incident electrons are backscattered while using thick silicon substrate. The backscattering coefficient increases while the acceleration voltage decrease, indicating that electrons with lower incident energy exhibit higher probability being deflected in the silicon substrate with large angle. In the case where the acceleration voltage is below 30 kV, the backscattering coefficient decrease while decreasing acceleration voltage further. This observation is due to insufficient electron energy that the electron has lost most of the energy before escaping from the polymer surface. Such more than 10% backscattered electrons will result in a wide range electron trajectory profile (> 40 μm radius from the incident beam position) in the polymer film, and also create non-uniform energy deposition profile across the polymer film depth. The ratio of backscattered electrons is significantly reduced to be less than 0.2% while replacing the thick silicon substrate by a 50 nm free standing silicon nitride membrane. The backscattered electron is even less than 0.05% while using a 100 kV acceleration voltage. This achievement is significantly important for high aerial image quality EBL since every beam spot can in principle deposit uniform energy profile across the polymer film without interfering with other beam spots, except the adjacent ones, through the backscattering effect. The aerial image contrast (i.e. ILS) is then independent to the feature size designed for patterning.

The energy deposition profile in a 100 nm pHOST layer with a 50 nm silicon nitride membrane as the substrate created by a single electron beam (50,000 incident electrons, with 8 nm in diameter) is simulated and the result is shown in figure 6.11. A single Gaussian profile is obtained as expected since the energy deposited by backscattered electrons is eliminated. The intensity deposition profiles along the beam cross-section (y=0 nm) at different depths (z=10, 50, and 90 nm) of the pHOST film are also illustrated in figure 6.12. The intensity deposition profile showed no dependence on

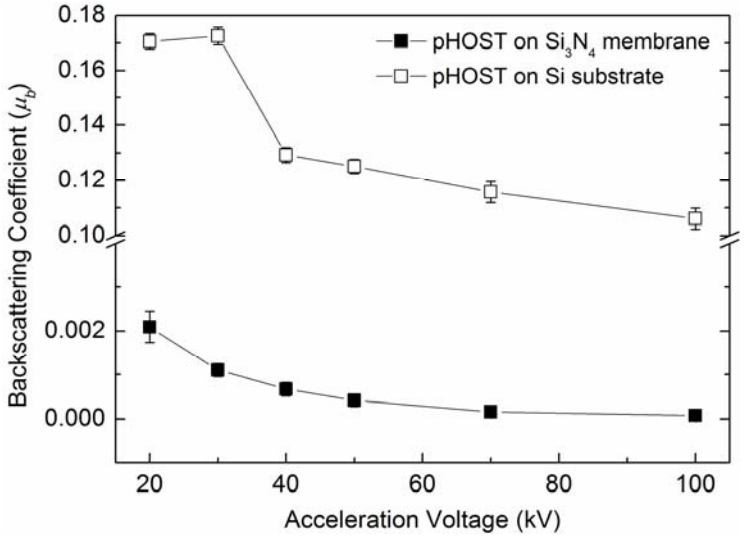

Figure 6. 10 Dependence of electron backscattering coefficient of two-layer models with different substrates on electron acceleration voltage.

film depth, demonstrating that the patterning method used in this work can provide uniform energy deposition through the whole film depth and in principle can give uniform resist profile control (i.e. constant resist line CD and straight side wall) through the whole resist film depth. Such pattern uniformity can facilitate the use of a simple top-down SEM image analysis to evaluate resist intrinsic resolution, LER, and pattern collapse behavior of the resist material. The ILS of a single beam intensity profile is calculated being 0.6 nm^{-1}. As shown in previous discussion, there is no long range interference between beam spots when backscattering effect is eliminated. If using the scanning of this beam to write a line pattern with 50 nm line width, the corresponding NILS is calculated being 30 which is not achievable by any modern 193 nm and EUV lithography equipments currently available in the world. This high aerial image quality lithography can also eliminate possible effects introduced by the lithography tool on resist patterning performance and can more faithfully represent the correlation between resist material design and its performance.

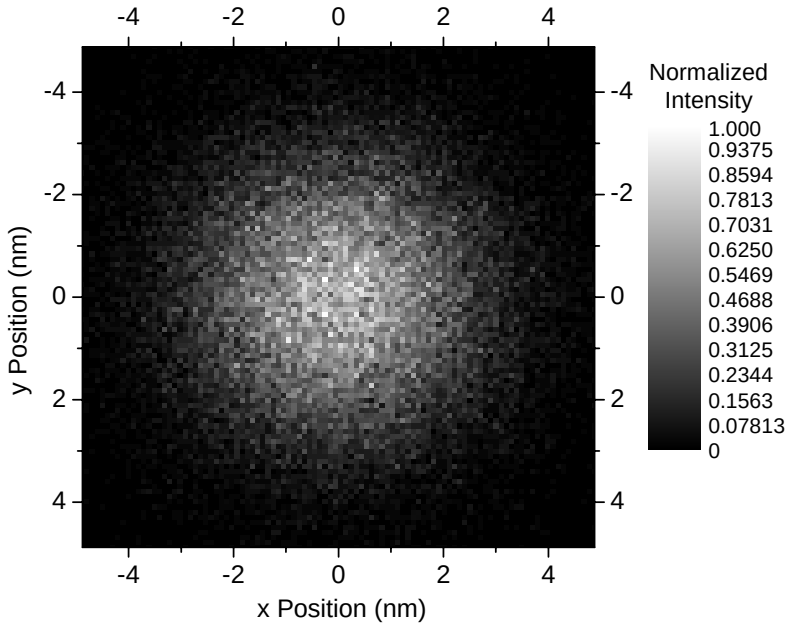

Figure 6. 11 Energy deposition contour in a 100 nm pHOST film on a 50 nm silicon nitride membrane created by a 8 nm electron beam.

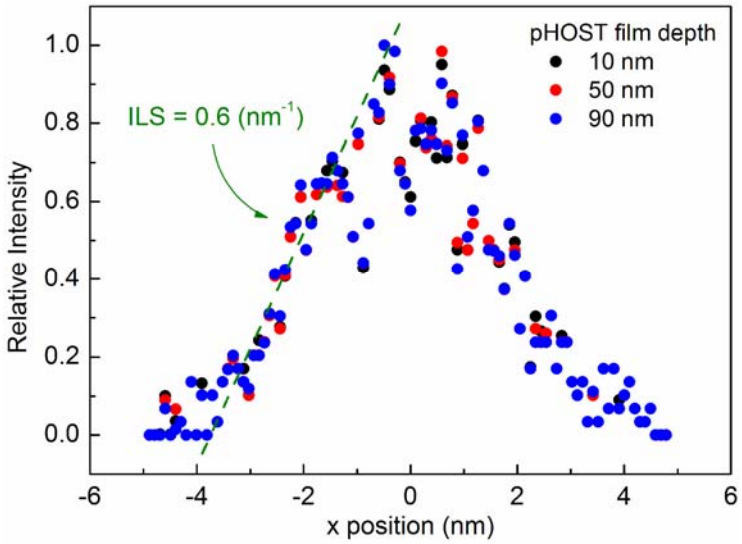

Figure 6. 12 Single electron beam energy deposition profiles at different film depths of a 100 nm pHOST film on a 50 nm silicon nitride membrane.

6.3.2 Lithographic Performance

The performance of the lithography technique developed in this chapter is experimentally evaluated and compared with other lithography facilities by using the same resist materials and processing conditions. For the comparison with 193 nm lithography, a polymer-bound-PAG resist, as well as a blended-PAG analog, are used as the testing materials.[9] The polymer-bound-PAG terpolymer (GB-EA-TPS.F4.MBS) is prepared by free-radical polymerization of 2-ethyl-2-adamantyl-methacrylate (EA), γ-butyrolactone methacrylate (GB), and triphenylsulfonium salt 4-(methacryloxy) 2.3.5.6-tetrafluorobenzenesulfonate (TPS.F4.MBS). The blended-PAG resist is prepared by blending triphenylsulfonium salt 4-(isobutyloxy) 2.3.5.6- tetrafluorobenzenesulfonate (TPS.F4.IBBS) with GB-EA copolymers with similar GB-to-EA molar ratios used in the polymer-bound-PAG resist. The structures of the resist material are illustrated in figure 6.13, and the compositions are listed in table 6.1.

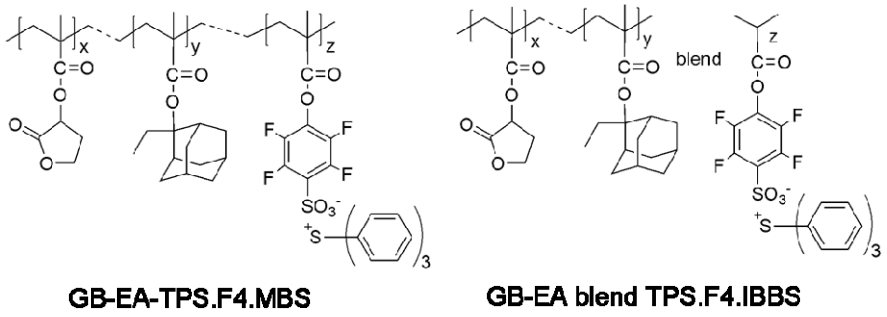

Figure 6. 13 Structures of GB-EA-TPS.F4.MBS and GB-EA blend TPS.F4.IBBS resists.

Table 6. 1 Composition of GB-EA-TPS.F4.MBS and GB-EA blend TPS.F4.IBBS resists.

Resist Material	Composition (mol%)			Mw [a] (PID)	Stability (°C)	Tg (°C)
	GB	EA	PAG			
GB-EA-TPS.F4.MBS	49.3	40.3	10.4	3800 (2.2)	170	112
GB-EA blend TPS.F4.IBBS	52.0	42.7	5.3	5600 (2.5)	144	112

[a] The molecular weight was determined by GPC with THF as the mobile phase using polystyrene standards.

The dry 193 nm lithography is performed using a ASML 5500/950B optical lithography system, with 0.63 NA at the NSF National Nanotechnology Center, Raleigh, NC.[2] SEM images of the smallest dense patterns (1:1 line/space) achieved by this 193 nm tool and the lithography method developed in this work are shown in figure 6.14. The 193 nm tool gives a 110 nm resolution for both resists while the method developed in this work gives 60 nm and 80 nm resolutions for GB-EA-TPS.F4.MBS and GB-EA blend TPS.F4.IBBS resists, respectively. Obviously both resists intrinsically possess sub-100 nm resolution capability according to the results produced by this lithography technique. This technique also characterized that GB-EA-TPS.F4.MBS resist has improved resolution and less LER compared with the blended-PAG analog. Although the ASML 193 nm tool characterized the difference in LER behavior as well, the lack of sub-100 nm resolution capability of the ASML 193 nm tool due to the low achievable NA can not faithfully represent the intrinsic resolution limitation of these two resist materials.

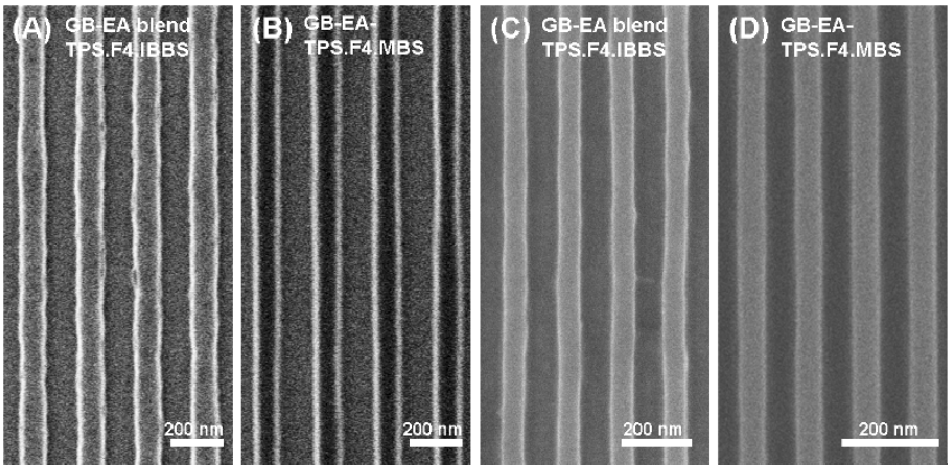

Figure 6. 14 SEM images of GB-EA-TPS.F4.MBS and GB-EA blend TPS.F4.IBBS resists showing the minimum achievable dense line resolutions patterned by (A and B) dry 193 nm ASML tool and (C and D) the technique developed in this work.

The lithographic performance of EUV resists under modern EUVL tools and the high resolution method are also evaluated and compared. Another set of polymer-bound-

PAG and blended-PAG analogs for EUVL application are tested.[10] The polymer-bound-PAG terpolymer (HS-EA-TPS.F4.MBS) is prepared by free-radical polymerization of hydroxystrene (HS, AZ Electronic Materials), 2-ethyl-2-adamantyl methacrylate (EA, AZ Electronic Materials), and TPS.F4.MBS. The blended-PAG analog is prepared by blending TPS.F4.IBBS with the HS-EA copolymer. The chemical structures of these two materials are shown in figure 6.15, and the compositions are listed in table 6.2.

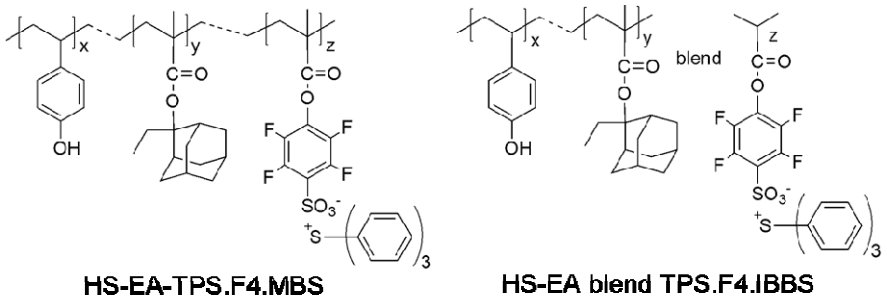

Figure 6. 15 Structures of HS-EA-TPS.F4.MBS and HS-EA blend TPS.F4.IBBS resists.

Table 6. 2 Compositions of HS-EA-TPS.F4.MBS and HS-EA blend TPS.F4.IBBS resists.

Resist Material	Composition (mol%)			Mw [a] (PID)	Stability (°C)	Tg (°C)
	HS	EA	PAG			
HS-EA-TPS.F4.MBS	35.0	57.9	7.1	3600 (1.6)	145	N/A[b]
HS-EA blend TPS.F4.IBBS	44.7	53.0	2.3	4500 (2.5)	131	113

[a] The molecular weights were determined by GPC with DFM as the mobile phase using polystyrene standards.
[b] Molecular weight can not be determined by DSC.

EUV exposure is conducted using an EUV Micro-Exposure Tool (EUV-MET) at Lawrence Berkeley National Laboratory, USA.[11] The 0.3 NA MET based micro-exposure station is designed to deliver a aerial image with a diffraction-limited resolution of approximately 30 nm under conventional illumination and < 15 nm resolution while using dipole illumination. The smallest dense feature resolution achieved by EUV-MET are 50 nm and 45 nm for HS-EA blend TPS.F4.IBBS and HS-EA-TPS.F4.MBS resists, respectively. The measured LERs (3σ) of the 50 nm resist lines patterned on HS-EA

blend TPS.F4.IBBS and HS-EA-TPS.F4.MBS resists are 12.1 nm and 11.0 nm, respectively. SEM images of the achievable minimum feature sizes of the same resists patterned by the lithography technique developed in this work are shown in figure 6.16. Both resists show 30 nm dense pattern resolution which are not observed in the EUV-MET patterning test. On the other hand, HS-EA-TPS.F4.MBS resist shows significant lower 3σLER (3.2 nm) than the blended-PAG analog (5.4 nm). In contrast to the technique developed in this work, the intrinsic resist resolution and LER behavior may be interfered and degraded by insufficient aerial image quality delivered by EUV-MET. Although EUV-MET can deliver aerial image with sub-30 nm resolution, the insufficient NILS of EUV-MET may introduce low aerial image contrast and significant shot noise statistics (5~10% intensity of the nominal exposure dose) at the resist line edge that results in low resolution and undistinguishable LER performance.

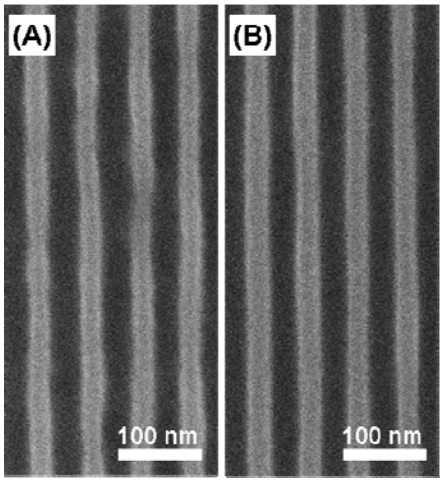

Figure 6. 16 SEM images of (A) HS-EA blend TPS.F4.IBBS and (B) HS-EA-TPS.F4.MBS resists showing minimum achievable dense line resolutions patterned by the technique developed in this work.

Another negative-tone molecule resist for EUV lithography is also used to test the capability of the developed lithography technique in probing resist intrinsic patterning performance. The molecule resist is composed of 95.0 mol% 1,1,2,2-tetra(4-

hydroxyphenyl)ethane tetraglycidyl ether (4-Ep, Sigma-Aldrich) and 5.0 mol% triphenylsulfonium hexafluoroantimonate (TPS.SbF_6, Midori Kagaku Co., Ltd.). The structures of the molecule resist are illustrated in figure 6.17.

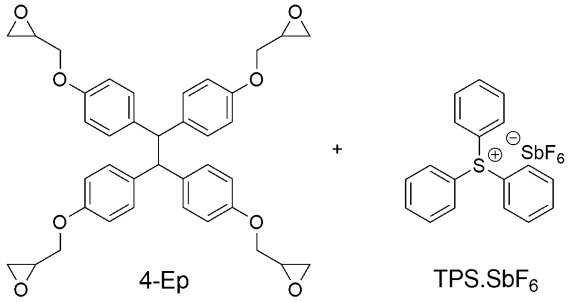

Figure 6. 17 Structures of a negative-tone molecule resist composed of 4-Ep and TPS.SbF_6.

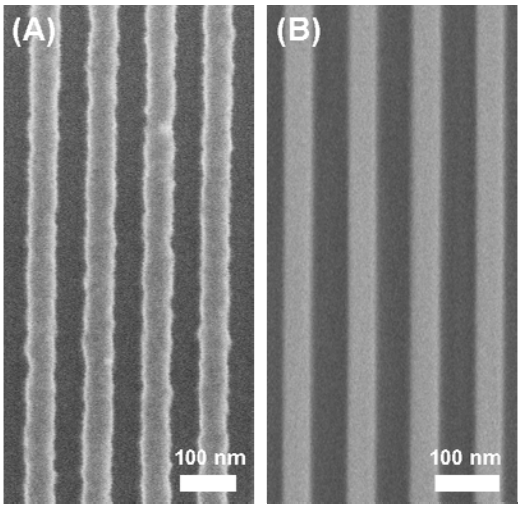

Figure 6. 18 SEM images of 50 nm half-pitch lines of 4-Ep blend TPS.SbF_6 molecule resist patterned by (A) EUV-IL tool at PSI and (B) the lithography technique developed in this work.

EUV exposure is conducted using an EUV Interference Lithography (EUV-IL) tool at Paul Scherrer Institute (PSI), Switzerland. The EUV-IL tool provides periodic EUV interference lithography (EUV-IL, 1:1 line/space) with resolution down to 12.5 nm.[12] The SEM images of 50 nm dense pattern written by EUV-IL and the developed

technique are shown in figure 6.18. The resulting LER (3σ) of the line feature patterned by the technique developed in this work (2.3 nm) is significantly lower than that patterned by EUV-IL tool (5.0 nm). The aerial image quality delivered by the EUV-IL tool is still not sufficient for investigating the intrinsic patterning performance of resist materials for sub-50 nm resolution applications.

A 45^{o} tilted cross-section view of 100 nm dense lines patterned on 4-Ep blend TPS.SbF_6 molecule resist using the developed lithography technique is shown in figure 6.19. The resist profile shows uniform CD along the resist film depth that confirms the uniform energy deposition calculated in previous section. The energy profile provided by the developed technique can be faithfully translated into uniform resist line pattern that can facilitate the investigation and characterization of resist CD, LER, and other more advanced properties.

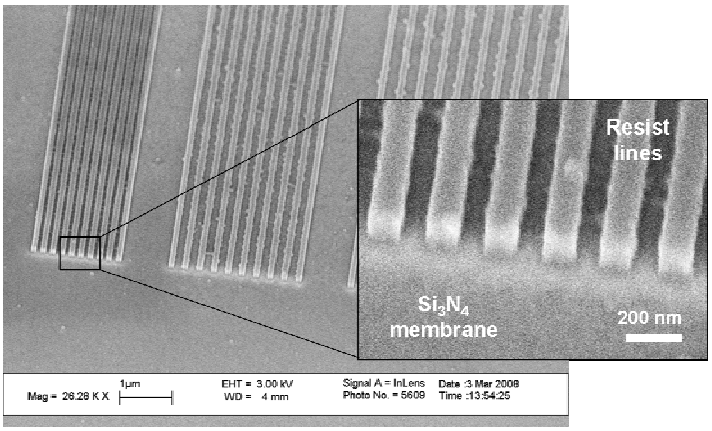

Figure 6. 19 A 45^{o} tilted cross-section SEM images of 100 nm dense lines patterned on a 4-Ep blend TPS.SbF_6 molecule resist using the developed lithography technique.

6.4 Conclusions

In this chapter, an ultra-high aerial image quality lithography technique is developed by using a 100 kV EBL system as the exposure tool and an ultra-thin free-

standing silicon nitride membrane as the substrate. This method is theoretically evaluated by a Monte Carlo simulator modeling the trajectory of the incident electrons and the corresponding energy deposition profile in the polymer film. The simulation results suggest electron backscattering effect is eliminated while replacing the thick silicon substrate by a 50 nm silicon nitride membrane. Energy deposition profiles of a single electron-beam at different film depths are characterized being uniform, and the spreading of the beam diameter at the bottom of a 100 nm pHOST film is less than 1.0 nm. The patterning capability of this lithography technique is also experimentally evaluated and compared to currently available 193 nm and EUV exposure tools by investigating the lithographic performance of selected resist materials. The results show that the intrinsic lithographic performance of a resist material, such as resolution, CD bias, CD uniformity, and LER, can be more faithfully represented by the lithography technique developed in this work than other modern lithography tools. The uniform energy deposition profile throughout the whole polymer film depth also provides uniform CD of the resist line across the whole film depth. For the polymer-bound-PAG resists investigated here, the direct incorporation of the PAG unit into the polymer main chain shows improved resolution and LER. Such improvement can not be clearly identified using other modern exposure techniques due to their low aerial image quality which may transfer into the resist film and degrade the achievable patterning performance of the resist.

6.5 References

[1] Levinson, H. J., Optical pattern formation, in *Principles of Lithography*, SPIE Optical Engineering Press **2004**, Bellingham, Washington, USA

[2] ASML 193 nm 5500/950B Stepper, NSF National Nanotechnology Center, Raleigh, NC, USA (http://www.advancedmaterials.unc.edu/chanl-instruments-asml-stepper.htm).

[3] Gronheid, R.; Goethals, A. –M.; Roey, F. V.; Leunissen, P.; Solak, H. H.; Ekinci, Y.; Schenau, K. V. I.; Vannuffel, C.; Jouve, A., Microstepper vs. interference EUV lithography: Effects on resist profiles, *EUV Symposium* **2005**, San Diego, California, USA.

[4] Brown, D. K.; Murali, R., Current nanolithography research update and summary, Microelectronics Research Center (MiRC), Georgia Institute of Technology, Atlanta, GA, USA (http://www.nanolithography.gatech.edu/ EBL_current_research.htm).

[5] Drouin, D; Couture, A. R.; Joly, D.; Tastet, X.; Aimez, V.; Gauvin, R., Casino V2.42 – A fast and easy-to-use modeling tool for scanning electron microscopy and microanalysis users, *Scanning* **2007**, *29*, 92-101.

[6] Drouin, D.; Hovington, P.; Gauvin, R., CASINO: A new era of Monte Carlo code in C language for the electron beam interaction - Part II: Tabulated values of Mott cross section, *Scanning* **1997**, *19*, 20–28.

[7] Joy, D. C.; Luo, S., An empirical stopping power relationship for low-energy electrons, *Scanning* **1989**, *11*, 176–180.

[8] McCord, M. A.; Rooks, M. J., Electron beam lithography, in *Handbook of Microlithography, Micromachining, and Microfabrication Vol.1 Microlithography*, SPIE Optical Engineering Press **1997**, Bellingham, Washington USA.

[9] Wang, M.; Jarnagin, N. D.; Lee, C. –T.; Henderson, C. L.; Yueh, W.; Roberts, J. M.; Gonsalves, K. E., Novel polymeric anionic photoacid generators (PAGs) and corresponding polymers for 193 nm lithography, *J. Mater. Chem.* **2006**, *16*, 3701-3707.

[10] Wang, M.; Gonsalves, K. E.; Rabinovich, M.; Yueh, W.; Roberts, J. M., Novel anionic photoacid generators (PAGs) and corresponding PAG bound polymers for sub-50 nm EUV lithography, *J. Mater. Chem.* **2007**, *17*, 1699-1706.

[11] Naulleau, P.; Goldberg, K. A.; Anderson, E. H.; Bradley, K.; Delano, R.; Denham, P.; Gunion, R.; Harteneck, B.; Hoef, B.; Huang, H.; Jackson, K.; Jones, M. G.; Kemp, D.; Lidlle, J. A.; Oort, R.; Rawlins, A.; Rekawa, S.; Salmassi, F.; Tackaberry, R.; Chung, C.; Hale, L.; Phillon, D.; Sommargren, G.; Taylor, H., Status of EUV microexposure capabilities at the ALS using the 0.3-NA MET optic, *Proc. SPIE* **2004**, *5374*, 881-891.

[12] Solak, H. H.; Ekinci, Y.; Kaser, P.; Park, S., Photon-beam lithography reaches 12.5 nm half-pitch resolution, *J. Vac. Sci. Technol. B* **2007**, *25*, 91-95.

CHAPTER 7

DEVELOPMEMT AND CHARACTERIZATION OF NOVEL POLYMER-BOUND-PAG RESISTS[†]

Substantially improved resist material designs, which can provide higher photosensitivity, precise CD control, and less LER/LWR, will be required to enable the implementation and application of NGL technologies to the production of future IC device generations using sub-50 nm technology nodes. The development and characterization of novel resist platforms which can solve the aforementioned basic problems with traditional CARs is essential and is already one of the major subjects of modern lithography research. In that regard, early development of a variety of 193 nm and EUV resists that contain PAG units covalently bond to polymer resin backbone has been reported. However, the detailed structure-property relationships between this direct attachment of the PAG functional group to the polymer and the resulting patterning performance have not yet been rigorously characterized. In addition, more advanced design of polymer-bound-PAG resists for superior patterning performance has not been processed neither. In this chapter, the development of advanced polymer-bound-PAG resists designed for 193 nm and EUV lithography, as well as the characterization of their

---

[†] Material presented in this chapter has appeared in part in previously published articles:

Lee, C. –T.; Henderson, C. L.; Wang, M.; Gonsalves, K. E.; Yueh, W., Effects of photoacid generator incorporation into the polymer main chain on 193 nm chemically amplified resist behavior and lithographic performance, *J. Vac. Sci. Technol. B* **2007**, *25*, 2136-2139.

Lee, C. –T.; Wang, M.; Jarnagin, N. D.; Gonsalves, K. E.; Roberts, J. M.; Yueh, W.; Henderson, C. L., Photosensitivity and line-edge roughness of novel polymer-bound PAG photoresists, *Proc. SPIE* **2007**, *6519*, 65191E.

Lee, C. –T.; Wang, M.; Gonsalves, K. E.; Yueh, W.; Roberts, J. M.; Henderson, C. L., Single-component polymeric chemically amplified resists: A strategy for improving lithography performance and resist process window, *Nanotechnology*, submitted.

patterning performance, are studied. The effects of direct incorporation of PAG into the resist polymer on the resolution, photosensitivity, and LER/LWR of CAR are characterized using the techniques developed in previous chapters. The effects of direct PAG binding on resist process window, such as the exposure and focal latitudes, are also experimentally characterized and discussed. This chapter provides the experimental characterization details about the patterning performance and advantages of polymer-bound-PAG CARs for NGL technologies.

7.1 Introduction

NGL technologies and resist materials that can provide mass production of IC devices with sub-50 nm feature resolution while maintaining extremely low feature edge roughness are essential to continued advance and development of microfabrication and modern semiconductor industry. For the NGL technologies introduced in chapter 1, the state-of-art 193 nm lithography technologies such as immersion lithography and double patterning are poised as the near-term solutions to provide further extension of current optical patterning capability down to 32 nm technology node. Beyond 32 nm resolution, EUVL is the most promising candidate for mass production. Significant efforts from both industrial and academic parties have been made on the development of EUVL technology. Direct-writing EBL, which can provide nanometer scale resolution and potentially high aerial image quality, is another promising technology for photomask making and advance device fabrication. However, all these techniques still require advanced resist materials which possess satisfactory patterning performance for translating the aerial image delivered by these exposure tools into a physical relief image. Unfortunately current resist material design does not appear to be able to provide the required set of performance metrics for NGL technologies.

Resist material plays a critical but challenging role for the realization of NGL technologies. As introduced in chapter 2, CARs have served for more than twenty years as the high sensitivity, high resolution patterning media for transferring designed patterns from the photomask to underlying thin films. Traditional CARs are blended-PAG, multi-component materials which have been known to have a number of potential problems, including low PAG solubility and thus low maximum PAG loadings, PAG aggregation and segregation that lead to non-uniform resist film composition, and acid diffusion that can lead to defects such as the loss of CD control and unacceptable LER/LWR. Moreover, traditional CAR platform ultimately creates a tradeoff between achieving the desired characteristics of high resolution, high sensitivity, and low LER/LWR (i.e. the RSL constraint) through possible formulation and material structure changes, as shown in figure 7.1. This tradeoff is brought out by the blend nature of a multi-component CAR and exposes the main challenge of advanced resist materials design for the NGL technologies.

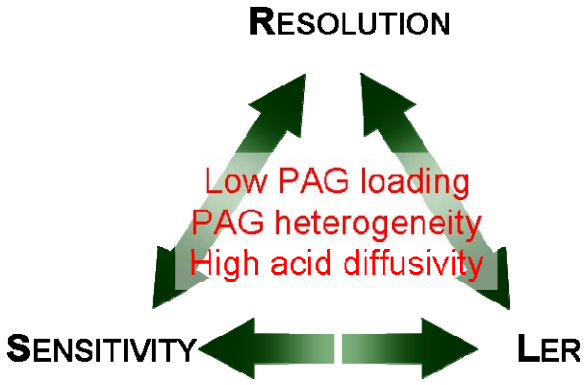

Figure 7. 1 The RSL constraint and the fundamental problems of traditional multi-component CARs.

Novel design of resist materials which can achieve all these three characteristics (i.e. high resolution, high photospeed, and low LER/LWR) and provide larger resist

processing window is critical for the continued success of high resolution patterning in integrated circuit manufacturing. The concept of direct incorporation of PAG into the polymer main chain has been developed recently and has been shown to be one promising route to high performance resist materials design.[1-3] A general synthesis scheme of 193 nm and EUV polymer-bound-PAG resists is illustrated in figure 7.2. These polymer-bound-PAG resists have showed photospeeds and resolutions comparable to traditional blended-PAG resists. In this chapter, the development of advanced polymer-bound-PAG resists for 193 nm and EUV lithography applications, as well as the characterization of their photosensitivity, dense feature resolution, PAG distribution and segregation, and LER behavior are investigated. The effects of direct PAG incorporation into the polymer main chain on the lithographic performance are studied by comparing the polymer-bound-PAG resists to their blended-PAG analogs.

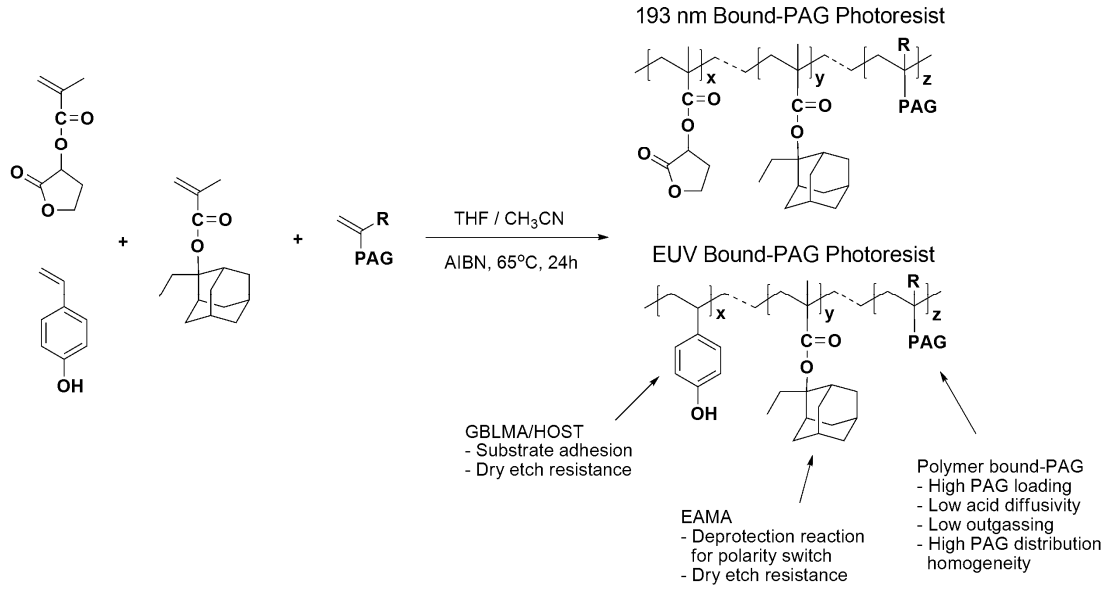

Figure 7. 2 General synthesis scheme of polymer-bound-PAG resists for 193 nm and EUV lithography applications.

7.2 Experimental Procedure

7.2.1 Polymer-Bound-PAG Resist Materials

Polymer-bound-PAG resist materials used in this study are synthesized and prepared by methods described in previous publications.[4-6] For 193 nm lithography, the bound-PAG terpolymers is prepared by free-radical polymerization of the 2-ethyl-2-adamantyl-methacrylate (EA, AZ Electronic Materials, Ltd.) and γ-butyrolactone methacrylate (GB, AZ Electronic Materials, Ltd.), and (4-methylphenyl) dimethylsufonium trifluoromethylsulfonate (MPDMS.TFMS) or triphenylsulfonium salt 4-(methacryloxy) 2.3.5.6-tetrafluorobenzenesulfonate (TPS.F4.MBS). The analogous blended-PAG resist is prepared by blending the triphenylsulfonium salt 4-(isobutyloxy) 2.3.5.6-tetrafluorobenzenesulfonate (TPS.F4.IBBS) with GB-EA copolymers of similar GB:EA molar ratios to that of the polymer-bound-PAG resist. For EUV lithography, the bound-PAG and the blended-PAG resists are prepared through the same scheme as mentioned in 193 nm resist preparation, however using hydroxystrene (HS, AZ Electronic Materials) in replacement of GB as the substrate adhesive and etch resistant subunit of the polymer. The chemical structures and the compositions of the bound-PAG polymers and the blended-PAG analogous are shown in figure 7.3 and table 7.1 respectively. The resist solutions are made by dissolving 4 wt% solids (including polymer resin and PAG) in cyclohexanone (Sigma Aldrich, Inc.) and filtered through a 0.2 μm Teflon syringe filter.

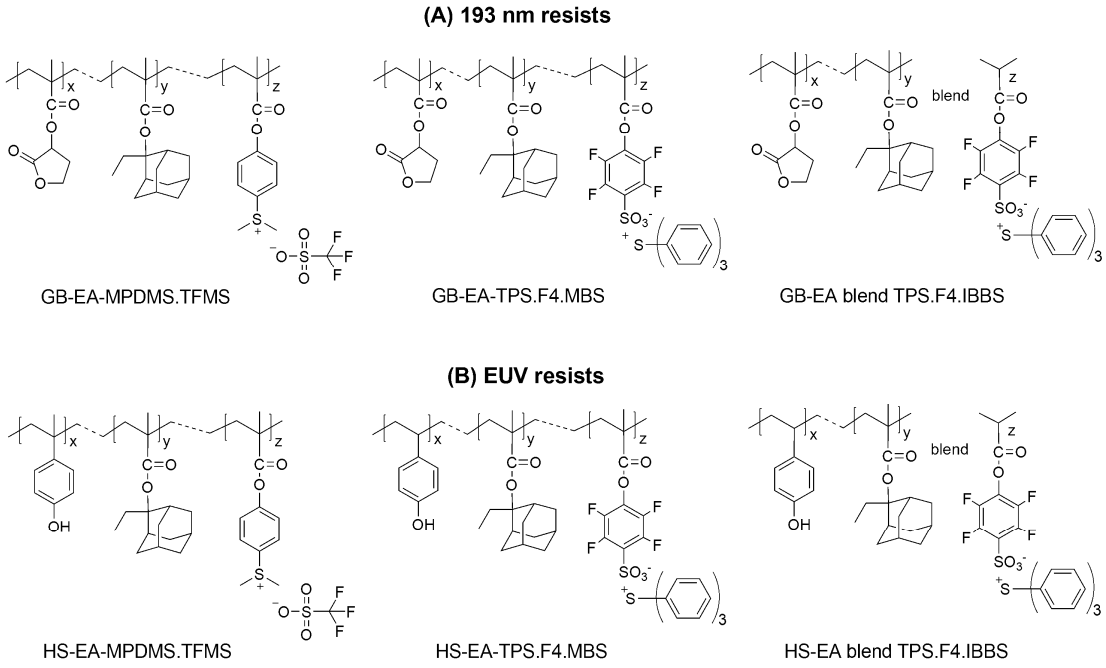

Figure 7. 3 Structures of polymer-bound-PAG and blended-PAG resists for (A) 193 nm and (B) EUV lithography.

Table 7. 1 Composition of resist materials used in this work.

Resist Material	Composition (mol%)			Mw [a] (PID)	Stability (^{o}C)	Tg (^{o}C)
	GB or HS	EA	PAG			
GB-EA-MPDMS.TFMS	52.1	39.2	8.7	12,000 (1.2)	185	129
GB-EA-TPS.F4.MBS	49.3	40.3	10.4	3,800 (2.2)	170	151
GB-EA blend TPS.F4.IBBS	52.0	42.7	5.3	5,600 (2.5)	144	112
HS-EA-MPDMS.TFMS	46.0	49.0	5.0	2,500 (1.8)	165	137
HS-EA-TPS.F4.MBS	35.0	57.9	7.1	3,600 (1.6)	145	N/A [b]
HS-EA blend TPS.F4.IBBS	44.7	53.0	2.3	4,500 (2.5)	131	113

[a] The molecular weights of GBLMA and HOST included polymers were determined by GPC with THF and DFM as the mobile phase respectively using polystyrene standards.
[b] Molecular weight can not be determined by DSC.

7.2.2 Resist Processing and Characterization

Resist films (100 +/- 5 nm film thickness) for measuring DUV and EB photospeeds and resist contrast curves are prepared by spin-coating the resist solutions onto a prime grade silicon wafer dehydration baked and primed with a solution containing 20 vol% 1,1,3,3,3-hexamethyl-disilazane (HMDS, ICN Biomedicals) and 80 vol% propylene glycol-1-monomethyl ether 2-acetate (PGMEA, Sigma Aldrich Inc.). A post-applied bake is performed at 100 ^{o}C for 90 seconds to remove the residual solvent in the resist film. Resist films (80 +/- 5 nm film thickness) for determining resolution and LER performance are prepared by spin-coating the resist solution onto a 50 nm free-standing silicon nitride membrane through the same process. DUV exposure of resist film is performed by using an Oriel Instruments exposure source (model # 87530-1000, Hg-Xe arc lamp) equipped with a 248 nm band-pass filter (bandwidth ~ 11 nm, FWHM). The intensity of the lamp source is measured to be 1.01 mW/cm^2 using a Molectron PM3 power probe and EPM2000 energy meter. EB exposure of resist film is performed by using a JEOL JBX-9300FS EBL system with a 100 kV acceleration voltage and a 2 nA beam current. The exposed resist film is then post-exposure baked at 100 ^{o}C for 90 seconds and developed with a standard 0.26N tetramethylammonium hydroxide (TMAH) developer (AZ-300MIF, AZ Electronic Materials) for 15 seconds. The developed resist film is than rinse with deionized water and dried with nitrogen blow. For the basic characterization of the patterned resist film, the film thickness is measured using a variable angle spectroscopic ellipsometer (V-VASE, J. A. Woollam Inc.) by fitting the ellipsometry data with a Cauchy model for the resist film in the non-absorption wavelength region (400~1000 nm). PAG acid generation in the resist film upon DUV exposure is determined by the method using on-wafer ellipsometry of acid-sensitive dye developed in chapter 4. The ultra-high aerial image quality lithography technique

developed in chapter 6 is applied to the characterization of resist intrinsic patterning performance.

Resist pattern is imaged in a top-down mode using a LEO 1530 thermally assisted field emission SEM with a 3 kV acceleration voltage and a 100,000 magnification. Half-pitch resolution, line edge positions, and LER of the resist line are determined using an off-line image analysis program developed in chapter 6. The 3σLER of resist dense line pattern is determined by averaging the values obtained from 5 different resist lines with 10 nm measurement pitch and 1.0 μm inspection length. Spatial-frequency analysis of resist line edge is also performed to investigate the origin of LER.

7.3 Results and Discussion

7.3.1 Cationic Polymer-Bound-PAG Resists

The first generation of polymer-bound-PAG resists is the resist materials which have the direct incorporation of PAG cation into the polymer main chain. GB-EA-MPDMS.TFMS and HS-EA-MPDSM.TFMS resists belong to this category, and their lithographic performance is investigated using the high resolution patterning method. The SEM images of grating features of GB-EA-MPDMS.TFMS resist are shown in figure 7.4. The obtained minimum achievable dense line feature is 70 nm 2:1 L/S which is far below the resolution requirements for 193 nm immersion and double exposure lithography applications (65 nm 1:1 L/S). The resist features show significant image blur (> 40 nm at the line edge) that even a 100 nm 1:1 L/S dense pattern can not survive after the development. On the other hand, the resist image blur also degrades the edge contrast of the resist line as shown in figure 7.4. The significant image blur is mainly due to the acid diffusion during PEB. The cationic incorporation of MPDMS.TFMS PAG may improve PAG loading capability and distribution uniformity of in the resist film, however the acid

generated through PAG photodecomposition is a free TFMS acid which is small and has no mechanism to confine its diffusion in the resist film.

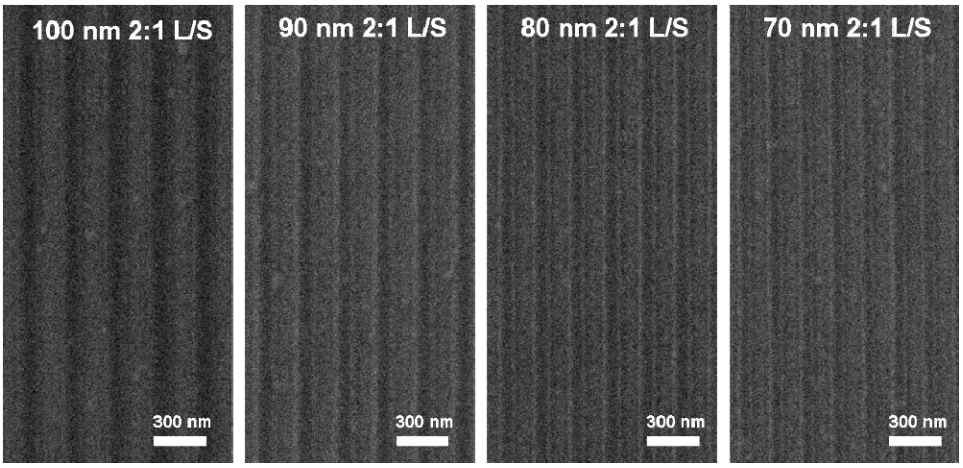

Figure 7. 4 SEM images of GB-EA-MPDMS.TFMS resist resolution test.

SEM images of grating features of the other cationic polymer-bound-PAG resist, HS-EA-MPDMS.TFMS, designed for EUV lithography application, are shown in figure 7.5. The obtained minimum achievable dense line feature is 45 nm 1:1 L/S which is still below the resolution requirements for EUV lithography applications (32 nm 1:1 L/S). The failing mechanism of the 40 nm 1:1 L/S pattern is mainly due to the collapse of the resist lines during the drying process after resist development and rinse. Although the photodecomposition of cationic-bound MPDMS.TFMS PAG generates the same free TFMS acid, the dense line resolution of HS-EA-MPDMS.TFMS resist is significantly higher than GB-EA-MPDMS.TFMS resist and no serious resist image blur is observed. The presence of HS subunit contributes to the resolution enhancement by introducing significant amount of hydroxyl groups which possess higher electron affinity and polarity that can enhance resist line adhesion to the substrate and reduce acid diffusion in the resist film. Obviously the cationic polymer-bound-PAG resists which have the incorporation of PAG cation into the polymer main chain still surfer from the lack of

mechanism which can efficiently confine acid diffusion and improve resist resolution. In addition to the acid diffusion issue, the incorporation of the methacryloyl group to PAG chromophore for polymerization purpose also decrease the efficiency of PAG acid generation.[7]

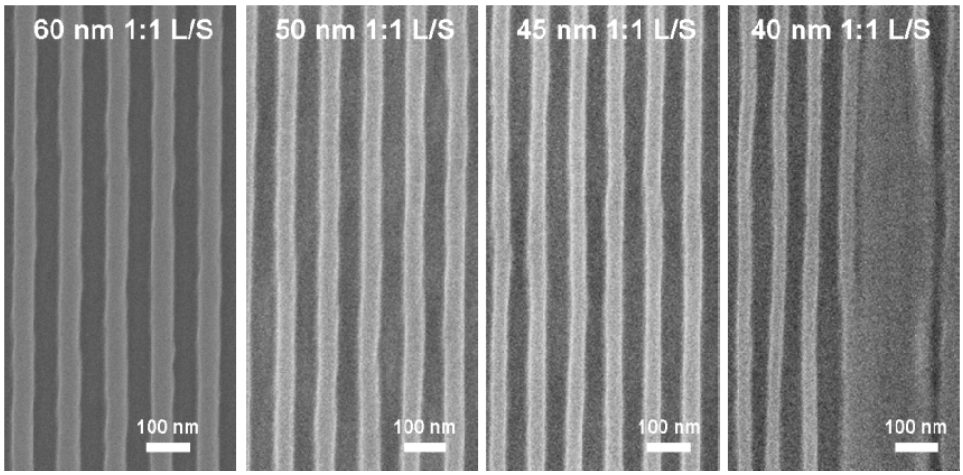

Figure 7. 5 SEM images of HS-EA-MPDMS.TFMS resist resolution test.

7.3.2 Anionic Polymer-Bound-PAG Resist for 193 nm Lithography

In order to control acid diffusivity and prevent possible effects of modifying PAG chromophore structure on PAG acid generation efficiency, the second generation of polymer-bound-PAG resists which have the PAG anion directly incorporated into the polymer main chain is developed and the lithographic performance is investigated in more detail. For resist materials designed for 193 nm lithography applications, DUV photosensitivity and resist contrast of GB-EA-TPS.F4.MBS and GB-EA blend TPS.F4.IBBS resists are shown in figure 7.6(A). The corresponding acid concentration upon DUV exposure is also shown in figure 7.6(B). GB-EA-TPS.F4.MBS resist showed significantly improved photospeed (15.0 mJ/cm^2) and resist contrast (8.9) as compared to its blended-PAG analog (20.0 mJ/cm^2 and 5.5). By looking at the combination of figures

7.6(A) and 7.6(B), it is observed that at the exposure condition where both resists generates the same acid concentration (0.015 M), approximately 10% GB-EA-TPS.F4.MBS and 95% GB-EA blend TPS.F4.IBBS resist film losses are obtained. Since both resists has approximately the same composition except PAG loadings, their dissolution properties under the same development condition should be approximately the same. This result supports the idea that the deprotection catalytic chain length and diffusivity of the acid in GB-EA-TPS.F4.MBS resist is significantly smaller than the free acid in the GB-EA blend TPS.F4.IBBS resist. By looking at the exposure dose at which both resists have the same resist thickness loss (50%) in figure 7.6(A), the corresponding acid concentration (0.018 M) in GB-EA-TPS.F4.MBS resist is 50 mol% higher than that (0.012 M) in GB-EA blend TPS.F4.IBBS resist. Although the bonding of the PAG anion to the polymer chain may reduce the acid diffusivity and thus decrease acid catalytic chain length, the ability to incorporate much higher PAG loadings in a polymer-bound-PAG resist material can enable the generation of substantially higher acid concentrations under the same exposure dose that can compensate for the reduced acid catalytic chain length. The end result is that it can be possible to produce higher photospeed materials in the polymer-bound-PAG resists as compared to blended-PAG resists even with the reduced acid diffusivity. Furthermore, the photolysis of the PAG and the resulting acid anion formed on the polymer may serve to further increase the degree of the polarity change in the polymer between the exposed and unexposed material that can act in concert with the deprotection reaction to increase the development contrast in the case of the polymer-bound PAG materials.

GB-EA-TPS.F4.MBS resist also shows the capability to resolve higher resolution features than GB-EA blend TPS.F4.IBBS and the first generation, cationic polymer-bound-PAG resists reported in section 7.3.1. As illustrated in figure 7.7, the minimum isolated space width obtained from a GB-EA-TPS.F4.MBS resist film is 39.3 nm, which is significantly smaller than a 76.2 nm minimum space size obtained from a GB-EA

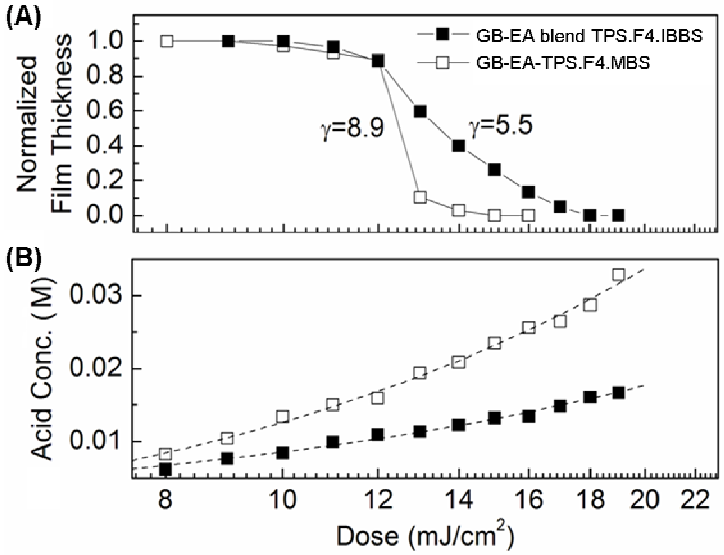

Figure 7. 6 (A) DUV resist contrasts and (B) acid generation behavior of GB-EA-TPS.F4.MBS and GB-EA blend TPS.F4.IBBS resists.

blend TPS.F4.IBBS resist film. The fact that these isolated space features are patterned using the scanning of single pixel wide electron beam exposures on a backscattering eliminated substrate. This lithography setup allows one to determine a crude estimate of the corresponding acid diffusion lengths in these materials. One measure of acid diffusion length that can be used to compare the materials is the minimum resist half space width produced from the single pixel wide exposure minus the approximate half single pixel electron beam diameter, which we refer to here as the acid diffusion length. Since the single pixel electron beam diameter is 8 nm, the acid diffusion lengths in this work were calculated for GB-EA-TPS.F4.MBS and GB-EA blend TPS.F4.IBBS resists being 15.6 nm and 34.1 nm respectively under identical resist processing conditions. This result supports the hypothesis that incorporating PAG anion into the polymer main chain can provide the mechanism that can significantly reduce acid diffusivity and can dramatically reduce acid diffusion induced image blur.

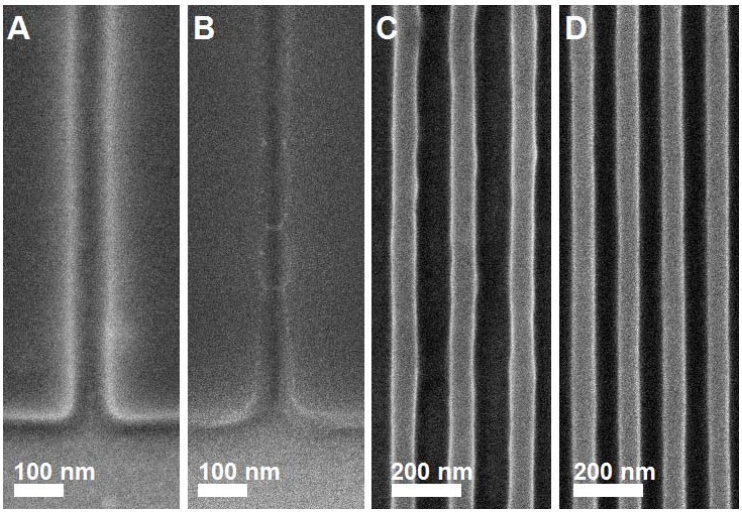

Figure 7. 7 SEM images of obtained minimum space width of (A) GB-EA blend TPS.F4.IBBS and (B) GB-EA-TPS.F4.MBS resists, as well as the minimum half-pitch resolution of (C) GB-EA blend TPS.F4.IBBS and (B) GB-EA-TPS.F4.MBS resists.

The half-pitch resolution achieved by GB-EA-TPS.F4.MBS resist is also superior to that of GB-EA blend TPS.F4.IBBS resist, as shown in figure 7.8. GB-EA blend TPS.F4.IBBS resist shows much more significant line width slimming (12.7 nm smaller than the smallest 1:1 nominal 80 nm feature that is obtained for that resist, or an approximately 16% CD error) than that of GB-EA-TPS.F4.MBS resist (3.3 nm smaller than the nominal resist CD of 60 nm, the highest resolution 1:1 L/S feature obtained for that resist). The limitation of half-pitch resolution is mainly due to the collapse of patterned resist lines during resist rinse and drying processes. Pattern collapse of 1:1 L/S dense feature originates from the uneven capillary force acting on the resist line side wall that causes either the mechanical deformation, bending, and breakage of the resist line itself, or the unstuck of the resist lines from the underlying substrate (resist adhesion failure). For both pattern collapse mechanisms, less resist line slimming can provide wider resist line and the contacting area with the substrate; hence provide higher mechanical strength and adhesion force against the stress generated by the capillary force

during resist rinse and drying processes. Resist line with better CD control (i.e. less resist CD slimming and image blur) in principle can generally possess better mechanical and physical properties and survive at smaller feature size.

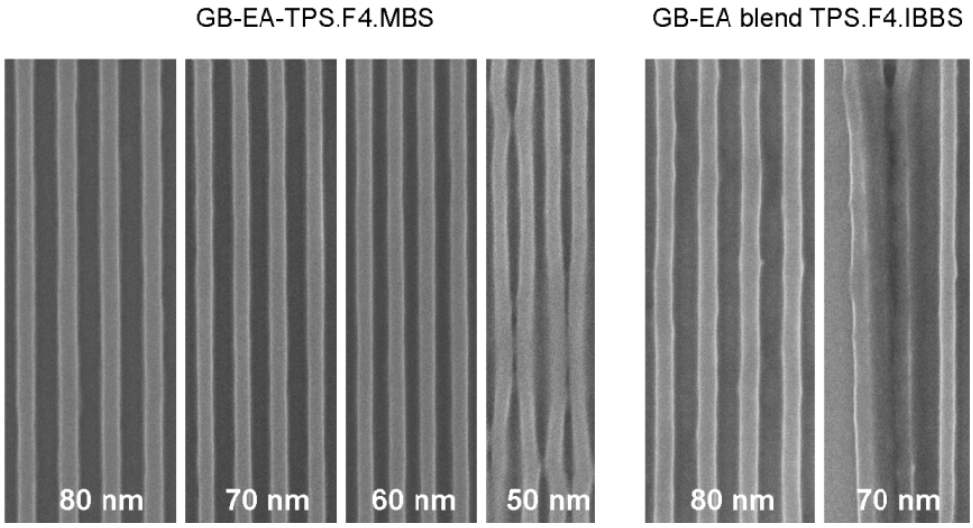

Figure 7. 8 Half-pitch resolution and the pattern collapse behavior of GB-EA-TPS.F4.MBS and GB-EA blend TPS.F4.IBBS resists.

The line pattern of GB-EA blend TPS.F4.IBBS resist shows obvious line width and edge position fluctuations when compared to that of GB-EA-TPS.F4.MBS resist. The high resolution half-pitch SEM images shown in figure 7.7 (C) and (D) are one clear example of this dramatic difference. The spatial-frequency distributions of LER of line patterns of both resists are investigated and the power spectra at the best half-pitch resolutions (i.e. 60 nm for GB-EA-TPS.F4.MBS and 80 nm for GB-EA blend TPS.F4.IBBS) are shown in figure 7.9. Clearly the major improvement of LER is in the low-spatial frequency region ($K < 10^{-2}$ nm^{-1}). This region is approximately the length scale at which the roughness might be expected to become dominated by acid diffusion and heterogeneous PAG distribution effects. The 3σLWR of GB-EA-TPS.F4.MBS and

GB-EA blend TPS.F4.IBBS resists are calculated being 6.0 nm and 11.3 nm respectively. The reduced acid diffusivity in GB-EA-TPS.F4.MBS resist couples with the higher PAG loading lead to more uniform acid distribution after exposure and higher resist contrast after PEB. These effects may lead to the observed reduction in LER. In essence, the binding of the PAG anion to the polymer and the incorporation of a higher PAG loading produces a higher density but smaller deprotection volumes created by acid molecules at the deprotection front when compared to the blended-PAG resist. These overlapping deprotection smaller volumes result in a smoother and finer edge transition at the developed feature edge and lower LER.

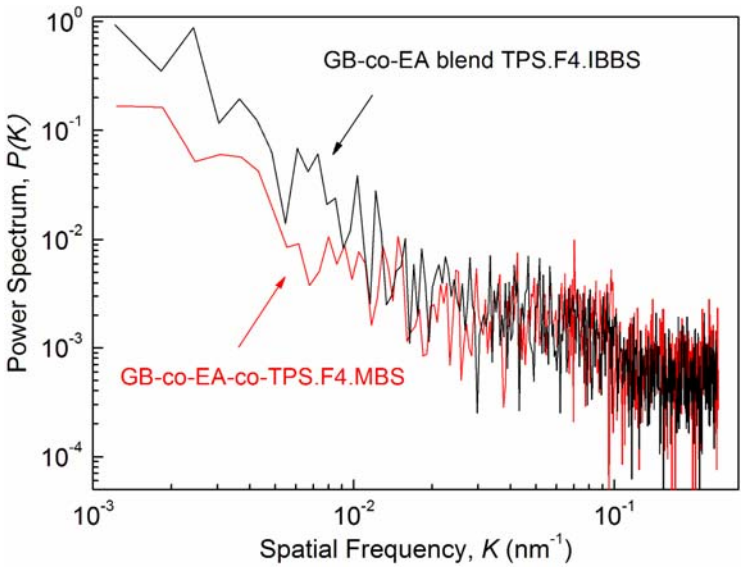

Figure 7. 9 Spatial frequency analysis of LER of GB-EA-TPS.F4.MBS (60 nm 1:1 L/S) and GB-EA blend TPS.F4.IBBS (80 nm 1:1 L/S) resist patterns.

One additional benefit of binding PAG functionality to polymer resin is that phase separation or PAG aggregation during film casting should be eliminated. This is in contrast to the known examples of PAG surface segregation and heterogeneous

distribution that have been previously reported in the literature for blended-PAG materials.[8,9] Since the PAG molecule is bound and dispersed into the polymer main chain, its ability to undergo any significant micro-phase separation or aggregation is virtually eliminated by the polymer chain orientation in a resist film. The distribution of PAG in GB-EA-TPS.F4.MBS and GB-EA blend TPS.F4.IBBS resist films is probed to confirm this advantage. In this case, X-ray photoelectron spectroscopy (XPS) is applied to determine if there is any preferential aggregation of PAG to the polymer film surface as might be expected in the case of the fluorinated PAG used in this work. Both resist films are formulated to have the same PAG loading (1.9 mol%) and thus approximately the same carbon-to-fluorine atom ratio (174.9:1 and 179.4:1 for GB-EA-TPS.F4.MBS and GB-EA blend TPS.F4.IBBS resists, respectively). The carbon and fluorine binding energy spectra obtained from XPS spectrometry for both resist films are shown in figure 7.10. Under identical PAG loadings, the GB-EA blend TPS.F4.IBBS resist film shows higher fluorine content (i.e. PAG content) at the film surface than the GB-EA-TPS.F4.MBS resist film, indicating that the GB-EA blend TPS.F4.IBBS resist film indeed exhibits preferential aggregation of PAG at the film surface. In fact, using ratios of the fluorine to carbon peak areas, it is determined that the GB-EA-TPS.F4.MBS resist film exhibits a fluorine surface concentration that is closer to a PAG uniformly distributed film. The prevention of aggregation and leaching of PAG molecules from the resist film in the case of the polymer-bound-PAG resist may also be partially responsible for the improved LER performance observed in that material. The anionic PAG incorporation may also facilitate the use of 193 nm immersion lithography techniques since the leaching of PAG or acid molecules into the immersion fluid during exposure can be prevented.

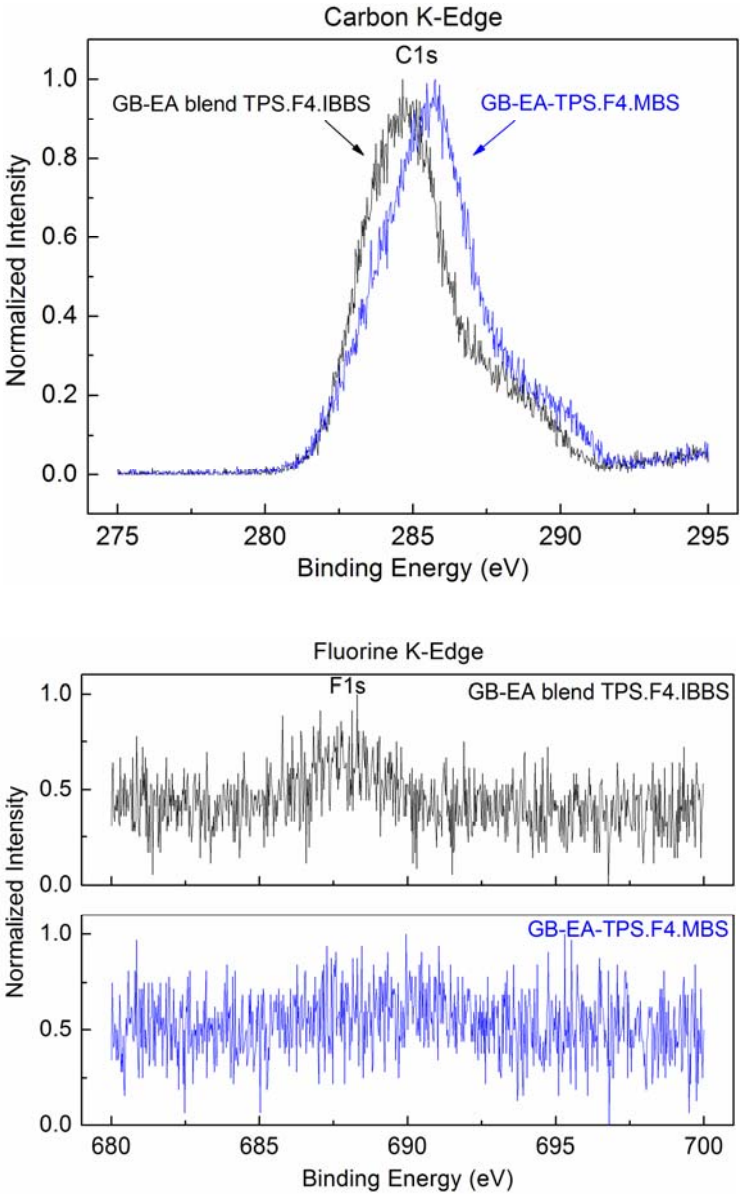

Figure 7. 10 Carbon and fluorine K-edges of XPS spectra of GB-EA-TPS.F4.MBS and GB-EA blend TPS.F4.IBBS resist films formulated with identical PAG loadings and approximately the same carbon-to-fluorine atom ratio.

7.3.3 Anionic Polymer-Bound-PAG Resist for EUV Lithography

The lithographic performance of the anionic polymer-bound-PAG resist (HS-EA-TPS.F4.MBS), as well as a blended-PAG analog (HS-EA blend TPS.F4.IBBS), designed for EUVL applications are also characterized in detail. In addition to these two CARs, two main stream non-chemically amplified electron-beam resists, ZEP520A (Mw 57,000, Zeon) and poly(methyl methacrylate) (pMMA, Mw 950,000, MicroChem), are used and compared to the performance of CARs. Both HS-EA-TPS.F4.MBS and HS-EA blend TPS.F4.IBBS resists show comparable sensitivity when using silicon nitride membrane as the substrate (124 and 120 $\mu C/cm^2$ dose-to-size respectively) for patterning 30 nm half-pitch lines. The achievable minimum feature size of these non-optimized resist materials already satisfy the resolution requirement for fabricating 32 nm technology node using EUVL technology. However, at the dose-to-size, the patterned line width of the HS-EA-TPS.F4.MBS resist film (28.5 nm) is close to the nominal CD while the line width of the HS-EA blend TPS.F4.IBBS resist film (25.3 nm) still shows unacceptable slimming. The HS-EA-TPS.F4.MBS resist film also exhibits significantly smaller 3σLER (3.2 nm) than the HS-EA blend TPS.F4.IBBS resist film (5.4 nm). The corresponding SEM images of the minimum feature sizes patterned on these resist films, including the non-chemically amplified resists, ZEP520A and pMMA, are shown in figure 7.11.

The reduced CD bias of the HS-EA-TPS.F4.MBS resist film may due to the direct binding of the PAG anion into the polymer main chain which reduces acid diffusivity during the thermally-induced acid-catalyzed deprotection of the resist polymer. Again although more confined PAG anion diffusivity may essentially decrease the achievable deprotection volume of each acid molecule and therefore reduce resist sensitivity, higher PAG loading capability may help the polymer-bound-PAG resist to retain its sensitivity by generating more acids under the same exposure dose. The direct incorporation of PAG anion into the polymer resin resulted in not only a more confined acid diffusivity, but in

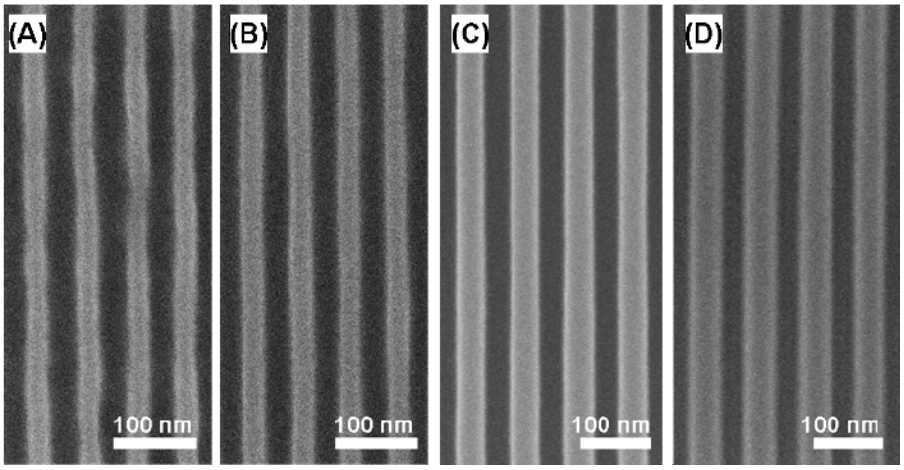

Figure 7. 11 The minimum achievable half-pitch resolution of (A) HS-EA blend TPS.F4.IBBS (30 nm 1:1 L/S), (B) HS-EA-TPS.F4.MBS (30 nm 1:1 L/S), (C) ZEP520A (25 nm 2:1 L/S), and (D) pMMA (25 nm 2:1 L/S) resists.

fact a single-component resist which may eliminate phase compatibility problem and reduced PAG or polymer aggregation phenomenon generally experienced in multi-component resist materials. Every acid molecule deprotects a volume of resist resin during the PEB process, and the deprotection volume is proportional to the acid diffusivity. The overlapping of smaller deprotection volume created by anionically-bound acids eventually create a smoother and finer dissolution front which contributes to better CD control and lower LER. The spatial frequency analysis of the LER distribution is illustrated in figure 7.12. HS-EA-TPS.F4.MBS resist shows significant smaller power spectrum intensity at the low-spatial frequency region (< 0.03 nm^{-1}) which has been theoretically and experimentally proved highly correlated to statistical fluctuations such as acid distribution and diffusion, PAG and polymer aggregation, as well as resist process condition.[8-14] Since both resists are processed under the same condition, and exhibited approximately the same dose-to-size, the LER difference caused by the process effects can be neglected. The resultant lower LER suggests that the material nature of HS-EA-TPS.F4.MBS resist results in superior lithographic performance than HS-EA blend

TPS.F4.IBBS resist. Among those major factors associated with the material nature of the resist film, it is possible that the improved LER performance of a anionic polymer-bound-PAG resist is mainly due to the increase of PAG loading and the reduce of acid diffusivity. For example, HS-EA-TPS.F4.MBS resist shows more than three-fold higher PAG loading than HS-EA blend TPS.F4.IBBS resist. If simply assuming no PAG distribution improvement is achieved in the HS-EA-TPS.F4.MBS resist film through binding the PAG into the polymer (i.e. both resists have the PAG distribution property), this three-fold PAG loading increase in the HS-EA-TPS.F4.MBS resist can decrease 42.3% distribution uncertainty of the number of PAG molecules found in a certain resist volume of the HS-EA blend TPS.F4.IBBS resist film. Detailed modeling analysis of PAG loading and acid diffusion effects on resist LER is performed and reported in chapter 8.

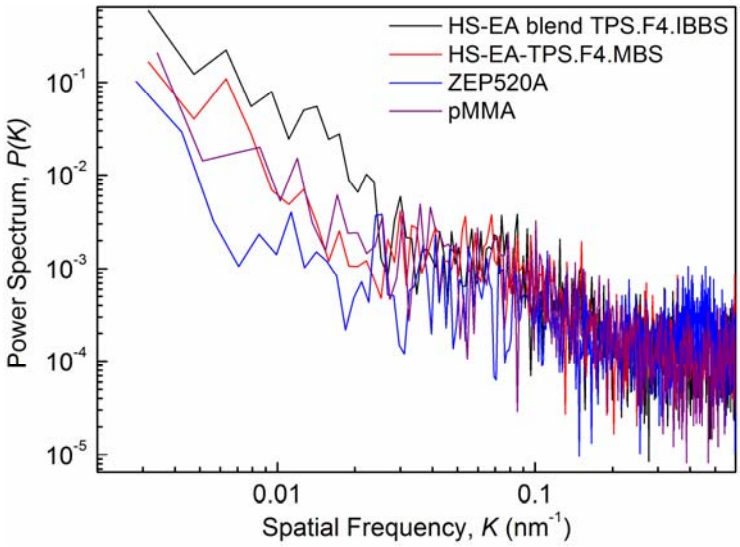

Figure 7. 12 Spatial frequency analysis of LER of HS-EA-TPS.F4.MBS (30 nm 1:1 L/S), HS-EA blend TPS.F4.IBBS (30 nm 1:1 L/S), ZEP520A (25 nm 2:1 L/S), and pMMA (25nm 1:1 L/S) resist patterns.

The incorporation of PAG anion into the polymer resin also improved resist sensitivity and contrast. The contrast curves of resist materials under DUV and 100 keV EB exposures are illustrated in figure 7.13. HS-EA-TPS.F4.MBS resist with 7.1 mole% PAG loading shows significant increase of resist contrasts (γ_{DUV}=8.5, γ_{EB}=8.5) when compared with HS-EA blend TPS.F4.IBBS resist (γ_{DUV}=3.2, γ_{EB}=7.0). A higher PAG loading HS-EA-TPS.F4.MBS resist (15.1 mole% PAG loading) shows even higher resist contrasts (γ_{DUV}=9.5, γ_{EB}=12.2). HS-EA-TPS.F4.MBS resist also shows superior lithographic performance when compared with the non-chemically amplified resists for EBL. Under optical exposure such as DUV used in this work, the increase of PAG loading can increase the acid generation rate as shown in figure 7.13(A). A resist with faster photospeed can be made by increasing the PAG loading from 7.1 mol% to 15.1 mol%. The increased acid generation rate is mainly due to the increase of PAG loading that increases the absorption of radiation and thus PAG photodecomposition for acid generation. However in the case that a high-energy radiation such as the 100 keV EB is applied, the increase of PAG loading does not guarantee the increase of acid generation rate, as shown in figure 7.13(B). There are two major factors affecting PAG acid generation under high-energy exposure. First, under high-energy radiation, the photon energy is much higher than the ionization potential of most organic materials (~ 10 eV), and the exposure source is often called ionization radiation. The radiation energy deposition becomes atomic absorption, rather than a molecular absorption of low-energy optical radiation. Such ionization radiation is not selective to the molecule structure of the resist material. Hence, the high energy photons are not only absorbed by PAG molecules, but also absorbed by the polymer matrix. Second, ionization radiation exposure generally requires high vacuum working environment to eliminate energy absorption by the molecules in the atmosphere. The accessibility of proton source for PAG acid generation under such high vacuum environment becomes another issue for PAGs which require external proton source to generate acid. Thus, resist composition effect, such as polymer

resins and additives used in resist formulation, becomes significant to PAG decomposition and acid generation under ionization radiation exposure. Investigation of the relationships between resist material structure and PAG acid generation behavior is essential for further improving PAG acid generation efficiency using ionization radiation exposure tools, such as EUVL and EBL. In terms of the applicability for EBL, although two main stream electron-beam resists, ZEP520A and pMMA, still exhibit lower 3σLER (2.1 nm and 2.8 nm respectively) due to the non-chemically-amplified, chain-scission and unzip mechanisms and the required high exposure dose for imaging can eliminate the LER originated from shot noise, PAG distribution, and acid diffusion existed in CARs.[15,16] HS-EA-TPS.F4.MBS resist shows comparable resolution and at least 3.5 folds higher sensitivity than ZEP520A and pMMA. The improved photospeed can greatly relieve the throughput problem experienced by EBL community.

Again, XPS is used to determine if there is any preferential aggregation of PAG molecules to the resist film surface as might be expected in the case of the fluorinated PAG used in this work. Both resist films containing the same PAG loading (2.1 mol%) and approximately the same carbon-to-fluorine atom ratio (167.6:1 and 164.6:1 for HS-EA-TPS.F4.MBS and HS-EA blend TPS.F4.IBBS resists, respectively) are prepared for XPS analysis. The carbon and fluorine binding energy spectra obtained from XPS for both resist samples are shown in figure 7.14. Under identical PAG loadings, the HS-EA blend TPS.F4.IBBS resist film shows higher fluorine contents (i.e. PAG contents) at the film surface than the polymer-bound-PAG resist film, indicating that the HS-EA blend TPS.F4.IBBS resist film exhibits preferential PAG aggregation at the film surface. This observation again confirms the capability of the polymer-bound-PAG resist for preventing PAG aggregation and leaching from the resist film that may be partially responsible for the observed LER improvement.

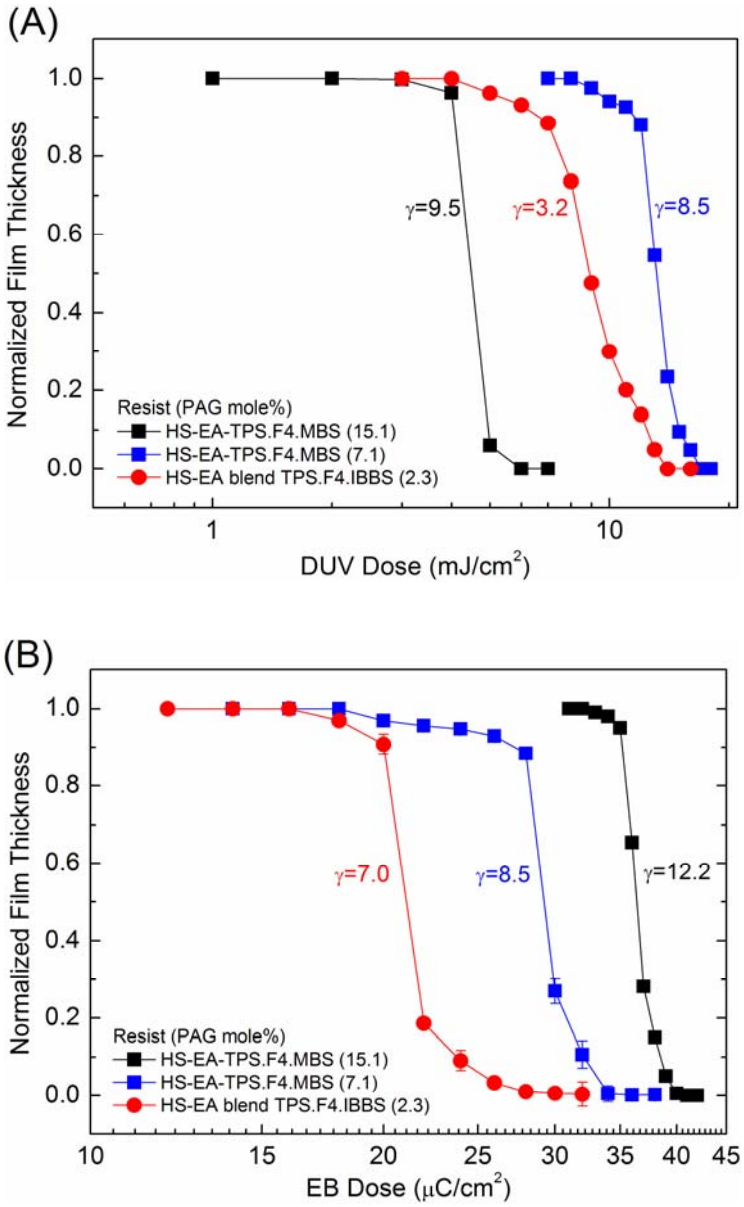

Figure 7. 13 (A) DUV and (B) 100 keV EB photospeeds and resist contrast curves of HS-EA-TPS.F4.MBS and HS-EA blend TPS.F4.IBBS resists.

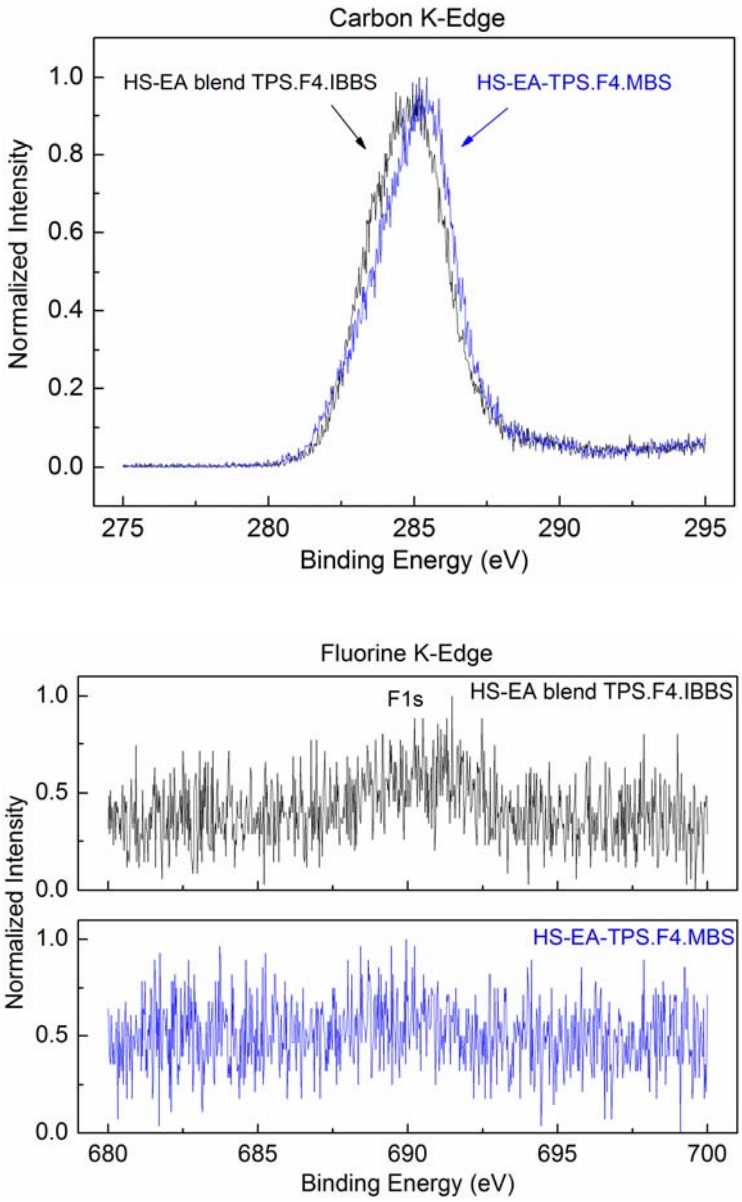

Figure 7. 14 Carbon and fluorine K-edges of XPS spectra of films of the HS-co-EA-co-TPS.F4.MBS and HS-co-EA blend TPS.F4.IBBS resist films formulated with identical PAG loadings and approximately the same carbon-to-fluorine atom ratio**.**

The extremely-high aerial image quality delivered by the patterning technique developed in chapter 6 further serves as the high-sensitivity tool in probing the response of the resist material when subject to exposure dose and focal position variations. Semi-

dense line features (100 nm 2:1 L/S) with different exposure doses (70~160 μC/cm^2) and focal position offsets (0~150 μm) are delivered by a JEOL JBX-9300FS EBL system with a 100 kV acceleration voltage to provide aerial images with gradually degraded quality. These aerial images provided subtle exposure dose and NILS variations at the image edge that can be used to probe the response of resist CD and LER to aerial image quality. The dependence of resist CD on exposure dose at the in-focus position is termed as the *exposure latitude* of the resist. Resist exposure latitude is defined as the range of the exposure dose within it the resist CD error is acceptable. The exposure latitudes of both EUV resists under EBL are illustrated in figure 7.15. By taking +/- 2.5% CD as the maximum allowable CD error, HS-EA-TPS.F4.MBS resist shows 2.5 fold larger exposure latitude (100~150 μC/cm^2) than HS-EA blend TPS.F4.IBBS resist (90~110 μC/cm^2). The difference between the aerial and resist image CDs has been defined as the intrinsic CD bias of the resist material.[17] Larger intrinsic bias indicates larger image blur which is in principle due to significant acid diffusion during PEB. HS-EA-TPS.F4.MBS resist structurally fixes the acid diffusion problem by binding the PAG anion to the polymer main chain that can provide smaller intrinsic resist CD bias and superior capability to maintain resist CD when subject to exposure dose variation. On the contrary, each acid molecule in HS-EA blend TPS.F4.IBBS resist creates larger deprotection volume due to its higher acid diffusivity. The variation of small amount exposure dose at the pattern edge caused by over- or under-dose exposure may results in small amount acids variation however large deprotection volume change. This phenomenon may cause HS-EA blend TPS.F4.IBBS resist to have worse CD control than HS-EA-TPS.F4.MBS resist.

The responses of resist CD and LER on exposure focal position offset is termed as the *focal latitude* of a resist material. Resist forcal latitude is defined as the focal position range where the resist CD error is within the acceptable range. The focal latitudes of both resists are illustrated in figure 7.16. Apparently HS-EA-TPS.F4.MBS resist shows more

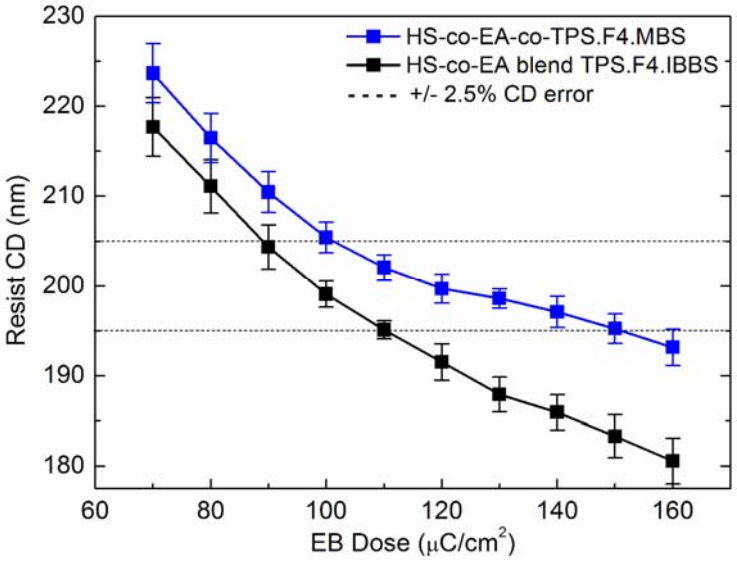

Figure 7. 15 Exposure latitudes of HS-EA-TPS.F4.MBS and HS-EA blend TPS.F4.IBBS resist at in-focus position.

robustness of CD and LER control when subject to EB focal position offset. From 0 to 150 μm EB focal position offset, HS-EA-TPS.F4.MBS resist shows 7.3% decrease in CD and 1.7 nm increase in 3σLER that are significantly superior than HS-EA blend TPS.F4.IBBS resist (19.1% decrease in CD, 2.9 nm increase in 3σLER). HS-EA-TPS.F4.MBS resist also shows statistically stable CD and LER behavior as indicated by the small error bar in figure 7.16. When larger focal position offset distance is applied, the steepness of NILS of the aerial image is expected to drop down and create a broader dose transition region between zero-dose and dose-to-clear. A gradient acid concentration is expected to be generated in this region and may create gradient deprotection front at the resist line edge during PEB and result in resist CD error and LER increase. Since HS-EA-TPS.F4.MBS resist has smaller deprotection volume created by each acid molecule due to confined acid diffusivity, the deprotection volumes created by acids generated in the dose transition region may have less probability to overlap with those generated in

nominal dose region. The non-overlapped deprotection volumes may not transfer to the resist profile after development and hence show higher robustness to the degradation of the aerial image quality. This hypothesis is theoretically confirmed by modeling resist lithography behavior demonstrated in chapter 8.

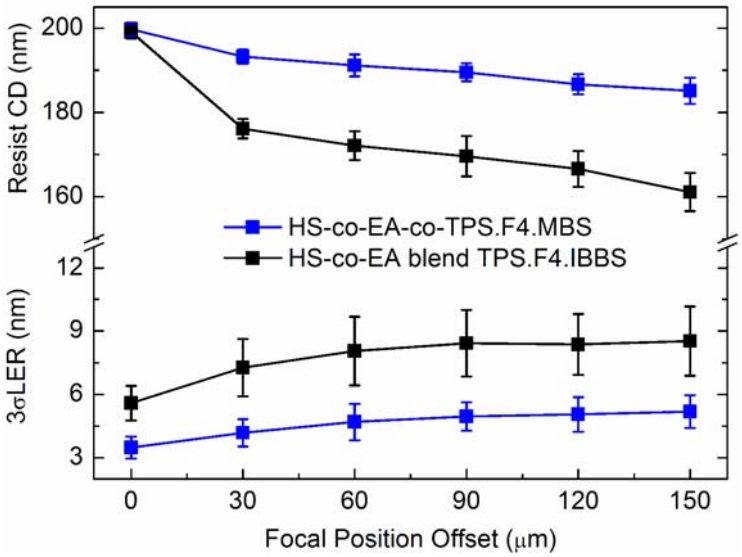

Figure 7. 16 Focal latitudes of HS-EA-TPS.F4.MBS and HS-EA blend TPS.F4.IBBS resists at dose-to-size.

SEM images of both resists under different focal position offsets are shown in figure 7.17. In addition to the poorer CD and LER robustness to focal position offsets, HS-EA blend TPS.F4.IBBS resist even shows randomly distributed 20~60 nm protrusions which were not observed in HS-EA-TPS.F4.MBS resist. Such protrusions are believed due to the presence of polymer or PAG aggregates that result in non-uniform polymer deprotection remaining at the line edge after development. Traditional blended-PAG resists show inevitable trade-off between achieving resolution and LER, (i.e. higher acid diffusivity may smooth resist line edge but loss CD control, and vice versa). In this chapter the concept of designing a single-component resist material which contains full

resist functionality that can eventually improve resolution and LER simultaneously is experimentally demonstrated. Polymer-bound-PAG resists also possess robustness to the variation of lithography conditions and provide larger resist process window that can reduce the cost associated with lithography condition maintenance and process control.

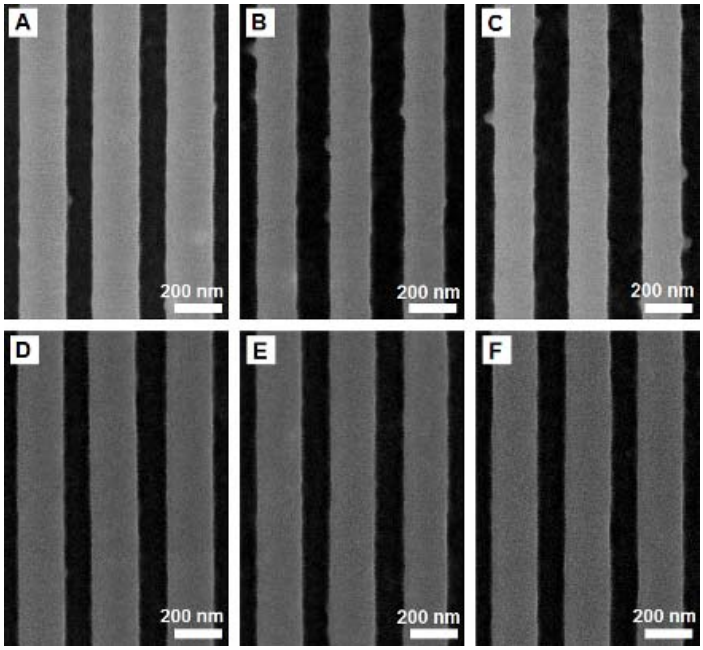

Figure 7. 17 SEM images of 100 nm 2:1 L/S features with different focal position offset of EBL: (A) 0.0 μm, (B) 60.0 μm, (C) 120.0 μm offset distance of HS-EA-TPS.F4.MBS resist, and (d) 0.0 μm, (e) 60.0 μm, (f) 120.0 μm offset distance of HS-EA blend TPS.F4.IBBS resist.

7.4 Conclusions

In conclusion, the effects of direct PAG incorporation into the polymer main chain on lithographic performance and behavior of CARs have been studied in this work. The first generation polymer-bound-PAG resists, which have the PAG cation binding to the polymer main chain, have no acid diffusion control mechanism and shows significant

resist image blur under standard resist processing. The second generation polymer-bound-PAG resists, which have the PAG anion binding to the polymer, exhibit significantly improved half-pitch resolution, lower LER, higher photosensitivity, and higher resist contrast than their blended-PAG analogs. XPS analysis of the composition of resist film surface suggests that binding PAG anion to the polymer main chain eliminates PAG aggregation at the resist film surface. Based on these experimental results, the improved lithographic performance of the anionic polymer-bound-PAG resist is believed to be a combination of high PAG loadings, reduced acid diffusivity, and reduction of heterogeneous distribution of PAG molecules in the resist film. These results suggest that a single-component resist material design, of which the PAG functionality is covalently-incorporated into the resist resin, can relieve the perceived limitations and tradeoffs between achieving resolution, LER, and photospeed in traditional multi-component blended-PAG CARs. Using this new material design paradigm, it is possible to develop resist material solutions that none of the three critical characteristics (i.e. sensitivity, resolution, and LER) has to be sacrificed to achieve acceptable performance in other characteristics. In a more general sense, this work also provides the prove of concept that the basic design concept of using single-component resists, either polymer or molecule glass, is a very promising route to develop advanced resist materials with lithographic performance sufficient for NGL applications.

7.5 References

[1] Wu, H.; Gonsalves, K. E., Preparation of a photoacid generating monomer and its application in lithography, *Adv. Funct. Mater.* **2001**, *11*, 271-276.

[2] Wu, H.; Gonsalves, K. E., Novel positive-tone chemically amplified resists with photoacid generator in the polymer chains, *Adv. Mater.*, **2001**, *13*, 670-672.

[3] Thiyagarajan, M.; Dean, K.; Gonsalves, K. E., Improved lithographic performance for EUV resists based on polymers having a photoacid generator (PAG) in the backbone, *J. Photopolymer Sci. Technol.,* **2005**, *18*, 737-741.

[4] Jarnagin, N. D.; Gonsalves, K. E.; Wang, M. X.; Roberts, J. M.; Yeuh, W., Resists for sub-100 nm patterning at 193 nm exposure, *Proc. SPIE* **2006**, *6153*, 61534P.

[5] Wang, M.; Jarnagin, N. D.; Lee, C.-T.; Henderson, C. L.; Wang, Y.; Roberts, J. M.; Gonsalves, K. E., Novel polymeric anionic photoacid generators (PAGs) and corresponding polymers for 193 nm lithography, *J. Mater. Chem.,* **2006**, *16*, 3701-3707.

[6] Wang, M.; Gonsalves, K. E.; Yueh, W.; Roberts, J. M., Novel anionic photoacid generators (PAGs) and corresponding PAG bound polymers, *Macromolecular Rapid Communication*, **2007**, *27*, 1590-1595.

[7] Lee, C. –T.; Jarnagin, N. D.; Wang, M.; Gonsalves, K. E.; Roberts, J. M.; Yueh, W.; Henderson, C. L., Fundamental studies of the properties of photoresists based on resins containing polymer-bound photoacid generators, *Proc. SPIE* **2006**, *6153*, 61532E.

[8] Jablonski, E. L.; Prabhu, V. M.; Sambasivan, S.; Lin, E. K.; Fischer, D. A.; Goldfarb, D. L.; Angelopoulos, M.; Ito, H., Near edge x-ray absorption fine structure measurements of surface segregation in 157 nm photoresist blends, *J. Vac. Sci. Technol. B,* **2003**, *21*, 3162-3165.

[9] Jablonski, E. L.; Prabhu, V. M.; Sambasivan, S.; Fischer, D. A.; Lin, E. K.; Goldfarb, D. L.; Angelopoulos, M.; Ito, H., Surface and bulk chemistry of chemically amplified photoresists: segregation in thin films and environmental stability issues, *Proc. SPIE*, **2004**, *5376*, 302-311.

[10] Karim, A.; Slawecki, T. M.; Kumar, S. K.; Douglas, J. F.; Satija, S. K.; Han, C. C.; Russell, T. P.; Liu, Y.; Overney, R.; Sokolov, J.; Rafailovich, M. H., Phase-separation-induced surface patterns in thin polymer blend films, *Macromolecules* **1998**, *31*, 857-862.

[11] Lin, Q.; Sooriyakumaran, R.; Huang, W.-S., Toward controlled resist line-edge roughness: material origin of line-edge roughness in chemically amplified positive-tone resists, *Proc. SPIE*, **2000**, *3999*, 230-239.

[12] Yamaguchi, T.; Namatsu, H.; Nagase, M.; Yamazaki, K.; Kurihara, K., Nanometer-scale linewidth fluctuations caused by polymer aggregates in resist films, *Appl. Phys. Lett.*, **1997**, *71*, 2388-2390.

[13] Lenhart, J. L.; Jones, R. L.; Lin, E. K.; Soles, C. L.; Wu, W.; Fischer, D. A.; Sambasivan, S.; Goldfarb, D. L.; Angelopoulos, M., Probing surface and bulk chemistry in resist films using near edge x-ray absorption fine structure, *J. Vac. Sci. Technol. B*, **2002**, *20*, 2920-2926.

[14] Cao, H. B.; Yueh, W.; Rice, B. J.; Roberts, J. M.; Bacuita, T.; Chandhok, M., Sources of line-width roughness for EUV resists, *Proc. SPIE*, **2004**, *5376*, 757-764.

[15] Broers, A. N.; Harper, J. M. E.; Molzen, W. W., 250-Å linewidths with PMMA electron resist, *Appl. Phys. Lett.*, **1978**, *33*, 392-394.

[16] Nishida, T.; Notomi, M.; Iga, R.; Tamamura, T., Quantum wire fabrication by e-beam elithography using high-resolution and high-sensitivity e-beam resist ZEP-520, *Jpn. J. Appl. Phys. Part 1*, **1992**, *31*, 4508-4514.

[17] Pawloski, A. R.; Acheta, A.; Levinson, H. J.; Michaelson, T. B.; Jamieson, A.; Nishimura, Y.; Willson, G. C., Line edge roughness and intrinsic bias for two methacrylate polymer resist systems, *J. Microlithography Microfabrication Microsystems*, **2006**, *5*, 23001-1-23001-16.

CHAPTER 8

EFFECTS OF PAG LOADING AND ACID DIFFUSIVITY ON LITHOGRAPHIC PERFORMANCE OF POLYMER-BOUND-PAG RESISTS[†]

Resist CD control and LER/LWR reduction has been the most challenging issues for sub-50 nm resolution patterning in semiconductor industry. Among those factors dominating CD and LER, acid distribution homogeneity and diffusivity are major elements associated with resist material design and have direct impacts on the lithographic performance of the resist material. In chapter 7, the development and characterization of novel polymer-bound-PAG resists show that polymer-bound-PAG resists which have the PAG anion binding to the polymer main chain exhibit high photosensitivity, improved CD control, and reduced LER. Polymer-bound-PAG resists have high PAG loading and low acid diffusivity that may contribute to their advanced lithographic performance. In this chapter, a two-dimensional mesoscale stochastic modeling of resist lithography process, derived from the full acid reaction-diffusion model developed in chapter 5 for studying acid diffusivity in a resist film, is applied to investigate the joint effect of PAG loading and acid diffusivity on resist lithographic performance. Effects of PAG loading and acid diffusivity on resist CD and LER behavior are studied. Correlations and scaling factors between fundamental resist properties and the observed resist CD and LER performance are also analyzed and reported. Simulation results suggest high PAG loading and low acid diffusivity of the polymer-bound-PAG resist system can provide superior lithographic performance than the traditional blended-

---

[†] Material presented in this chapter has appeared in part in a previously published article:

Lee, C. –T.; Lawson, R. A.; Henderson, C. L., Understanding the effects of photoacid distribution homogeneity and diffusivity on critical dimension control and line edge roughness of chemically amplified resist, *J Vac. Sci. Technol. B* **2008**, accepted.

PAG CAR system that is in well agreement with the experimental characterization results reported in chapter 7. The modeling results also suggest that resist image blur can be well scaled by the square root of the product of acid number generated at the line edge and its diffusion coefficient. LER can be well scaled by the standard deviation of the deprotection level and the reciprocal of the deprotection gradient of the resist film alone the pattern line edge.

8.1 Introduction

The advance of microlithography technology has realized the fabrication of modern IC device with dramatically increasing density and efficiency in semiconductor industry for more than four decades. While pushing to sub-50 nm technology nodes with NGL technologies such as the state-of-art 193 nm immersion/double patterning and EUVL techniques, successful implementations of these technologies still require resist materials capable of translating their aerial images into a satisfactory physical relief image in the underlying thin films and substrates for fabrication.

While attempting to further extend the use of CARs for sub-50 nm patterning with satisfactory lithographic performance (i.e. high resolution and precise CD control, fast photospeed, and low LER), the blending nature of the traditional CAR platform has placed the tri-lateral tradeoff between achieving these requirements.[1,2] The low PAG loading capability leads to the requirement of high acid diffusivity (i.e. long acid catalytic chain length) in order to achieve fast photospeed, however high acid diffusivity causes resist image blur and the loss of resist CD control that decrease the achievable resolution and increase LER. A polymer-bound-PAG resist system has been developed and experimentally demonstrated improving lithographic performance by directly binding the PAG anion into the polymer main chain as reported in chapter 7. This resist platform

allows the control of acid diffusivity to reduce image blur while maintaining the photospeed via improving PAG loading capability and thus acid generation. The polymer-bound-PAG resists also demonstrate larger resist process window (i.e. exposure and focal latitudes) than their blended-PAG analogs. Although polymer-bound-PAG resists have experimentally demonstrated superior lithographic performance than traditional blended-PAG resists, the joint effect of high PAG loading and low acid diffusivity on the advance of lithographic performance is still unknown. The correlations between fundamental properties of polymer-bound-PAG resists and their lithographic behavior are not well addressed yet.

8.2 Resist Lithography Model Description

8.2.1 Mesoscale Resist Model

In this chapter, a modeling work has been developed to investigate the correlation between resist properties and the lithographic performance. A mesoscale stochastic modeling, derived from the mesoscale stochastic acid reaction-diffusion model developed in chapter 5, is applied to simulate resist lithography process, including exposure, PEB and development processes, of a resist film. The resist model is built by a two-dimensional (2D) lattice containing 28,000 square cells (140×200) with the same size to represent the top-down view of the resist film simulated. The edge length l of each cell is set as 1.0 nm that represents the approximate volume occupied by a polymer subunit or an acid molecule in a typical resist film. For an example resist film containing fully *tert*-butoxycarbonyl (t-BOC) protected poly(p-hydroxystyrene) (pHOST) resin (pTBOCST) and 4-(methacryloxy) 2.3.5.6-tetrafluorobenzenesulfonate (F4.MBS acid), the structure of the 2D lattice model is shown in figure 8.1.

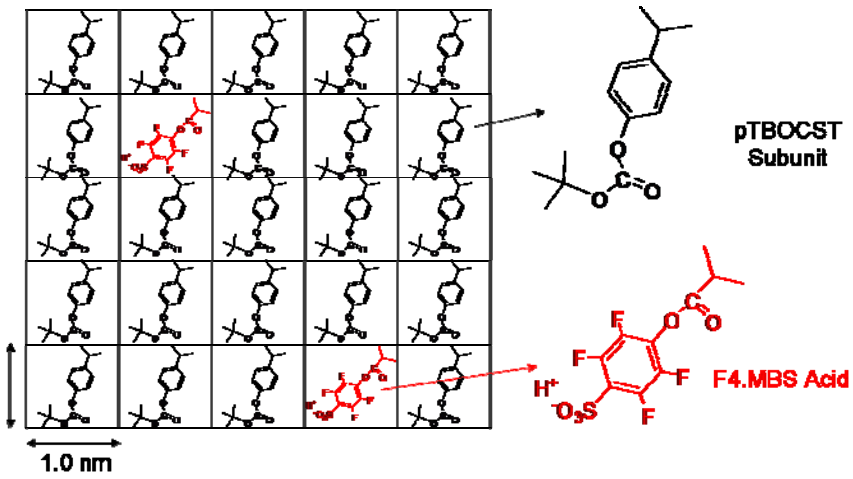

Figure 8. 1 A standard 2D mesoscale lattice model representing a resist film containing pTBOCST resin and F4.MBS acids.

8.2.2 Aerial Image and Initial Acid Distribution Profile

In the beginning of a resist lithography simulation, an aerial image intensity profile $I(x,y)$ representing a 70 nm wide line feature delivered by a exposure optics is generated according to a sigmoid function described in equation (8.1).

$$I(x,y) = \frac{1}{1+e^{-\alpha(x-x_L)}} - \frac{1}{1+e^{-\alpha(x-x_R)}} \tag{8.1}$$

Here α is the threshold likelihood of the intensity profile, and x_L and x_R are the left and right edges of the line image, respectively. For a given α and a nominal CD (CD_{Nom}=x_R-x_L) representing the line width of the aerial image, the aerial image contrast can be quantified by calculating the NILS using equation (8.2).

$$NILS = CD_{Nom}\frac{1}{I(x,y)}\frac{dI(x,y)}{dx} = \frac{CD_{Nom}\alpha}{2} \tag{8.2}$$

Aerial image profile with different NILS is generated and used to represent the possible aerial image quality delivered by exposure equipments. In the exposure part of the modeling work, the focus is placed on the effect of the lateral variation of the dose transition regions located at the edges of the aerial image on the response of PAG acid generation, resist deprotection, and the resultant CD and LER performance. Exposure dose and NILS variations are applied to mimic two major factors, exposure dose and focal offset, affecting the properties of the dose transition region at the aerial image line edges. Exposure doses variations (10 ~ 70 mJ/cm^2) and NILS variations (3.5 ~ 35) are applied to this study and the exposure dose and aerial image intensity profiles across *x*-axis are shown in figure 8.2.

The probability of finding a PAG in a cell of the 2D lattice resist model can be assumed as the Poisson distribution and can be represented by the average initial PAG loading (P_{PAG}, mol%) of the resist. The probability of converting a PAG into an acid under a value of exposure dose can also be assumed as the Poisson distribution and determined by an average first-order photodecomposition kinetics.[3] For a given acid generation rate constant C, an aerial image intensity profile $I(x,y)$, and an exposure time t, the joint probability, $P_{Acid}(x,y)$, of generating an acid at the cell position (x,y) is determined by equation (8.3).

$$P_{Acid}(x,y) = P_{PAG}\left(1 - e^{-CI(x,y)t}\right) \tag{8.3}$$

For the initiation of each modeling work, acid molecules are first assigned to the cells of the 2D lattice according to equations (8.1), (8.3), and the resist formulation. The remaining empty cells are then filled with ptotected polymer subunits to complete the initial acid distribution profile.

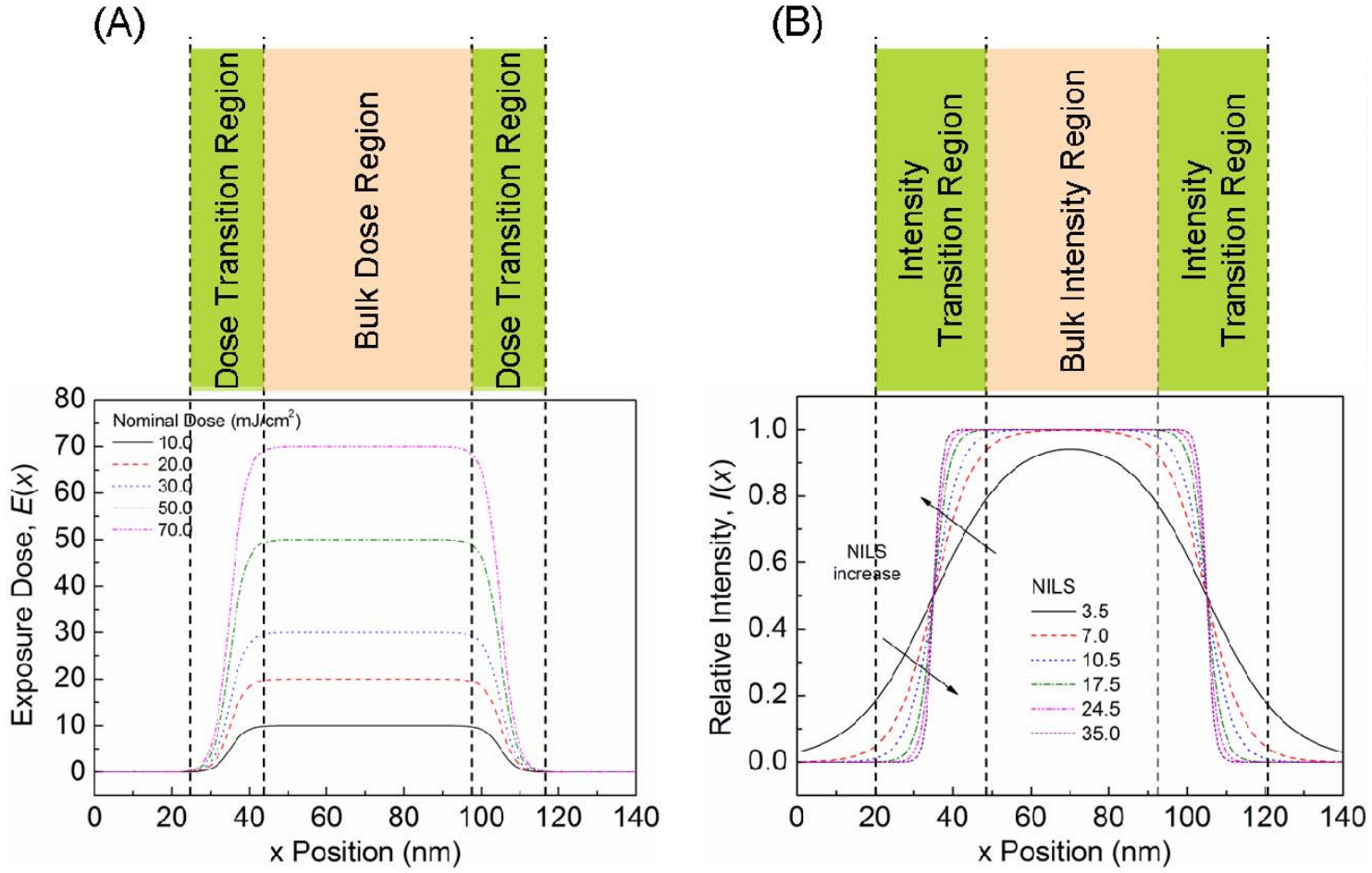

Figure 8. 2 Illustrations of (A) exposure dose and (B) aerial image intensity profile variations, as well as the bulk and transition regions of the aerial image profile used in the modeling work for resist CD and LER behavior study.

8.2.3 Acid Diffusion and Resist Deprotection

A Monte Carlo stochastic process derived from the full acid reaction-diffusion model developed in chapter 5 is applied to describe the random walk nature of acid diffusion behavior in the resist film during PEB. First of all, a diffusion-limited assumption is applied to describe the reaction-diffusion process during PEB since the time scale of acid diffusion is significantly larger than that of acid-catalyzed reaction in typical CAR formulations.[4] The deprotection reaction occurs immediately when an acid molecule moves to a protected cell. Since the focus of this work is to investigate the joint effect of PAG loading and acid diffusivity on resist lithographic performance, a single acid diffusion coefficient in the resist film is assumed to simplify modeling complexity. Under these model conditions, acid reaction-diffusion modeling in this work can prevent the use of the exact stochastic simulation algorithm applied in chapter 5 since there is one single acid diffusion rate constant exists in the model. The acid diffusion modeling process can be simplified by making a random hop of all acid molecules simultaneously as the simulation time proceed. Giving an effective diffusion coefficient D_{eff} to represent the diffusivity of acid molecules in the resist film, the required step time τ for every acid molecule to jump from one cell to another adjacent cell can be derived from equation (5.8) and described by equation (8.4).

$$D_{eff} = \frac{l^2}{2d\tau} \tag{8.4}$$

Here d is the dimensionality of the lattice. In this work acids are allowed to randomly move from its original cell to an adjacent cell in a 2D lattice. Diagonal moves are not allowed for simplification purpose. A periodic boundary condition is applied to the lattice model to represent a dense line pattern simulation. In principle a larger D_{eff} gives a

smaller τ for every acid molecule to move one cell distance. An acid with higher diffusivity can make more moves within a certain PEB time and results in a larger diffusion length. For every set of initial acid distribution profile, the acid reaction-diffusion modeling is repeated for 100 times and an average deprotection probability $P(x,y)$ of each cell after PEB is calculated.

8.2.4 Resist Development

On the length scale relevant to LER interested in this work (i.e. several tens nanometers, low-spatial frequency), a simple infinite contrast development model is sufficient to give good prediction of resist profile after development. A polymer subunit is removed if its protection probability $P(x,y)$ is lower than a threshold value of 0.5. Remaining resist blocks which are not connected to bulk remaining resist regions (i.e. the unexposed regions) are removed as well. After the final resist profile is obtained, the resist line edge position, and thus the space CD and the low-spatial frequency LER can be determined. Standard outputs of the modeling work, including acid initial distribution profile, resist deprotection profile, and the final resist development profile, are shown in figure 8.3.

8.3 Results and Discussion

8.3.1 Exposure Dose and NILS Effects

In the material part of this modeling work, the focus is to study the fundamental contributions to the improved lithographic performance of the polymer-bound-PAG resists and compare with the experimental results reported in chapter 7. Two resist

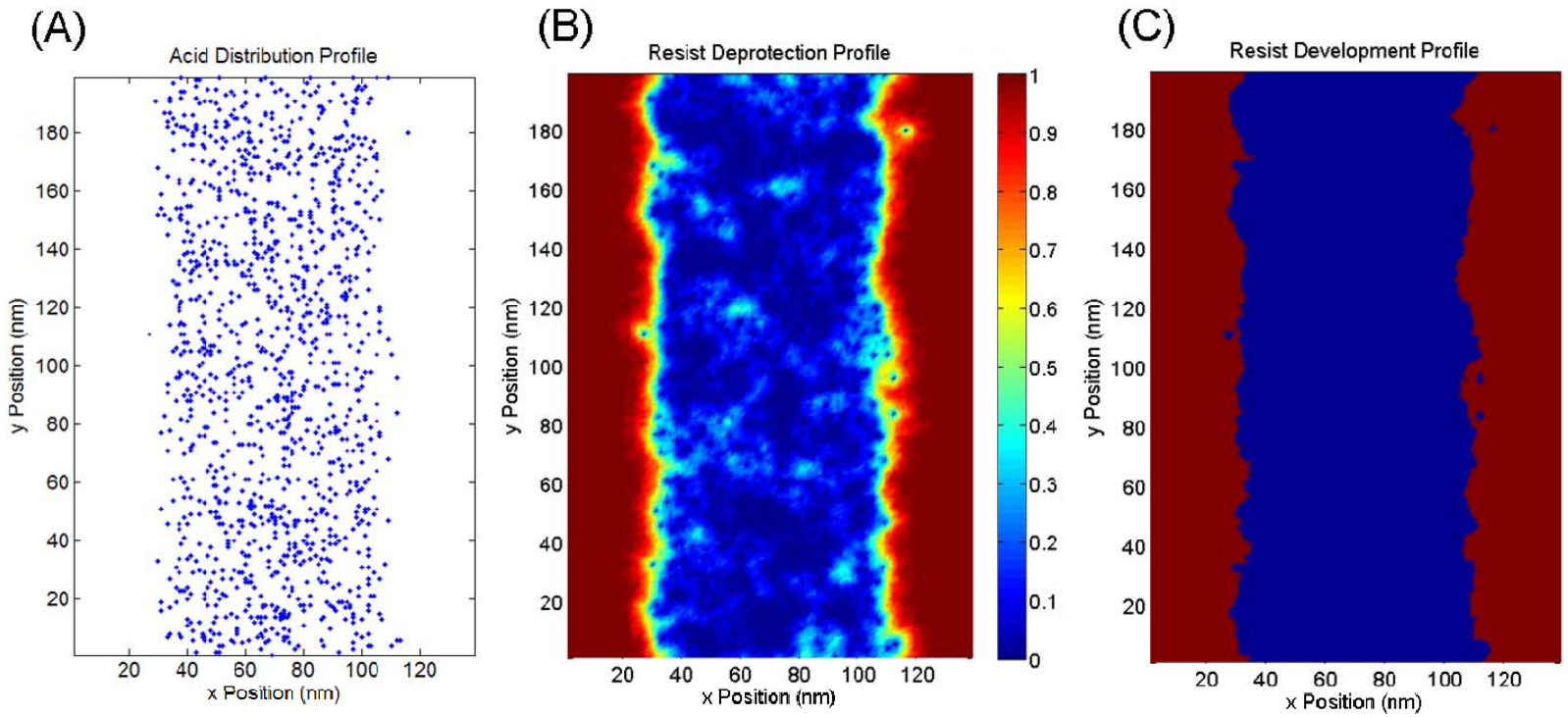

Figure 8. 3 Standard outputs of mesoscale stochastic resist lithography modeling: (A) acid initial distribution profile after exposure, (B) resist deprotection profile after PEB, and (C) resist profile after development.

models are built to represent the anionic polymer-bound-PAG and the traditional blended-PAG resists. The *bound-PAG* resist has high PAG loading (10.0 mol%) and low acid diffusivity (0.07 nm^2/sec), while the *blended-PAG* resist has low PAG loading (2.0 mol%) and high acid diffusivity (0.5 nm^2/sec). These two resist models are designed to have the same sizing dose (CD_{Nom}=70 nm at 17 mJ/cm^2) under the same *NILS* (=17.5) to represent two resists with equal photosensitivity. The PAG loadings are chosen according to general PAG loadings formulated in polymer-bound-PAG and blended-PAG resists. The acid diffusivities are chosen according to the range of acid diffusivity in resist films reported thus far. Resist deprotection and development profiles of both resist models near the resist line edge are shown in figure 8.4. The bound-PAG resist model shows higher deprotection contrast along the resist line edge, as well as less LER.

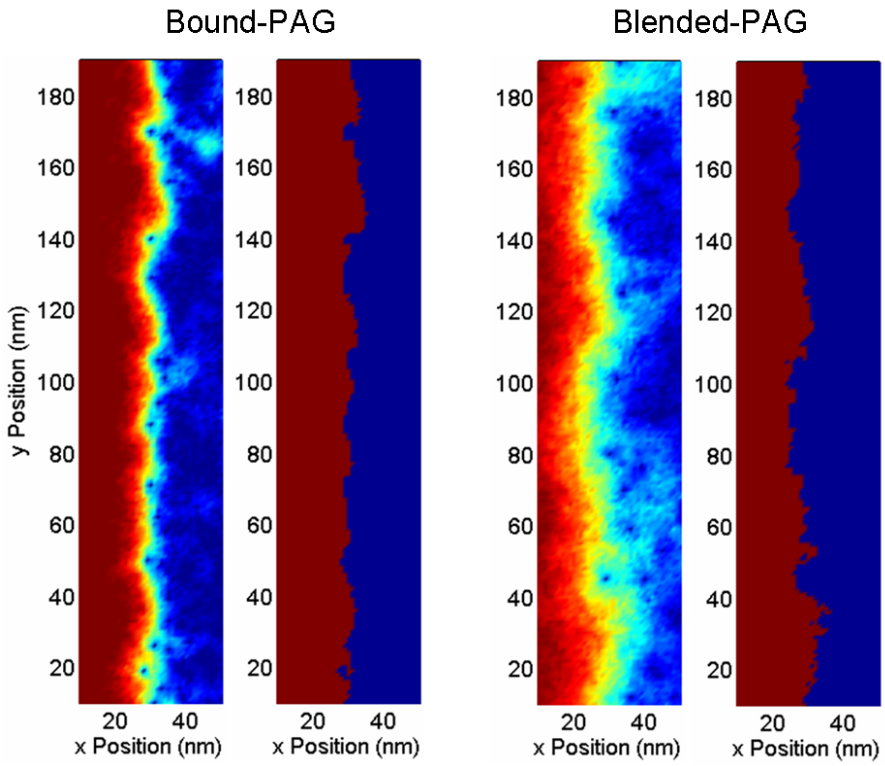

Figure 8. 4 Modeling results of resist deprotection and development profiles of bound-PAG and blended-PAG resist models.

The dependence of resist CD control, CD fluctuation, and LER on exposure dose and NILS variations are investigated and compared to experimental results in chapter 7. As shown in figure 8.5, under the same NILS both resists show space CD increase and LER decrease towards saturation as exposure dose increase. However the bound-PAG resist shows less increase and fluctuation of space CD and LER than the blended-PAG resist. By taking +/- 10% of CD_{Nom} as the maximum allowable CD error and calculating the exposure latitudes, the bound-PAG resist shows more than 2-fold larger exposure latitude (112%) than the blended-PAG resist (47%). The bound-PAG resist also shows at least 50% improvement of LER of the blended-PAG resist within the exposure dose range analyzed.

The effect of NILS on resist space CD and LER of both resist models under the same exposure dose (30 mJ/cm^2) are shown in figure 8.6. Both resist models show the increase of space CD and LER upon NILS decrease, however the bound-PAG resist maintains lower CD error and smaller LER, as well as less fluctuation than the blended-PAG resist. From the maximum to the minimum NILS values tested in this work, the bound-PAG resist shows less space CD increase (18.9%) than the blended-PAG resist (20.7%). The bound-PAG resist also shows less 3σLER increase (16.3 nm) than the blended-PAG resist (19.4 nm). The trends of simulating exposure and focal latitudes of the bound-PAG and blended-PAG models lead to the same conclusions as the experimental characterization results of polymer-bound-PAG and the blended-PAG analogs in chapter 7.

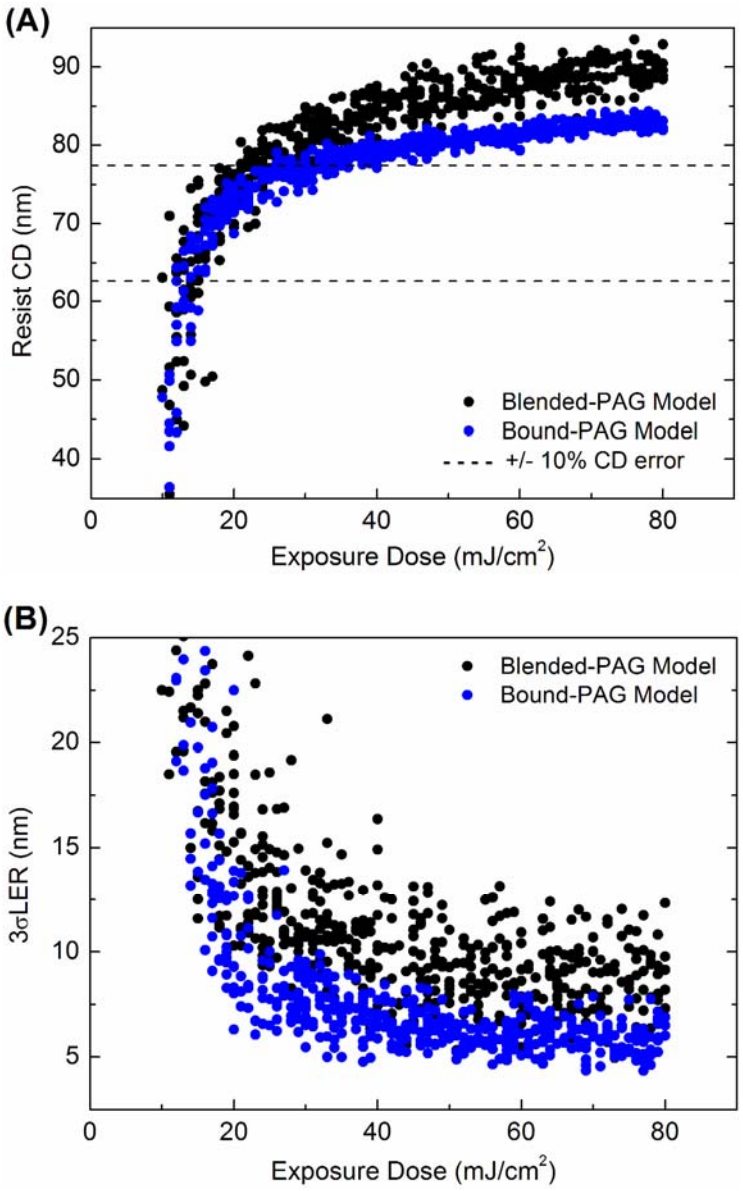

Figure 8. 5 Effect of exposure dose on (A) space CD and (B) LER of both resist models under the same NILS (17.5).

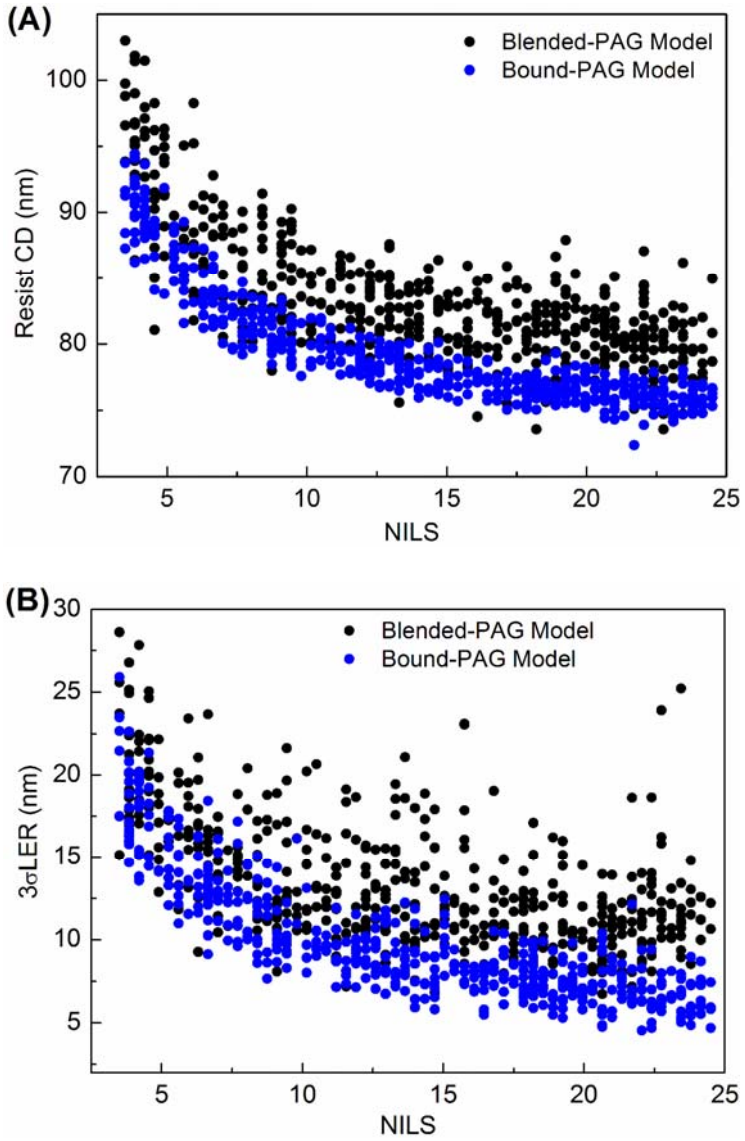

Figure 8. 6 Effect of NILS on (A) space CD and (B) LER of both resist models under the same exposure dose (30 mJ/cm^2).

8.3.2 Scaling Factors for Resist CD Bias and LER

Resist CD bias (i.e. the difference between final resist CD and CD_{Nom}) has been correlated to exposure dose and acid diffusivity during PEB.[2,4,5] By calculating resist CD bias and the corresponding root mean square of the product of the number of acid

molecules generated beyond the aerial image line edge position ($n_{Acid,edge}$, toward the unexposed region) and acid diffusivity, the correlations between these two factors of two resist models under different exposure doses are plotted in figure 8.7.

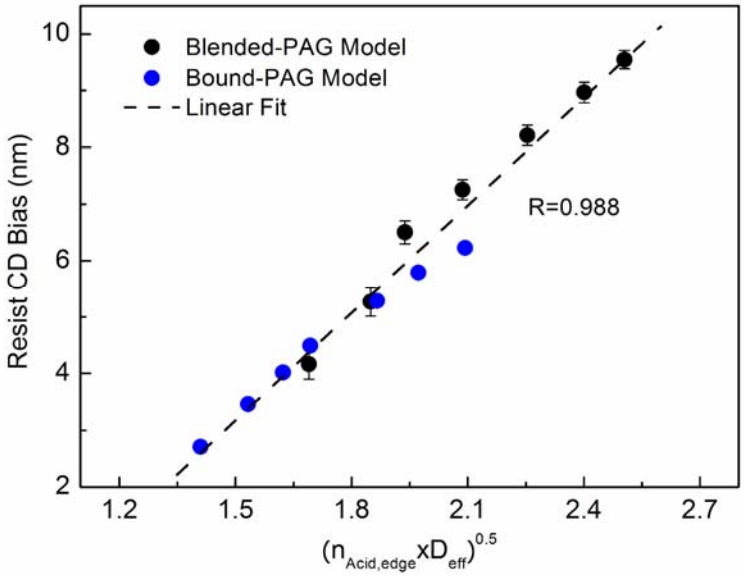

Figure 8. 7 The correlation between resist CD bias and the square root of the number of acid molecules at the aerial image line edge times their diffusivity.

A global linear relationship between these two factors is found to describe both resist models, and the observed resist CD bias can be well scaled by equation (8.5). This correlation indicates that the increased space CD upon exposure dose increase is mainly due to the coupling effect of the increase of acid molecules generated at the aerial image line edge and their diffusivity. This coupling effect is essentially the summation of the diffusion length contributed by each acid molecule generated near the resist line edge. The small deviation from the linear fit at high exposure dose is mainly due to the overlapping between deprotection volumes created by acids at the resist line edge. Such scaling factor can be applied to the prediction of resist CD bias once the PAG acid

generation rate and acid diffusion coefficient of the resist are known. In principle, resist CD bias can be reduced if the diffusivity of the acid in the resist film can be reduced and controlled.

$$\text{Resist CD Bias} \propto \sqrt{n_{Acid,edge} \times D_{eff}} \propto \sum_{edge} \text{Acid Diffusion Length} \qquad (8.5)$$

Resist CD fluctuation and LER have been theoretically and experimentally proved originating from a number of statistically fluctuating effects, such as the exposure tool, resist physicochemistry, and post-exposure processing.[2,6-8] Effects caused by the physicochemistry of resist materials are resist deprotection homogeneity and gradient (i.e. resist contrast) at the line edge after PEB. These effects are the direct consequence of initial acid distribution homogeneity and acid diffusivity in a resist film. By calculating the number of acid molecules in a pre-selected resist volumes (1×11 cells for each resist volume used in this work), a fractional uncertainty of the number of acid molecules U_{Acid} of all the investigated resist volumes can be defined as equation (8.6) and can be used to determine acid distribution homogeneity of a resist film.

$$U_{Acid} = \frac{\sigma_{Acid}}{< n_{Acid} >} = \frac{\sqrt{\frac{1}{N}\sum\left(n_{Acid,i} - \frac{1}{N}\sum n_{Acid,i} \right)^2}}{\frac{1}{N}\sum n_{Acid,i}} \qquad (8.6)$$

Here σ_{Acid} and $<n_{Acid}>$ are the standard deviation and the average number of acid molecules of all investigated resist volumes, respectively. N the total number of resist volumes analyzed. $n_{Acid,i}$ the number of acid molecules in resist volume i. In principle, a lower value of U_{Acid} indicates higher acid distribution homogeneity in the resist film, and

vice versa. For example, a value of U_{Acid} equal to 0.5 means a 50% variation of the number of acid molecules among all the resist volumes investigated. The calculation scheme of U_{Acid} from an initial acid distribution profile is illustrated in figure 8.8.

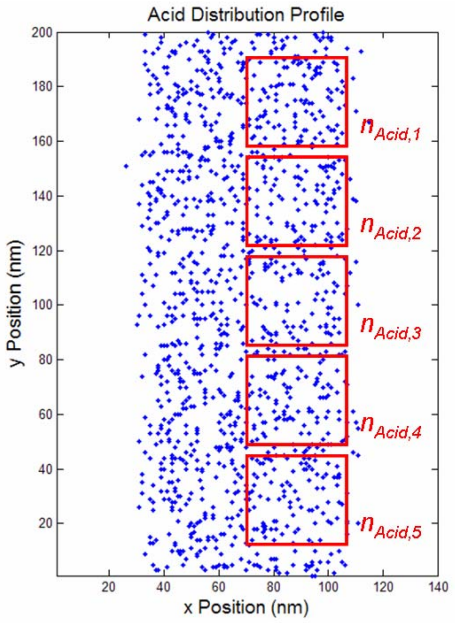

$$U_{Acid} = \frac{\sigma_{Acid}}{< n_{Acid} >} = \frac{\sqrt{\frac{1}{N}\sum (n_{Acid,i} - \frac{1}{N}\sum n_{Acid,i})^2}}{\frac{1}{N}\sum n_{Acid,i}}$$

- Low U_{Acid} → High distribution homogeneity
- U_{Acid}=0.5 means a 50% variation of the average number in a resist volume.

Figure 8. 8 Scheme of calculating acid distribution homogeneity from an initial acid distribution profile generated in the resist model.

Under the same aerial image intensity profile (NILS=17.5) as shown in figure 8.9(A), the uncertainty of the number of acid molecules of both resists along the *x*-axis under the same exposure dose (40 mJ/cm^2) is shown in figure 8.9(B). A 5-fold higher PAG loading of the bound-PAG resist model provides a 60% lower U_{Acid} at the bulk exposure region than the blended-PAG resist model. The increase of PAG loading indeed improves the PAG distribution homogeneity of the whole resist film, as well as the initial acid distribution homogeneity at the bulk exposure region of the resist film. However at the aerial image line edge where the CD fluctuation and LER actually occur, the decrease of exposure dose also causes the decrease of the number of generated acid molecules and

thus increases U_{Acid} of the bound-PAG resist model to a level comparable to that of the blended-PAG resist model. However in reality the bound-PAG resist exhibits lower LER than the blended-PAG resist. According to this analysis, it is clear that using the initial acid distribution only is not sufficient to evaluate resist CD fluctuation and LER since both resist models have high and comparable U_{Acid} at the aerial image line edge. On the other hand, the diffusion of acid molecules during PEB may enhance or smooth the acid distribution heterogeneity caused by initial acid distribution and transfer to the resist deprotection profile.

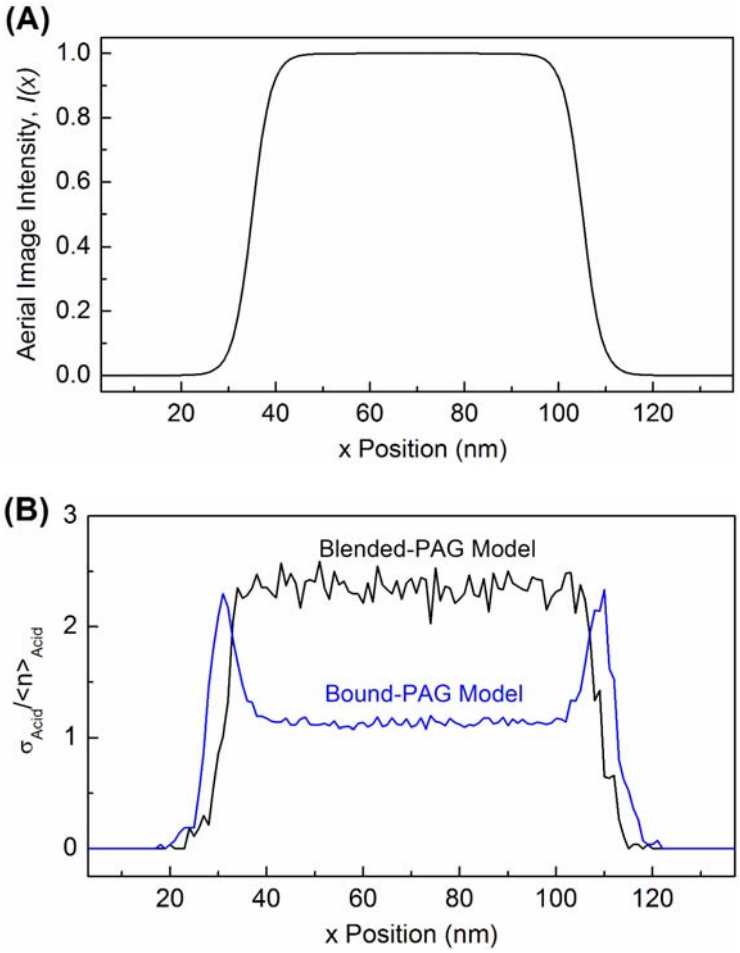

Figure 8. 9 (A) Applied aerial image intensity profile and (B) the resulting fractional uncertainty of initial acid distribution $U_{Acid}(x)$ of blended-PAG and bound-PAG resist models.

Since initial acid distribution is not a fair criterion for comparing resist CD fluctuation and LER performance between resist models, a combinatorial standard which can represent the joint effect produced by initial acid distribution and acid diffusivity is essential for a better evaluation of CD fluctuation and LER. In this case, resist deprotection profile becomes a more effective indication of predicting CD fluctuation and LER. Two parameters are calculated to evaluate the effects of resist deprotection statistics on resist lithographic performance. A standard deviation of resist deprotection probability $\sigma_P(x)$, along the y-axis, at each x position is calculated according to equation (8.7) and represents the deprotection heterogeneity of the resist model. A deprotection gradient $dP(x)/dx$, averaged from the value at each y position, for each x position is also calculated according to equation (8.8) and represents resist deprotection contrast.

$$\sigma_P(x) = \sqrt{\frac{\sum_{i=1}^{N_y} (P(x, y_i) - < P(x, y) >)^2}{N_y}} \tag{8.7}$$

$$\frac{dP(x)}{dx} = \frac{\sum_{i=1}^{N_y} \frac{dP(x, y_i)}{dx}}{N_y} \tag{8.8}$$

Here N_y is the total number of y position investigated (i.e., N_y=200 in this resist model). In principle, a smaller $\sigma_P(x)$ indicates a higher deprotection homogeneity, and a larger $dP(x)/dx$ indicates a higher resist deprotection contrast. The scheme of calculating $\sigma_P(x)$ and $dP(x)/dx$ from a simulated resist deprotection profile is illustrated in figure 8.10.

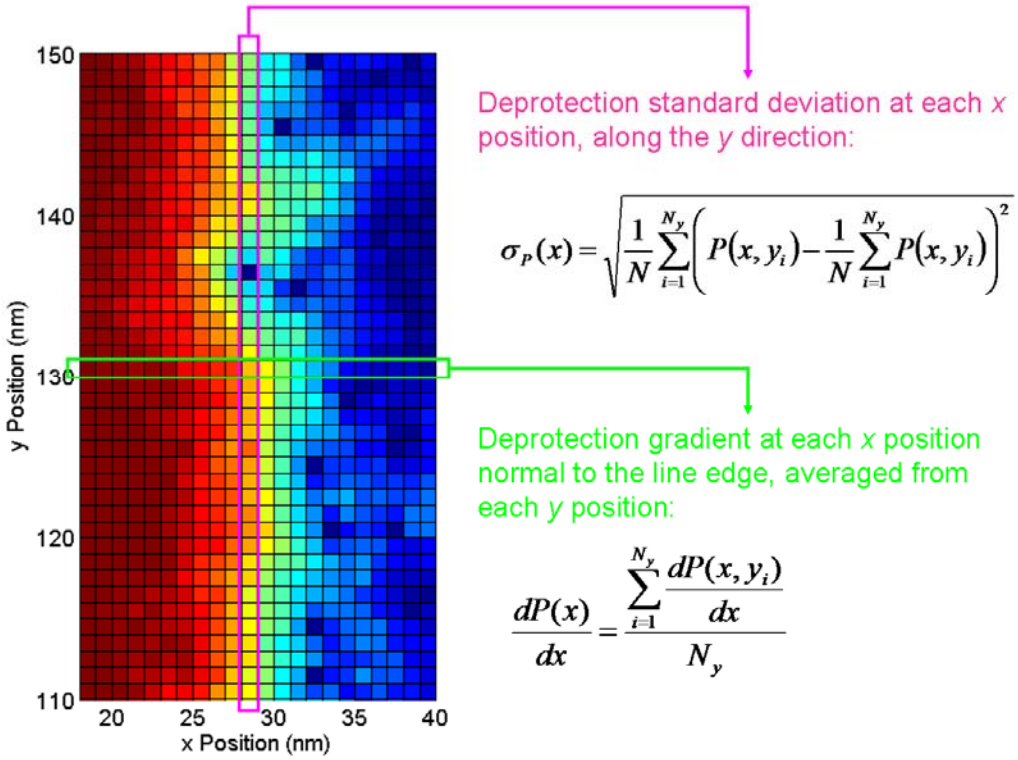

Figure 8. 10 Scheme of calculating resist deprotection statistics (i.e. standard deviation $\sigma_P(x)$ and gradient $dP(x)/dx$) from a simulated resist deprotection profile.

Figure 8.11 shows the standard deviation $\sigma_P(x)$ and the gradient $dP(x)/dx$ of the resist deprotection profile along the x-axis after PEB. At the resist line edge positions of resist models, the deprotection heterogeneity of the blended-PAG is actually lower than that of the bound-PAG resist, as shown in figure 8.11(A). The effect of the initial acid distribution heterogeneity at the line edge of the blended-PAG resist is smoothed out in the resist deprotection profile due to high acid diffusivity and leads to a lower σ_P than the bound-PAG resist. However the high acid diffusivity of the blended-PAG resist model also degrades the resist deprotection gradient at the line edge and leads to a lower resist contrast than the bound-PAG resist model, as shown in figure 8.11(B).

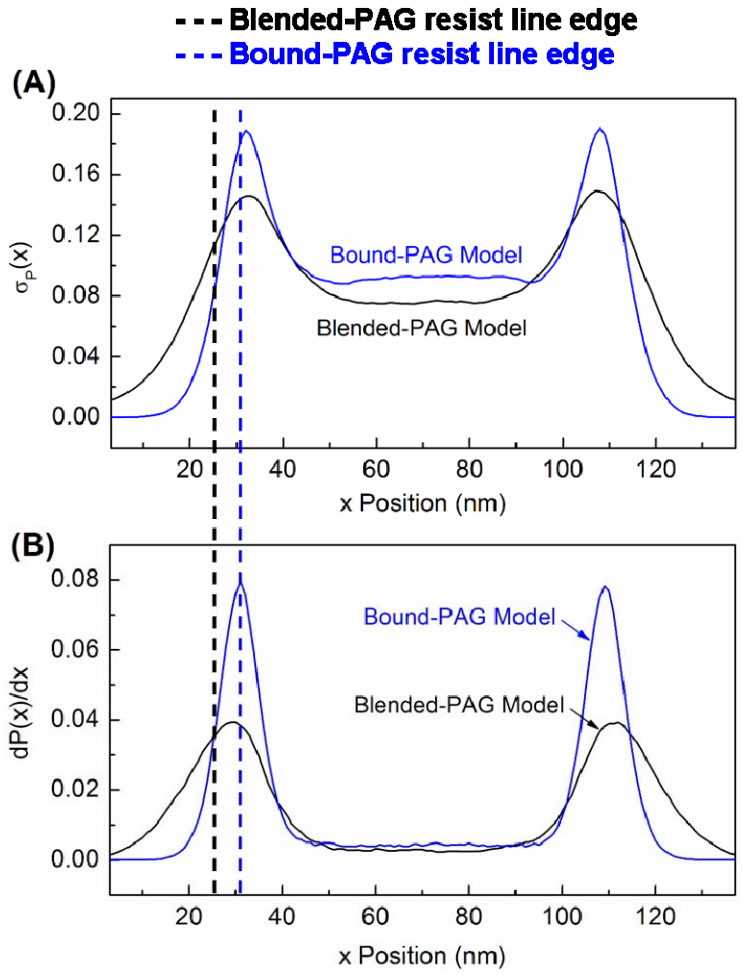

Figure 8. 11 Standard deviation of the resist deprotection profile $\sigma_P(x)$ and the resist deprotection gradient $dP(x)/dx$ of blended-PAG and bound-PAG resist models. Dash lines indicate the positions of resist line edge after development.

The next attempt is to correlate the resist deprotection statistics to the observed resist CD fluctuation and LER behavior. Resist deprotection gradient (i.e. resist contrast) has been proved experimentally having a direction impact on LER.[6] LER of traditional blended-PAG resists decrease while the resist contrast increase and reaches a minimum value around 5 nm (3σ). According to the resist deprotection statistics illustrated in figure 8.11, the first assumption is that the main effect of resist CD fluctuation and LER behavior of the two resist models studied in this work are mainly due to the change of

resist contrast. The relationship between 3σLER and the reciprocal of resist deprotection gradient at the line edge is plotted in figure 8.12. Two reasonably linear relationships are obtained for individual resist model, indicating the increase of resist contrast can decrease LER as expected. However the behavior of both resist models can not be fitted and correlated using a global scaling factor which simply includes the resist contrast effect.

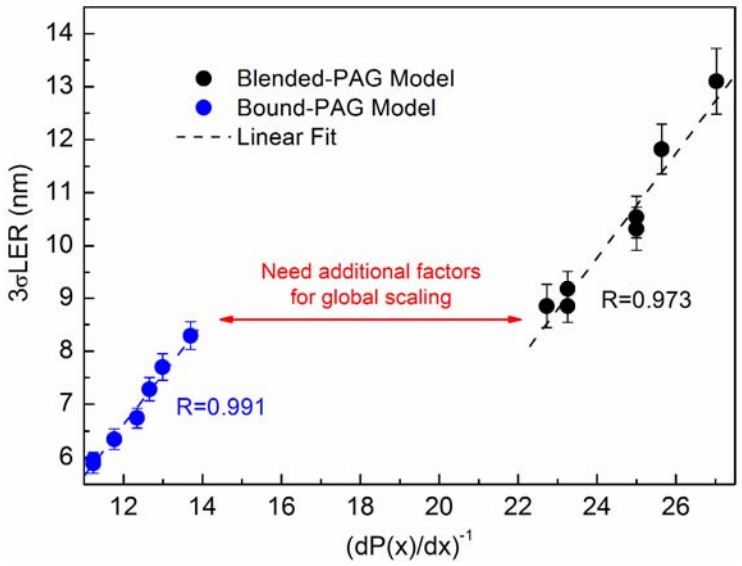

Figure 8. 12 The correlation between resist 3σLER and the reciprocal of resist deprotection gradient at the line edge.

The gap between two resist models, as shown in figure 8.12, indicates the existence of other effects that may also significantly affect the LER of a resist. Additional scaling factors are necessary for a faithful description of the cause of resist LER and the correlation between observed LER and resist material properties. The gap is probably related to the initial acid distribution homogeneity, and thus the resist deprotection homogeneity, at the resist line edge. By plotting 3σLER and the corresponding $\sigma_P/(dP(x)/dx)$ of both resist models as shown in figure 8.13, a global linear relationship is found for these two resist models with excellent correlation, and LER can be well scaled by the statistics of resist deprotection profile as indicated in equation (8.9).

$$LER \propto \frac{\sigma_P(x)}{dP(x)/dx} \propto \frac{\text{Deprotection Inhomogeneity}}{\text{Resist Contrast}} \tag{8.9}$$

This result indicates that although high PAG loading of the bound-PAG resist may have limited contribution to increasing initial acid distribution and resist deprotection homogeneity at the resist line edge, the low acid diffusivity of the bound-PAG resist can significantly increase resist deprotection gradient and thus the resist contrast that contributes to significant improvement of resist CD fluctuation and LER. In principle, reducing acid diffusion can reduce resist CD fluctuation and LER. Improving initial acid distribution homogeneity may further improve resist CD fluctuation and LER by reducing the initial acid distribution and resist deprotection heterogeneity at the resist line edge.

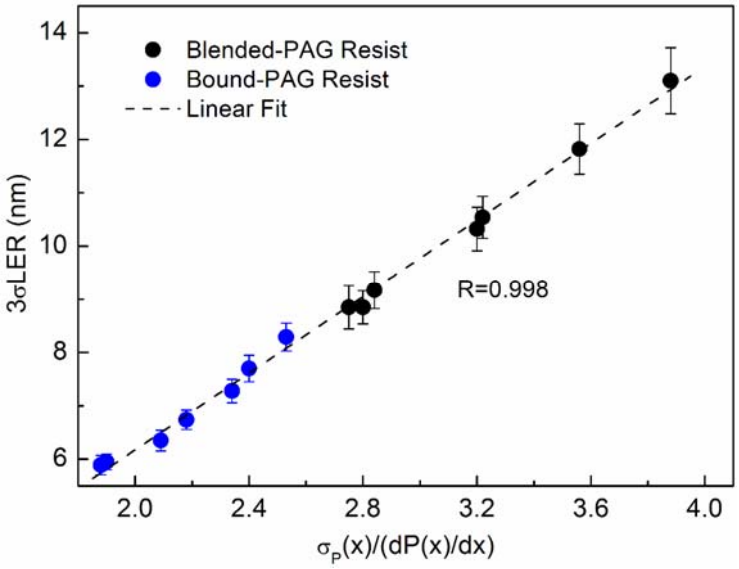

Figure 8. 13 The correlation between resist 3σLER and the standard deviation of resist deprotection profile divided by the resist deprotection gradient at the resist line edge.

8.4 Conclusions

In conclusion, the effects of exposure dose and aerial image quality on resist CD control and LER behavior of two resist models have been investigated via a mesoscale stochastic acid reaction-diffusion simulation of the resist lithography process. In the case of two resist models having the same photosensitivity, the bound-PAG resist, which possess high PAG loading and low acid diffusivity, shows less resist CD bias, less LER, and larger resist process window than the blended-PAG resist which has relatively low PAG loading and high acid diffusivity. The trends of the simulation results are in well agreement with the experimental characterization results of the polymer-bound-PAG resists presented in chapter 7. Advanced analysis using this modeling work is performed to further study the relationships between resist fundamental properties and lithographic performance. The results suggest that resist CD variation can be well scaled by the root square of the product of the number of acid molecules at the resist line edge and acid diffusivity. Resist LER can be well scaled by the standard deviation of the resist deprotection profile divided by resist deprotection gradient at the line edge. The improved lithographic performance of the bound-PAG resist is mainly due to the reduced acid diffusivity that leads to a high resist contrast and thus small resist CD bias and less LER. Although increasing PAG loading does not show benefits for improving resist CD fluctuation and LER performance in this modeling work, low acid diffusivity is the direct consequence of increasing PAG loading in order to maintain resist CD control, and such low acid diffusivity can provide high resist contrast and superior lithographic performance of a resist material. A cartoon illustrating the difference of resist CD bias and LER behaviors between blended-PAG and bound-PAG resist models in responding to the same aerial image profile is shown in figure 8.14. Under a perfect digital aerial image profile, the bound-PAG resist has lower acid diffusivity and results in less resist CD bias than the blended-PAG resist. The low acid diffusivity may also create higher

resist deprotection contrast at the line edge which provides lower resist CD fluctuation and LER than the blended-PAG resist. In a general case where the aerial image is not perfect and the dose transition regions exist, small deprotection volumes created by acids of a bound-PAG resist may not overlap with the resist line edge profile and may not contribute to resist image blur and LER.

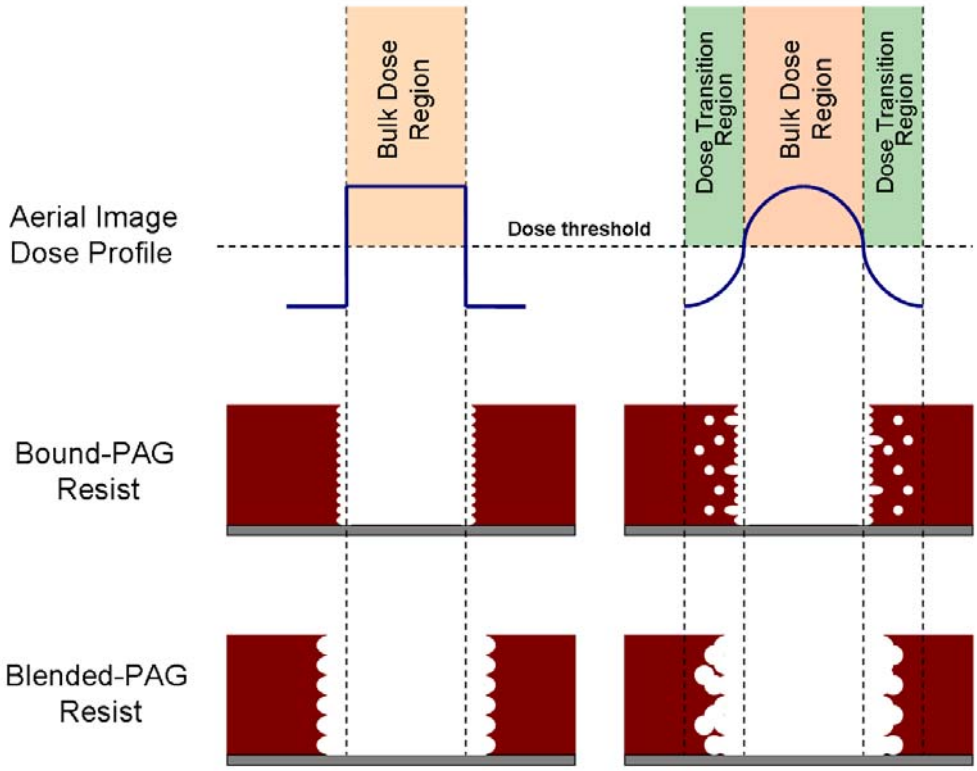

Figure 8. 14 Illustration of the difference of the resist CD and LER behaviors between the blended-PAG and bound-PAG resist models in responding to the same aerial image dose profile.

8.5 References

[1] Bristol, R. L., The tri-lateral challenge of resolution, photospeed, and LER: scaling below 50nm, *Proc. SPIE* **2007**, *6519*, 65190W.

[2] Gallatin, G. M., Resist blur and line edge roughness, *Proc. SPIE* **2005**, *5754*, 38-52.

[3] Dill, F. H.; Hornberger, W. P.; Hauge, P. S.; Shaw, J. M., Characterization of positive photoresist, *IEEE Trans. Electron Devices* **1975**, *22*, 445-452.

[4] Houle, F. A.; Hinsberg, W. D.; Sanchez, M. I.; Hoffnagle, J. A., Influence of resist components on image blur in a patterned positive-tone chemically amplified photoresist, *J. Vac. Sci. Technol. B* **2002**, *20*, 924-931.

[5] Kawakami, T.; Nagai, T.; Nishimura, Y.; Shima, M.; Kusumoto, S.; Shimokawa, T., Various factors of the image blur in chemically amplified resist, *Proc. SPIE* **2007**, *6519*, 65193K.

[6] Pawloski, A. R.; Acheta, A.; Levinson, H. J.; Michaelson, T. B.; Jamieson, A.; Nishimura, Y.; Willson, C. G., Line edge roughness and intrinsic bias for two methacrylate polymer resist systems, *J. Microlith. Microfab. Microsyst.* **2006**, *5*, 1-16.

[7] Lin, Q.; Sooriyakumaran, R.; Huang, W. -S., Toward controlled resist line edge roughness: material origin of line edge roughness in chemically amplified positive-tone resists, *Proc SPIE* **2000**, *3999*, 230-238.

[8] Ercken, M.; Leunissen, L. H. A.; Pollentier, I.; Patsis, G. P.; Constantoudis, V.; Gogolides, E., Effects of different processing conditions on line edge roughness for 193nm and 157nm resists, *Proc SPIE* **2004**, *5375*, 266-274.

CHAPTER 9

EFFECT OF PAG AND BASE QUENCHER INCORPORATION INTO THE POLYMER MAIN CHAIN ON RESIST LITHOGRAPHIC PERFORMANCE[†]

The lithographic performance and the correlations between material properties and lithographic performance of polymer-bound-PAG resists have been experimentally and theoretically investigated in chapters 7 and 8. The results indicate that polymer-bound-PAG resists exhibit improved lithographic performance in both 193 nm and EUV lithographic applications as compared to their traditional blended-PAG analogs. Base additives have been introduced into the formulation of traditional blended-PAG resists for improving the lithographic performance and environmental stability (i.e. more resistant to airborne base contamination). The incorporation of base into the resist polymer backbone is therefore a potential route for further improving resist performance and processing window by further eliminating acid migration at the resist exposure edge. In this chapter, the third generation polymer-bound-PAG resists which have both PAG and base quencher functional groups incorporating into the polymer main chain for 193 nm and EUV lithography are introduced and reported. The effect of base quencher incorporation into polymer-bound-PAG resists on the lithographic performance of these materials is also investigated.

9.1 Introduction

The second generation of polymer-bound-PAG resists which have the PAG anion

---

[†] Material presented in this chapter has appeared in part in a previously published article:

Wang, M.; Lee, C. –T.; Henderson, C. L.; Yueh, W.; Roberts, J. M.; Gonsalves, K. E., Incorporation of photoacid generator (PAG) and base quencher into the resist polymer main chain for sub-50 nm resolution patterning, *J. Mater. Chem.* **2008**, *18*, 2704-2708.

binding to the polymer main chain have demonstrated as an advanced resist platform for achieving sub-50 nm feature size resolution with high photosensitivity and small LER. However the several nanometers image blur induced by acids with small diffusivity, as well as the still high LER may again become critical and limit the capability for future technology nodes with sub-32 nm resolution. As resist requirements listed in The International Technology Roadmap for Semiconductors 2007 edition (ITRS 2007), at the year 2010, the required resist CD control for printing a 30 nm gate of a micro processor unit (MPU) is 1.9 nm (3σ). The corresponding low-spatial frequency LWR requirement is 2.4 nm (3σ).[1] Currently there is no resist materials, even for the second generation polymer-bound-PAG resists, can meet these requirements. Thus, the advance of current polymer-bound-PAG resist platform with more precise CD control and LER reduction is essential for the continued implementation of CARs for EUVL application.

The inherent incompatibility of different constituents in a multi-component CAR can lead to various phenomena such as PAG aggregation or clustering, non-uniform acid distribution in the resist film after exposure, and serious acid migration during the resist processing. To alleviate these problems, polymer-bound-PAG resists with PAG anion covalently incorporated into the polymer main chain have been developed. The incorporation of PAG anion into the main chain of the resist polymer shows improved 193 nm and EUV lithographic performance characteristics, such as faster photospeed, higher thermal stability, lower outgassing, and lower LER/LWR, as compared to their blended-PAG analogs. Base quencher is commonly used as an additive in traditional blended-PAG resist formulations for a variety of reasons including: (1) improvement of the environmental stability of the resist (i.e. reduce the impact of airborne base contamination exposure during resist processing), (2) reducing acid diffusion outside of the nominally exposed regions of the resist to improve resist resolution, and (3) reducing LER/LWR.[2-5] Base additives may also have the potential to improve current polymer-bound-PAG resist platform. However, as might be expected, the addition of free small

basic molecules may also exacerbate the component distribution heterogeneity problem experienced in multi-component CARs. In this chapter, the third generation polymer-bound-PAG resists which incorporate both PAG and base quencher functional groups into the resist polymer main chain are reported. The *base-incorporated polymer-bound-PAG resists* discussed in this chapter are based on polymer-bound-PAG resists developed in chapter 7 and are intended for 193 nm and EUV lithographic applications. The lithographic performance including resist sensitivity, CD control, and LER behavior is investigated. The effects of base incorporation on lithographic performance of polymer-bound-PAG resists are also investigated.

9.2 Resist Materials and Experiments

9.2.1 Preparation of PAG- and Base-Incorporated Polymers

For the synthesis of base-incorporated polymer-bound-PAG resists for 193 nm and EUV lithography, (4-methylphenyl) dimethylsufonium trifluoromethylsulfonate (MPDMS.TFMS) and triphenylsulfonium salt 4-(methacryloxy) 2.3.5.6-tetrafluorobenzenesulfonate (TPS.F4.MBS) are prepared as the PAGs and characterized using methods as described in previous reports.[6,7] γ-Butyrolactone methacrylate (GB, AZ Electronic Materials, Ltd.), hydroxystrene (HS, AZ Electronic Materials), and 2-ethyl-2-adamantyl-methacrylate (EA, AZ Electronic Materials, Ltd.) are used as the etch resistant and protecting subunits in the resist formulation. 1-Vinyl-2-pyrrolidinone (Sigma Aldrich, Inc.), 1-vinylimidazole (Tokyo Kasei Kogyo Co., Ltd.), and 4-vinylpyridine are used as the base for the polymerization. Resist tetrapolymers are prepared by free radical polymerization of monomers, PAG, and base in a freshly distilled anhydrous tetrahydrofuran (THF, Sigma Aldrich) and acetonitrile solution with azobisisobutyronitrile (AIBN, Sigma Aldrich) as the initiator, as shown in figure 9.1. The

basic characterization results of resist polymers for 193 nm and EUV lithography are listed in table 9.1 and 9.2.

Table 9. 1 Compositions of 193 nm base-incorporated polymer-bound-PAG resists.

Polymer	Polymer composition (mol%)				Yield (%)	M_w[a] (PDI)	T_{dec} (^oC)	T_g[b] (^oC)
	GB	EA	PAG	Base				
GB-EA-TPS.F4.MBS	49.3	40.3	10.4		36.2	3800 (2.2)	170	151
GB-EA- TPS.F4.MBS - Pyrrolidinone	42.6	49.9	6.8	0.7	36.1	3200 (1.6)	179	150
GB-EA- TPS.F4.MBS - Imidazole	41.6	50.0	7.7	0.7	39.5	3300 (1.7)	194	165
GB-EA- TPS.F4.MBS - Pyridine	45.3	46.5	7.5	0.7	38.3	2800 (1.7)	189	154

[a] The molecular weight was determined by GPC with THF as the mobile phase and polystyrene as narrow standards.

Table 9. 2 Compositions of EUV base-incorporated polymer-bound-PAG resists.

Polymer	Polymer composition (mol%)				Yield (%)	M_w[a] (PDI)	T_{dec} (^oC)	T_g[b] (^oC)
	HS	EA	PAG	Base				
HS-EA-MPDMS.TFMS	46.0	49.0	5.0		72.0	2500 (1.8)	165	137
HS-EA- MPDMS.TFMS - Pyrrolidinone	36.8	56.7	6.0	0.5	38.7	1900 (2.4)	161	123
HS-EA- MPDMS.TFMS - Imidazole	39.4	52.6	7.5	0.5	42.8	1700 (2.8)	164	116
HS-EA- MPDMS.TFMS - Pyridine	42.7	53.2	3.8	0.3	37.6	1800 (3.1)	170	131
HS-EA-TPS.F4.MBS	35.0	57.9	7.1		37.3	3600 (1.6)	145	N/A
HS-EA- TPS.F4.MBS - Pyrrolidinone	39.2	52.3	7.9	0.6	31.4	1800 (2.8)	153	
HS-EA- TPS.F4.MBS - Imidazole	42.6	50.8	6.3	0.3	28.5	2800 (2.0)	159	
HS-EA- TPS.F4.MBS - Pyridine	41.3	51.5	6.7	0.5	27.0	3100 (1.9)	163	

[a] The molecular weight was determined by GPC with THF as the mobile phase and polystyrene as narrow standards.

[b] Tg of HS-EA-F4 PAG-Base polymers could not be determined by DSC, probably due to the rigidity of these polymers contributed by the bulky adamantyl and triphenylsulfonium moiety of the PAG.

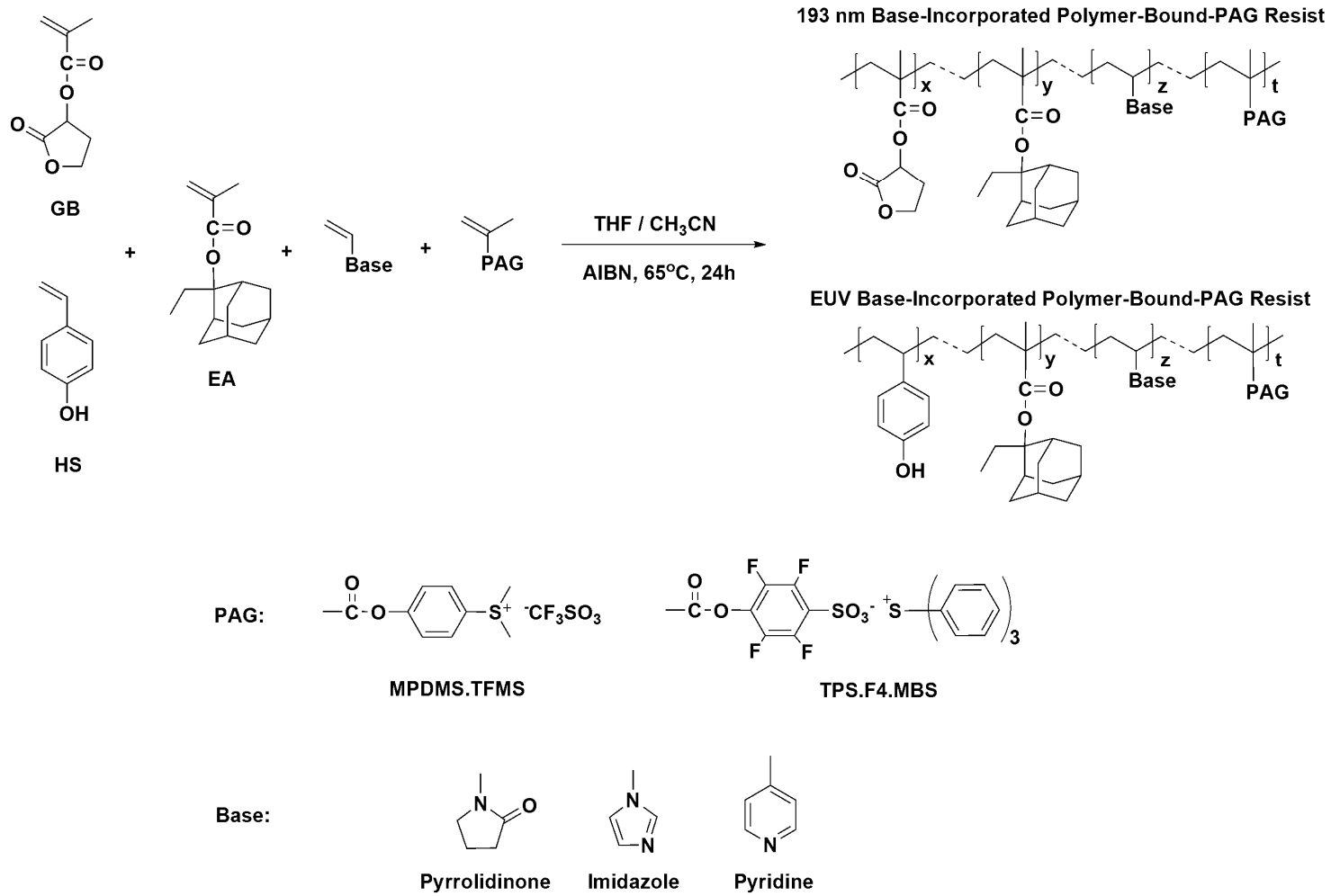

Figure 9. 1 Polymerization scheme and structures of base-incorporated polymer-bound-PAG resists.

MPDMS.TFMS incorporated 193 nm resists are not discussed in this work since the characterization results in chapter 7 suggest that the half-pitch resolution of GB-EA-MPDMS.TFMS is less than 100 nm. Base-incorporation into GB-EA-MPDMS.TFMS is not expected to enhance resist performance to a satisfactory level for sub-50 nm applications. On the other hand, the amount of base subunits incorporated into the resist polymer is relatively small (less than 1.0 mol% of molar feed ratio for polymerization), the quantification accuracy of base composition in these polymer is limited by the resolution of a general proton-1 nuclear magnetic resonance equipment (^{1}H NMR, JEOL 500 spectrometer, JEOL USA Inc.) and may not correspond to some of the characterization results of resist lithographic performance in this chapter.[8]

9.2.2 Resist Processing and Lithography Characterization

Resist solutions (5 wt% solid) are prepared by dissolving solid polymer powder in cyclohexanone (Sigma Aldrich, Inc.) and filtered through 0.2 mm syringe filters. For photospeed and resist contrast tests, bare silicon wafers are first primed with a solution containing 20 vol% 1,1,3,3,3-hexamethyl-disilazane (HMDS, ICN Biomedicals) and 80 vol% propylene glycol-1-monomethyl ether 2-acetate (PGMEA, Sigma Aldrich Inc.). The resist film is prepared by spin-coating the resist solution onto the primed wafer followed by a post-application bake at 100 ^{o}C for 90 seconds using contact baking on a hotplate. Resist film thickness is measured using a variable-angle spectroscopic ellipsometer (V-VASE, J. A. Woollam). For resist resolution tests, wafers containing low-stress silicon nitride membrane are used as the substrate and the patterning technique developed in chapter 6 is used. Resist films are prepared on these silicon nitride window substrates in a manner similar to that used for photospeed test. Grating features with different resolutions and pitches are patterned in areas covering the silicon nitride windows by using a JEOL JBX-9300FS EBL system at an acceleration voltage of 100 kV.

The beam current is set as 2 nA and the single pixel beam diameter is measured to be approximately 8 nm under these conditions. DUV exposure of resist film is performed by using an Oriel Instruments exposure source (model # 87530-1000, Hg-Xe arc lamp) equipped with a 248 nm band-pass filter (bandwidth ~ 11 nm, FWHM). The intensity of the lamp source under these conditions is measured to be 1.05 mW/cm^2 using a Molectron PM3 power probe and EPM2000 energy meter. The exposed resist film is subjected to a PEB at 100 ^oC for 90 seconds after removal from the exposure tools and subsequently developed in a conventional 0.26N tetramethylammonium hydroxide (TMAH, AZ Electronic Materials) developer for 15 seconds and rinsed with deionized water. After exposure and development, the backside of the silicon nitride membrane for resolution test is sputtered with a 20 nm gold acting as a charge dissipation layer for subsequent SEM imaging. Resist patterns are imaged in a top-down mode using a LEO 1530 thermally assisted field emission SEM with a 3 kV acceleration voltage and a 30,000 magnification. The remaining film thickness of the exposed squares (50μm×50μm) on the EB photospeed and resist contrast test wafers after development is measured using a profilometer (P-15 Profiler, KLA-Tencor Corp.).

9.3 Results and Discussion

9.3.1 Base-Incorporated Polymer-Bound-PAG resists for 193 nm Lithography

As listed in table 9.1 and 9.2, the resulting resist tetrapolymers exhibit high thermal stabilities and essentially no significant difference between various samples are found. MPDMS.TFMS incorporated polymers exhibit glass transition temperatures (Tg) between approximately 116 and 165 ^oC which is good for the thermal treatment in general lithography process. High Tg is found for 193 nm polymers incorporating

TPS.F4.MBS unit and no obvious Tg is found for EUV polymers incorporating TPS.F4.MBS unit, suggesting that these polymers are probably quite rigid due to the restrictions on chain motion as a result of the bulky triphenylsulfonium moiety of TPS.F4.MBS when bound into the polymer chain. This result corresponds to the behavior of analogous rigid polymers reported by another group that show no glass transition was observed below the polymer decomposition temperature.[9]

DUV contrast curves of base-incorporated GB-EA-TPS.F4.MBS resist films (100 +/- 5 nm film thickness) are shown in figure 9.2. The corresponding resist photospeed and contrast data are listed in table 9.3. The incorporation of base subunit into the polymer main chain results in a decrease of photospeed as expected. However base incorporation shows no obvious improvement of resist contrast. The photo-generated acids in the exposed region may be deactivated or neutralized at the presence of base subunits and results in a shift of the resist contrast curve toward higher dose region. However the increases of exposure dose due to base incorporation do not correspond to the loadings of bases listed in table 9.1. For example GB-EA-TPS.F4.MBS-Imidazole has the highest PAG loading among all the 193 nm base-incorporated resists, however this resist shows the lowest photosensitivity in the test. This behavior is probably due to the base property effect or the inaccuracy of base loading quantification. Advanced control of base-incorporation ratio or quantification method is essential for further understanding of base-incorporation effects on resist photospeed and contrast behavior.

The resolution capability of 193 nm base-incorporated polymer-bound-PAG resists are evaluated using the patterning technique developed in chapter 6 and the SEM images showing the resultant half-pitch resolution of these resist materials are shown in figure 9.3. Base incorporation into the resist polymer degrades the achievable half-pitch resolution of the original GB-EA-TPS.F4.MBS polymer. The failure mechanism of the base-incorporated resists is the collapse of resist line pattern. Pattern collapse has become one of the major concerns that limit the achievable resolution of resist materials.[10,11]

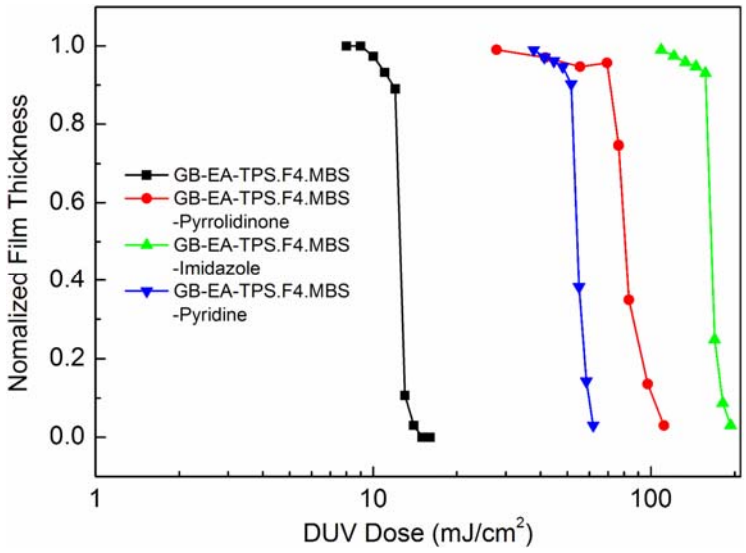

Figure 9. 2 DUV contrast curves of base-incorporated GB-EA-TPS.F4.MBS resist polymers

Table 9. 3 DUV photospeed, contrast, and water contact angle of 193 nm base-incorporated polymer-bound-PAG resists.

Resist	DUV Photospeed (mJ/cm^2)	DUV Contrast	Water Contact Angle (degree)	Relative Capillary Force [a]
GB-EA-TPS.F4.MBS	12.5	8.9	89.2	1
GB-EA-TPS.F4.MBS-Pyrrolidinone	100.1	7.3	76.6	16.6
GB-EA-TPS.F4.MBS-Imidazole	109.2	9.2	81.9	10.1
GB-EA-TPS.F4.MBS-Pyridine	60.5	8.2	85.8	5.2

[a] Relative to GB-EA-TPS.F4.MBS resist with the same space width between two resist lines.

Resist pattern collapse occurs during the development step of lithography. After the rinse of developer solution or solvent, a drying step is applied to the resist film to remove the remaining rinsing water or solvent at the resist film surface. When removing the water or solvent in the trench between two resist lines, the unbalanced capillary force acting on the side wall of the resist lines causes a pressure difference normal on the side wall of the resist line. The resist line may bend or break if the force acting on the resist side wall is beyond the stiffness (i.e. the modulus) of the resist line. On the other hand,

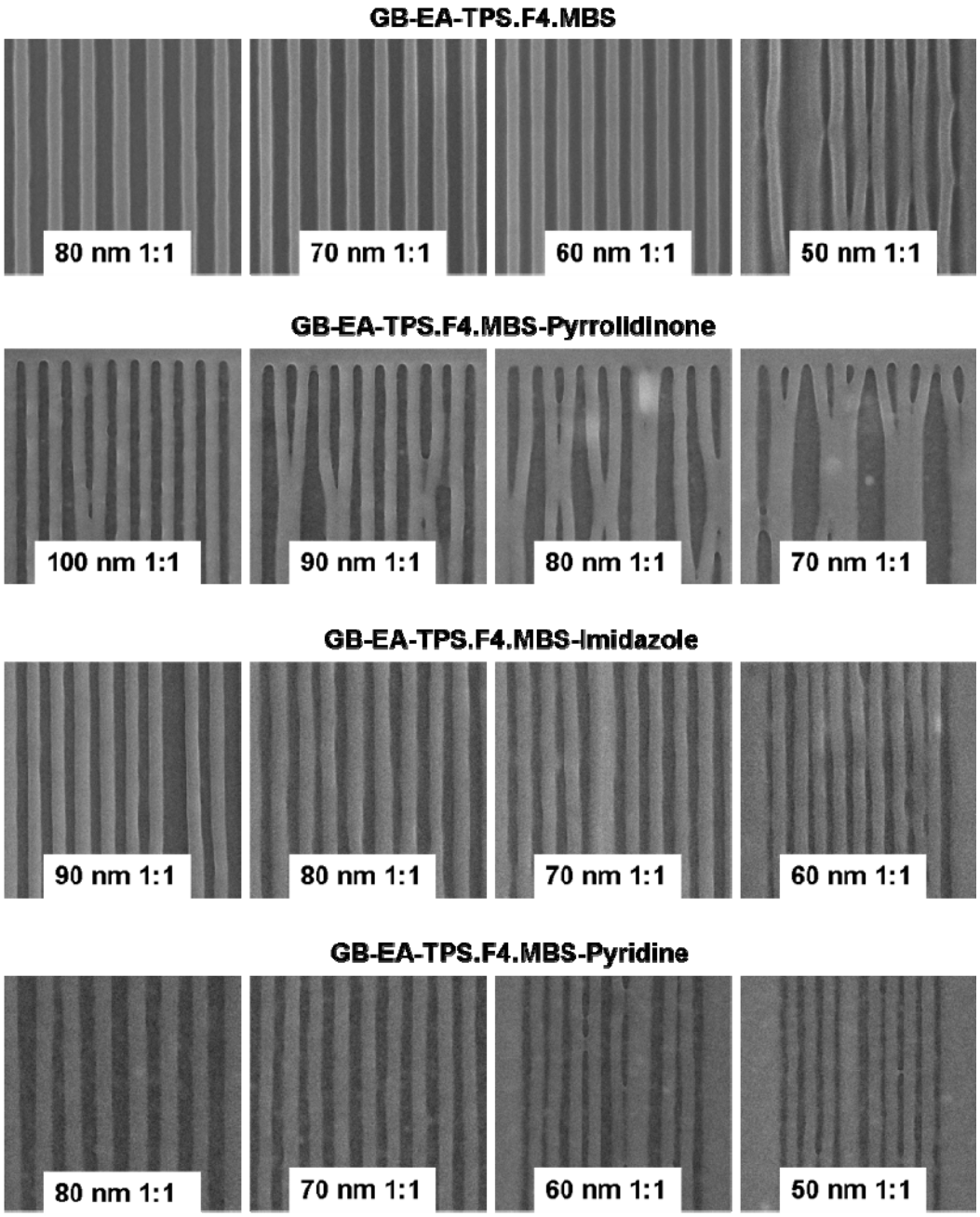

Figure 9. 3 SEM images of the half-pitch resolution of 193 nm base-incorporated polymer-bound-PAG resists.

the resist line may have enough mechanical strength and modulus to sustain the pressure difference, however the unbalanced force acting on the side wall results in a stress which is beyond the critical stress the resist line have at the resist/substrate interface. Resist line

unstuck or adhesion failure occurs under this condition and results in resist pattern collapse. The observed pattern collapse in base-incorporated polymer-bound-PAG resists is mainly the adhesion failure of resist lines. Resist pattern collapse caused by resist line deformation and adhesion failure is illustrated in figure 9.4.

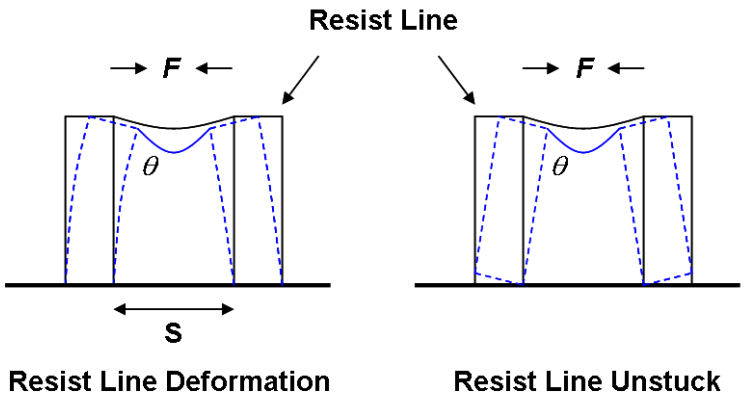

Figure 9. 4 Illustration of resist pattern collapse caused by resist line deformation and unstuck from the substrate

Since the driving force of resist pattern collapse behavior is the strength of the unbalanced capillary force acting on the side wall of the resist line during the resist film drying process, resist pattern collapse behavior is directly correlated to the interaction between the rinsing liquid, resist side wall, and the substrate at the interface. The capillary force $F_{Capillary}$ acting on resist lines as illustrated in figure 9.4 can be calculated by equation (9.1).

$$F_{Capillary} = \frac{2\gamma \cos\theta}{S} HL \tag{9.1}$$

Here γ is the surface tension of the rinsing liquid, θ the contact angle of the rinsing liquid at the resist side wall, S the space width between two resist lines, H the height of the resist line, L the length of the resist line. As listed in table 9.3, base-incorporated

polymer-bound-PAG resist films show lower static water contact angle than the base free resist film. The incorporation of base quencher into the resist polymer may increase the hydrophilicity of the polymer due to the polar nature of the base quencher. Assuming all the resist films have the same line and space width on the same substrate, the relative capillary forces acting on the side wall of the resist line are calculated and listed in table 9.3. The decrease of 3.4~12.6 degrees of water contact angle results in 5.2~16.6 folds capillary force increase, relative to the base free resist. On the other hand, the ultra-thin silicon nitride substrate used in this work is more hydrophobic than silicon and silicon dioxide. The increase of the hydrophilicity of the resist film may lower the compatibility and the adhesion force between the resist line and the substrate. These effects explain the observed down grade of resist resolution and the pattern collapse behavior of the base-incorporated polymer-bound-PAG resists.

9.3.2 Base-Incorporated Polymer-Bound-PAG resists for EUV Lithography

For the base-incorporated polymer-bound-PAG resists for EUV lithography, resist photospeed and contrast curves under EB exposure are measured since both EB and EUV belong to ionization radiation and have been reported having analogous mechanisms for PAG acid generation.[12] Photospeeds and resist contrasts of base-incorporated HS-EA-MPDMS.TFMS resists (cationic bound-PAG resists) are shown in figure 9.5. The corresponding photospeeds of resists are listed in table 9.4. Again the incorporation of base quencher into the polymer decreases the photospeed of the resist as expected. However in this set of resist materials, the incorporation of imidazole and pyridine improves resist contrast under EB exposure. The increase of resist contrast can reduce the resist CD bias and improve resist resolution and LER performance as demonstrated in chapter 8. The use of imidazole and pyridine may provide improved control of free TFMS acid diffusion. A significant decrease of resist contrast is observed for HS-EA-

MPDMS.TFMS-Imidazole resist when the normalized film thickness is below 0.15 (10 nm). Such resist contrast change indicates a possible resist dissolution behavior switch near the resist-substrate interface.

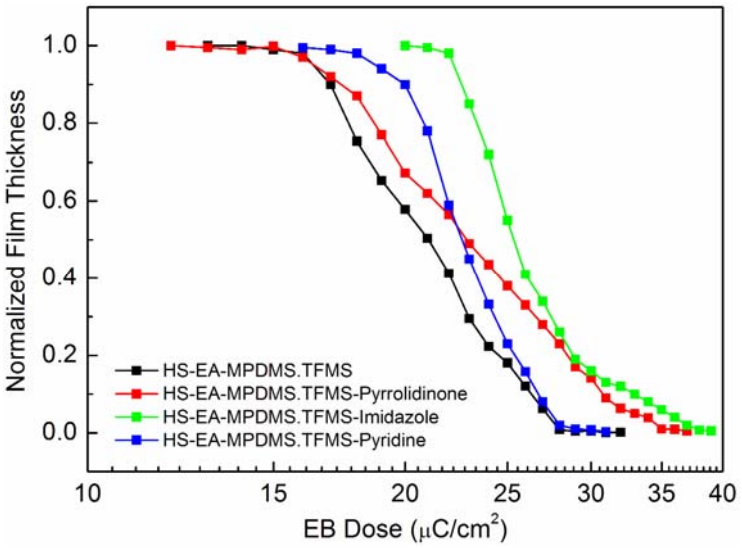

Figure 9. 5 EBL contrast curves of base-incorporated HS-EA-MPDMS.TFMS resists.

Table 9. 4 Lithographic performance of PAG and base quencher incorporated resists for EUV lithography

Polymer	PAG-to-EA ratio	Base-to-PAG ratio	Film Thickness (nm)	Photospeed (μC/cm^2)	Resolution (nm)
HS-EA-MPDMS.TFMS	0.10	0.0	75.1	27.5	40.0
HS-EA- MPDMS.TFMS -Pyrrolidinone	0.11	0.08	75.7	35.0	100.0[a]
HS-EA- MPDMS.TFMS -Imidazole	0.14	0.07	83.2	37.0	100.0[a]
HS-EA- MPDMS.TFMS -Pyridine	0.07	0.08	75.2	30.0	35.0
HS-EA-TPS.F4.MBS	0.12	0.0	84.8	33.0	30.0
HS-EA- TPS.F4.MBS - Pyrrolidinone	0.15	0.08	73.4	70.5	80.0
HS-EA- TPS.F4.MBS - Imidazole	0.12	0.05	74.7	93.0	50.0
HS-EA- TPS.F4.MBS - Pyridine	0.13	0.08	79.1	N/A[b]	N/A[b]

[a] Higher resolution can not be achieved due to serious dense line bridging problem.
[b] Photospeed and resolution can not be determined due to extremely low EBL sensitivity.

EB Photospeeds and resist contrasts of base-incorporated HS-EA-TPS.F4.MBS resists (anionic bound-PAG resists) are shown in figure 9.6. The corresponding photospeeds of resists are listed in table 9.4. Different from the behavior of cationic bound-PAG resists, the incorporation of base quencher shows no improvement of resist contrast. The incorporation of pyridine even dramatically degrades the photosensitivity and contrast of HS-EA-TPS.F4.MBS resist. Unlike the cationic bound-PAG resists which generate free acids with high diffusivity after exposure, acids generated in anionic bound-PAG resists have limited diffusivity due to the binding of acid anion to the polymer main chain. The incorporation of base quencher into a low acid diffusivity material may decrease resist deprotection efficiency and thus the resist contrast. On the other hand, the comparatively larger decrease in photospeed (i.e. as compared to the polymers not containing basic functional groups) in the case of polymer incorporating both base and TPS.F4.MBS PAG as compared to the polymer containing both base and MPDMS.TFMS PAG is likely due to the shorter acid catalytic chain length of the fixed F4.MBS acid generated upon exposure in the case of base incorporated HS-EA-TPS.F4.MBS resists.

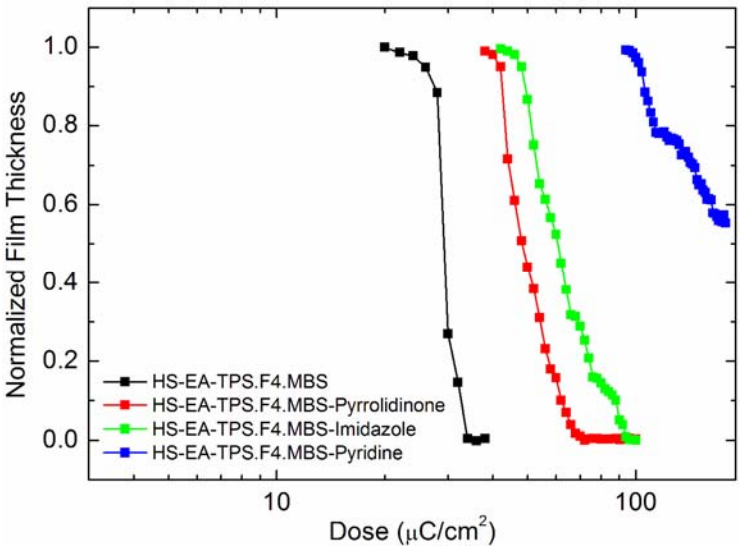

Figure 9. 6 EBL contrast curves of base-incorporated HS-EA-TPS.F4.MBS resists.

SEM images of half-pitch resolution line features patterned in MPDMS.TFMS incorporated resists are shown in figure 9.7. The HS-EA-MPDMS.TFMS resist without base quencher can achieve a 45 nm half-pitch resolution. The direct incorporation of different base quenchers into the HS-EA-MPDMS.TFMS polymer main chain shows different effects on resist performance depending on the nature of the basic functional group used. The incorporation of moderate basic functional group, pyridine (pKa=5.39), into the polymer backbone shows an improvement in resist resolution (35 nm half-pitch) as compared to the base free HS-EA-MPDMS.TFMS resist. However, the incorporation of a stronger (imidazole, pKa=6.07) or a weak (pyrrolidinone, pKa=-0.34) basic functional group causes the resist to exhibit patterning defects and reduced resolution. Serious bridging randomly appears between patterned resist lines in the cases of these imidazole and pyrrolidinone that limits the resist resolution to approximately 100 nm half-pitch. Cross-section view SEM images of 300 nm 1:1 L/S patterns further demonstrate the existence of giant residue and bridging problems of these resist materials, as shown in figure 9.8. The bridging problem may be due to heterogeneous inter-chain and intra-chain functional group distribution. The lack of compatibility between the base, PAG, and other polymer constituents may lead to some form of nanoscale distribution heterogeneity in the resist film. The differences in the reactivity ratios between the various monomers during polymerization may also lead to the non-uniform distribution of components in the final resist polymers. The bridging problem of the HS-EA-MPDMS.TFMS-Imidazole resist may explain the observed resist contrast decrease behavior near the resist-substrate interface.

SEM images of half-pitch resolution line features patterned in TPS.F4.MBS incorporated resists are illustrated in figure 9.9. The resolution of the HS-EA-TPS.F4.MBS resists decreases in all cases when base quencher is incorporated into resist polymer. The major cause of resist resolution loss is resist pattern collapse due to adhesion failure. Addition of polar base quenchers to the polymer increases the

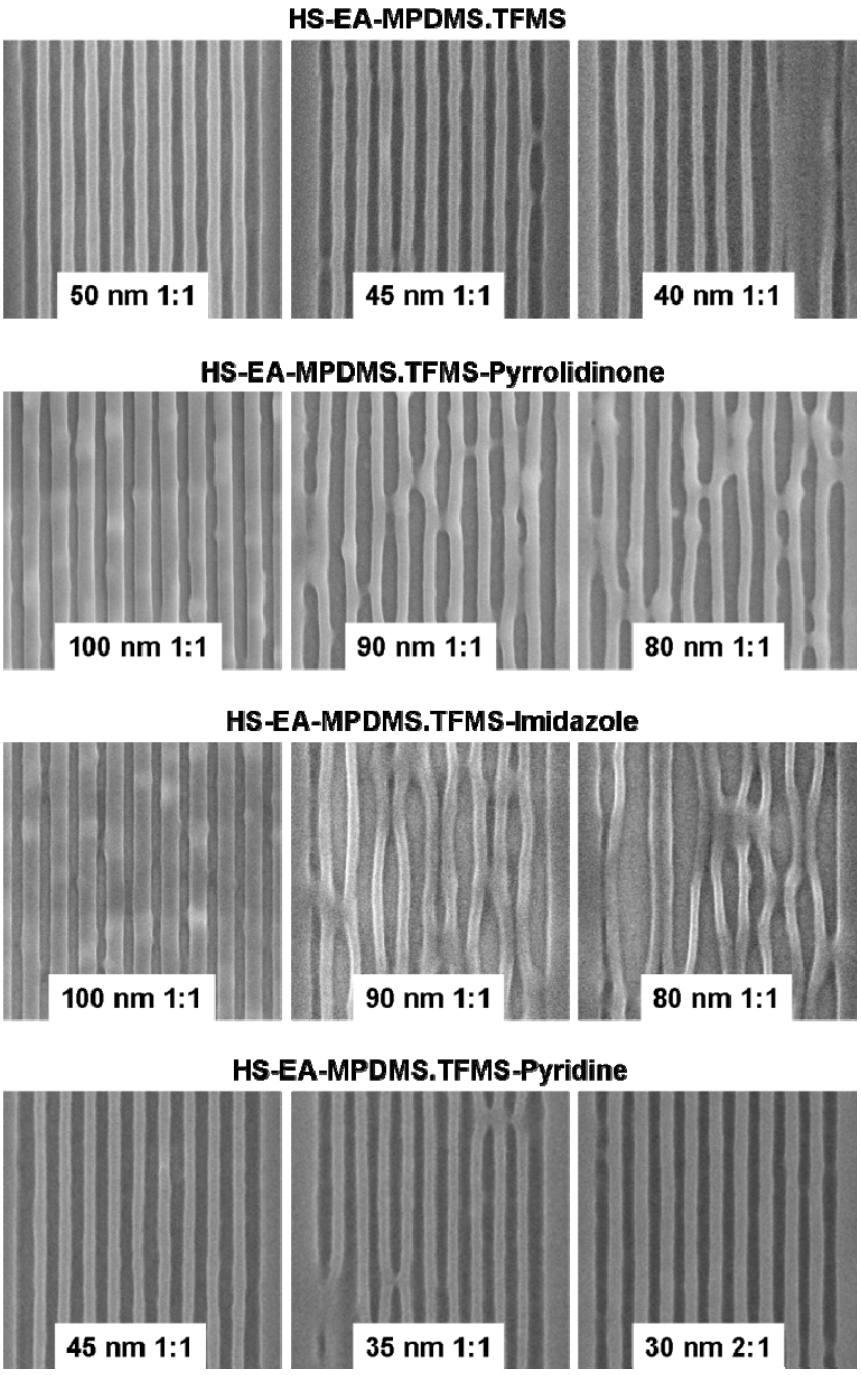

Figure 9. 7 SEM images of the half-pitch resolution of base-incorporated HS-EA-MPDMS.TFMS resists.

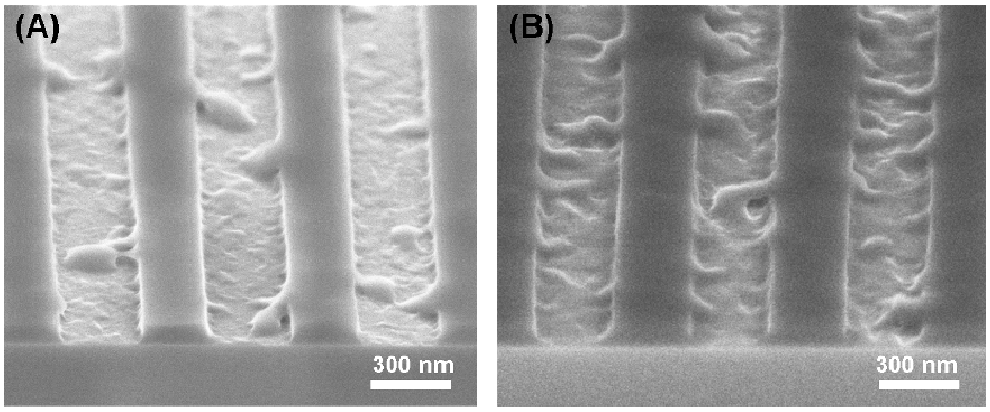

Figure 9. 8 SEM images showing the bridging defects of (A) HS-EA-MPDMS.TFMS-Pyrrolidinone and (B) HS-EA-MPDMS.TFMS-Imidazole resist films.

hydrophilicity of the resist polymer, and again this increased hydrophilicity can result in stronger capillary forces during development, rinsing, and drying which leads to more significant resist pattern collapse. A water contact angle study of these resist materials is made to further quantify the effect of base incorporation into the polymer on the hydrophilicity and surface energy of the polymer film. The HS-EA-TPS.F4.MBS polymer is found to have a static water contact angle value of 89.9 degrees, while in contrast the base-incorporated HS-EA-TPS.F4.MBS resists show much lower water contact angles in the range between 32.9 to 51.6 degrees. These data again clearly show that the polymers incorporating base quencher are more hydrophilic, and thus the unbalanced capillary forces exerted on patterned structures during the drying process are expected to be larger. Thus, even this relatively minor level of 0.5 mol% base incorporation into the polymer is sufficient to dramatically affect the pattern collapse behavior in these materials. It is also likely that this minor level of base incorporation into the polymer significantly affects the adhesion property of the resist polymer with the underlying substrate. In this work the silicon nitride membrane is more hydrophobic than flat silicon substrate. It might be expected that the adhesion energy of the resist to the

substrate might be degraded, thus causing the pattern collapse problem exacerbated by the more hydrophilic resist polymer during drying to be even more severe.

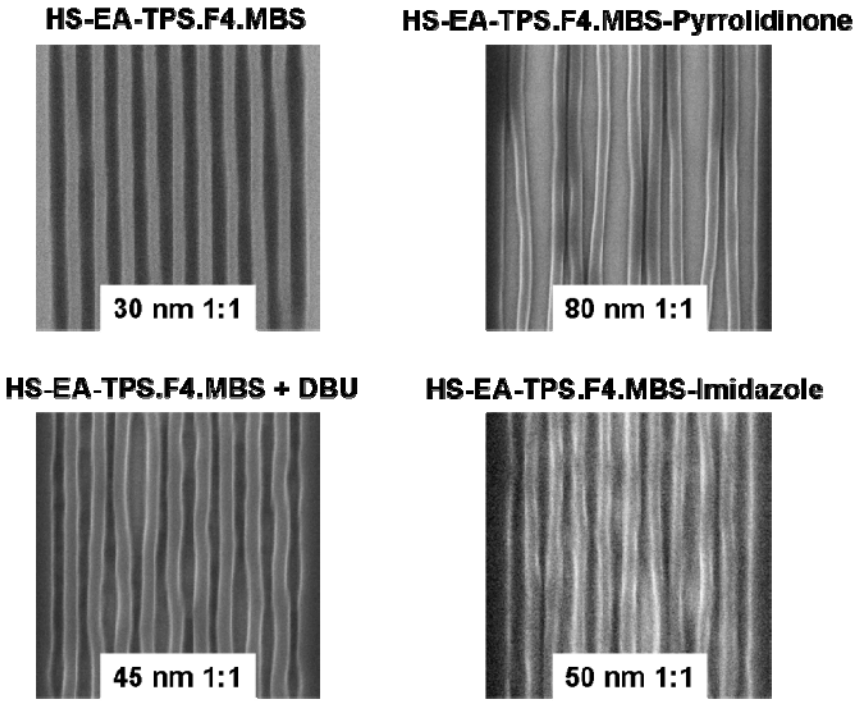

Figure 9. 9 SEM images of half-pitch resolution of base-incorporated HS-EA-TPS.F4.MBS resists.

Since the materials reported here are intended to serve as high resolution CARs for IC device fabrication, the pattern edge roughness of such materials is an important characteristic that must be considered. Therefore, in cases where the resist materials looked promising and the resulting line-space patterns from those materials are not distorted by pattern collapse or bridging, LER and LWR for the resist films are measured. The resulting 3σLERand 3σLWR values for HS-EA-TPS.F4.MBS resist are found to be 3.2 nm and 4.5 nm, respectively, for 30 nm 1:1 L/S patterns. The 3σLER and 3σLWR values for HS-EA-MPDMS.TFMS resist are found to be 7.7 nm and 11.4 nm, respectively, for 45 nm 1:1 L/S patterns. The 3σLER and 3σLWR values for HS-EA-

MPDMS.TFMS-Pyridine resist are found to be 5.1 nm 7.3 nm, respectively, for 45nm 1:1 L/S patterns. The incorporation of pyridine into HS-EA-MPDMS.TFMS polymer is observed to improve both resolution and LER/LWR by helping to confine acid diffusion and increase resist contrast in this system. It should be remembered that acid diffusion in that particular material is still an important consideration since a free TFMS acid is generated from such a cationic bound-PAG resist. However, overall the simple anionic bound-PAG resist (HS-EA-TPS.F4.MBS) showed the highest resolution and best LER/LWR performance even without base addition due to the restricted acid diffusion provided by binding of the PAG anion to the resist polymer backbone.

9.4 Conclusions

A series of PAG and base incorporated resist polymers (the third generation of polymer-bound-PAG resists) are developed and the thermal and lithographic performance is investigated. The synthesis scheme results in moderate-to-good yields for all the resist materials used in this work. Polymers show good thermal stability and high glass transition temperatures that can facilitate resist processing and longer resist shelf life. The lithographic performance under EBL shows that the resolution of cationic polymer-bound-PAG resist (HS-EA-MPDMS.TFMS) is improved by incorporating pyridine as a base quencher into the polymer backbone without a significant loss of photospeed. The anionic polymer-bound-PAG resists (GB-EA-TPS.F4.MBS and HS-EA-TPS.F4.MBS) show decreased resolution due to the loss of resist-substrate adhesion that led to more substantial resist pattern collapse at larger feature sizes. The HS-EA-MPDMS.TFMS system gives higher photospeeds as compared to the fluorinated TPS.F4.MBS PAG system. Significant resist line bridging problems are observed in several resist polymers that incorporated stronger basic functional groups, suggesting that possibly poor

monomer compatibility and resist polymer compositional heterogeneity due to monomer reactivity ratio differences could be problematic in such cases. A successful development of this class of material need to focus on the design of resist materials with more compatible PAG and base quencher functional groups. The effects of direct base incorporation on resist contrast, resolution, line edge roughness, and resistance to airborne base contamination are also important factors to evaluate.

9.5 References

[1] *International Technology Roadmap for Semiconductors (ITRS)* **2007**. (http://www.itrs.net/Links/2007ITRS/Home2007.htm).

[2] Kawai, Y.; Otaka, A.; Tanaka, A.; Matsuda, T., The effect of an organic base in chemically amplified resist on patterning characteristics using KrF lithography, *Jpn. J. Appl. Phys.* **1994**, *33*, 7023-7027.

[3] Askawa, K.; Ushirogouchi, T.; Nakase, M., Effect of basic additives on sensitivity and diffusion of acid in chemical amplification resists, *Proc. SPIE* **1995**, *2438*, 563-570.

[4] Pasini, D.; Klopp, J. M.; Frechet, J. M. J., Design, synthesis, and characterization of carbon-rich cyclopolymers for 193 nm microlithography, *Chem. Mater.* **2001**, *13*, 4136-4146.

[5] Houle, F. A.; Hinsberg, W. D.; Sanchez, M. I., Acid-base reactions in a positive tone chemically amplified photoresist and their effect on imaging, *J. Vac. Sci. Technol. B,* **2004**, *22*, 747-757.

[6] Wang, M.; Jarnagin, N. D.; Lee, C. –T.; Henderson, C. L.; Yueh, W.; Roberts, J. M.; Gonsalves, K. E., Novel polymeric anion photoacid generators (PAGs) and corresponding polymer for 193 nm lithography, *J. Mater. Chem.* **2006**, *16*, 3701-3707.

[7] Wu, H.; Gonsalves, K. E., Preparation of a photoacid generating monomer and its application in lithography, *Adv. Funct. Mater.* **2001**, *11*, 271-276.

[8] Personal communication with Dr. Mingxing Wang at Department of Chemistry, University of North Carolina, Charlotte, NC, USA.

[9] Michaelson, T. B.; Jamieson, A. T.; Pawloski, A. R.; Byers, J.; Acheta, A.; Willson, C. G., Understanding the role of base quenchers in photoresists, *Proc. SPIE* **2004**, *5376*, 1282-1293.

[10] Jouve, A.; Simon, J.; Pikon, A.; Solak, H.; Vannuffel, C.; Tortai, J. H., Overcoming pattern collapse on e-beam and EUV lithography, *Proc. SPIE* **2006**, *6153*, 61531C.

[11] Cao, H. B.; Nealey, P. F.; Domke, W. D., Comparison of resist collapse properties for deep ultraviolet and 193 nm resist platforms, *J. Vac. Sci. Technol. B* **2000**, *18*, 3303-3307.

[12] Kozawa, T.; Tagawa, S.; Oizumi, H.; Nishiyama, I., Acid generation efficiency in a model system of chemically amplified extreme ultraviolet resist, *J. Vac. Sci. Tehcnol. B* **2006**, *24*, L27-L30.

CHAPTER 10

OTHER STRUCTURE-PROPERTY RELATIONSHIPS OF CHEMICALLY AMPLIFIED RESISTS[†]

The major lithographic properties of three generations of polymer-bound-PAG resists (i.e. cationic bound-PAG, anionic bound-PAG, and base-incorporated bound-PAG resists) have been experimentally and theoretically studies in detail in previous chapters. Among the major lithographic performance such as sensitivity, resolution, and LER, Polymer-bound-PAG resists still exhibit insufficient sensitivity under ionization radiation such as EUV and EB. The increase of PAG loading of polymer-bound-PAG resists may not enhance the photospeeds as illustrated in chapter 7. PAG acid generation behavior under ionization radiation is affected by not only the PAG structure itself, but also the polymer matrix structure of the resist material. The absorption of high energy photon is non-selective to PAG molecule anymore, and polymer sensitization for PAG acid generation becomes dominant due to the majority of polymer composition in the resist formulation. A thorough understanding of relationships between PAG and polymer structures and the PAG acid generation behavior under ionization radiation is important for improving acid generation efficiency (i.e. photospeed) of the resist material. On the other hand, the demand of high resolution resist material requires the use of ultra-thin resist film (i.e. less than 150 nm) for preventing resolution damaging factors such as shallow depth of focus of the exposure tool and pattern collapse behavior of the resist

---

[†] Material presented in this chapter has appeared in part in previously published articles:

Lee, C. –T.; Wang, M.; Gonsalves, K. E.; Yueh, W.; Roberts, J. M.; Younkin, T. R.; Henderson, C. L., Effect of PAG and Matrix Structure on PAG acid generation behavior under DUV and high-energy radiation exposure, *Proc. SPIE* **2008**, *6923*, 69232F.

Lee, C. –T.; Henderson, C. L.; Wang, M.; Gonsalves, K. E.; Yueh, W.; Roberts, J. M., The effect of direct PAG incorporation into the polymer main chain on reactive ion etch resistance of 193 nm and EUV chemically amplified resists, *Microelectron. Eng.* **2008**, *85*, 963-965.

feature. Plasma etch resistance of the resist material has become another major factor dominating the capability of a resist material for sub-50 nm resolution applications. Understanding the effects of PAG incorporation to the main chain of a polymer-bound-PAG resist on its plasma etch resistance is important for the continued development of this class of resist materials. This chapter covers the study and investigation of these two topics.

10.1 PAG and Matrix Structure Effects on PAG Acid Generation Behavior under Excitation and Ionization Radiations

CARs have successfully facilitated the development of DUV and 193 nm lithography techniques for more than two decades due to their acid-catalyzed deprotection scheme that enhances their photospeed. This acid-catalyzed mechanism provides a method for amplifying the initial chemical reactions caused by interaction of radiation with the resist film, thus making each interaction event between radiation and resist more productive. However, when switching from low energy photolysis to high energy radiolysis, changes in the manner in which the radiation interacts with the resist material can alter the acid generation efficiency and mechanism of PAG excitation. In high energy radiation cases where the radiation energy exceeds the ionization potential of the PAG and the polymer resin, the radiation absorption in the resist film becomes non-selective. The ratio of PAG excited by direct excitation as compared to polymer or matrix sensitization pathways can shift heavily in favor of matrix sensitization in such high energy exposure cases. Such sensitization pathways may become a potential method for enhancing resist sensitivity under high energy radiation through careful selection of matrix and PAG materials. A better understanding and study the efficiency of acid generation through direct and indirect PAG excitation pathways and the effect of PAG

and matrix structure on these pathways would be extremely valuable for the design of future high sensitivity resist materials. In this work, acid generation of typical ionic (onium salt) and non-ionic PAGs under DUV (248 nm) and EB exposure in polymer film have been studied. The effect of PAG type and structure on its acid generation under photolysis and radiolysis has been determined. The effect of polymer resin structure on PAG photoacid generation under photolysis and radiolysis has also been investigated. Concepts for PAG and polymer design for producing enhanced sensitivity resists for excitation and ionization exposures is discussed

10.1.1 Radiation Energy Absorption of PAG

CARs have been widely employed as a lithographic material for nanoscale fabrication in the semiconductor industry for more than two decades due to their high resolution and fast photospeed. The fast photospeed of positive tone CARs is enabled by the use of an acid-catalyzed deprotection reaction scheme that modulates the solubility of the resist through a two step reaction sequence. First, an acid is generated through the photolysis of a PAG in the resist during exposure. Subsequently, this acid catalytically reacts with polymer resin to render it soluble in an aqueous alkaline developer.[1,2] In this way, the chemical modification of the polymer and the resulting impact on the resist solubility is greatly amplified as compared to the initial number of photochemical reaction events. EUVL and 193 nm immersion lithography are promising technologies for patterning sub-50 nm feature size resolution. However when switching from KrF (248 nm) radiation source to shorter exposure wavelength such as ArF (193 nm) and EUV (13.5 nm) radiations, the cost of generating such high energy photon increase exponentially and requirement of sensitive CARs has become one of the major requirements for enabling these technologies. Especially for EUVL, the need of highly sensitive resist material has placed one of the most critical challenges of modern resist

material design and development. Understanding the PAG photoreaction is therefore an important factor for novel resist material design.

PAG acid generation in solid state polymer film is mainly through direct PAG absorption of photon energy and PAG decomposition under excitation radiation such as KrF and ArF exposure.[3-5] PAG acid generation through polymer sensitization pathway under excitation exposure has also been reported.[6,7] This behavior has been reported as the polymer can absorb photon energy and jump to its first excited state, and the photon energy can then be transferred to the PAG through an electron transfer mechanism. The radiation chemistry of PAG when exposed to high energy exposure source such as EUV, X-ray, and electron-beam has also been proposed.[8,9] When switching from low energy optical exposure to high energy radiation exposure source, the photon energy has exceed the ionization potential, which is usually ~10 eV, of organic materials commonly used in photoresist formulation and lead to non-selective photon energy absorption. High percentage of the radiation energy is then absorbed by the polymer matrix since its majority in resist composition and the acid generation through direct PAG radiation absorption and decomposition becomes inefficient. PAG acid generation through poly(p-hydroxylstyrene) (pHOST) and poly(methyl methacrylate) (pMMA) sensitization pathway under ionization radiation has also been reported.[10,11] The design of next generation resist material applied to high energy exposure source will requires the knowledge of suitable PAG and polymer structure design for taking the advantage on both direct PAG excitation and polymer sensitization pathways for significantly enhanced acid generation efficiency. However a systematic study of PAG and polymer matrix structure effects on PAG acid generation efficiency under excitation and ionization radiation sources has not been reported yet.

10.1.2 PAG Acid Generation Experiments

In this work, the effects of PAG and polymer structure on PAG acid generation efficiency in polymer film DUV and 100 kV EB exposure sources are investigated. The technique which utilizes on-wafer ellipsometry of acid-sensitive dye to quantify acid concentration in polymer films, developed in chapter 4, is employed to determine acid generation efficiency under exposure. Ionic PAGs with sulfonium and iodonium chromophores and various anion structures are used in this study for determining PAG structure effect on its acid generation efficiency and the exposure source effect on its acid generation behavior. A non-ionic PAG, the norbornene dicarboximidyl nonaflate (ND.PFBS, Sigma Aldrich), is also included in this study. The structures of PAGs used in this work are illustrated in figure 10.1.

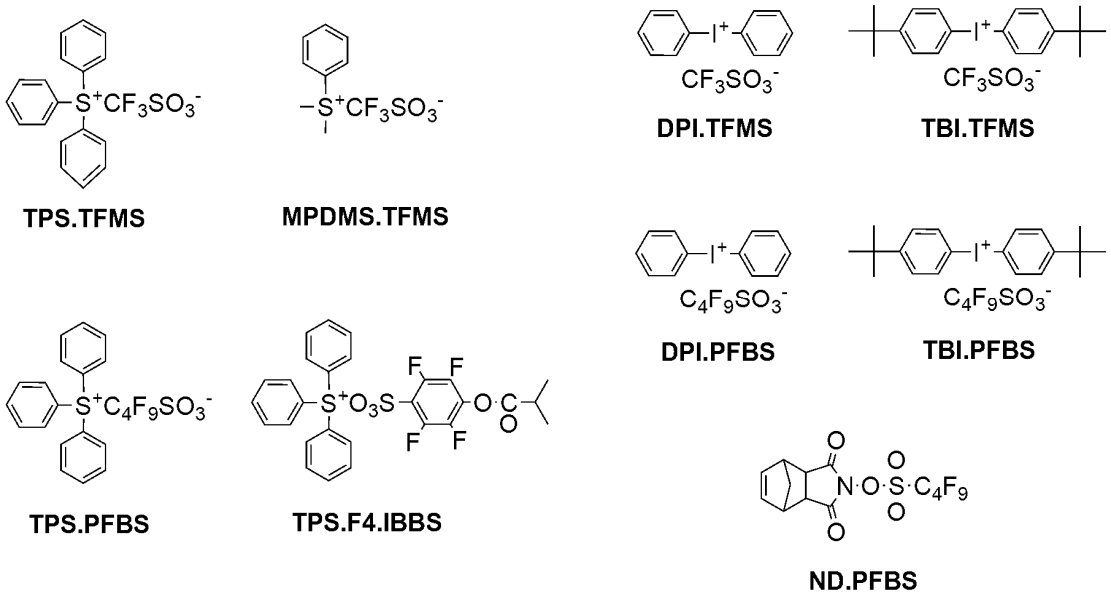

Figure 10. 1 The structures of PAGs: Sulfonium salts (triphenylsulfonium triflate (TPS.TFMS), triphenylsulfonium nonafalte (TPS.PFBS), triphenylsulfonium 4-(methacryloxy)-2,3,5,6-tetrafluorobenzenesulfonate (TPS.F4.IBBS), and dimethylsulfonium triflate (MPDMS.TFMS)); Iodonium salts (diphenyliodonium triflate (DPI-Tf), Diphenyliodonium nonaflate (DPI.PFBS), bis-4-t-butylphenyl iodonium triflate (TBI.TFMS), and bis-4-t-butylphenyl iodonium nonaflate (TBI.PFBS)); Non-ionic PAG (norbornene dicarboximidyl nonaflate (ND.PFBS)).

Homo-polymers with different functional groups are used to study the polymer structure effect on PAG acid generation under different exposure sources, and their structures are illustrated in figure 10.2. Coumarin 6 (C6, Mw 350.44, Sigma Aldrich) is used as a proton indicator to monitor photoacid production in the polymer film upon exposure. Polymer solutions are prepared by dissolving polymer resin (97.2 mol%), PAG (1.4 mol%), and C6 (1.4 mol%) in cyclohexanone (reagentplus grade, Sigma Aldrich). Polymer films (~150 nm in thickness) are prepared by spin-coating the solution onto prime silicon wafers and prebaking at 100 ^{o}C for 2 minutes to remove the residual solvent. For excitation exposure study, polymer films are exposed using an Oriel Instruments exposure source (model 87530-1000, Hg-Xe arc lamp) filtered by a 248 nm bandpass filter (bandwidth ~11 nm, FWHM). For ionization radiation study, polymer films are exposed using a JEOL 9300FS EBL system with a 100 kV acceleration voltage and a 60 nA beam current. The exposed films are post-exposure baked at 70 ^{o}C for 1 minute to enhance proton-C6 contact in polymer film. Spectroscopic ellipsometry (V-VASE, J. A. Woollam) is used to measure ellipsometry spectra and determine the film thickness, DUV optical constants, energy deposition profile, and $C6^{+}$ absorbance of the polymer film as the method demonstrated in chapter 4.[12]

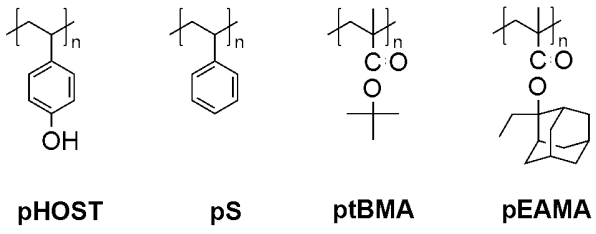

Figure 10. 2 Structures of homo-polymers: poly(p-hydroxystyrene) (pHOST), poly(styrene) (pS), poly(t-butyl methacrylate) (ptBMA), and poly(2-ethyl-2-adamantyl-methacrylate) (pEAMA).

Calibration between protonated-C6 ($C6^+$) absorption and acid concentration in different polymer films are made by mixing varying amounts of trifluoromethanesulfonic acid ($H^+CF3SO3^-$, Mw 150.08, Fluka) with the polymer and C6 dye into cyclohexanone and casting films from these solutions. The linear relationships between $C6^+$ absorbance and acid concentration in polymer films are shown in figure 10.3. The amount of acid generated though PAG decomposition when exposure to radiation can be quantified by determining the absorption of the $C6^+$.

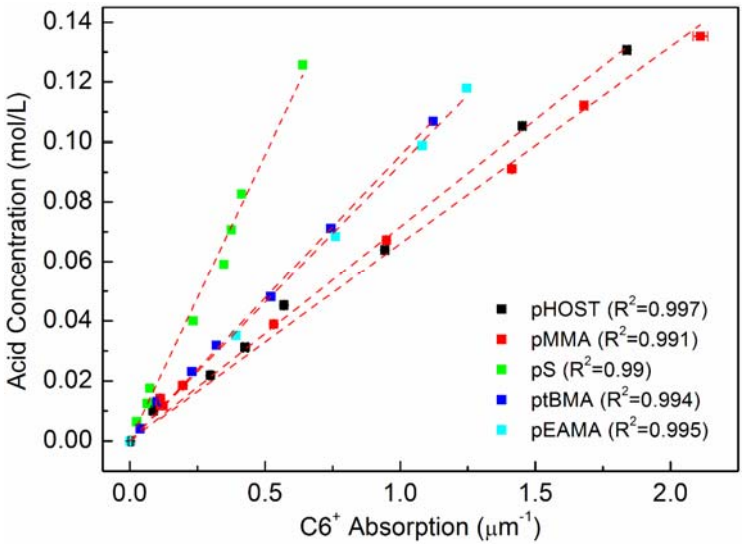

Figure 10. 3 Calibration curves between $C6^+$ absorption and acid concentration in different polymer films.

10.1.3 Results and Discussion

Polymer matrices pHOST and ptBMA are used to study PAG structure effect on acid generation behavior through direct PAG excitation and polymer sensitization pathways. UV/VIS spectrometry shows that pHOST exhibits significant higher molar absorbance (ε=440 $cm^{-1}M^{-1}$) at 248 nm wavelength than ptBMA which is relatively transparent. By measuring PAG acid generation in ptBMA matrix, the polymer sensitization pathway is minimized due to ptBMA's negligible absorbance when

compared to PAG absorbance, and the capability of acid generation through direct PAG excitation can be determined. By comparing PAG acid generation in pHOST and ptBMA matrices, the effect of PAG structure on pHOST sensitization for acid generation can be determined. Figure 10.4 shows the normalized acid yield (the ratio of acid concentration to initial PAG concentration) of PAGs in both pHOST and ptBMA matrices under the same DUV exposure dose (10 mJ/cm^2). Sulfonium salts, except TPS.F4.IBBS, typically show higher acid generation rate through direct PAG excitation than iodonium salts. However when polymer sensitization pathway is involved in PAG acid generation in pHOST matrix, iodonium salts show significantly enhanced acid generation rate than sulfonium salts. This result indicates iodonium salts may possess higher acid generation efficiency though polymer sensitization pathway than sulfonium salts.

The mechanism of PAG acid generation through polymer sensitization has been reported as the energy transfer from the excited polymer matrix to the ground state PAG molecule through an electron transfer process.[6] The probability of this electron transfer mechanism can be predicted by calculating the free energy (ΔG_{ET}) required for the oxidation of the excited polymer subunit and the reduction of the PAG molecule as shown in equation (10.1). The calculation of the electron affinity of the PAG may be a reliable prediction of the electron transfer probability from the excited polymer to the PAG molecule. The electron affinity (-*EA*) of a molecule can be expressed as the heat of formation of the molecule anion subtracts the heat of formation of the neutral molecule and the electron as shown in equation (10.2). The electron affinities of PAGs used in this work are calculated using HyperChem^{TM} with a Neglect of Differential Diatomic Overlap (NDDO) semi-empirical method and the results are shown in table 10.1. Iodonium salts showed higher electron affinity (3.36~3.86 eV) than sulfonium salts (2.58~3.21 eV) that support the experimental observation of more efficient polymer sensitization pathway of PAG acid generation of iodonium salts than that of sulfonium salts.

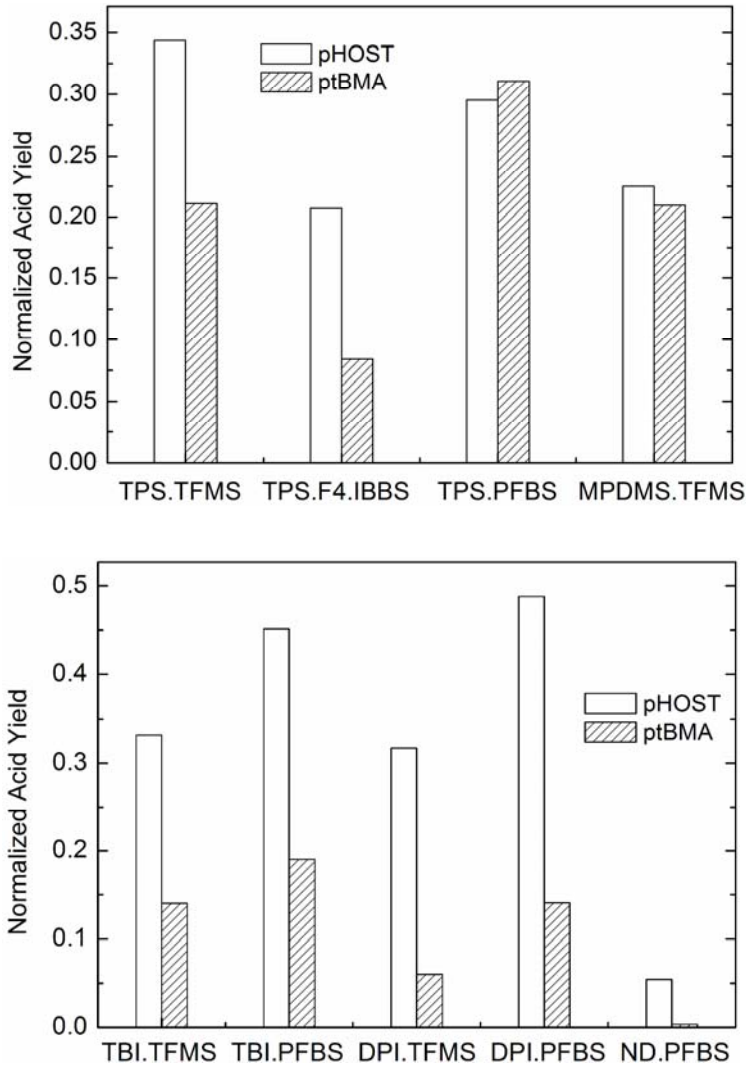

Figure 10. 4 Normalized acid yield of onium salts and ND.PFBS in pHOST and ptBMA films under 248 nm wavelength exposure (10 mJ/cm^2).

The non-ionic PAG, ND.PFBS, is transparent under 248 nm wavelength radiation. ND.PFBS does generate acid through polymer sensitization when placed in pHOST matrix, and the calculated electron affinity (3.85 eV) also suggests the high probability of polymer sensitization pathway. Acid generation of TPS.PFBS supposedly shows polymer sensitization effect, more significant than TPS.TFMS, according to the results of electron affinity calculation, however the experimental result shows nearly identical acid generation rate in both pHOST and ptBMA matrix. The cause of this acid generation

behavior is still unknown and might be the increased PAG absorption of 248 nm photon. Further investigation is required to determine the real cause of this observation.

$$\Delta G_{ET} = E_{oxidation}(Polymer^*) - E_{reduction}(PAG) - E_{excitation}(Polymer) \quad (10.1)$$

$$-EA = H_f(PAGe^-) - H_f(PAG) - H_f(e^-) \quad (10.2)$$

Table 10. 1 Electron affinity of PAGs used in this work.

Sulfonium PAGs		Iodonium and non-ionic PAGs	
PAG	-EA (eV)	PAG	-EA (eV)
TPS.TFMS	2.83	DPI.TFMS	3.44
TPS.PFBS	2.97	DPI.PFBS	3.86
TPS.F4.IBBS	3.21	TBI.TFMS	3.36
MPDMS.TFMS	2.58	TBI.PFBS	3.79
		ND.PFBS	3.85

Polymer matrix can be ionized by absorbing high energy radiation and the resulting cation may be deprotonated and provide the proton for Bronsted acid formation.[10,11] The hydroxystyrene molecule has been proved having high probability to release proton when ionized under high energy radiation, on the other hand the styrene molecule is less reactive in its ionized form and has less tendency to release proton.[12] pHOST and pS are hence used to study the effect of proton source from the polymer matrix on PAG acid generation under high-vacuum electron-beam exposure. The normalized acid yields of PAGs in pHOST and pS matrices under 100 kV EB exposure (40 μC/cm^2) are shown in figure 10.5. All sulfonium slats and diphenyliodonium salts show inefficient acid generation in pS matrix, however their acid productions are significantly enhanced in pHOST matrix. This result indicates the proton source from polymer matrix is essential for these PAGs to generate acid under high-vacuum ionization radiation. However bis(t-4-butylphenoliodonium) salts and ND.PFBS PAG

show relative higher acid generation capability in pS matrix and are comparable to the acid yields in pHOST matrix. This result suggests that the reaction intermediates of these PAGs may provide easy proton source for acid generation under high-vacuum ionization radiation.

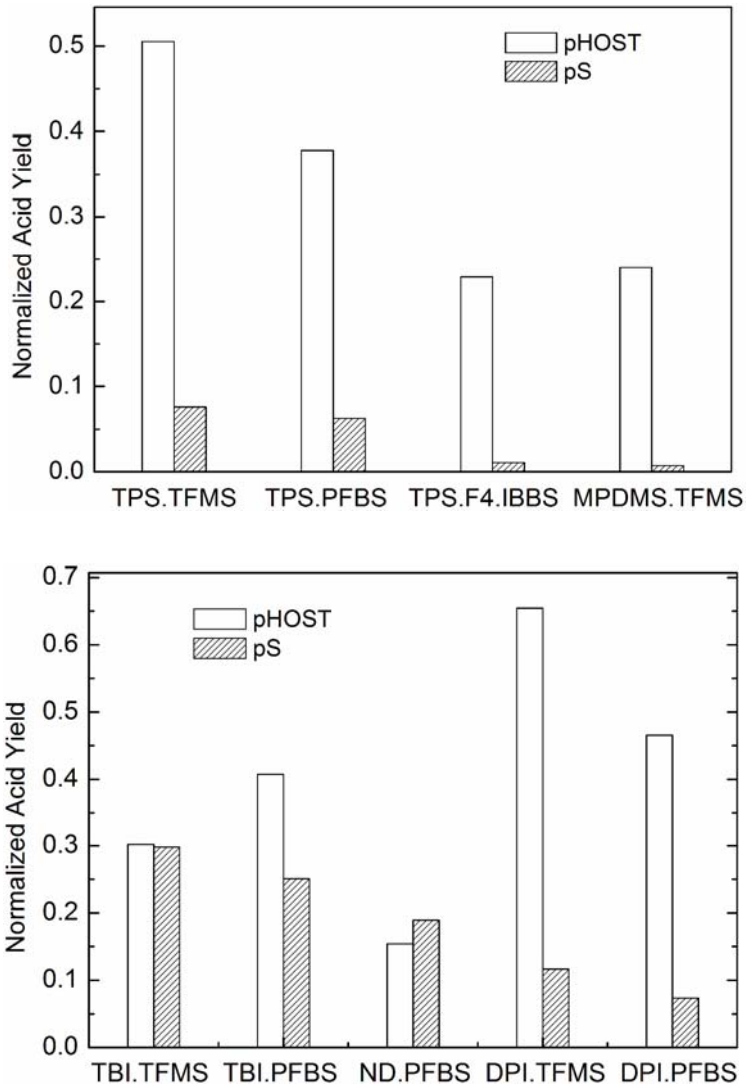

Figure 10. 5 Normalized acid yield of onium salts and ND.PFBS in pHOST and pS films under 100 kV EB exposure (40 μC/cm^2).

Polymer structure effect on PAG acid generation behavior under high-vacuum ionization radiation is also studied. Homo-polymers with different functional groups commonly used in modern photoresist composition are used as the polymer film to study their effect on PAG acid generation behavior. The normalized acid yields of selected sulfonium, iodinium, and non-ionic PAGs in four homo-polymer matrices under 100 kV EB exposure (40 $\mu C/cm^2$) are illustrated in figure 10.6. Among polymer structures screened in this study, PAGs show less acid generation efficiency in pS matrix as expected due to the lack of proton source for Bronsted acid formation under high vacuum exposure environment. TPS.TFMS and DPI.TFMS show enhanced acid yields in pHOST matrix if compared with their acid yields in pS matrix. All PAGs show significantly enhanced acid generation yield in poly(methacrylate) (pEAMA and ptBMA) matrices when compared with their acid yields in pS matrix. Moreover, the acid generation of TBI.TFMS and ND.PFBS is further enhanced when compared with those in pHOST matrix. The PAG acid generation efficiency may be determined by the combinatorial effects of polymer radiation absorption, polymer ionization, and proton acquisition for Bronsted acid formation, however the results here suggest poly(methacrylate) may also provide easy proton source for acid generation under high-vacuum ionization exposure. In the case of TBI.TFMS and ND.PFBS, poly(methacrylate) showed significant higher acid generation efficiency (~ 2 folds) than other polymer matrices studied in this work.

10.1.4 Conclusions

Effects of polymer and PAG structures on PAG acid generation under DUV and electron-beam exposure are studied using the on-wafer ellipsometry of acid-sensitive dye method developed in chapter 4. PAG acid generation through direct PAG excitation/ionization and polymer sensitization under low-energy excitation and high-energy ionization exposures is also discussed. Iodonium slats show significant polymer

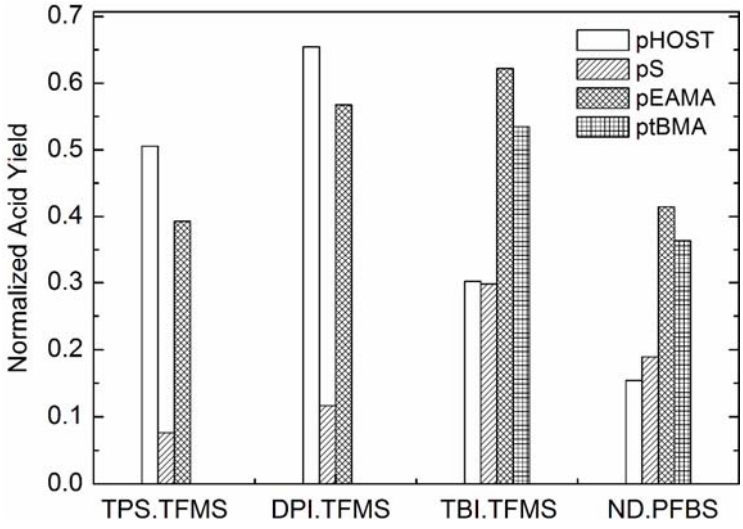

Figure 10. 6 Normalized acid yield of PAGs in different polymer matrices under 100 kV EB exposure (40 μC/cm^2).

sensitization effect for acid generation under DUV exposure, and the behavior is qualitatively determined being correspond to the calculated electron affinity of the PAG molecule. Basically higher electron affinity provides higher probability of being an electron acceptor and higher acid generation efficiency through the polymer sensitization pathway. Under high-vacuum ionization exposure such as 100 kV EB radiation, proton source has become one of the major effect on PAG acid generation. Most of the sulfonium, iodonium, and non-ionic PAGs show significantly improved acid generation yield in pHOST matrix, if compared with the acid yield in pS matrix, due to the easy proton source from the hydroxystyrene cation. The inefficient acid generation in pS matrix may be due to the lack of proton source from the less reactive styrene cation. TBI and ND.PFBS PAGs show comparable acid generation in both pHOST and pS, indicating possible proton source from the intermediates of PAG decomposition reactions. Poly(methacrylate) also enhances PAG acid generation under electron-beam exposure,

indicating that the ionized methacrylate subunit may also provide easy proton source for PAG acid generation.

10.2 Direct PAG Incorporation on Reactive Ion Etch Resistance of Chemically Amplified Resists

The incorporation of PAG functional groups directly into the resist polymer backbone has shown improved lithographic performance in achieving high resolution, high sensitivity, and low LER/LWR simultaneously in CARs, as reported in previous chapters. However, the effect of direct PAG incorporation into the resist polymer on the reactive ion etch (RIE) performance of such materials has not been studied and reported. This section discusses the effects of PAG loading and structure on the plasma etch resistance of polymer-bound-PAG resists. Increased PAG loadings in both 193 nm and EUV polymer-bound-PAG resist platforms shows significant improvement in polymer etch resistance. Current polymer etch rate correlations and models are not able to accurately predict the trend of etch behavior within each polymer-bound-PAG resist family.

10.2.1 Resist Plasma Etch Resistance

Photoresists serve two important roles in modern microelectronic fabrication processes as a: (1) medium for creating a physical relief pattern from a mask image and (2) a masking material for transferring the resist relief image into the underlying film stacks via plasma etch processes. The dramatic downward scaling of IC device feature sizes has now approached the sub-50 nm size scale. This has also required a scaling down in the resist film thicknesses used to pattern such high resolution features with current

optical lithography techniques due to depth of focus and pattern collapse limitations. Currently, ultra-thin photoresist layers (< 150 nm) have been used in manufacturing, and moving forward even thinner films will likely be required.[13] Development of resists that can provide increased resolution and lower line edge roughness with high sensitivity, while still providing sufficient etch resistance as film thicknesses diminish, will be required for future IC device generations

Traditional blended-PAG CARs suffer from the tri-lateral trade-off between achieving high resolution, high sensitivity, and low line edge roughness due to heterogeneous distribution of PAG and the uncontrolled photoacid diffusion.[14,15] A series of novel polymer-bound-PAG CAR has been shown in chapter 7 and 9 that the direct binding of PAG into the polymer main chain can provide CAR with improved resolutions, lower LER, and higher sensitivity as compared to their blended-PAG analogs. Although the success of polymer-bound-PAG resists in improving lithographic performance has been shown, the effects of binding the PAG anion into the resist polymer and the effect of high PAG loadings on the plasma etch resistance of these materials has not been reported. The purpose of this work is to characterize the effect of PAG incorporation into the polymer main chain on resist etch behavior and determine if any of the standard etch resistance correlations could be used to reasonably predict this behavior.

10.2.2 Resist Materials and Experimental Procedures

A series of resist materials are synthesized to determine the effect of PAG structure and loading on plasma etch performance of polymer-bound-PAG resists.[16,17] The structures and compositions of the resist materials used in this work are shown in figure 10.7 and table 10.2. Resists containing γ-butyrolactone methacrylate (GB) and hydroxystyrene (HS) are prepared for comparing the etch resistance of 193 nm and EUV resist platforms, respectively. Resists incorporating triphenylsulfonium salt PAG

functional groups with 4-(methacryloxy)-2,3,5,6-tetrafluorobenzenesulfonate (TPS.F4.MBS), 4-(methacryloxy)benzenesulfonate (TPS.MBS), and 4-(vinyl)-benzenesulfonate (TPS.VBS) as acid anions are prepared to determine the effect of fluorine atom and ester group content of the PAG on resist dry etch resistance. Both 193 nm and EUV resist platforms with different PAG loadings are prepared to study the effect of PAG loading on dry etch resistance. Standard materials including poly(tert-butyloxycarbonyl hydroxystyrene) (pTBOCST), poly(methyl methacrylate) (pMMA, Sigma Aldrich), and 1:1 chloromethacrylate-co-methylstyrene (ZEP520A, Zeon Chemicals) are also characterized for comparison purposes. Resist films are spin-coated onto prime grade silicon wafers and post-applied baked at 100 ^{o}C for 90 seconds to produce films of 100 nm in thickness. Reactive ion etch (RIE, Plasma-Therm) using silicon dioxide and polymer etching recipes are performed for the etch rate studies.

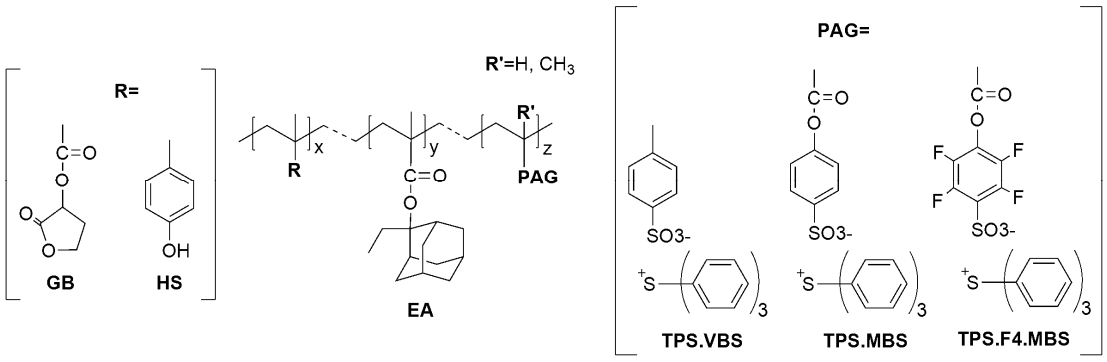

Figure 10. 7 Structures of the 193 nm and EUV polymer-bound-PAG resists studied in this work.

10.2.3 Results and Discussion

The effect of PAG loading on the etch resistance of TPS.F4.MBS PAG containing forms of the polymer-bound PAG resists is illustrated in figure 10.8. For both GB-EA-TPS.F4.MBS and HS-EA-TPS.F4.MBS resists, linear correlations are found between increasing PAG loading and decreasing etch rate in both etch recipes. Although the

Table 10. 2 Composition and etch rate of polymer-bound PAG resists.

Resist	Polymer composition			Mw (PID)	Etch rate [b]	
	HS/GB	EA	PAG		R_1 [c]	R_2 [d]
GB-EA-TPS.F4.MBS	49.2	48.9	1.9 [a]	3800 (1.9)	1.31	1.32
	53.6	44.3	2.1	4100 (2.3)	1.22	1.25
	52.0	42.7	5.3 [a]	4100 (2.3)	1.14	1.15
	49.3	40.3	10.4	3800 (2.2)	1.05	0.99
HS-EA-TPS.F4.MBS	39.7	58.2	2.1	3800 (1.8)	1.21	1.00
	35.0	57.9	7.1	3600 (1.6)	1.08	0.96
	40.2	51.6	8.2	3100 (1.9)	1.01	0.93
	36.2	45.7	15.1	2700 (1.9)	0.82	0.89
HS-EA-TPS.MBS	37.7	55.8	6.5	3800 (1.7)	0.98	0.98
HS-EA-TPS.VBS	41.7	48.6	9.7	3700 (1.7)	0.84	0.93

[a] Blended-PAG
[b] Relative to pTBOCST
[c] SiO_2 etch recipe: CHF_3 22.5 sccm, O_2 2.5 sccm, 80 mTorr, 150 W
[d] Polymer etch recipe: O_2 40.0 sccm, Ar 4.0 sccm, 80 mTorr, 50 W

higher PAG loading introduces higher fluorine and unsaturated carbon content into the polymer, the polymer etch performance is improved due to the increased polymer aromaticity which arises from the use of the triphenylsulfonium PAG chromophore. This increased aromaticity dominates the etch resistance effect of the varying PAG loading.

In cases where the PAG monomers are simply blended and not bound to the resist polymer and compared to the polymer-bound-PAG cases, no statistically significant difference is observed in their relative etch performance. For example, the GB-EA-TPS.F4.MBS samples shown in table 10.2 contain two blended-PAG samples and two polymer-bound-PAG samples, and in these cases they follow the same general linear etch rate trend with increasing PAG loading.

The relative etch rates of all the resists are illustrated in table 10.2. Comparisons of etch resistance between polymer-bound-PAG resists show a clear trend (GB-EA-TPS.F4.MBS < HS-EA-TPS.F4.MBS < HS-EA-TPS.MBS < HS-EA-TPS.VBS). Incorporation of the HS subunit in the EUV resist platform (HS-EA-TPS.F4.MBS) as compared to the GB subunit used in the 193 nm platform show significant improvement

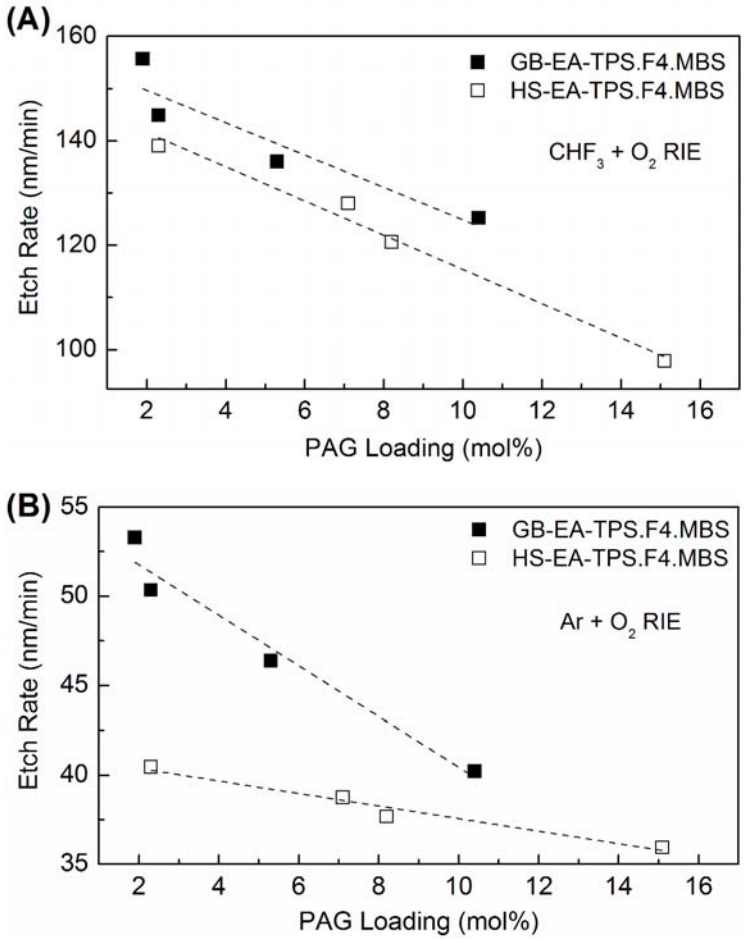

Figure 10. 8 Effect of PAG loading of GB-EA-TPS.F4.MBS and HS-EA-TPS.F4.MBS resists on etch rate using (A) silicon dioxide and (B) polymer recipes.

in the etch resistance. This result is as expected since the six-member unsaturated phenyl ring in the HS monomer offers superior etch resistance to that of the five-member saturated ring in GB. There is a small etch performance gain when switching from the fluorine-containing PAG (HS-EA-TPS.F4.MBS) to the fluorine-free PAG (HS-EA-TPS.MBS). The fluorinated ring PAG is used in the 193 nm resist to modulate the PAG spectral absorption behavior and the resist absorbance to an acceptable level when using elevated PAG loadings in the polymer-bound-PAG materials. It is clear though that there is at least some small cost in etch performance for this design choice. The oxide etch performance of the resist containing the fluorinated PAG is slightly worse than the

fluorine-free PAG, and conversely the oxygen etch rate of the fluorinated PAG polymer is lower than that of the fluorine free materials.

Another significant increase in etch resistance is found when switching from resists that contain PAGs connected to the polymer main chain via an ester linkage (e.g. HS-EA-TPS.MBS and HS-EA-TPS.F4.MBS) to PAG that do not contain such ester linkage (e.g. HS-EA-TPS.VBS). This result suggests that the electron-rich ester structure may be efficiently attacked by the active plasma species, such as electrons, ions, and free radicals, during the plasma processing and this initiation of etch degradation of the polymer significantly degrades the overall etch performance of the resist. While such ester linkage makes synthesis of the PAGs and polymers more facile and can perhaps be used to test variations in monomer structure on lithographic performance of the resist, it is likely that the use of such ester-linked PAG monomers should be avoided in design of the final resist materials.

In order to provide some rational guidance for further resist design with respect to etch performance, attempts are made to correlate the etch rates of various materials studied using several existing polymer etch rate models. Figure 10.9 shows the etch rate data from the various polymers plotted using three common etch rate correlation models. While in general the three etch rate models provide reasonable correlations between different classes of polymers (i.e. pMMA vs. GB-EA-PAG polymers vs. HS-EA-PAG polymers), the correlation within either the GB-EA-PAG polymers or the HS-EA-PAG polymers is quite poor. The improved etch resistance via increased PAG loading can not be well predicted by any of the etch rate models used in this work. This suggests that a higher level effect may exist to improve etch performance when increasing PAG loading in the polymer (e.g. better orientation of resist polymers in the film due to the bulky pendent PAG unit, etc.). Further work on understanding these effects is important for determining the fundamental effects on such improved resist dry etch resistance.

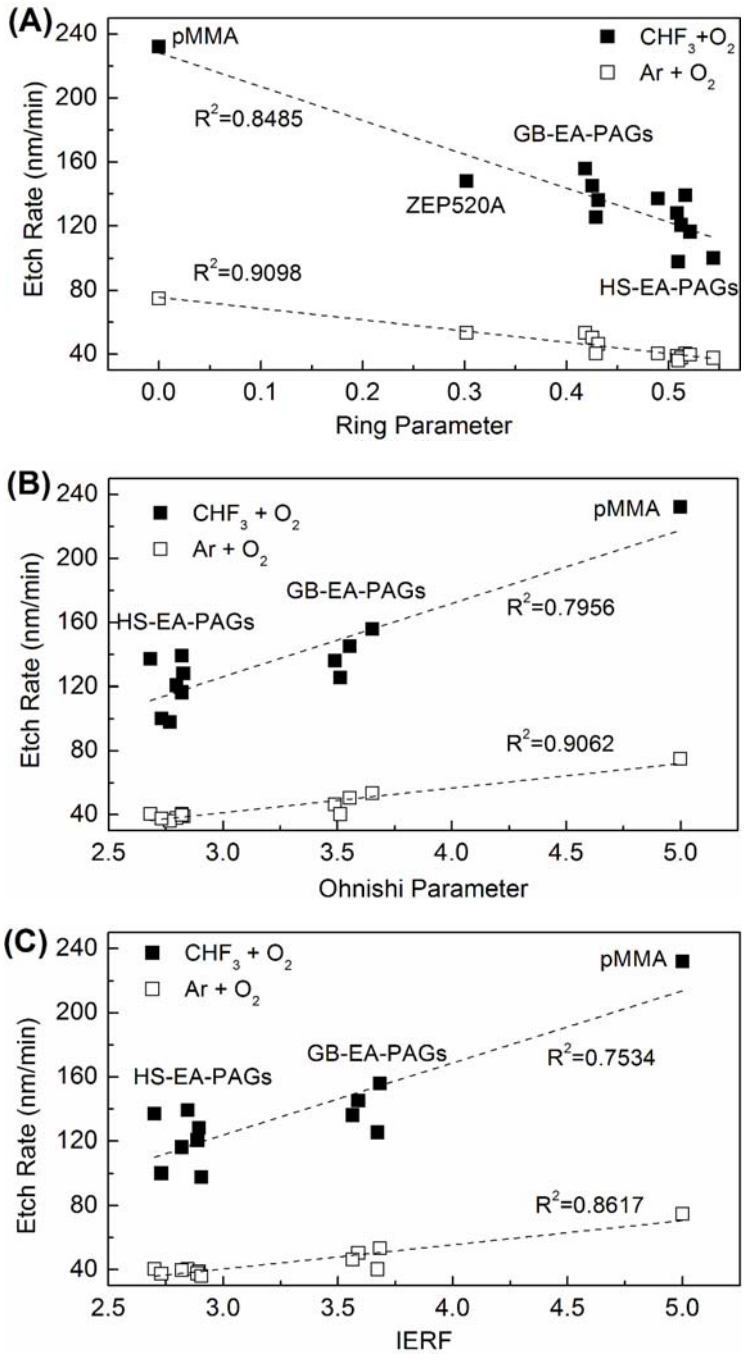

Figure 10. 9 Etch rate model fitting of resists: (A) the Ring parameter[18], (B) the Ohnishi parameter[19], and (C) the Index for Etch Resistance of Fluoropolymers (IERF).[20]

10.2.4 Conclusions

The effects of PAG loading and structure on the reactive ion etch performance of a series of polymer-bound PAG resists is studied. Increasing the PAG loadings (for the triphenylsulfonium type PAGs used in this work) in the resists shows a linear correlation with decreasing etch rate in these materials using both silicon dioxide and polymer etch recipes. The HS containing EUV resist platform shows significantly better etch resistance as compared to the analogous GB containing 193 nm resist platform. The elimination of electron-rich ester linkages and fluorine in the PAG anions is shown to further improve the etch resistance of the materials. The observed etch performance of the polymer-bound-PAG materials containing various levels of PAG loading and different PAG structures can not be well predicted using any current polymer etch rate model tested. Further work on providing useful predictive etch rate models for future resist design applications is essential for understanding the fundamental effects on the improved dry etch resistance.

10.3 References

[1] Ito, H., Willson, C. G., Chemical amplification in the design of dry developing resist materials, *Polym. Eng. Sci.* **1983**, *23*, 1012-1018.

[2] Ito, H., Willson, C. G., Applications of photoinitiators to the design of resists for semiconductor manufacturing, *Org. Coat. Appl. Polym. Sci. Proc.* **1983**, *48*, 60-64.

[3] Dektar, J. L., Hacker, N. P., Photochemistry of triarylsulfonium salts, *J. Am. Chem. Soc.* **1990**, *112*, 6004-6015.

[4] Hacker, N. P., Leff, D. V., Dektar, J. L., Cationic photoinitiators: solid state photochemistry of triphenylsulfonium salts, *Mol. Cryst. Liq. Cryst.* **1990**, *183*, 505-511.

[5] Crivello, J. V., Cationic polymerization - iodonium and sulfonium salt photoinitiators, *Adv. Polymer Sci.* **1984**, *62*, 1-48.

[6] Hacker, N. P., Welsh, K. M., Mechanistic studies on the poly(4-tert-butoxycarbonyloxystyrene)/triphenylsulfonium salt photoinitiation process, *Proc. SPIE* **1991**, *1466*, 384-393.

[7] Hacker, N. P., Hofer, D. C., Welsh, K. M., Photochemical and photophysical studies on chemically amplified resists, *J. Photopolym. Sci. Technol.* **1992**, *5*, 35-46.

[8] Tagawa, S., Nagahara, S., Iwamoto, T., Wakita, M., Kozawa, T., Yamamoto, Y., Werst, D., Trifunac, A. D., Radiation and photochemistry of onium salt acid generators in chemically amplified resists, *Proc. SPIE* **2000**, *3999*, 204-213.

[9] Enomoto, K., Moon, S., Maekawa, Y., Shimoyama, J., Goto, K., Narita, T., Yoshida, M., Novel electron-beam-induced reaction of a sulfonium salt in the solid state, *J. Vac. Sci. Technol. B* **2006**, *24*, 2337-2349.

[10] Nakano, A., Okamoto, K., Kozawa, T., Tagawa, S., Pulse radiolysis study on proton and charge transfer reactions in solid poly(methyl methacrylate), *Jpn. J. Appl. Phys.* **2004**, *43*, 4363-4367.

[11] Shigati, T., Okamoto, K., Kozawa, T., Yamamoto, H., Tagawa, S., Kai, T., Shimokawa, T., Relationship between acid generator concentration and acid yield in chemically amplified electron beam resist, *Jpn. J. Appl. Phys*. **2006**, *45*, 5735-5737.

[12] Yamamoto, H., Kozawa, T., Tagawa, S., Cao, H. B., Deng, H., Lesson, M., Polymer-structure dependence of acid generation in chemically amplified extreme ultraviolet resist, *J. Jpn. J. Appl. Phys.* **2007**, *46*, L142-L144.

[13] *International Technology Roadmap for Semiconductors (ITRS)* **2007**. (http://www.itrs.net/Links/2007ITRS/Home2007.htm).

[14] Schmid, G. M.; Stewart, M. D.; Wang, C.-Y.; Vogt, B. D.; Prabhu, V. M.; Lin, E. K.; Willson, C. G., Resolution limitations in chemically amplified photoresist systems, *Proc. SPIE* **2004**, *5376*, 333-342.

[15] Lin, Q.; Sooriyakumaran, R.; Huang, W.-S., Toward controlled resist line-edge roughness: material origin of line-edge roughness in chemically amplified positive-tone resists, *Proc. SPIE* **2000**, *3999*, 230-239.

[16] Wang, M.; Jarnagin, N. D.; Lee, C.-T.; Henderson, C. L.; Wang, Y.; Roberts, J. M.; Gonsalves, K. E., Novel polymeric anionic photoacid generators (PAGs) and corresponding polymers for 193 nm lithography, *J. Mater. Chem.,* **2006**, *16*, 3701-3707.

[17] Wang, M.; Gonsalves, K. E.; Rabinovich, M.; Wang, Y.; Roberts, J. M., Novel anionic photoacid generators (PAGs) and corresponding PAG bound polymers for sub-50 nm EUV lithography, *J. Mater. Chem.* **2007**, *17*, 1699-1706.

[18] Kunz, R. R.; Palmateer, S. C.; Forte, A. R.; Allen, R. D.; Wallraff, G. M.; DiPietro, R. A.; Hofer, D. C., Limits to etch resistance for 193-nm single-layer resists, *Proc. SPIE* **1996**, *2724*, 365-376.

[19] Gokan, H.; Esho, S.; Ohnishi, Y., Dry etch resistance of organic materials, *J. Electrochem. Soc.* **1983**, *130*, 143-146.

[20] Kishimura, S.; Endo, M.; Sasago, M., New 157-nm resist platform based on etching model for fluoropolymers, *Proc. SPIE* **2002**, *4690*, 200-211.

CHAPTER 11

SUMMARY AND RECOMMENDATIONS

11.1 Summary of Thesis Work

The development of next generation resist materials, as well as the advance of characterization techniques for studying the correlations between resist material structure/composition and the corresponding lithographic properties, is essential for the successful implementation of the NGL technologies for patterning components of future IC devices with sub-50 nm feature size resolution. Works presented in this thesis first demonstrate the design and development of advanced techniques for studying major resist parameters, such as sensitivity, acid diffusion, resolution, and LER. The structure-function relationships of novel polymer-bound-PAG resists are studied and characterized in the second part of the thesis work.

New techniques for determine PAG acid generation in the resist film upon exposure to radiation are developed and demonstrated in chapter 3 and 4. The first technique employs quantitative FTIR spectrometry of resist film deprotection behavior to measure *in situ* PAG acid generation in real resist film, while the second technique employs the ellipsometry method to monitor the absorption behavior of an acid-sensitive dye for measuring PAG acid generation. Models for describing PAG acid generation behavior and determining acid generation rate constant (i.e. the Dill C parameter) are also developed for these two techniques. The validity of these techniques is verified and shown high accuracy by comparing the results of selected PAG/polymer combinations with results reported by previous studies using different methods. The applicability and accuracy of using these techniques in different resist materials and experimental

conditions are also analyzed and discussed. These techniques provides major advantages including high precision and resolution, non-invasive and non-destructive experimental operation, material-saving and efficient acid quantification protocols, and the general applicability in various exposure and lithography equipments. The experimental design also demonstrates the capability of using these techniques to probe the effects of PAG and polymer matrix structures on PAG acid generation through direct PAG excitation and indirect polymer sensitization pathways.

An *in situ* experimental-modeling technique for studying acid reaction-diffusion behavior in a solid-state resist film is developed in chapter 5. The technique utilizes a newly-developed mesoscale resist model to represent the spatial composition of a resist film and a detailed stochastic acid reaction-diffusion process to simulate the physics and chemistry of a resist film during PEB. This technique requires only the deprotection behavior of a flood-exposed resist film baked at elevated temperature to extract acid diffusion coefficient with high precision. This advantage significantly simplifies the experimental operation and prevents the complication of characterizing initial acid distribution profile. These benefits eliminate possible errors introduced by complex experimental design and characterization, and extend the applicability of this technique to resist materials designed for various lithography technologies and exposure sources. This technique is verified by comparing the extracted acid diffusion coefficients of a resist film system to those extracted by a previously reported method. This technique also demonstrates the capability of studying effects of acid and polymer structures/properties on acid diffusivity in the resist film.

An ultra-high aerial image quality lithography technique is developed in chapter 6 for exploring the intrinsic patterning performance of resist materials. This technique combines the use of a high electron acceleration voltage EBL system and an ultra-thin free-standing silicon nitride membrane substrate to deliver ultra-high quality and resolution aerial image for resist film patterning. This technique is theoretically proved

having eliminated electron backscattering effect and uniform energy deposition profile through the whole polymer film depth using a Monte Carlo simulator modeling the trajectory of the incident electrons and the corresponding energy deposition profile in the polymer film. The patterning performance is experimentally evaluated having the capability of representing the intrinsic patterning performance, such as resolution, CD bias, CD uniformity, and LER, of a resist material that can not be clearly identified using other modern exposure techniques with poor to moderate aerial image quality and resolution.

Advanced characterization techniques developed in chapter 3~6 are applied to the study and investigation of novel resist materials for NGL technologies. The effects of direct PAG incorporation into the polymer main chain on the lithographic performance and resist behavior of the polymer-bound-PAG resists are studied in chapter 7. Polymer-bound-PAG resists, which have the PAG anion binding to the polymer main chain, exhibit significantly improved half-pitch resolution, lower LER, higher resist contrast, and comparable or higher sensitivity, larger resist processing window (i.e. larger exposure and focal latitudes) than its blended-PAG analogs. The improved lithographic performance of the anionic polymer-bound-PAG resist is speculated to be due to the combinatorial effect of high PAG loadings, reduced acid diffusivity, and homogeneous PAG distribution in such resist material. This work suggests the design of a single-component resist which can relieve the perceived limitations and tradeoffs between achieving sensitivity, resolution, and LER in traditional multi-component blended-PAG resists. This work also demonstrates the design concept that using single-component resists, either of polymer or molecule glass, is a very promising route to develop advanced resist materials with lithographic performance sufficient for NGL applications.

Beyond the experimental study, the fundamental effects of PAG incorporation into the polymer main chain on the lithographic performance of anionic polymer-bound-PAG resists are investigated in chapter 8 using a mesoscale stochastic resist lithography

modeling. In the case of equal sensitivity, the anionic polymer-bound-PAG resist shows less resist CD bias, less LER, and larger resist process window than the blended-PAG analogs. The simulated resist behavior is in well agreement with the experimental characterization results in chapter 7. This work clarify that the major contribution to improved lithographic performance of the anionic polymer-bound-PAG resists is the reduced acid diffusivity that leads to a high resist contrast and thus small resist CD bias and less LER. This study also provides correlations and scaling factors between resist lithographic performance (i.e. resist CD bias and LER) and the fundamental parameters of a resist material (i.e. PAG loadings and acid diffusivity). These characterized structure-function relationships can help the future design and evaluation of novel resist materials.

A series of PAG and base incorporated resist polymers (the third generation of polymer-bound-PAG resists) are developed and their lithographic performances are investigated in chapter 9. These polymers show good thermal stability and high glass transition temperatures that can facilitate resist processing and longer resist shelf life. However only one base-incorporated cationic polymer-bound-PAG resist shows improved resolution and comparable LER without a significant loss of photospeed. Anionic polymer-bound PAG resists shows decreased resolution due to the loss of resist-substrate adhesion that led to more substantial resist pattern collapse at larger feature sizes. Significant resist line bridging problems are also observed in several resist polymers, suggesting that possibly poor monomer compatibility and resist polymer compositional heterogeneity due to monomer reactivity ratio differences could be problematic in such resist material design. A successful development of this class of material requires the design of resist composition with more compatible PAG and base quencher functional groups.

Other important structure-function relationships of resist materials are investigated in chapter 10. The effect of polymer and PAG structure on PAG acid

generation under excitation (DUV) and ionization (EB) radiations are studied using the on-wafer ellipsometry of acid-sensitive dye method. Iodonium slats show significant polymer sensitization effect under DUV exposure. The higher electron affinity of the iodonium salts may provide higher probability of being an electron acceptor and higher acid generation efficiency through the polymer sensitization pathway. Most of the sulfonium, iodonium, and non-ionic PAGs show significantly improved acid generation efficiency in pHOST matrix if compared with the efficiency in pS matrix under high-vacuum EBL. The inefficient acid generation in pS matrix may be due to the lack of proton source from the less reactive styrene cation. Poly(methacrylate) also enhances PAG acid generation under EBL, indicating that the ionized methacrylate subunit may provide easy proton source for PAG acid generation.

Increasing PAG loadings in the resist film shows linear correlations with decreasing reactive ion etch rate using silicon dioxide and polymer etch recipes. Polymer-bound-PAG resists for EUVL shows higher etch resistance than those for 193 nm lithography due to the replacement of GB with HS subunit. Resist etch resistance is further improved by eliminating electron-rich ester linkages and fluorine atoms in PAG structures. However the observed etch performance of the polymer-bound-PAG materials containing various levels of PAG loading and different PAG structures can not be well predicted using current polymer etch rate models. This study suggests possible effects other than the primary polymer structure and composition may contribute to the improvement of plasma etch resistance of high PAG loading polymer-bound-PAG resists.

11.2 Recommendations of Future Work

11.2.1 Advanced Resist Characterization Techniques

The advanced resist characterization techniques developed in this thesis can be further extend and modified to enhance their accuracy and applicability to various resist materials and lithography conditions. For the technique which utilizes FTIR spectrometry to quantify resist film deprotection and determine PAG acid generation rate, the original model can be extend to study PAG acid generation in resist polymer with low-activation energy of deprotection by using detailed kinetic models to describe both the acid-catalyzed and auto-catalyzed deprotection reactions of the resist polymer during PEB. The applicability of this technique to ultra-thin resist film (< 100 nm) can also be achieved by using a multi-bounce attenuated total reflection FTIR (ATR-FTIR) spectrometry setup to enhance the sensitivity and signal-to-noise ratio of resist deprotection quantification.

For the technique which measures PAG acid generation behavior in a polymer film using the on-wafer ellipsometry to quantify the absorption behavior of acid-sensitive dyes doped in the polymer film, a more detail physical model can be developed to replace the F parameter and further enhance the accuracy of this technique. In current model a single F parameter is used to describe proton-dye contact ratio in polymer films under different exposure dose, and thus different acid concentration. However in reality the proton-dye contact ratio is a function of acid concentration in a polymer film with constant dye loading. Exposure dose variation, as well as the energy deposition profile in the resist film (i.e. the standing wave intensity deposition profile) may contribute to variations of F parameters. Investigating the dependence of proton-dye contact probability on acid concentration in a polymer film can help to develop a more precise model for extracting PAG acid generation with this technique. On the other hand, studying the dependence of proton-dye contact on different acid property, such as acid strength and acid diffusivity, may also helpful to modify the current model and extend its applicability to the study of various novel PAGs.

For the mesoscale stochastic experimental-modeling technique for determine acid diffusivity in resist film, current stochastic acid reaction-diffusion model can precisely describe acid diffusion behavior in resist matrix containing two different polymer subunits. Although the development of resist material tends to design resist polymer with multiple subunits to obtain the desired resist properties, the use of two acid diffusion coefficients may be already adequate to describe acid diffusion behavior in such matrix since the deprotected polymer subunits are usually much more polar than other subunits in the matrix, and a two acid diffusivity model can well represent this acid diffusivity switch behavior. This model can still be further extended to a model containing three or more acid diffusion coefficients to describe acid diffusion behavior in resist matrix containing more than two polymer subunits. However the use of model with many acid diffusion coefficients may result in the dependences between extracted acid diffusion coefficients. This effect should be evaluated before implementation.

11.2.2 Structure-Function Relationships of Resist Materials

The development and characterization of polymer-bound-PAG resists demonstrated in this thesis show the promising route of designing a single-component resist material which can relieve the tri-lateral tradeoff between achieving sensitivity, resolution, and LER through increasing PAG loading capability, improving PAG distribution homogeneity, and confining acid diffusivity. This concept works well under optical lithography since the increase of PAG subunits is proportional to the increase of acid concentration under the same exposure dose. However current polymer-bound-PAG resists still surfer from the lack of sensitivity under EUV and EB lithography. Under high-vacuum ionization radiation such as EUV and EB, the mechanisms of PAG decomposition and acid generation are different from those under excitation radiation and the absorption of high-energy photons becomes non-specific to PAG molecules. Polymer

sensitization on the contrary becomes the major mechanism for PAG acid generation under ionization radiation as illustrated in chapter 10. The experience and rules built for PAG acid generation under excitation radiation can not be directly applied and utilized to novel resist material design. Systematic studies using the techniques developed in this thesis for investigating the dependences of PAG and polymer structures on PAG acid generation under ionization radiation are essential and will be highly useful for designing more sensitive PAGs and resist materials for ionization radiations exposure techniques.

One major limitation of resist resolution is the resist image blur induced by acid diffusion during PEB. Although current polymer-bound-PAG resists can achieve 30 nm 1:1 L/S intrinsic patterning capability with several nanometer image blur as illustrated in chapter 7, such several-nanometer image blur will eventually become critical for future sub-30 nm resolution requirements. Acid diffusivity can be affected by acid and polymer properties as illustrated in chapter 5 that complicates the predictability of acid diffusivity and image blur behavior of a resist material. Moreover, as ultra-thin resist film (< 150 nm) is required for printing features with sub-50 nm resolution, the physical and mechanical properties of an ultra-thin resist film may be different to a thicker film since the interface effects may start to interfere and dominate the ultra-thin resist film property. Acid diffusivity in such ultra-thin resist film may be different to that in thicker resist films. A thorough study of the structure-function relationships between acid diffusivity and resist material properties will be of significant importance for more precise control and elimination of resist image blur caused by acid diffusion.

Another major limitation of resist resolution is the collapse of resist lines during the resist processing. As depicted in chapter 9, resist pattern collapse is mainly due to the unbalanced capillary force induced by the rinsing water/solvent in the trench between resist lines during the drying process. This capillary force is dependent on the surface tension of the rinsing water/solvent and the surface energy of the side wall of the resist line. As the continued shrink down of feature sizes printing on the resist film, the

reduction of resist pattern dimension results in a reduction of the mechanical strength of the resist pattern and the adhesion force at the resist line/substrate interface. Small change in resist composition may lead to dramatic response of resist pattern collapse behavior as illustrated in chapter 9. Figure 11.1 shows the structures of polymer-bound-PAG resists based on hydroxystyrene (HS), 2-ethyl-2-adamantyl methacrylate (EA), and triphenylsulfonium salt of 1,1,2 –trifluorobutanesulfonate methacrylate (TPS.TFBSM) PAG. The corresponding compositions and properties of these resist polymers are listed in table 11.1. SEM images of the maximum achievable dense feature resolutions of these resist materials are shown in figure 11.2. HS-EA-TFBSM resist shows a 45 nm 1:1 L/S resolution. Less than 5 mol% incorporation of fullerene (C60) or adamantanol (HA) subunits lead to dramatic losses of resolution due to serious resist line adhesion failure that cause pattern collapse problems. On the other hand, the side wall of a positive-tone resist line usually contains partially-deprotected polymer. The polar deprotected polymer subunits introduce hydrophilicity to the resist line and thus increase the capillary force acting on the resist line during the drying of the resist film. Based on these facts, it is expected that resist pattern collapse will become the most dominating factor of resist materials for sub-50 nm lithography applications.

A thorough study of the structure-function relationships between resist material properties and resist pattern collapse behavior will be necessary for understanding the fundamental causes of resist pattern collapse. Development of methods for reducing the surface energy of the resist line surface (i.e. the affinity between the surface of the resist line and the rinsing solvent) through the use of surfactants or cross-linkers will provide the direct impact on relieving resist resolution limit dominated by pattern collapse behavior.

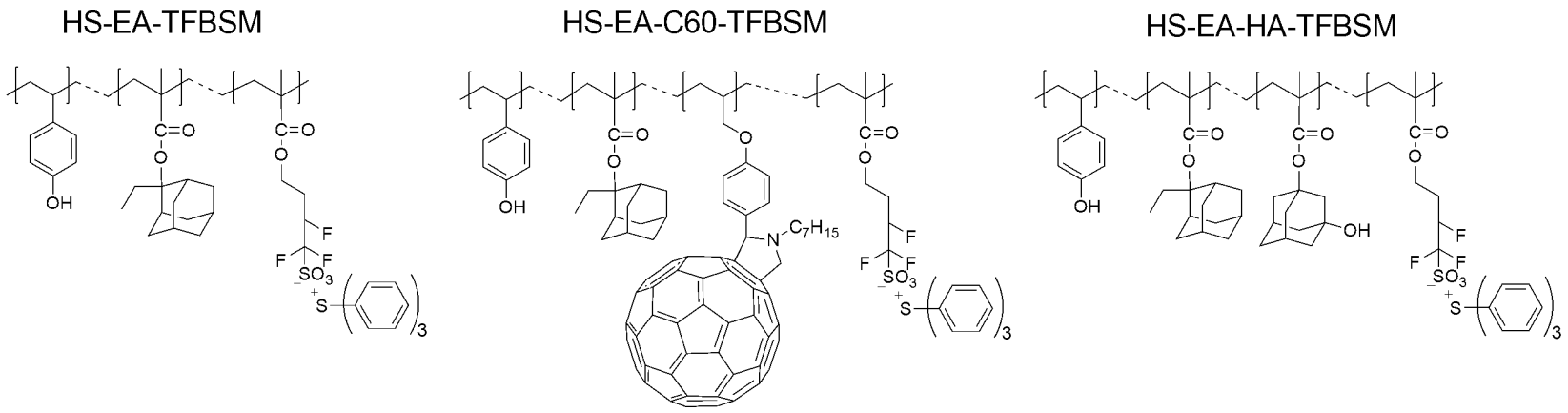

Figure 11. 1 Structures of HS-EA-TFBSM based polymer-bound-PAG resists.

Table 11. 1 Compositions and thermal properties of HS-EA-TFBSM based polymer-bound-PAG resists.

Resist Polymer	Polymer Composition				Mw (PDI)	Stability (^{o}C)	Tg (^{o}C)
	HS	EA	C60/HA	TFBSM			
HS-EA-TFBSM	38.5	56.2	0.0	5.3	2600 (1.6)	170	117
HS-EA-C60-TFBSM	37.6	51.7	4.4	6.3	4300 (2.2)	203	162
HS-EA-HA-TFBSM	40.8	46.3	4.7	8.2	2900 (1.7)	172	145

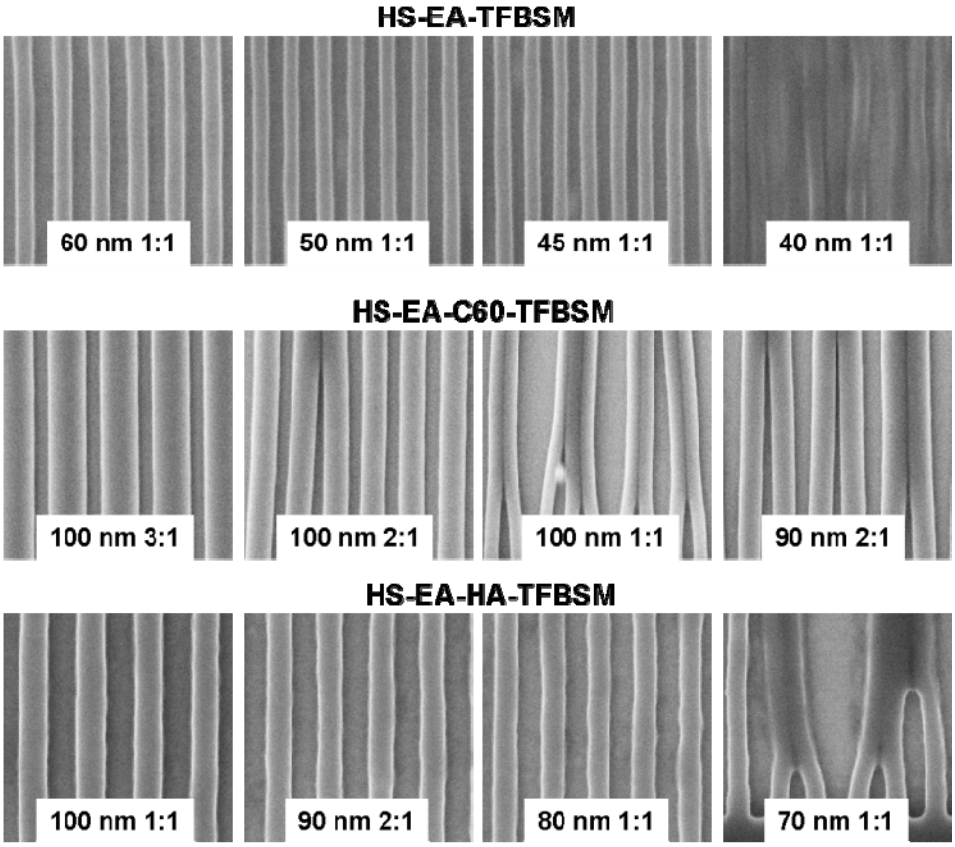

Figure 11. 2 SEM images showing the dense feature resolution of HS-EA-TFBSM based polymer-bound-PAG resists.

The ultra-high aerial image quality patterning technique developed in chapter 6 provides the best protocol for studying resist pattern collapse behavior. The straight and uniform side wall of the resist line produced by this technique can facilitate the precise quantification of pressure and capillary force acting on the side wall of the resist line. An example resist pattern design for monitoring resist pattern collapse behavior is shown in figure 11.3.[1] For a specific pattern dimension as shown in figure 11.3, the corresponding pressure difference *P* acting on the side wall of the resist line during the drying process can be calculated by equation (11.1).

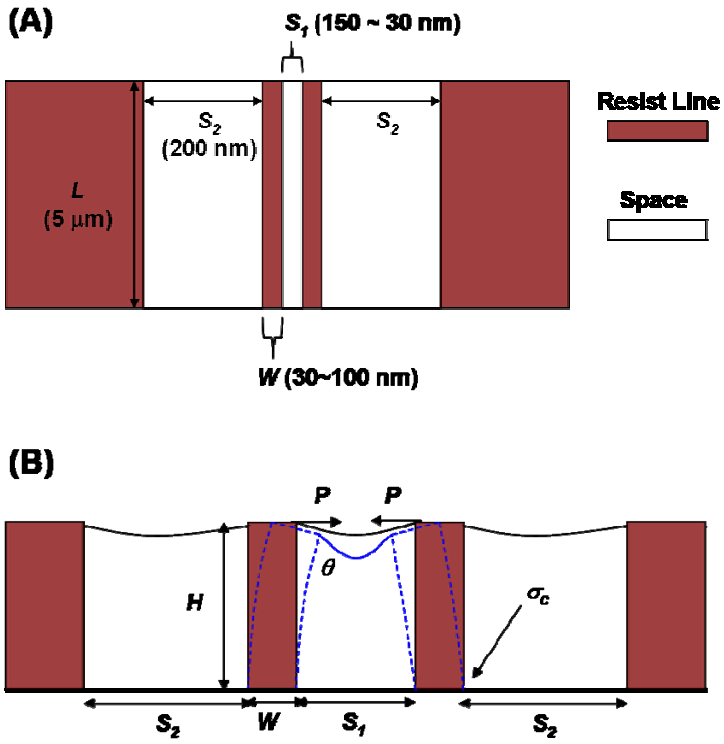

Figure 11. 3 Design of resist pattern for studying resist pattern collapse behavior: (A) top-down view and (B) cross-section view.

$$P = 2\gamma \cos\theta \left(\frac{1}{S_1} - \frac{1}{S_2} \right) \tag{11.1}$$

Here γ is the surface tension of the rinsing water/solvent. The pressure difference acts on the side wall of the resist line that causes the bending of the resist line. The maximum tensile stress σ_{max} exerting on the outermost of the resist line/substrate interface is correlated to the Young's modulus and the bending curvature of the resist line, This tensile stress can be calculated by equation (11.2).[2]

$$\sigma_{max} = 6\gamma \cos\theta \left(\frac{H}{W} \right)^2 \left(\frac{1}{S_1} - \frac{1}{S_2} \right) \tag{11.2}$$

At a certain point right before the resist lines permanently bend or unstuck from the substrate and resist pattern collapse occur, the critical stress σ_c in figure 11.3(B) describing the maximum tensile stress under which the resist line can sustain is approximately equal to the maximum tensile stress σ_{max} experienced by the resist line at that point. The use of the high resolution patterning technique and the specific resist pattern design for the study of the pattern collapse behavior of a molecular resist composed of 95.0 mol% 1,1,2,2-tetra(4-hydroxyphenyl)ethane tetraglycidyl ether (4-Ep, Sigma-Aldrich) and 5.0 mol% triphenylsulfonium hexafluoroantimonate (TPS.SbF_6, Midori Kagaku Co., Ltd.) is performed and the resultant SEM image is shown in figure 11.4. The rinsing solvent for this resist material is isopropyl alcohol (IPA, Sigma Aldrich) which has a surface tension of 23.0 mN/m and a statistic contact angle of 6 degrees on the resist film surface. The width (W) and height (H) of resist lines are 40 nm and 275 nm, respectively. The width of the outer space (S_2) is 200 nm. While continuously reducing the inner space width (S_1) from 150 nm to 30 nm, resist lines start to collapse at a 125 nm inner space width. The narrower the inner space width, the more serious the pattern collapse behavior. The corresponding critical stress (σ_c) of the resist lines are calculated having the value of 10.2 MPa. Resist line critical stresses of a 4-Ep blend TPS.SbF6 negative-tone molecule resist and a partially protected t-BOC pHOST blend TPS.SbF6 polymeric resist are shown in figure 11.5. The mechanical strength of a negative-tone epoxide cross-linking resist is significantly higher than a polymeric positive-tone resist. Moreover, the critical stress of the 4-Ep negative-tone resist decreases when the resist film thickness is below 80 nm. This result demonstrates the existence of ultra-thin resist film effect on resist mechanical strength. Such results demonstrate the capability of studying the correlations between resist material properties and pattern collapse behaviors.

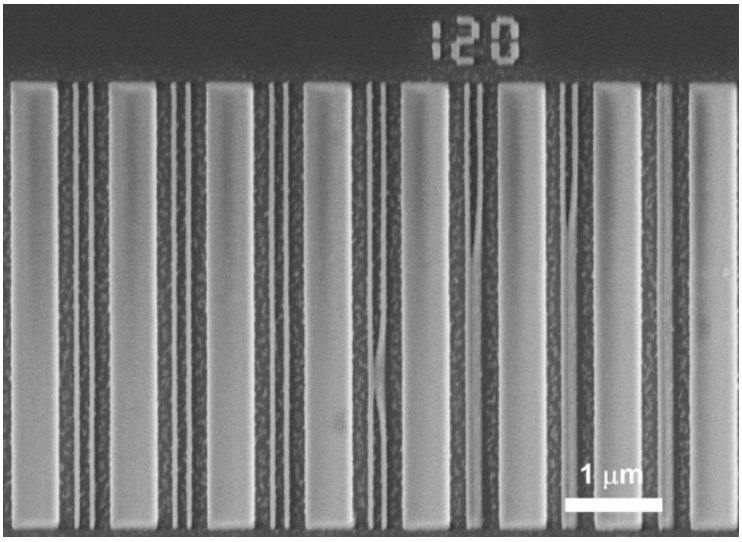

Figure 11. 4 SEM image showing the pattern collapse analysis of a 4-Ep blend TPS.SbF_6 molecular resist.

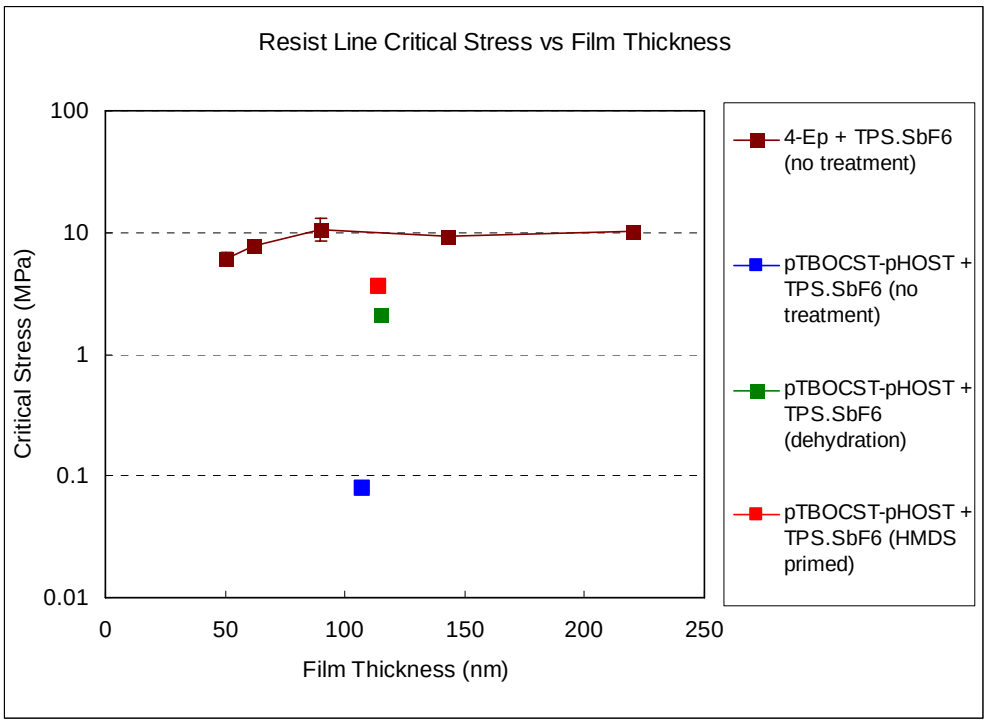

Figure 11. 5 Dependence of resist line critical stress on resist film thickness of a 4-Ep blend TPS.SbF6 negative-tone molecule resist and a partially protected t-BOC pHOST blend TPS.SbF6 positive-tone resist.

11.3 References

[1] Stoykovich, M. P.; Cao, H. B.; Yoshimoto, K.; Ocola, L. E.; Nealey, P. F., Deformation of nanoscopic polymer structures in response to well-defined capillary forces, *Adv. Mater.* **2003**, *15*, 1180-1184.

[2] Namatsu, H.; Kurihara, K.; Nagase, M.; Iwadate, K.; Murase, K., Dimensional limitations of silicon nanolines resulting from pattern distortion due to surface tension of rinse water, *Appl. Phys. Lett.* **1995**, *20*, 2655-2657.

APPENDIX A

ACID GENERATION BEHAVIOR OF PAGS

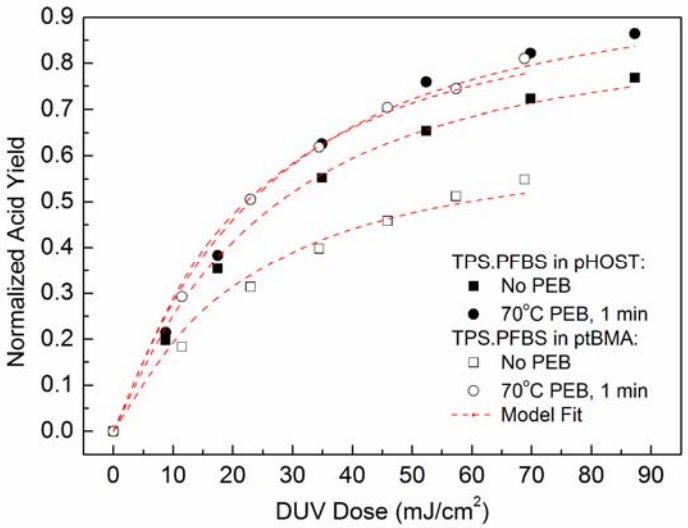

Figure A. 1 TPS.PFBS acid generation under DUV exposure.

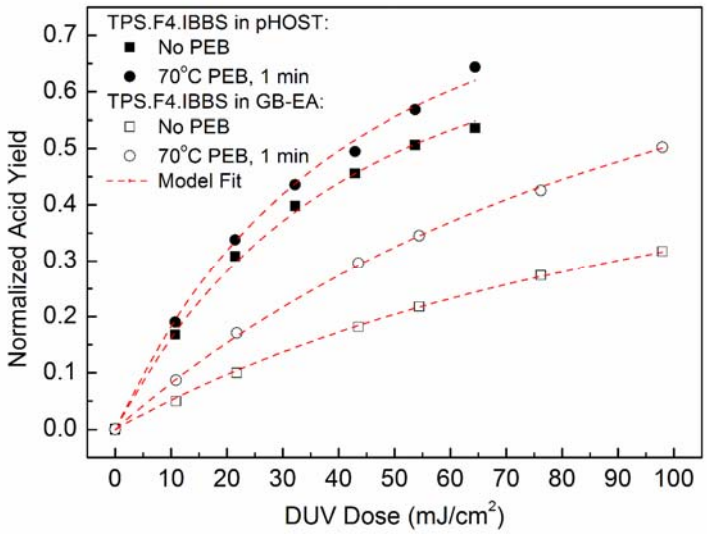

Figure A. 2 TPS.F4.IBBS acid generation under DUV exposure.

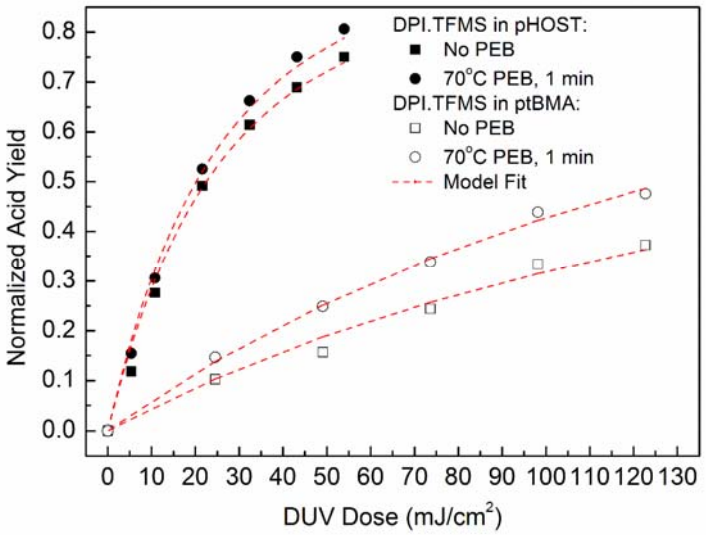

Figure A. 3 DPI.TFMS acid generation under DUV exposure.

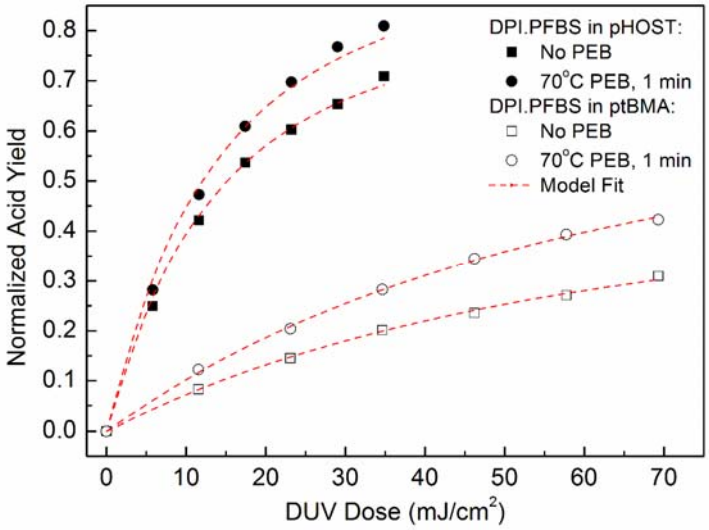

Figure A. 4 DPI.PFBS acid generation under DUV exposure.

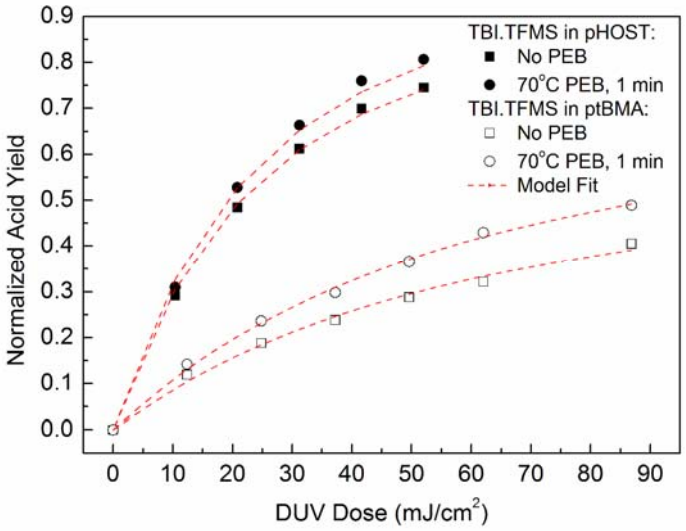

Figure A. 5 TBI.TFMS acid generation under DUV exposure.

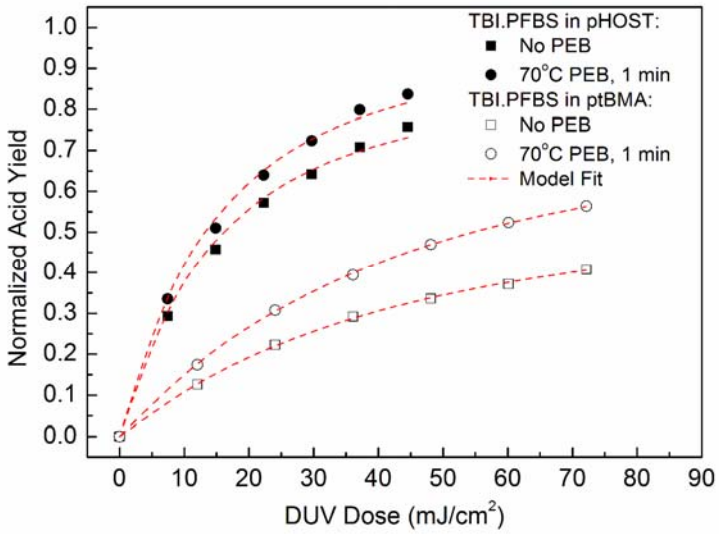

Figure A. 6 TBI.PFBS acid generation under DUV exposure.

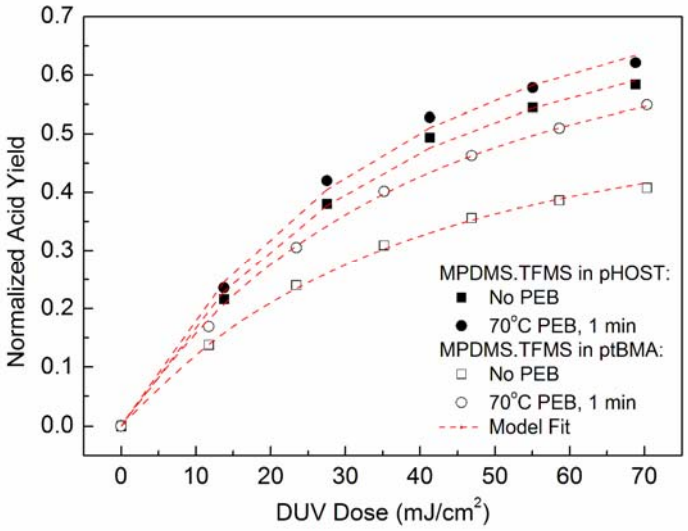

Figure A. 7 MPDMS.TFMS acid generation under DUV exposure.

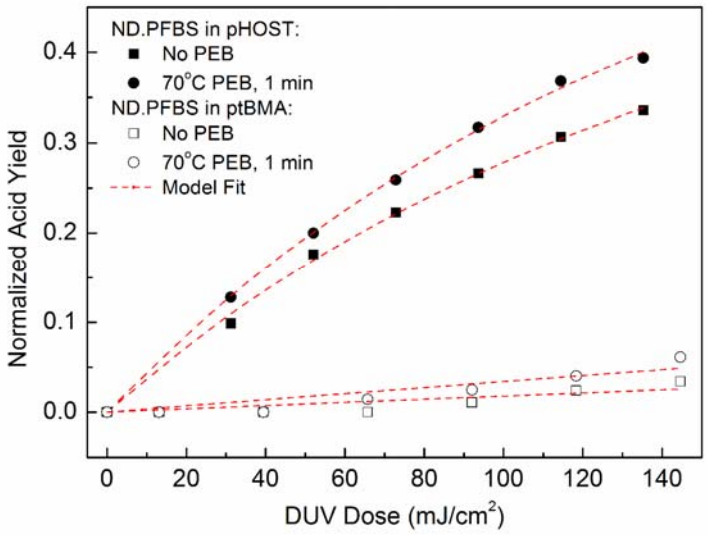

Figure A. 8 ND.PFBS acid generation under DUV exposure.

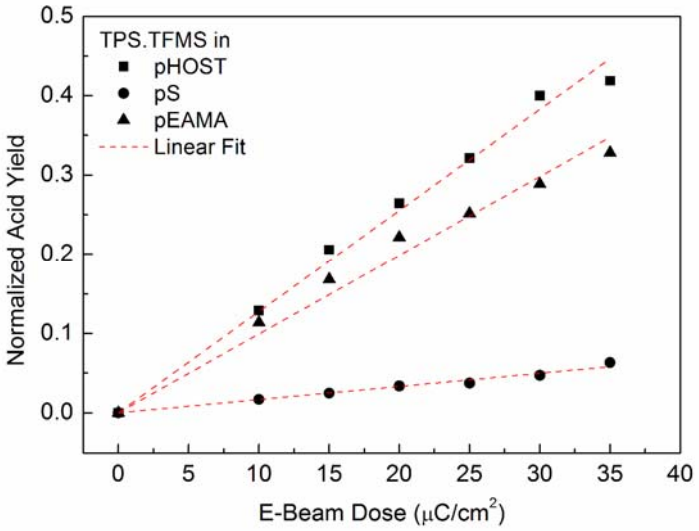

Figure A. 9 TPS.TFMS acid generation under EB exposure.

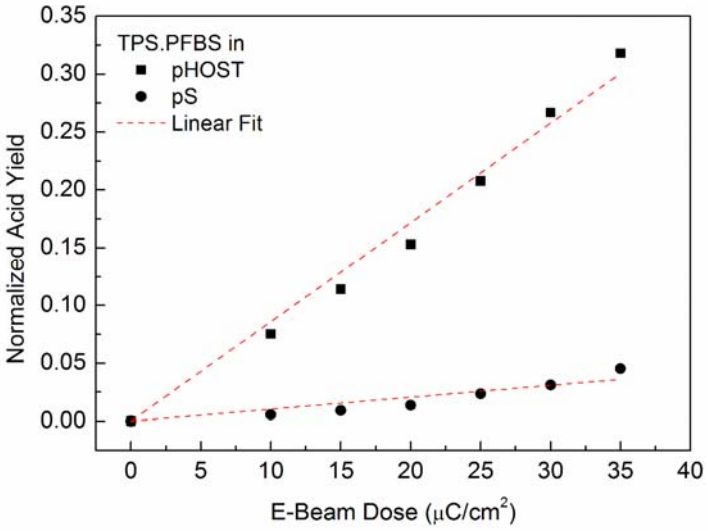

Figure A. 10 TPS.PFBS acid generation under EB exposure.

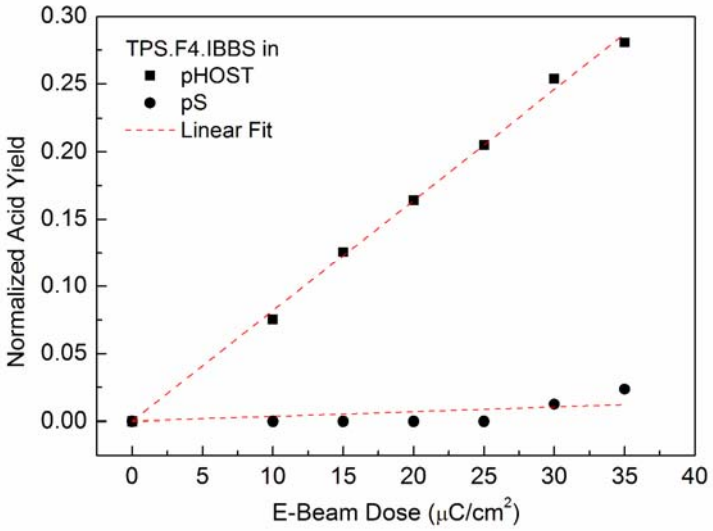

Figure A. 11 TPS.F4.IBBS acid generation under EB exposure.

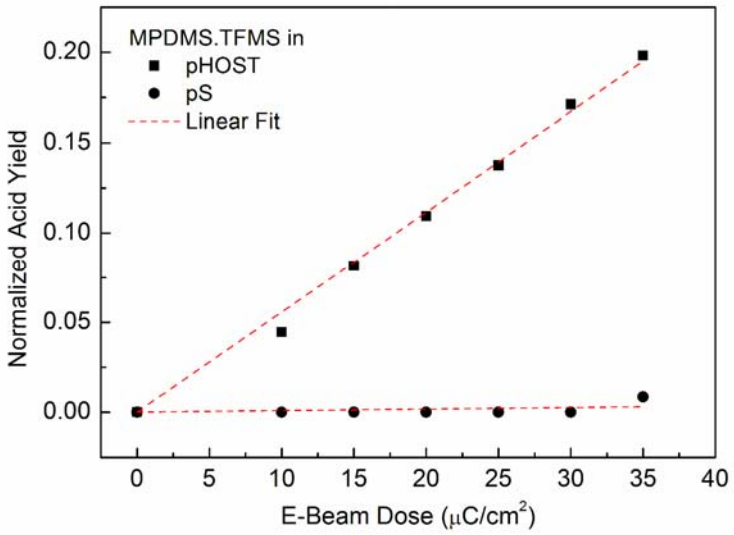

Figure A. 12 MPDMS.TFMS acid generation under EB exposure.

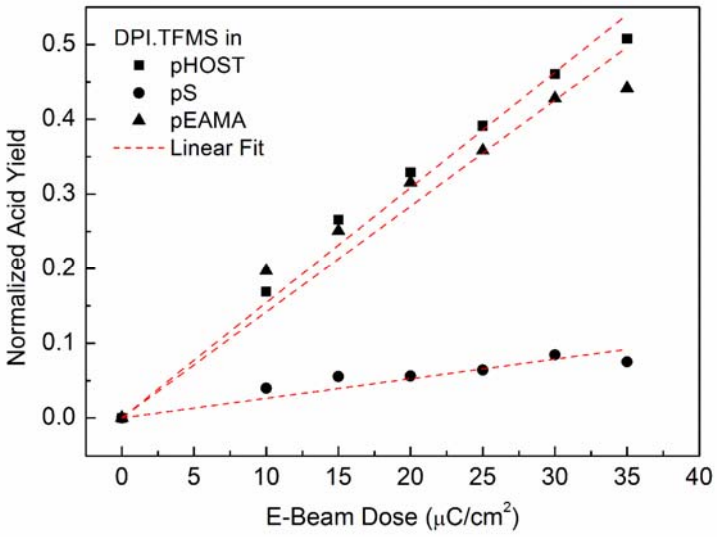

Figure A. 13 DPI.TFMS acid generation under EB exposure.

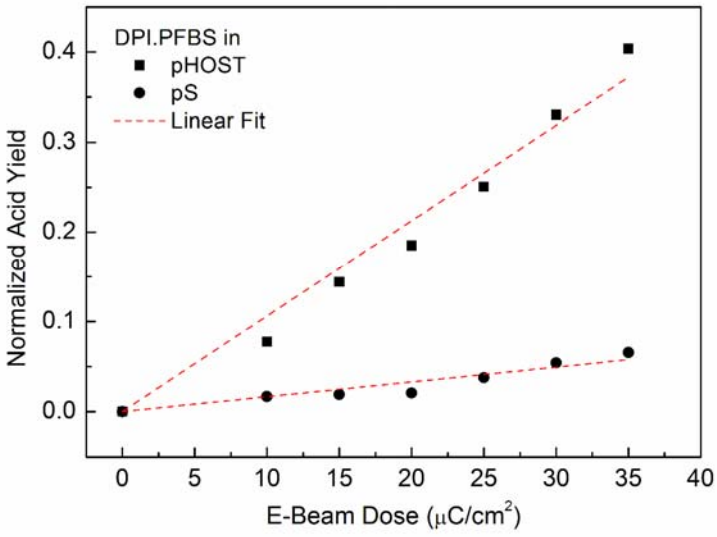

Figure A. 14 DPI.PFBS acid generation under EB exposure.

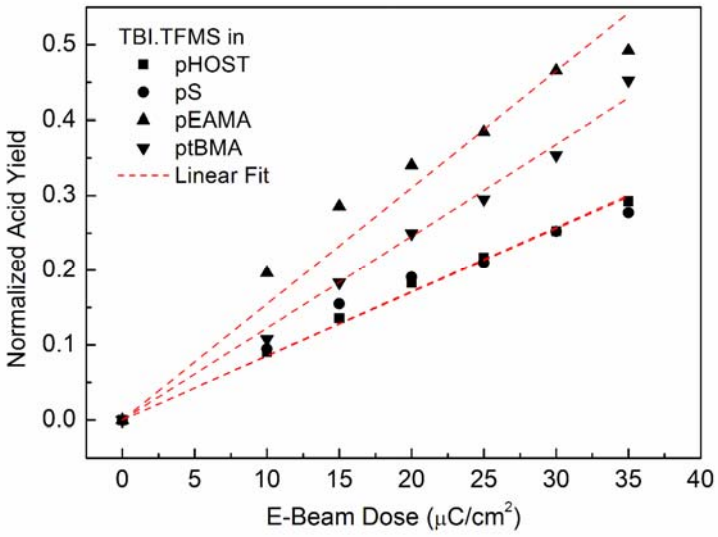

Figure A. 15 TBI.TFMS acid generation under EB exposure.

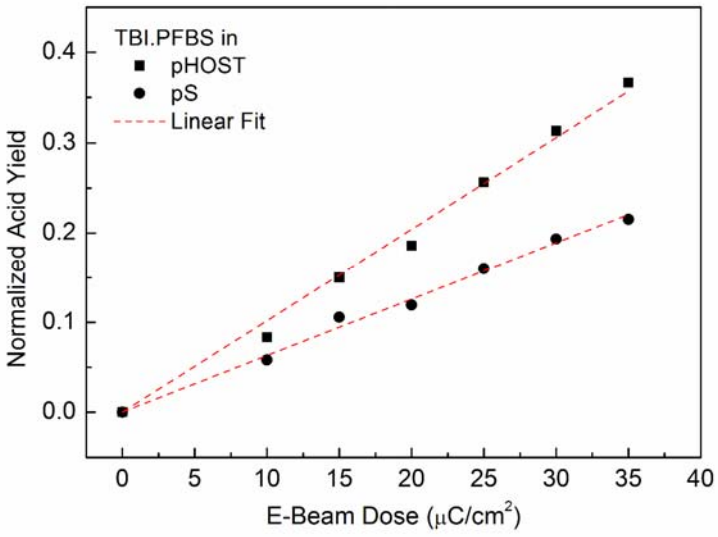

Figure A. 16 TBI.PFBS acid generation under EB exposure.

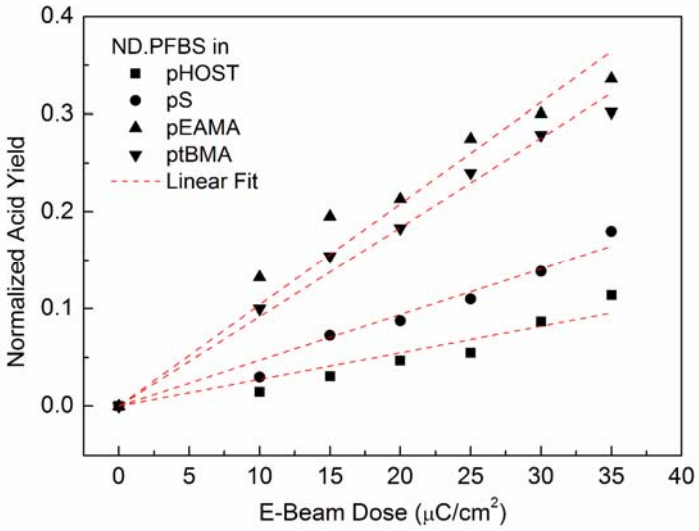

Figure A. 17 ND.PFBS acid generation under EB exposure.

APPENDIX B

MATLAB CODES FOR RESIST LINE SEM IMAGE ANALYSIS

```
clear

% Parameters for SEM image process and analysis
FILE_NAME='file_name.tif';              % Set image file name
FILTER_SIZE=2;                          % Set Gaussian filter size (pixel)
BACKGROUND=70;                          % Set background intensity subtraction
LINENO=1;                               % Set # of lines measured
IMAGE_ROTATE=0.75;                      % Image rotate angle

% Resist line parameters
X_MEASURE_L1=810;                       % Set start X measurement pixel (left edge)
X_MEASURE_R1=870;                       % Set end X measurement pixel (right edge)
Y_MEASURE_START=90;                     % Set start Y measurement pixel
Y_MEASURE_END=660;                      % Set end Y measurement pixel
SIGNAL_THRESHOLD_LEFT=0.55;             % Set signal threshold (left edge)
SIGNAL_THRESHOLD_RIGHT=0.55;            % Set signal threshold (right edge)

fprintf('-----------------------------------------\n');
fprintf('Line Edge Roughness (LER) analysis program\n');
fprintf('1: Line edge profile analysis\n');
fprintf('2: Sigma(L) vs L analysis\n');
fprintf('3: Height-height correlation analysis\n');
fprintf('4: Spatial-frequency analysis of LER\n');
fprintf('-----------------------------------------\n');

ACTNO=input('Choose one analysis method:');

% SEM image input & modification
[z_origin,map] = imread(FILE_NAME);                     % Read original image
z_input=imrotate(z_origin,IMAGE_ROTATE,'bilinear');     % Rotate original image
z=wiener2(z_input,[FILTER_SIZE FILTER_SIZE]);           % Filter rotated image
z_sub=double(z)-BACKGROUND;                             % Background intensity substation
z_sub_nofilter=double(z_input)-BACKGROUND;
z_max=max(max(z_sub(1:660,:)));                         % Maximum pixel intensity
z_max_nofilter=max(max(z_sub_nofilter(1:660,:)));
z_sub_norm=z_sub/double(z_max);                         % Normalize pixel intensity
z_sub_norm_nofilter=z_sub_nofilter/double(z_max_nofilter);

% Pixel size calibration
x_calib_left=200;                       % SEM scale bar left edge (pixel)
x_calib_right=350;                      % SEM scale bar right edge (pixel)
y_calib=716;                            % SEM scale bar Y position (pixel)
calib_length=100; % nanometer           % Scale of scale bar (nm)

x_size=size(z,2);
y_size=size(z,1);
x=linspace(1,x_size,x_size);
y=linspace(1,y_size,y_size);
x_calib_peak=zeros(1,1);
```

```
peakno=1;
for xi=x_calib_left:x_calib_right
   if z_input(y_calib,xi)<200
      x_calib_peak(peakno,1)=xi;
      peakno=peakno+1;
   end
end

if size(x_calib_peak,1)==6
   pix_length=calib_length/((x_calib_peak(4,1)+x_calib_peak(6,1))/2-(x_calib_peak(1,1) +
         x_calib_peak(3,1))/2)
end
if size(x_calib_peak,1)==4
   pix_length=calib_length/((x_calib_peak(4,1)+x_calib_peak(3,1))/2-(x_calib_peak(1,1) +
         x_calib_peak(2,1))/2)
end
if size(x_calib_peak,1)==2
   pix_length=calib_length/((x_calib_peak(2,1)-(x_calib_peak(1,1))))
end

% Determine line edge position
Line_measured=1
x_measure_left=X_MEASURE_L1;
x_measure_right=X_MEASURE_R1;

measure_no=0;
for yi=Y_MEASURE_START:1:Y_MEASURE_END

   x_thred=0;
   measure_no=measure_no+1;

   for xi=x_measure_left:int16((x_measure_right+x_measure_left)/2)
      if z_sub_norm(yi,xi)>SIGNAL_THRESHOLD_LEFT
         x_thred=x_thred+1;
         x_measure_thred(x_thred,1)=xi;
      end
   end

   for xi=int16((x_measure_right+x_measure_left)/2):x_measure_right
      if z_sub_norm(yi,xi)>SIGNAL_THRESHOLD_RIGHT
         x_thred=x_thred+1;
         x_measure_thred(x_thred,1)=xi;
      end
   end

   y_measured(measure_no)=yi;
   l_edge(line_measured,measure_no)=double(x_measure_thred(1,1));
   r_edge(line_measured,measure_no)=double(x_measure_thred(x_thred,1));
   clear x_measure_thred
end

l_edge_avg(line_measured)=mean(l_edge(line_measured,:));
r_edge_avg(line_measured)=mean(r_edge(line_measured,:));
l_edge_avg_plot(line_measured,1:measure_no)=l_edge_avg(line_measured);
r_edge_avg_plot(line_measured,1:measure_no)=r_edge_avg(line_measured);
```

```
% Option 1: Line edge profile check
if ACTNO==1
   subplot(2,1,1), plot(linspace(1,x_size,x_size), z_sub_norm(300,:),'-k', linspace(1,x_size,x_size),
         z_sub_norm_nofilter(300,:), '--k', linspace(1,x_size,x_size),
         SIGNAL_THRESHOLD_LEFT, '-.k'),;
   subplot(2,1,2), plot(l_edge,linspace(Y_MEASURE_END, Y_MEASURE_START,
         (Y_MEASURE_END-    Y_MEASURE_START+1)), 'k.',
         r_edge,linspace(Y_MEASURE_END, Y_MEASURE_START,     (Y_MEASURE_END-
         Y_MEASURE_START+1)), 'k.', l_edge_avg_plot,linspace(Y_MEASURE_END,
         Y_MEASURE_START, (Y_MEASURE_END-Y_MEASURE_START+1)), 'r-',
         r_edge_avg_plot, linspace(Y_MEASURE_END, Y_MEASURE_START,
         (Y_MEASURE_END-Y_MEASURE_START+1)) ,'r-');

   for yi=Y_MEASURE_START:1:Y_MEASURE_END
      z_input(yi,l_edge(:,yi-Y_MEASURE_START+1))=0;
      z_input(yi,r_edge(:,yi-Y_MEASURE_START+1))=0;
   end
   imwrite(z_input,'lercontour.tif','tif');                    % Mark edge profile on SEM image
end

% Option 2: Sigma(L) vs L plot

if ACTNO==2
   m_pitch=3;
   for edge_pix_length=90:m_pitch:560
      for i=1:(edge_pix_length)/m_pitch
         l_edge_pickup(line_measured,i)=l_edge(line_measured,i*m_pitch+10);
         r_edge_pickup(line_measured,i)=r_edge(line_measured,i*m_pitch+10);
      end

      % Calculation of CD and LER
      l_edge_pickup_avg=mean(l_edge_pickup');
      r_edge_pickup_avg=mean(r_edge_pickup');
      CD=(r_edge_pickup_avg-l_edge_pickup_avg)*pix_length;

      sum_LER_l=0;
      sum_LER_r=0;
      for j=1:edge_pix_length/m_pitch
         sum_LER_l=sum_LER_l+((l_edge_pickup(line_measured,j)-
          l_edge_pickup_avg(line_measured))*pix_length)^2;
         sum_LER_r=sum_LER_r+((r_edge_pickup(line_measured,j)-
          r_edge_pickup_avg(line_measured))*pix_length)^2;
      end
      LER_l(line_measured)=(sum_LER_l/(edge_pix_length/m_pitch))^0.5;
      LER_r(line_measured)=(sum_LER_r/(edge_pix_length/m_pitch))^0.5;

       LWR(line_measured)=((sum_LER_l/(edge_pix_length/m_pitch))+(sum_LER_r/(edge_pix_le
       ngth/m_pitch)))^0.5;

      line_length(edge_pix_length/m_pitch)=edge_pix_length*pix_length;
      CD_line_length(edge_pix_length/m_pitch)=mean(r_edge_pickup_avg-
          l_edge_pickup_avg)*pix_length;
      LER_line_length(edge_pix_length/m_pitch)=0.5*(mean(LER_l)+mean(LER_r));
      LWR_line_length(edge_pix_length/m_pitch)=mean(LWR);
   end
```

```
   subplot(2,1,1), plot(line_length,CD_line_length,'k.-');
   subplot(2,1,2), plot(line_length,LER_line_length,'k.-',line_length,LWR_line_length,'k.-');

   Average_3sLER=LER_line_length(end)*3
   Average_3sLWR=LWR_line_length(end)*3
   Average_CD=CD

end

%Option 3: Height-height correlation

if ACTNO==3
   d=pix_length;
   N=Y_MEASURE_END-Y_MEASURE_START+1;

   for line_measured=1:LINENO
      for m=1:600
         sum_G_l=0;
         sum_G_r=0;
         for i=1:N-m
            sum_G_l=sum_G_l+((l_edge(line_measured,i+m)-l_edge_avg(line_measured)) *
                  pix_length-(l_edge(line_measured,i)-l_edge_avg(line_measured))*pix_length)^2;
            sum_G_r=sum_G_r+((r_edge(line_measured,i+m)-r_edge_avg(line_measured)) *
                  pix_length-(r_edge(line_measured,i)-r_edge_avg(line_measured))*pix_length)^2;
         end
         G_l(line_measured,m)=(1/(N-m)*sum_G_l)^0.5;
         G_r(line_measured,m)=(1/(N-m)*sum_G_r)^0.5;
         r(m)=m*d*pix_length;
      end
   end

   G=0.5*(mean(G_l)+mean(G_r));
   plot(r,G,'k.-');
end

% Option 4: Spatial-frequency analysis of resist line

if ACTNO==4
   for line_measured=1:LINENO
      l_edge_fft(line_measured,:)=fft((l_edge(line_measured,:)-
         l_edge_avg_plot(line_measured,:))*pix_length);
      r_edge_fft(line_measured,:)=fft((r_edge(line_measured,:)-
         r_edge_avg_plot(line_measured,:))*pix_length);
      PS_l(line_measured,:)=(abs(l_edge_fft(line_measured,:))).^2/(Y_MEASURE_END-
         Y_MEASURE_START+1)^2;
      PS_r(line_measured,:)=(abs(r_edge_fft(line_measured,:))).^2/(Y_MEASURE_END-
         Y_MEASURE_START+1)^2;

   end
   PS=0.5*(PS_l+PS_r);
   Freq=(1:(Y_MEASURE_END-Y_MEASURE_START+1))/((Y_MEASURE_END-
         Y_MEASURE_START+1)*pix_length);
   plot(Freq(2:(Y_MEASURE_END-Y_MEASURE_START+1-10)),PS(2:(Y_MEASURE_END-
         Y_MEASURE_START+1-          10)),'k-');
end
```

VITA

CHENG-TSUNG LEE, the son of Yuan-Ching Lee and Jin-Jiu Huang, was born in Kaohsiung, Taiwan, on October 2nd, 1975. After graduating from the Taipei Municipal Jianguo High School in Taipei, Taiwan, in 1994, Cheng-Tsung enrolled in the National Chung-Hsing University in Taichung, Taiwan, and received his Bachelor of Science in Chemical Engineering in 1998. He enrolled in the National Tsing-Hua University in Hsinchu, Taiwan, and received a Master of Science in Chemical Engineering in 2000. After the completion of his master's degree, he served as a lieutenant in Army, R.O.C. for twenty months and joined in the Institute of Chemistry, Academia Sinica, in Taipei, Taiwan as a full-time research assistant for two years. He began pursuing his Ph.D. in Chemical Engineering at the Georgia Institute of Technology in the Fall of 2004 under the supervision of Professor Clifford L. Henderson.

Cheng-Tsung is a member of the International Society for Optical Engineering (SPIE) and the American Chemical Society. During the Ph.D. study, he has attend numerous conferences and has authored and co-authored over eighteen peer-reviewed papers and SPIE conference proceedings on the subject of advanced resist materials and characterization techniques.